Inaugural Dissertation

for

obtaining the Doctoral Degree

of the

Combined Faculty of Mathematics, Engineering and Natural Sciences

of the

Ruprecht-Karls-University
Heidelberg

Presented by

**M.Sc. Vera Thiel**

Born in Hamm

Oral examination: 16.06.2023

# Analysis of neuronal infiltration in healthy pancreas and pancreatic ductal adenocarcinoma

Referees: Prof Dr. Andreas Trumpp
Prof. Dr. Ingrid Lohmann

*für meine Familie*

# Declaration

The work presented in this dissertation was performed from June 2018 until April 2023 at the Division of Stem Cells and Cancer at the German Cancer Research Center (Deutsches Krebsforschungszentrum, DKFZ, Heidelberg) and the Heidelberg Institute for Stem Cell Technology and Experimental Medicine (HI-STEM gGmbH, Heidelberg) under the supervision of Prof. Dr. Andreas Trumpp and Dr. Martin Sprick.

Declarations according to § 8 (3) c), d) and h) of the Doctoral Degree Regulations:

c) I hereby declare that I have written the submitted dissertation myself and, in this process, have used no other sources or materials than those explicitly indicated.

d) I hereby declare that I have not applied to be examined at any other institution, nor have I used the dissertation in this way or any other form at any other institution as an examination paper nor submitted it to any other faculty as dissertation.

h) I hereby consent to the verification of the dissertation by means of electronic data processing programs against standing scientific standards.

# Summary

Pancreatic ductal adenocarcinoma (PDAC) is one of the most aggressive cancers with a current 5-year survival rate of about 8%. In early non-metastatic stages, surgical resection with chemotherapy may be curative, but because diagnosis is usually too late, surgery is useful in only 20% of cases. Current systemic chemotherapy and/or radiotherapy, targeted- or immunotherapies achieve only short survival benefit. This is probably due to a lack of understanding about the molecular regulatory mechanisms and disease-promoting factors in PDAC. One of the histopathological hallmarks of PDAC is its extensive desmoplastic tumor stroma that includes striking infiltration by peripheral nerve fibers. The peripheral nervous system (PNS) orchestrates physiological organ function during homeostasis and stress. Many cancers in the trunk including PDAC are infiltrated by PNS neurons as part of a dynamic and complex tumor microenvironment. The extent of nerve infiltration correlates directly with tumor aggressiveness. Despite these rather classical observations the molecular and cellular processes connecting infiltrating neurons and the healthy or cancerous pancreas as well as the consequences of these remain poorly understood. This is due to current technical limitations including the fact that the cell bodies of tumor infiltrating neurons are not present in the tumor mass itself, but instead are located in the paravertebral and pre-aortic ganglia of the PNS. Thus, current expression analysis, including single cell transcriptomic analyses of tumor masses exclude these neurons, as their cell bodies are located up to 2 cm distant from the actual tumor in mice.

Here, I first describe the complex array of sensory and sympathetic neurons innervating the normal pancreas and PDAC using three dimensional light sheet fluorescence microscopy imaging (LSFM) of iDISCO cleared full tissues. Second, I report my newly developed "Trace-n-seq" method, that combines retrograde axonal tracing from tissue back to the neuronal nuclei in the peripheral ganglia with FACS-based isolation of individual labeled PNS neurons. This allows to identify and isolate individual tissue infiltrating neurons which I further analyzed by single cell RNA sequencing. In total I characterized >2000 sympathetic and sensory neurons that infiltrate the healthy pancreas and PDAC as well as various other organs. My analysis identified novel types of infiltrating neuronal cells and provide a target-tissue specific transcriptomic landscape of the PNS. My data also suggests PDAC cell mediated reprogramming of infiltrating neuronal behavior. By using the transcriptomic data, I established a Pancreatic-Cancer-Nerve signature and dissected reciprocal neuronal interactions between PDAC cells and stromal cells generating a neuro-cancer-interactome. My data reveal that the reprogramming of neuronal behavior orchestrated by PDAC cells, persists after primary tumor resection. I show evidence that physical or pharmacological inactivation of sympathetic neurons reduces tumor burden.

Moreover, I show that Taxanes induce neuropathy of PDAC-infiltrating neurons as part of their anti-cancer activity, making them a stroma targeting drug beyond its role in inhibiting cell-cycle. In fact, inhibition of neuronal infiltration by systemic or local treatment strategies in combination with nab-Paclitaxel further increased anti-tumor efficacy.

In summary, I developed a new method that allows to identify and characterize infiltrating neurons at single cell resolution and offers new insights into the characteristics of the TME of PDAC. My data provides novel insights into the networks and functions of cancer-infiltrating neurons with direct clinical relevance. This opens new insights into how infiltrating neurons and PDAC cells interact offering novel targeting options and as mechanisms might be similar in other tumor entities, possibility to identify general tumor agnostic targeting options.

# Zusammenfassung

Das duktale Pankreaskarzinom (PDAC) ist eine aggressive Krebsentität mit einer 5-jährigen Überlebensrate von nur 8%. Eine chirurgische Resektion in Kombination mit Chemotherapie kann heilend sein, aber ist nur in 20% der Fälle aufgrund später Diagnosestellung möglich. Die derzeitigen systemischen Chemotherapien und/oder Strahlentherapien, oder Immuntherapien erzielen nur kurzfristige Überlebensvorteile. Dies ist teilweise auf ein mangelndes Verständnis molekularer Regulierungsmechanismen und krankheitsauslösender Faktoren zurückzuführen. Eine der histopathologischen Kennzeichen von PDAC ist das umfassende desmoplastische Tumorstroma, die eine markante Infiltration durch Nervenfasern aufweist. Das periphere Nervensystem (PNS) dirigiert die Organfunktion während der Homöostase und bei Stress. Viele Krebsarten, einschließlich des PDAC, sind von PNS-Neuronen als Teil eines dynamischen und komplexen Tumormikroumfelds infiltriert. Das Ausmaß der Nerveninfiltration korreliert direkt mit Tumoraggressivität. Obwohl diese Befunde einen neuen Forschungsbereich in Bezug auf PDAC eröffnen, bleiben diese Prozesse aufgrund aktueller technischer Einschränkungen unerforscht.

Dies liegt daran, dass die Zellkörper der tumorinfiltrierenden Neuronen nicht im Tumor selbst, sondern in den paravertebralen und preaortalen Ganglien des peripheren Nervensystems (PNS) liegen. Daher sind die aktuellen Expressionsanalysen, einschließlich scRNAseq-Bemühungen, von Tumormassen dieser Neuronen ausgeschlossen, da ihre Zellkörper bis zu 2 cm von dem tatsächlichen Tumor entfernt liegen.

Hier beschreibe ich zunächst das komplexe Array an sensorischen und sympathischen Neuronen, die das normale Pankreas und das PDAC mittels 3D-Lichtscheiben-Fluoreszenzmikroskopie-Bildgebung (LSFM) von iDISCO geklärten Vollgeweben innervieren. Zweitens berichte ich über meine neu entwickelte Methode "Trace-n-seq", die die retrograde axonale Verfolgung vom Gewebe zurück zu den neuronalen Zellkernen in den peripheren Ganglien mit der FACS-basierten Isolierung einzelner markierter PNS-Neuronen kombiniert. Dadurch können einzelne infiltrierende Neuronen identifiziert und isoliert werden, die ich durch Einzelzell-RNA-Sequenzierung weiter analysiert habe. Insgesamt charakterisierte ich > 2000 sympathische und sensorische Neuronen, die das gesunde Pankreas und das PDAC, sowie verschiedene andere Organe infiltrieren. Durch meine Analysen identifiziere ich neuartige neuronalen Zelltypen und stelle ein zielgewebespezifisches PNS-Transkriptomprofil zur Verfügung.

Meine Daten zeigen eine Neuprogrammierung des neuronalen Verhaltens, die von den Tumorzellen orchestriert wird, und ich etabliere eine Cancer-Nerve-Signatur, die sogar nach primärer Tumorresektion bestehen bleibt. Ich zeige, dass die physische oder pharmakologische Inaktivierung sympathischer Neuronen das Tumorvolumen reduziert. Darüber hinaus zeige ich, dass Taxane als Teil ihrer Anti-Krebs-Aktivität eine Neuropathie von PDAC-infiltrierenden Neuronen induzieren, wodurch sie zu einem Stroma-zielmedikament jenseits ihrer Rolle bei der Hemmung des Zellzyklus werden. Tatsächlich erhöht die Hemmung der neuronalen Infiltration durch systemische oder lokale Behandlungsstrategien in Kombination mit nab-Paclitaxel die Anti-Tumor-Wirksamkeit weiter.

Zusammenfassend habe ich eine neue Methode entwickelt, die es ermöglicht, infiltrierende Neuronen in Einzelzellauflösung zu identifizieren und zu charakterisieren, und neue Einblicke in die Eigenschaften des TME von PDAC bietet. Meine Daten liefern neue Erkenntnisse über die Netzwerke und Funktionen von Krebs-infiltrierenden Neuronen mit direkter klinischer Relevanz. Dies eröffnet neue Einblicke in die Interaktionen zwischen infiltrierenden Neuronen und PDAC-Zellen und bietet neue Zieloptionen. Da die Mechanismen möglicherweise in anderen Tumorarten ähnlich sind, besteht die Möglichkeit, allgemeine, tumoragnostische Zieloptionen zu identifizieren.

# Table of Contents

# 1 Introduction

## 1.1 Pancreatic Cancer

Pancreatic cancer is an aggressive disease with a dismal and poor prognosis [1]. The pancreas is located in the abdomen, behind the stomach and in front of the Aorta and Vena cava. It is situated between the duodenum (the first part of the small intestine) and the spleen and in physiological conditions produces hormones and enzymes that aid in digestion and regulate glucose metabolism. In the Western World, pancreatic cancer is the fourth leading cause of cancer-related deaths and is projected to become the second leading cause by 2030 [2]. The 5-year survival rate for pancreatic cancer is only ~9%, which is the lowest survival rate among all cancers [1]. The causes of pancreatic cancer are not well understood, but risk factors include age, smoking, obesity, and family history as well as inflammatory events like chronic pancreatitis and infectious agents [3, 4].

The pancreas comprises two distinct organs, the exocrine and endocrine pancreas. The former, which accounts for 95% of pancreatic tissue mass, produces digestive enzymes for nutrient assimilation [5]. The latter maintains glucose homeostasis through peptide hormone secretion [5, 6]. Pancreatic cancers are classified as exocrine or endocrine, with pancreatic ductal adenocarcinoma (PDAC) originating from the exocrine pancreas and pancreatic neuroendocrine tumors (PNETs) accounting for 1-20% of all pancreatic tumors. While PNETs were thought to arise from the endocrine islets, recent studies suggest they may develop from oligopotent cells in the ductal epithelium [7].

Environmental factors such as chronic pancreatitis, diabetes, obesity, smoking, and hereditary components, including several germline mutations (e.g., ATM, BRCA1/2, CDKN2A, FANCC, FANCG, PALB2, MLH1, PRSS1, STK11 or TP53), have been associated with pancreatic cancer development. Chronic pancreatitis, in particular, has been shown to increase the risk of pancreatic cancer by more than 13-fold and is characterized by progressive inflammatory disease involving fibrosis, acinar and islet cell loss [8, 9].

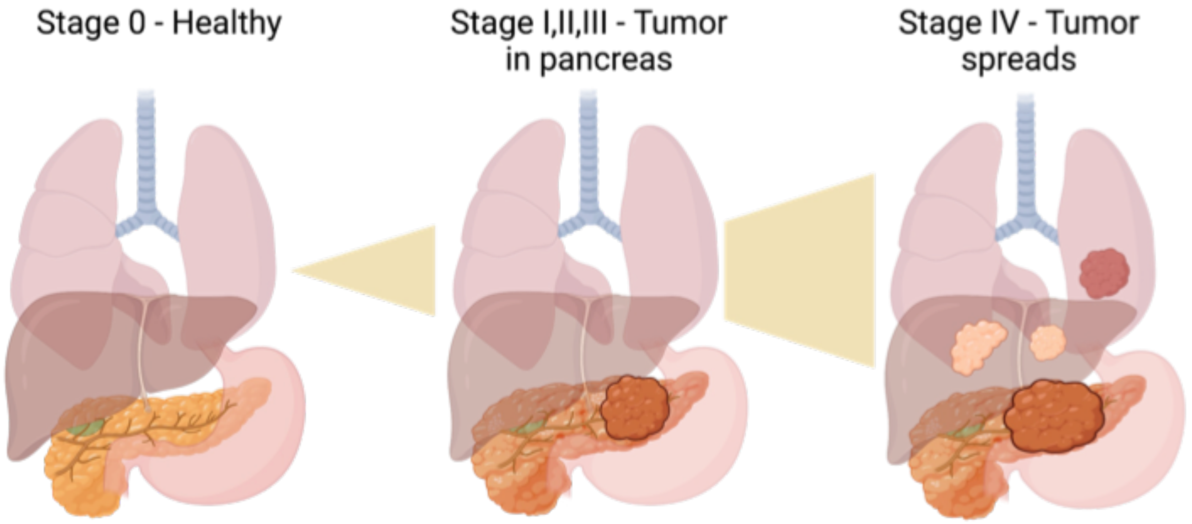

**Figure 1: Pancreatic cancer stages-** Pancreatic cancer is typically classified into four stages: developing from stage 0-the healthy pancreas: stage I, stage II, stage III and stage IV. Stage I is the earliest stage and it is characterized by the cancer being confined to the pancreas. In stage II, the cancer may have spread to nearby lymph nodes. In stage III the cancer has spread further and may have invaded nearby organs such as the stomach or the duodenum. In stage IV the cancer has metastasized and spread to distant organs such as the liver, lungs, or peritoneum. The stage of the cancer determines the treatment options and the prognosis.

Pancreatic cancer is often diagnosed at a late stage, with distant metastasis already present at diagnosis, which complicates treatments and reduces the chances of survival. The American Cancer Society states that only about 20% of cases are diagnosed in the early stages, when the cancer is still confined to the pancreas and local lymph nodes (Stage I-III). This is in part due to the lack of specific symptoms in the early disease stages and the lack of effective screening methods (**Figure 1**). Metastasis are most commonly detected in the liver, lungs, peritoneum (the lining of the abdominal cavity), and lymph nodes [3, 4, 10-12].

## 1.2 Different subtypes of pancreatic cancer

According to the World Health Organization (WHO) classification, there are several subtypes of pancreatic cancer that can occur, each with its own unique characteristics and prognosis [13].

Adenocarcinomas are the most common type of pancreatic cancer and initiates in the cells that line the ducts of the pancreas. It accounts for about 95% of all cases. This type of tumor arises from the exocrine cells of the pancreas and can manifest in different forms, such as ductal adenocarcinoma, mucinous cystadenocarcinomas, and signet ring cell carcinoma [13]. Ductal adenocarcinoma is the most common form, characterized by the presence of malignant cells within the ducts of the pancreas. Mucinous adenocarcinoma, on the other hand, is characterized by the presence of large amounts of mucus within the tumor, which can make it difficult to diagnose and treat [12]. Signet ring cell carcinoma, also known as colloid carcinoma, is a rare subtype of adenocarcinoma characterized by the presence of malignant cells that resemble small, oil droplets [14].

Pancreatic neuroendocrine tumors (PNETs) originate from the cells that produce hormones. PNETs account for about 1-2% of all cases. PNETs arise from the endocrine cells of the pancreas and can present in different forms, such as insulinoma, gastrinoma, and VIPoma [15].

Other rare forms are acinar cell carcinomas that start in the cells that make up the acinar cells or solid pseudopapillary tumor of the pancreas (SPT) which is a rare type of tumor that occurs mostly in young women and has better prognosis than adenocarcinoma.

It is important to note that the treatment and prognosis for each type of pancreatic cancer can vary depending on the specific subtype and the stage of the cancer at the time of diagnosis. Determining the specific subtype of the tumor is crucial for accurate diagnosis and effective treatment.

## 1.3 Pancreatic ductal adenocarcinoma (PDAC)

PDAC displays a highly infiltrative growth pattern, with a desmoplastic reaction and hypoxic microenvironment. The majority of PDAC cases (65%) arise in the pancreatic head, with the remainder in the body (15%) or tail (15%) [3, 4, 13, 16]. Obstruction of bile and pancreatic ducts, resulting in painless jaundice and pancreatitis, can be caused by tumors originating in the pancreatic head [17].

Early staged PDAC can be removed by surgery, however, 60 to 70% of the patients suffer from recurrence in the subsequent years [18]. Since the early detection is very difficult, most patients are diagnosed with advanced staged PDAC that has already spread to other organs. In fact, those patients only receive palliative treatment [19]. Advanced pancreatic cancer typically causes symptoms such as abdominal or back pain, jaundice, wasting syndrome, and nausea. As the disease progresses, systemic symptoms may appear, including weakness, loss of appetite, abnormal blood sugar levels, and new-onset diabetes mellitus [4].

The 8th edition of the American Joint Committee on Cancer (AJCC) staging system is used to stage PDAC based on local tumor grade, regional lymph node dissemination, and distant metastatic spread (TNM staging) [20, 21]. Molecular pathology suggests a stepwise progression from premalignant pancreatic lesions to invasive malignancy, with pancreatic intraepithelial neoplasia (PanIN) being the most common microscopic precursor lesion [16]. PanINs are subclassified as low-grade or high-grade depending on the degree of dysplasia and often display genetic alterations similar to those found in infiltrating pancreatic cancer (**Figure 2**) [11, 22-24].

Non-resectable PDAC is either treated with chemotherapy, radiotherapy, or a combination of both [25]. In the past years many regimens containing novel agents like immune-checkpoint inhibitors have been tested targeting PDAC, but failed [25, 26]. Since its approval by the Federal Drug Administration (FDA) in 1996, the chemotherapeutic agent gemcitabine is given as a standard treatment. It is a nucleoside analog that is incorporated into DNA during cell division and leads to a stop of the DNA strand synthesis [4]. Combinations of compounds, like gemcitabine and nab-paclitaxel were found to improve overall survival [27]. The FOLFIRINOX regimen that consists of a combination treatment of folinic acid, 5-fluorouracil, irinotecan and oxaliplatin has been reported to gain the highest increase in survival of 11.1 months observed in a phase III study on PDAC. The average survival was approximately four months longer than for patients that were treated with gemcitabine only [28]. Until now the effective regimens used for PDAC only contain classic chemotherapy agents that are accompanied by severe side-effects like peripheral neuropathy, which is often therapy limiting [2, 19, 25, 29].

Recent studies have questioned the traditional belief that PDAC arises solely from ductal cells, as early progenitor cells, exocrine cells, and even acinar and insulin-producing cells have been shown to give rise to PanIN lesions [30]. Thus, several models propose that PDAC precursors may originate in the acinar compartment and develop into PanIN and PDAC through acinar-to-ductal metaplasia [31, 32]. However, the exact cell origin of PDAC remains unclear and multiple origins may exist simultaneously.

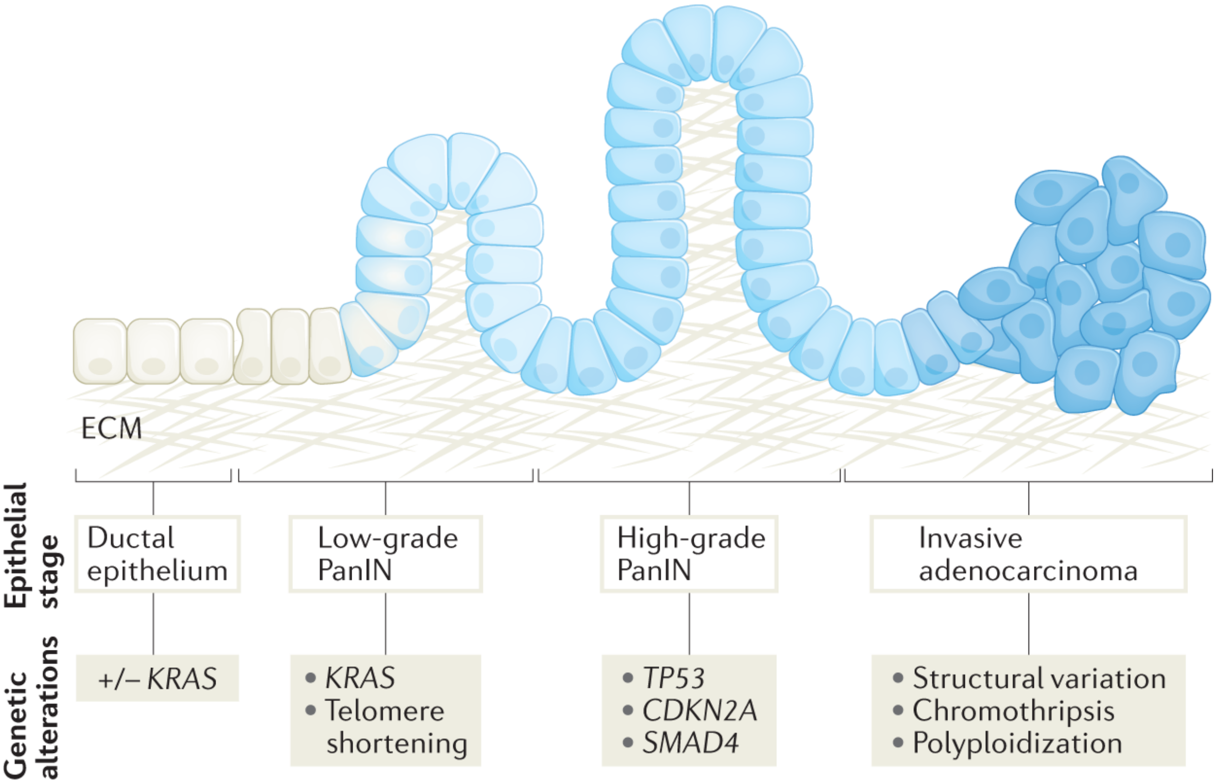

**Figure 2:** Schematic of progression from normal pancreatic ductal epithelium to low-grade and high-grade dysplastic pancreatic intraepithelial neoplasias (PanINs) to invasive adenocarcinoma. Corresponding genetic alteration are displayed with the epithelium stage. KRAS activating mutations occur in normal duct cell and low-grade PanINs bear the earliest somatic changes of KRAS oncogene activation and telomere shortening. Inactivation of TP53, CDKN2A and/or SMAD4 accumulates in high-grade PanINs. Invasive adenocarcinomas finally display structural and copy number variants. Adapted from Connor *et al.* [11].

The dominant mutations in PDAC are *KRAS, TP53, CDKN2A* and *SMAD4*. *KRAS* is the most common mutated gene and is an activating mutation. Telomere shortening and KRAS mutations occur earliest in low-grade PanIN [33]. Over 90% of low-grade PanIN contain KRAS mutations [34]. Activating point mutations in *KRAS* lead to the constant expression of RAS that induces cell proliferation and survival through the activation of the mitogen- activated protein kinase (MAPK) pathways [4, 35]. *CDKN2A, TP53* and *SMAD4* mutations occur later in high-grade PanIN and in 50-80% of invasive PDAC [36]. The inactivation of *TP53* induces pancreatic neoplastic progression. TP53 has a critical role in cell cycle arrest, DNA repair and induction of apoptosis and the loss of *TP53* enhances the accumulation of genetic alterations [4]. *CDKN2A* is a tumor suppressor leading loss of cell cycle control and increased cell growth and *SMAD4* deletion abrogates transforming growth factor signalling (TGFß) [4, 25]. Furthermore, oncogenes like *MYC, GATA6* and *MET* are commonly amplified in PDAC and epigenetic changes altering gene expression as well as altered expression in miRNAs influence the genetic landscape of precursor lesions and PDAC [37, 38].

One of the hallmarks of PDAC is the formation of a dense desmoplastic stroma. About 90% of the PDAC tumor mass is constituted by stroma containing activated fibroblasts, immune cells, blood vessels, matricellular proteins and neural cells [3, 39]. Activated Pancreatic Stellate Cells (PSC)s secrete ECM components and express various proteins [40]. PSCs control ECM turnover, cancer cell proliferation, migration, and metalloproteinase secretion. The stroma created by PSCs is associated with poor vascularization, a hypoxic microenvironment, and therapeutic resistance [39-41].

## 1.4 The peripheral nervous system

The peripheral nervous system (PNS) consists of all nerves that branch out of the brain and spinal cord. Functionally, the PNS can be divided into the autonomic and somatic nervous systems. These can be further subdivided into sympathetic and parasympathetic for the automatic and into sensory and motor divisions for the somatic nervous system [42]. Peripheral nerves represent an essential component of the cellular microenvironment of all tissues and organs. The term "neuron" refers to a specialized cell that transmits electrical and chemical signals in the nervous system, while "nerve" refers to a bundle of neurons and glia, including their axons, that convey information between the brain and other parts of the body. All human tissues are infiltrated by nerves except of cartilage and lens and they connect all organs to the central nervous system (CNS). The PNS transmits motor and sensory information between the CNS and peripheral body tissues. Neurons are necessary for sensation, cognition, locomotion and regulation of internal organs. They further effect tissue development, repair, and regeneration [43, 44]. The PNS in general coordinates the cellular-, molecular and organ-level processes in order to maintain homeostatic control in the body like controlling blood pressure, pH and metabolism [45]. The autonomic nervous system (ANS) controls involuntary cardiac, smooth and glandular cells, and consists of sympathetic and parasympathetic divisions. The somatic nervous system (SNS) controls voluntary skeletal muscles and somatic sensation processing. Afferent neurons carry information towards the CNS, while efferent neurons transmit information or impulses from the CNS to the PNS. Afferent nerves transmit general sensations and special senses, while efferent neurons initiate voluntary and involuntary motor functions in effector organs like smooth muscles, visceral organs, and glands. [46].

A human possesses 31 pairs of spinal nerves- eight cervical, twelve thoracic, five lumbar, five sacral, and one coccygeal. The numbers arise from their vertebral column exit level [29, 47]. Different subtypes of sensory neurons and their function in the body are well established. Photoreceptor neurons are specialized for detecting light, and are found in the retina of the eye.

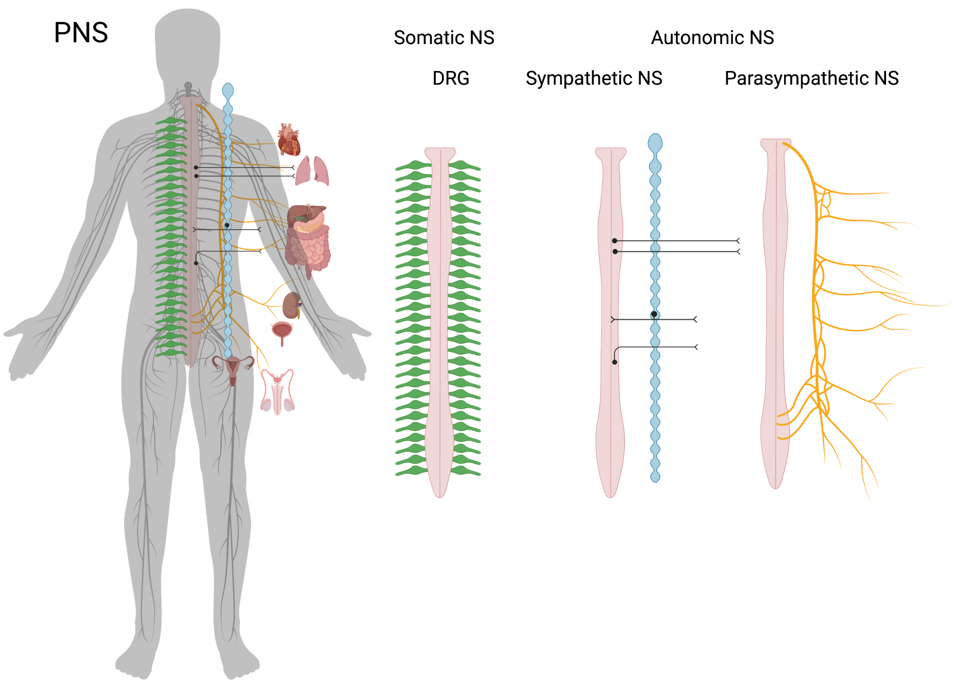

**Figure 3**: The peripheral nervous system (PNS) is the part of the nervous system that is located outside the brain and spinal cord. The PNS can be divided into two main branches: the somatic and the autonomic nervous systems: The somatic nervous system is responsible for the voluntary control of skeletal muscles, such as those used in moving the arms and legs. It is composed i.a. of sensory neurons that transmit information about touch, pain, temperature, and muscle position. The autonomic nervous system is responsible for the regulation of the body's internal organs and glands, such as the heart, lungs, and digestive tract. It is divided into two branches: the sympathetic nervous system, which activates the "fight or flight" response, and the parasympathetic nervous system, which regulates the "rest and digest" response.

Thermoreceptor neurons are specialized for detecting changes in temperature, and are found in the skin and other internal organs. They are responsible for sensing heat and cold, and play a role in regulating body temperature. Mechanoreceptors neurons are specialized for detecting mechanical stimuli, such as pressure, touch, and vibrations. They are found in the skin, muscles, and joints, and are responsible for sensing movement and providing feedback for muscle control. Nociceptors are specialized for detecting pain, and are found in the skin and internal organs. They are responsible for sensing injury and inflammation, and play a role in pain perception and the body's response to injury. Proprioceptors are specialized for detecting changes in body position, and are found in muscles, joints, and tendons. They are responsible for sensing movement and providing feedback for muscle control, and play a role in balance and coordination. And last, chemoreceptors are specialized for detecting chemicals, such as tastes, odors, and blood glucose levels. They are found in the tongue, nose, and other internal organs, and play a role in taste, smell, and nutrient metabolism [47]. Sensory axons synapse with sensory neurons and release various neuropeptides and neurotransmitters, such as substance P and calcitonin gene-related peptide (CGRP) among others, which are involved in the detection of pain, temperature, and other sensory information. Sensory axons are also present in blood vessels, where they are involved in sensing changes in blood pressure, flow, and temperature, and participate in the regulation of blood pressure and flow [48, 49].

The sympathetic and sensory innervation patterns of tissues vary depending on the specific tissue they innervate and the stage of development. In general, sympathetic axons originate from the spinal cord and project to various organs and tissues through the sympathetic trunk and prevertebral ganglia as the celiac ganglion, where they synapse with postganglionic neurons. In blood vessels, sympathetic axons are present in the adventitia, media and intima and play a role in controlling the diameter of blood vessels, thereby regulating blood flow and pressure [48]. The ANS controls involuntary functions and provides sensory and motor innervation to smooth muscles, blood vessels, glands, and internal organs thereby regulating visceral and glandular function- or in other words- maintaining homeostasis [50].

Single cell RNA sequencing (scRNA-seq) has emerged as a powerful tool to study the cellular heterogeneity and gene expression patterns of neurons in the peripheral nervous system (PNS). Several studies have utilized scRNA-seq to generate comprehensive datasets of neurons in various PNS tissues and enabled the comprehensive analysis of neuronal diversity in the PNS. scRNAseq datasets have provided insights into the molecular and functional diversity of sensory and autonomic neurons in various tissues, such as the dorsal root ganglia, sympathetic ganglia, and enteric nervous system. These studies have identified novel subtypes of neurons and revealed new markers for their classification, which may have important implications for understanding their roles in health and disease.

For example, a recent study by Usoskin *et al.* characterized the molecular diversity of sensory neurons in mouse dorsal root ganglia, identifying distinct subtypes and revealing their developmental trajectories. This study characterized the transcriptome of individual sensory neurons in the dorsal root ganglia of mice, identifying distinct subtypes of nociceptors, mechanoreceptors, and proprioceptors. [51]. Another study by Bai *et al.* and Kupari *et al.* analyzed gene expression profiles of neurons in human dorsal root ganglia, uncovering novel markers and potential therapeutic targets for pain and sensory disorders [52, 53]. Others like Renthal *et al.* describe specific injury signatures of dorsal root ganglia [54, 55].

Other scRNA-seq studies have focused on sympathetic ganglia, such as the work by Furlan *et al.* that identified transcriptional regulators and signaling pathways involved in sympathetic neuron control of goosebumps [51, 56].

Similarly, a study by Kabra *et al.* examined gene expression patterns in enteric ganglia of the mouse gut, highlighting the heterogeneity and complexity of this neural network [57].

The scRNA-seq studies by Zeisel *et al*. and Sharma *et al.* represent significant contributions to our understanding of the transcriptome of sensory and sympathetic neurons, respectively.

In 2018, Zeisel *et al*. provided a landmark study of the “Molecular Architecture of the Mouse Nervous System” including the characterization of the transcriptomic diversity of mouse neurons in the dorsal root ganglia and sympathetic trunk. By profiling over 23,000 individual cells (however mostly CNS neurons glia, smooth muscle cells), they identified dozens of distinct neuronal subtypes and revealed their molecular signatures, including unique combinations of ion channels, receptors, and neuropeptides. The authors also used their dataset to construct a comprehensive atlas of somatosensory neuron subtypes, which has become a valuable resource for researchers studying pain, touch, and other sensory functions [58]. In their study they identified three main sensory subtypes; Neurofilaments (NEFM), peptidergic- (PEP) and non-peptidergic (NPEP) sensory neurons. In general, neurofilament sensory neurons are characterized by their large diameter. They are also characterized by the presence of a high amount of neurofilaments, which are intermediate filament proteins that provide structural support to the neuron's cytoskeleton. They are also known to be fast-conducting and involved in the detection of pressure and vibrations. Peptidergic sensory neurons on the other hand are characterized by the release of peptide neurotransmitters, such as calcitonin gene-related peptide (CGRP), in response to noxious stimuli. These neurotransmitters are involved in the transmission of pain signals to the central nervous system and in the regulation of inflammatory responses. Peptidergic neurons are also known to be small-diameter neurons. Non-peptidergic sensory neurons are similar in size, but are characterized by the release of non-peptide neurotransmitters, such as glutamate and Gamma-aminobutyric acid (GABA), in response to noxious stimuli. They are also involved in the transmission of pain signals to the central nervous system and in the regulation of inflammatory responses [47, 59-62].

Similarly, in 2020 and 2021, Sharma *et al*. published a study using scRNA-seq to investigate the molecular diversity of sensory neurons in mouse dorsal root ganglia. Through the profiling of over 70,000 cells, they identified multiple subtypes of sensory neurons and characterized their gene expression patterns, including novel genes and signaling pathways involved in neuron development and function. The authors also used their dataset to construct a new classification system for sensory neuron subtypes, which has important implications for understanding the peripheral nervous system's role in physiology [61, 63].

To decipher the neuronal subtypes as annotated by Sharma *et al.* in more detail, the authors describe several different subtypes of somatosensory neurons that have unique functional characteristics.

Aβ-field-LTMR cells: These neurons are specialized for sensing light touch, such as the sensation of a feather brushing against the skin. They are found in the skin and are activated by gentle pressure.

Aβ-RA-LTMR cells: Similar to Aβ-field-LTMR cells, these neurons are also specialized for sensing light touch, but they are found in deeper tissues such as the muscles and joints.

Aδ-LTMR cells: These neurons are specialized for sensing fast, intense touch, such as the sensation of a pinprick. They are found in the skin and are activated by intense pressure or fast vibrations.

C-LTMR cells: These neurons are specialized for sensing cold temperatures. They are found in the skin and are activated by cold temperatures.

CGRP-α cells, CGRP-ε cells, CGRP-η cells, CGRP-γ cells, CGRP-θ cells, CGRP-ζ cells: These neurons are specialized for sensing pain. They are found in various tissues and are activated by various types of noxious stimuli. They are known as CGRP-expressing neurons, as they all express Calcitonin Gene-Related Peptide (CGRP)

MRGPRD cells: These neurons are specialized for sensing itch. They are found in the skin and are activated by various types of pruritogens.

Proprioceptors: These neurons are specialized for sensing the position and movement of the body, such as muscle stretch and joint position. They are found in muscles and joints.

SST cells: These neurons are specialized for sensing slow, sustained touch, such as the sensation of a firm handshake. They are found in the skin and are activated by slow, sustained pressure.

Cold thermoceptor cells: These neurons are specialized for sensing cold temperatures. They are found in skin and specifically in the Merkel cells of the epidermis, which are activated by cold temperatures.

Both studies provide unprecedented insights into the molecular diversity and functional roles of PNS neurons, demonstrating the power of scRNA-seq to reveal previously unknown aspects of neural biology. Overall, scRNA-seq datasets of PNS neurons have greatly expanded our understanding of their molecular identities and functional roles, providing a valuable resource for further investigation and potential therapeutic interventions. These different datasets have already led to new discoveries and are expected to continue to advance our understanding of the PNS and its associated disorders [47].

However, there are only very few studies that include information about the target tissues of neurons, as these neurons are not part of the tissue mass [56, 64-66] and none of those contain information about malignancies.

## 1.5 Impact of neuronal infiltration in PDAC

Over the past decades the contribution of the microenvironment to cancer progression has been extensively characterized and exploited to develop drugs targeting angiogenesis or reactivating immune checkpoints [67-70]. Our understanding of the different cell types present in the cancer has been revolutionized by the development of scRNA-seq techniques allowing for the isolation of rarer, unknown cell types and identification of different cell states with unique functional properties within known cell types like fibroblasts [71, 72]. However, the contribution of peripheral neurons to tumor progression has so far only been accessible to functional assays showing them to be an important modulator of cancer progression in various cancer types, with effects depending on the neuronal subpopulations investigated [44, 45]. As perikarya of the effector neurons of the peripheral nervous system are located within the sympathetic trunk or prevertebral ganglia (sympathetic neurons), dorsal root ganglia (sensory neurons), spinal cord (motoneurons) or adjacent to the target organ (parasympathetic neurons) [45], these cells are not included in scRNA-seq datasets of digested tissue.

One of the hallmarks of PDAC is the desmoplastic stromal ecosystem including various subtypes of immune, endothelial and stromal cells as well as massively hypertrophic neuronal structures [73, 74]. All these cell types interact and make up to 80% of the cellular content of a cancer. However, the absence of scRNA-seq dataset of neurons makes it difficult to analyze the interaction of these cells with surrounding cells of the tumor microenvironment (TME).

The healthy pancreas is innervated by both the sympathetic and parasympathetic nervous system. The sympathetic innervation comes from the celiac and superior mesenteric ganglia and the parasympathetic innervation from the vagus nerve.

The sympathetic and parasympathetic innervation of the pancreas has been shown to play a role in the development and progression of pancreatic cancer. Studies have shown that increased sympathetic activity in the pancreas is associated with a higher risk of developing pancreatic cancer, and that drugs that target the sympathetic nervous system may have potential as treatments for the disease [75]. Especially sympathetic neurons have been implicated in PDAC progression and pharmacological or surgical intervention has been proposed to increase survival in mouse models and retrospective analysis [76]. The sympathetic innervation in the healthy pancreas is responsible for vasoconstriction, regulating blood pressure, blood flow and hormone release, while the parasympathetic innervation controls exocrine and endocrine secretion [48]. In pancreatic cancer, the sympathetic innervation is often disrupted, leading to decreased enzyme and bicarbonate secretion. This can result in malabsorption and nutrient deficiencies [75]. On the other hand, the parasympathetic nervous system may have a protective role, as studies have found that it may inhibit the development and progression of pancreatic cancer [75].

Moreover, pain induced by perineural invasion of sensory neurons is a haunting feature of PDAC and associates with poor prognosis [77]. Recent studies have shown that sensory innervation, or the presence of nerve fibers that are sensitive to pain and other sensations, plays a role in the development and progression of pancreatic cancer. Research has found that tumors in the pancreas are highly innervated by sensory nerves, and that this innervation is associated with increased tumor growth, invasion, and metastasis [78, 79]. PDAC cells can induce axonogenesis by secreting factors like NGF and use nerves as structures for malignant outgrowth (perineural invasion) [74, 76]. Nevertheless, the interactions between neurons, immune, stromal and cancer cells itself remain poorly understood but understanding the underlying mechanisms holds major translational relevance.

In conclusion, the neuronal innervation of the pancreas plays a crucial role in both the normal function of the pancreas and in the progression of pancreatic cancer. Further research is needed to fully understand the mechanisms by which the sympathetic and sensory nervous systems regulate pancreatic cancer, in order to develop more effective treatments for this deadly disease.

## 1.6 3D Quantification of tissue innervating neurons

3D nerve quantification, tissue clearing, and light sheet microscopy are techniques used to visualize and study the 3D structure of nerve cells in tissue samples. Tissue clearing techniques such as CLARITY, SCALE, CUBIC or iDISCO enable researchers to render opaque tissues transparent, allowing for deeper imaging and more accurate quantification of nerve cells [80]. Light sheet microscopy is a high-resolution imaging technique that uses a thin sheet of light to capture 3D images of entire organs or tissues without the need for sectioning or slicing. This allows for fast, low-phototoxicity imaging of large samples, such as whole organisms or tissues [80, 81]. By combining these techniques, researchers are able to visualize and study the complex 3D structure of nerve cells in tissues such as the brain, spinal cord, and peripheral nervous system, and gain a deeper understanding of their functions and interactions. These techniques have the potential to advance our understanding of neuronal development, regeneration, and diseases such as neuropathies and neurodegenerative disorders.

3D quantification of nerve structures is necessary to obtain a more comprehensive understanding of the complexity and spatial organization of nerves within organs. In contrast to 2D imaging, which only provides a single plane of information, 3D imaging allows for the visualization of nerves in their full three-dimensional context, enabling the identification of nerve trajectories and connections that may be missed in 2D. This is particularly important in complex organs such as the brain or pancreas, where nerves are densely packed and have complex three-dimensional structures that cannot be fully captured in 2D. Additionally, 3D quantification allows for the accurate measurement of nerve length, volume, and branching patterns, which are important parameters for assessing nerve function and pathology as is recently being addressed in the field [80-82]. These patterns and the level of innervation can be quantified using machine learning algorithms. Machine learning is a subset of artificial intelligence that involves training algorithms to make predictions or decisions based on data. In science, machine learning algorithms have been applied to a variety of fields, including image and signal analysis, drug discovery, and predictive modeling of complex systems. In image analysis, machine learning algorithms can be used to classify and segment images, automatically identify features, and extract useful information [83].

Overall, 3D quantification provides a more detailed and accurate picture of nerve structure and function compared to 2D methods.

## 1.7 Identification of tissue innervating neurons

Retrograde tracing is a technique used to study the connections of neurons in the nervous system. The technique involves injecting a tracing agent, such as a virus or a dye, into a specific region of the body or into a specific target tissue, and then observing the distribution of the tracer in other areas of the nervous system [84, 85]. The tracer is typically taken up by the axons of neurons and the tracing agent then travels back (retrograde) up the axons of the neurons (i.e., in the opposite direction of normal axonal transport) that innervate the region or tissue where the tracer was injected, allowing researchers to visualize and identify the neuron cell bodies that are connected to that specific area. By examining the distribution of the tracer, researchers can infer the pattern of connectivity between different regions of the nervous system [84].

Horseradish peroxidase was the first retrograde tracer used to demonstrate connections in the nervous system [86]. Since 1978, fluorescent retrograde neuronal tracers and AAVs have been utilized to identify the cell bodies of axonal projections [87]. Currently, there are various commercial products available with varying efficacy for labeling neurons. The most common substances that can be used for retrograde tracing, are fluorescent dyes, lipophilic tracers, and viral vectors. Different tracers have different properties and are useful for different types of experiments. For example, fluorescent dyes can be used to visualize neurons *in vivo*, while viral vectors can be used to transfect neurons with a specific gene or barcode [84, 86, 87]. One commonly used retrograde tracer is Fluoro-Gold, which is taken up by neurons and transported along the axon to the cell body where it accumulates. Another retrograde tracer is cholera toxin subunit B (CTB), which is taken up by neurons and transported to the cell body via endocytosis. CTB can be conjugated to a variety of labels, such as fluorescent dyes or enzymes, for visualization and quantification [84].

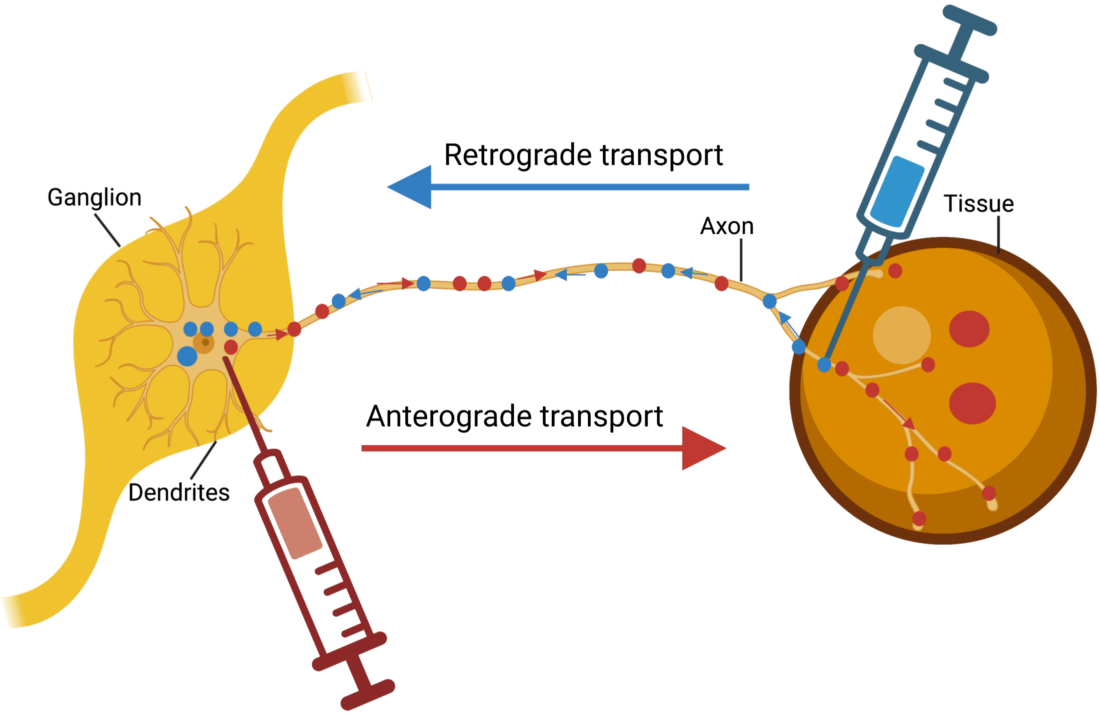

**Figure 4:** Schematic of anterograde and retrograde tracing. A tracer (AAV or dye) is injected either in the axon terminals of a tissue and is retrogradely transported into the cell bodies, or the tracer is injected into the ganglion and is anterogradely transported along the axons into the infiltrating tissue.

Adeno-associated viruses (AAVs) can also be used as retrograde tracers. AAVs are small, non-pathogenic viruses that are commonly used in gene therapy and neural circuit mapping. AAVs can be engineered to express fluorescent proteins or other reporters, which are transported in a retrograde direction along axons and can label the cell bodies of connected neurons. AAVs have the advantage of long-term expression, making them useful for long-term tracing experiments.

However, they can be limited by their tropism, or preference for certain types of neurons, and can potentially trigger an immune responses [85, 88].

The stability of retrograde tracers varies depending on the type of tracer and the experimental conditions. Some tracers, such as Fluoro-Gold, are stable for several weeks, while others are rapidly degraded and cleared from the tissue within a few days [84].

Retrograde tracing combined with single cell sequencing allows researchers to identify and study the specific neurons that innervate a target tissue or region and to identify the molecular characteristics of these neurons at a single cell level. This can provide insights into the diversity and functions of neurons in the nervous system, as well as the underlying mechanisms of disease or injury.

Anterograde nerve tracing is a technique used to trace the projections of neurons from their cell bodies to their synaptic targets. This technique involves labeling the cell bodies of neurons with a tracer that is then transported down the axon to the terminal, allowing researchers to map the connections of the neuron. One commonly used tracer for anterograde nerve tracing is biotinylated dextran amine (BDA), which is transported to the postsynaptic targets. Other tracers include Wheat Germ Agglutinin [84, 89].

*In vivo* anterograde nerve tracing has been used in various studies to investigate neural circuits and connections in the brain and peripheral nervous system [90].

## 1.8 The need for "Trace-n-Seq"

Single cell sequencing of peripheral neurons involves (1) isolating individual neurons from a sample and then (2) the use of high-throughput sequencing techniques to analyze the transcriptome of each cell. This can provide valuable insights into the diversity and characteristics of neurons within tissue specific neuronal populations. The data generated from single cell sequencing can be used to identify genes and pathways that are involved in the development, function, and disease of peripheral neurons. Additionally, single cell sequencing can be used to investigate the molecular differences between different types of peripheral neurons, such as sensory neurons, motor neurons, and autonomic neurons. This technology is particularly useful for studying rare or difficult to access neuronal subtypes and can provide a more detailed understanding of neural physiology and neural neurology. Single cell sequencing of peripheral neurons can provide a detailed understanding of the genetic and functional diversity of these cells. However, there are several challenges that need to be overcome to obtain accurate and reliable results [91] like sample preparation. Peripheral neurons are difficult to isolate and purify from other cell types, such as glial cells, which can lead to contamination of the sequencing data. Also, peripheral neurons are limited in numbers, which makes it difficult to obtain enough cells for representative sequencing results. Inherently, in single cell sequencing methods there is considerable variation in the quality and reliability of different sequencing platforms. Importantly, the high dimensional and complex data generated by single cell sequencing requires sophisticated computational and bioinformatic techniques to be analyzed effectively, however there are only few datasets available to compare and annotate cell quality and expression profiles. As peripheral neurons are a highly heterogeneous population, their genetic and functional diversity can be difficult to quantify in low numbers.

Despite these challenges, single cell sequencing of peripheral neurons is a powerful tool for understanding the underlying mechanisms of peripheral neuron physiology and potential therapeutic target discovery. With continued technical improvements and refined sample preparation techniques, the future of single cell sequencing of peripheral neurons is expected to yield exciting new insights into the biology of these cells.

There are several resources for studying pancreatic cancer and its associated cellular and molecular processes. The Cancer Genome Atlas (TCGA) has a pancreatic ductal adenocarcinoma (PDAC) dataset that includes genetic, transcriptomic, and proteomic data. Additionally, the Broad Institute's Cancer Cell Map has a database of PDAC cell lines, as well as information on their genetic and pharmacological profiles. Finally, the International Cancer Genome Consortium (ICGC) also has a Pancreatic Cancer project which aims to characterize the genomic changes in PDAC. Unfortunately, there does not seem to be a publicly available dataset specifically for PDAC or any other tumor innervating neurons. These cells lack in every single cell dataset of tumors except for the brain. However, the PNS neurons are responsible for sending and receiving signals to and from target organs and are associated with tumor progression. These datasets are a missing piece of the PDAC puzzle, as they include information on the different types of cells that make up this system and the TME, as well as the genes and proteins that are expressed in these cells. This information can help researchers understand how the PNS works and how it is affected by different diseases like cancer.

# 2 Aim of this study

The sympathetic and sensory nervous system play a key role in regulating organ function. A unique feature of PDAC is the strong infiltration by nerve fibers which correlates directly with tumor spread. Although different cell types of the TME have been molecularly analyzed, tumor-infiltrating neurons could not be considered so far, because their cell bodies are located in adjacent ganglia of the peripheral nervous system and thus are not part of the tumor mass. Using 3D light sheet fluorescence microscopy imaging (LSFM) of fully cleared pancreas and PDAC specimens, I investigated the complex innervation of PDAC by sensory and sympathetic neurons, and compared it to healthy tissue. I also proposed that cancer cells may reprogram the behavior of infiltrating neurons. To this aim, I developed a novel method called Trace-n-seq, which combines retrograde axonal tracing, FACS analysis, and scRNAseq to isolate and analyze individual neurons infiltrating tumors or their respective healthy organs. Thereby, I intended to identify previously undescribed neuronal cell types and provide a landscape of sympathetic and sensory neurons innervating the healthy pancreas as well as PDAC. I hypothesized that the single cell transcriptomic analysis reveals signs of reprogramming of neuronal behavior orchestrated by the tumor cells. I planned to show that a specific Pancreatic-Cancer-Nerve-Signature will be obtained from cell expression analysis. Moreover, an objective of this study was to investigate, whether targeting these neurons reduces tumor burden in order to identify a new mechanism of action of Nab-Paclitaxel treatment in PDAC. These datasets combined with single cell profiling of PDAC cells and its associated stroma can provide a first complete, unbiased insight into neurons infiltrating both healthy pancreas and PDAC [92].

# 3 Results

## 3.1 The pancreas is innervated by sensory and sympathetic neurons

Analyzing the innervation in tissues is challenging due to its complex 3D structure. It can be difficult to accurately quantify the nerve fibers as they project into the third dimension, which cannot be fully visualized in a 2D section, especially for thin nerve fibers mice (**Figure 5** A,B). To study the extent and type of neurons innervating the pancreas in our model systems, NSG and C57BL/6 (BL6) mice, I performed iDISCO based tissue clearing of whole pancreata and generated 3D reconstructions based on light sheet microscopy images. The advantages of 3D rendering of full tissues are highlighted by the comparison with 2D reconstruction of nerves, as it enables the visualization of the amount of innervation that is not readily visible in 2D (**Figure 5** C,D)

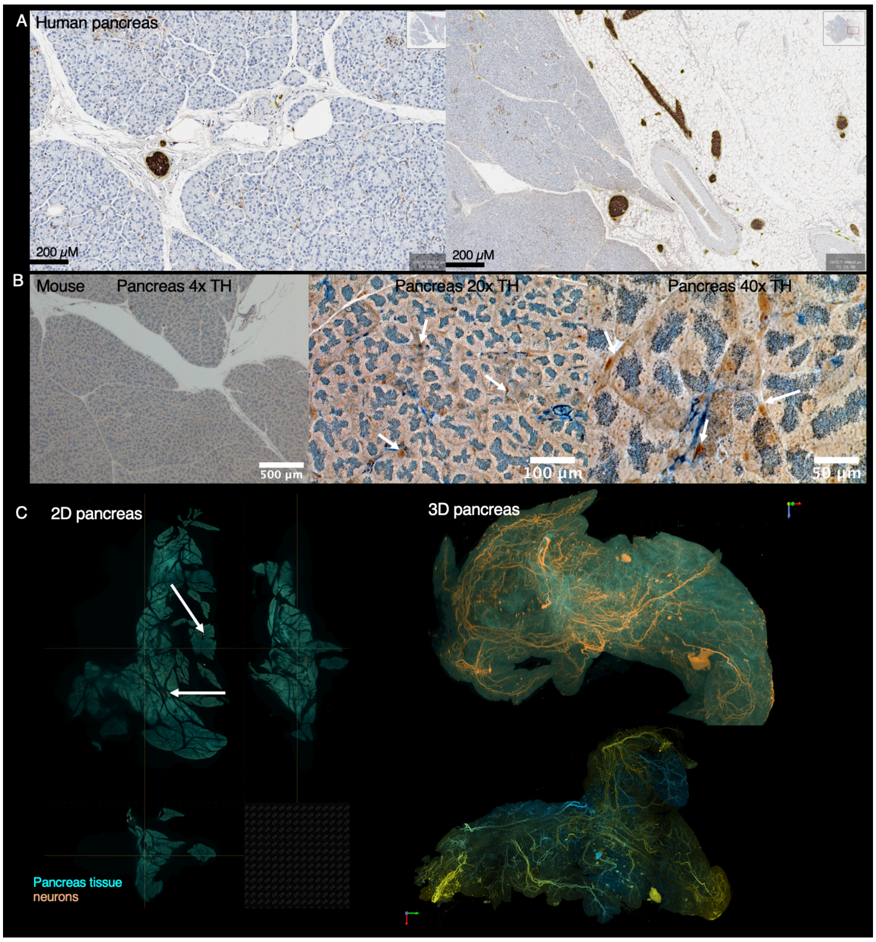

**Figure 5: Nerve staining of human and mouse pancreas.** (A) *2D* IHC staining of human pancreas specimen stained with S100. Scale bar as indicated (Human specimen staining performed by the Heidelberg Pathology Institute) (B) *3D* IHC staining of mouse pancreas specimen (4x, 20x, 40x) stained with tyrosin hydroxylase (TH). Positive staining for nerval structures marked with white arrows. Scale bar as indicated. *(C)* representative images of whole 3D tissue cleared pancreas containing antibody stained neuronal cells/axon obtained using light-sheet microscopy. Left side depicts a 2D x,y,z projections. Arrows point toward 2D nerve staining. Right side depicts 3D rendered images.

Neurons were identified by co-staining the pan-neuronal marker peripherin (PRPH) in combination with tyrosin hydroxylase (TH) marking sympathetic and CGRP specific to sensory neurons (**Figure 6**). Both were detected throughout the tissue, however sympathetic neurons showed more concentrated branching pattern while sensory neurons displayed a more ubiquitous distribution, and the staining overlap patterns indicated significant heterogeneity (**Figure 6**, **Figure 7**).

With further analysis using machine-learning-algorithms (MLA) by Daniel Azorin (AG Winkler) I identified distinct and unique innervating patterns with which I was able to distinguish between sympathetic and sensory innervation in more detail (**Figure 6**, **Figure 7**, **Figure 8**, **Figure 9**).

To decipher neuronal subtypes, Daniel Azorin employed the ML-based algorithm (AIVIA), projected the nerves (**Figure 7**) and quantified total and subtype-specific (sensory, sympathetic, all) innervation (**Figure 8** C). To identify and quantify neuronal innervation, we decided to utilized three different MLA techniques. Due to the large amount of data produced by 3D light sheet microscopy imaging of full tissue samples, we chose to test different approaches. Full annotation in 3D was difficult and resulted in technical problems and was therefore only feasible for small samples due to computer constraints. Therefore, we analyzed data by cutting it into several pieces and comparing it to the autofluorescence (equals tissue size **Figure 8** A) in a 3D to 2D projection (methods) (**Figure 7**, **Figure 8** B,C). Though, this approach resulted in the loss of some branching information. To correct for the branching pattern several sections (Volume Of Interest, VOI) of the same size in full 3D were analyzed, followed by stitching and averaging them per sample (**Supplementary Figure 1**, **Supplementary Figure 2**). However, full tissue annotation had the most reliable outcome, but was problematic for large tissues (**Figure 9**).

The arborization pattern differs between sensory and sympathetic nerve fibers. I detected sensory and sympathetic nerve fibers throughout the tissue with sympathetic neurons densely concentrated and with fewer fine branching and not heavily innervating the glands, while nerve ends of sensory neurons also aligned presumably with vasculature but were present ubiquitously (**Figure 6**, **Figure 7**, **Figure 8**).

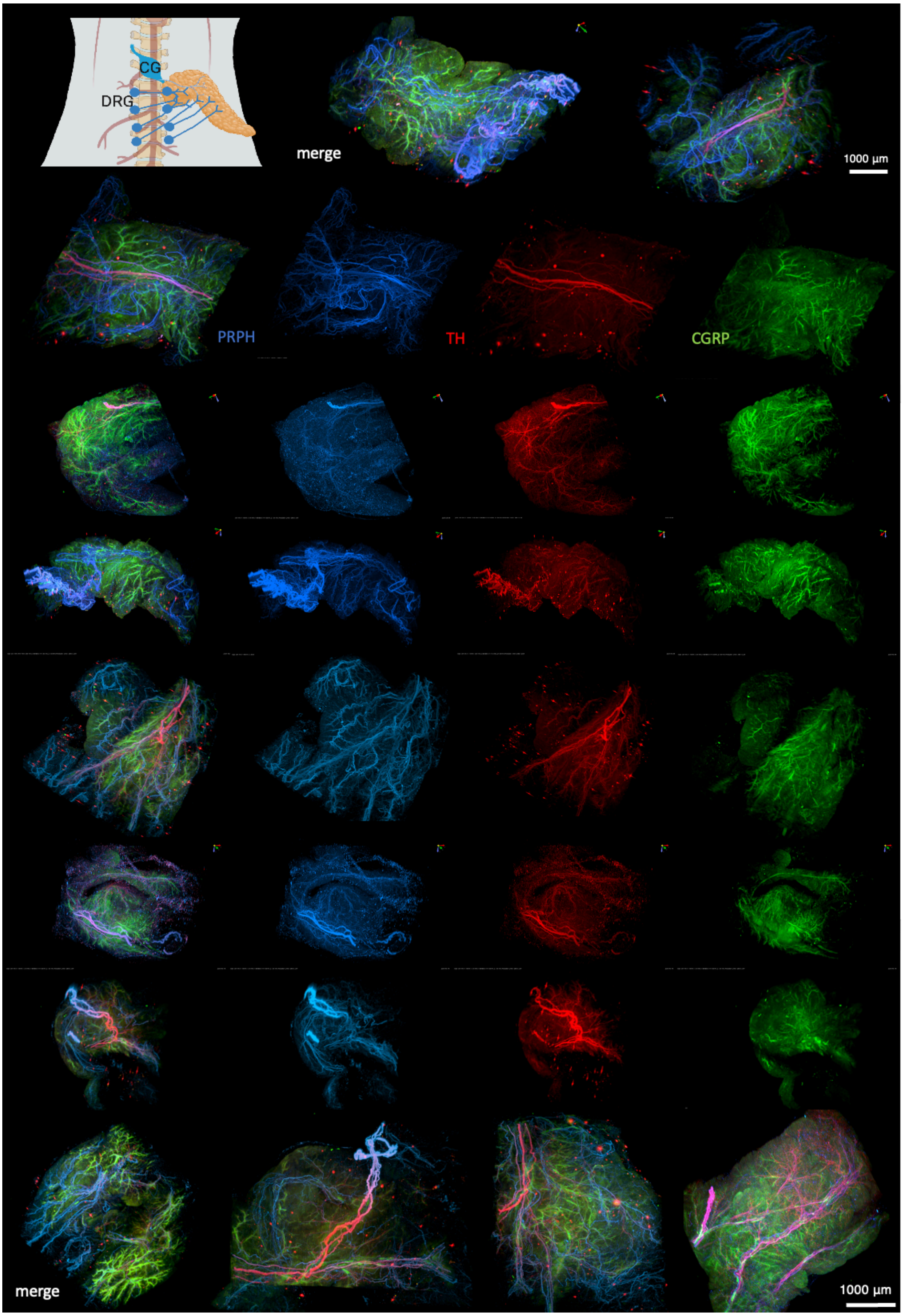

**Figure 6: The pancreas is innervated by different PNS subtypes.** Schematic of neuronal innervation of the pancreas and representative images of whole 3D tissue cleared pancreas containing antibody stained neuronal cells/axon obtained using light-sheet microscopy. Scale: size: 3.51x4.16x4.50 mm, Calibration XY 1.63 mm, Z 1.50 mm. Pan-neuronal marker PRPH (blue), Sympathetic marker TH (red), sensory marker CGRP (green).

This data is in line with already described innervation pattern of sympathetic and sensory nerve fibers [6, 48].

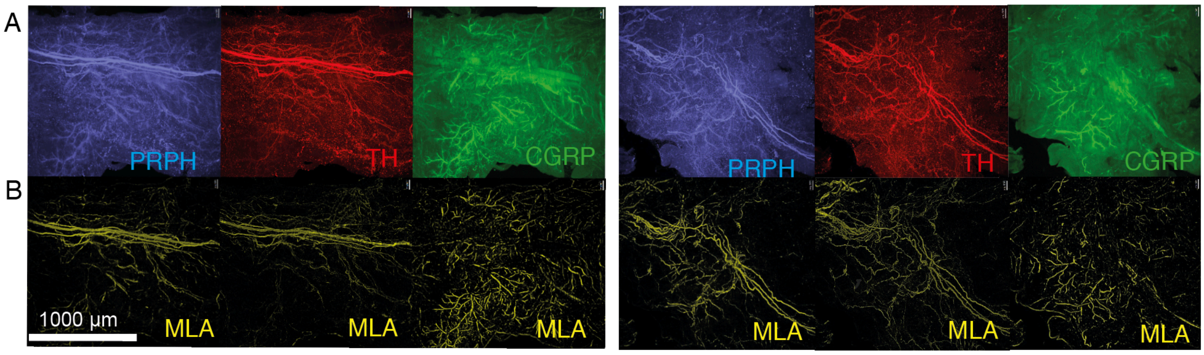

**Figure 7: Innervation pattern of sympathetic, sensory and pan-neuronal fibers with MLA prediction:** (A) Light sheet microscopy of neuronal innervation of full pancreata. PRPH (blue), TH (red), CGRP (green) positive staining was (B) MLA prediction of axons of neuron staining of full pancreata in a 3D to 2D algorithm (MLA yellow).

Additionally, TH$^-$, CGRP$^-$ but PRPH$^+$ neurons were detected, indicating heterogeneity of innervating neurons (**Figure 8** C, **Supplementary Figure 1**).

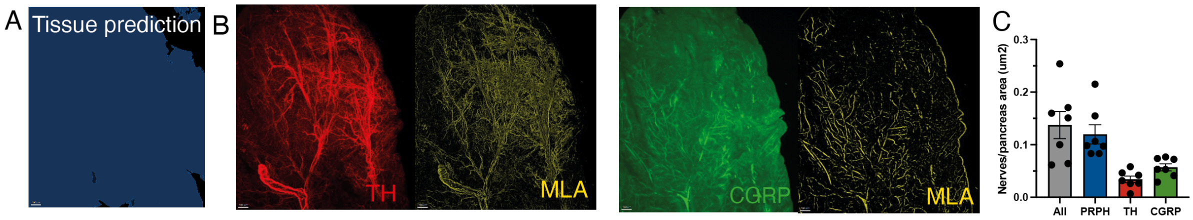

**Figure 8: MLA based quantification of sympathetic and sensory innervation of the pancreas**. (A) pancreas tissue area predicted by MLA. (B) Visualization of pancreas specimen of sympathetic TH+ and sensory CGRP+ axons and (C) MLA based quantification of different neuronal subtypes per channel and combined, (n=7 mice). Calculation of nerves per pancreas areas. Mean +/- SD is shown.

**Figure 9** shows the MLA based full 3D quantification which resulted in a higher nerve density compared to VOI quantification (**Supplementary Figure 2**).

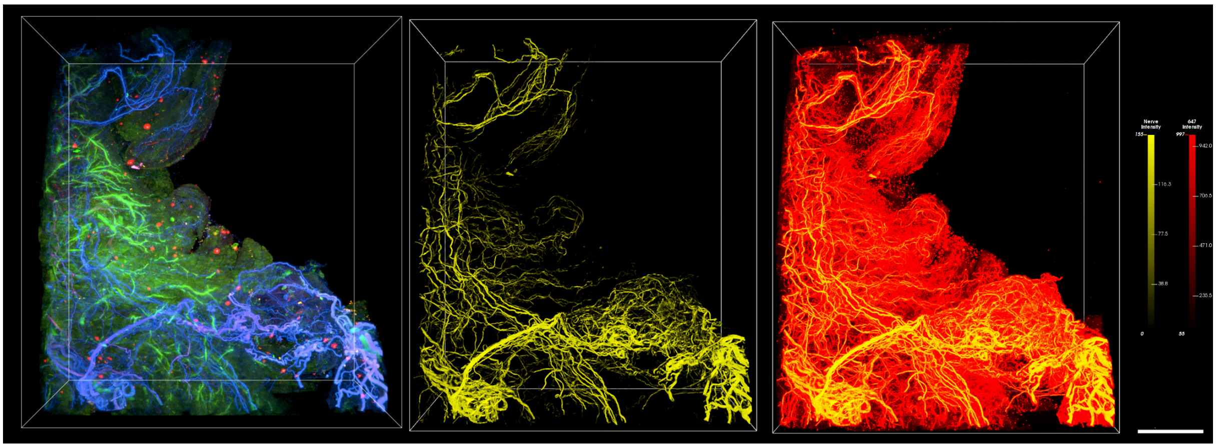

**Figure 9: 3D MLA prediction of incoming nerve fibers in the healthy pancreas.** Analysis of neuronal innervation using light sheet microscopy: PRPH (blue), TH (red), CGRP (green) positive staining was projected in a 3D algorithm and neuronal content (yellow) and tissue area was predicted (red).

The cell bodies of both sympathetic (TH$^+$) and sensory (CGRP$^+$) neurons are not located in the pancreas itself, but in the para- and pre-vertebral ganglia of the peripheral nervous system. In immunofluorescence (IF) images of these ganglia, all cells were PRPH positive, but neither CGRP nor TH were expressed in all neurons of the dorsal root ganglia (DRG) or celiac ganglia (CG) respectively, highlighting the cellular heterogeneity of peripheral neurons (**Figure 10**).

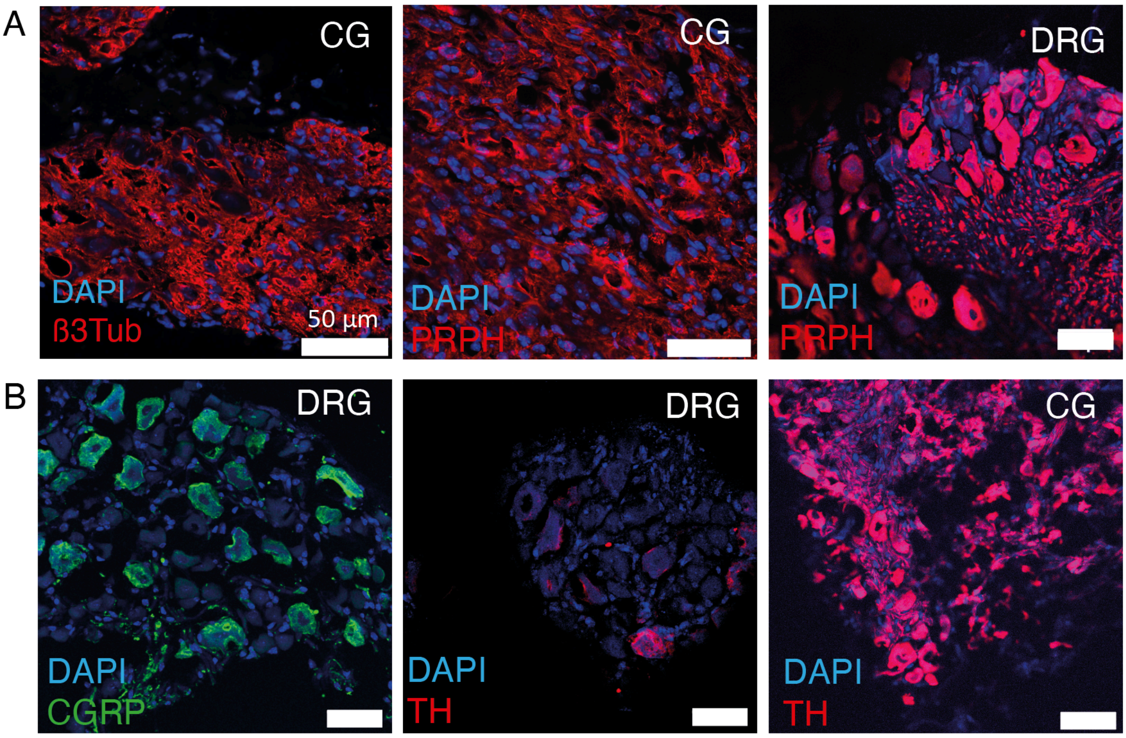

**Figure 10: Ganglia cells express pan- and subtype specific markers**. (A) Representative IF staining of full ganglia section (CG and DRG) stained with pan-neuronal marker ß3Tubulin (ß3TUB and Peripherin (PRPH). (B) Representative IF staining of full ganglia section (CG and DRG) stained with subtype specific neuronal marker CGRP and TH.

## 3.2 The “Trace-n-Seq” approach

Current scRNA-seq approaches of digested tissues exclude neurons, as their cell bodies are located up to 2 cm away from the target organ. To bridge this gap, I developed a new method, called "Trace-n-Seq" (**Figure 11**). In short, the retrograde tracer Fast Blue (FB) is intraoperatively injected into a target tissue as described in detail below. After a tracing period of 5-14 days the animal is sacrificed and the ganglia of interest (CG=sympathetic, DRG=sensory) are harvested, enzymatically digested and stained with dyes allowing life cell identification and labeling neurons. Next, I isolated FB positive neurons as single cells by fluorescence activated cell sorting (FACS) and used them for single cell sequencing protocols (**Figure 11**).

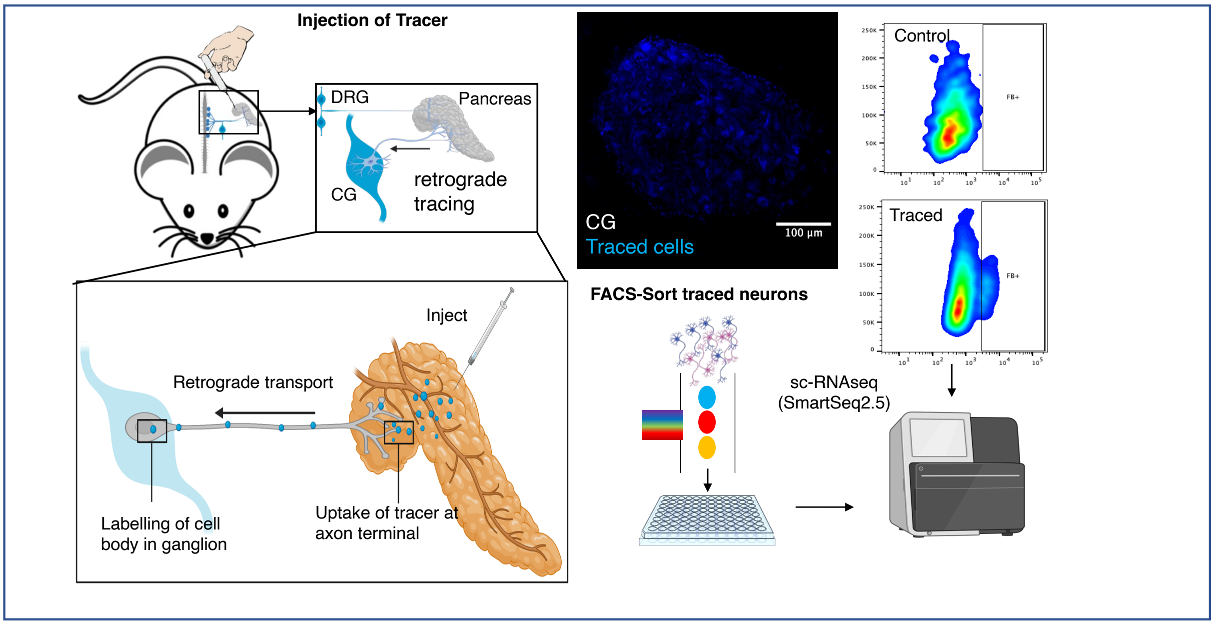

**Figure 11: The Trace-n-seq workflow.** FB is intraoperatively injected via microinjection into the pancreas. The dye retrogradely labels the cell bodies in the CG and DRG respectively. After a tracing period of 10 days the animal is sacrificed and the ganglia are dissected, dissociated into single cells and isolated by fluorescence activated cell sorting (FACS).

I validated retrograde labeling of pancreas-innervating neurons in DRGs and CG that I injected with Fast Blue (FB) (**Figure 12** A/B/C). To compare the effectiveness of FB detection by flow cytometry, I compared the frequency of $FB^+$ CG neurons detected by flow cytometry with IF microscopy. I identified that 70-90% of CG neurons innervate the pancreas (**Figure 12** B). I further analyzed sensory DRG innervation after intrapancreatic FB injection (**Figure 12** C). By analyzing FB tracing in individual ganglia from thoracic region (TH) 5-lubar region (L)2, I found mostly neurons from thoracic DRG 6-10 to project into the pancreas. Flow cytometry- and IF-based quantification gave similar results. Within the DRG, only about 2-30% of the neurons within a ganglion were labeled (**Figure 12** C). The unlabeled cells project into different organs like the skin.

In conclusion, the Trace-n-Seq method enables stable retrograde tracing that allows FACS bases isolation of labelled cells (**Figure 12** A)

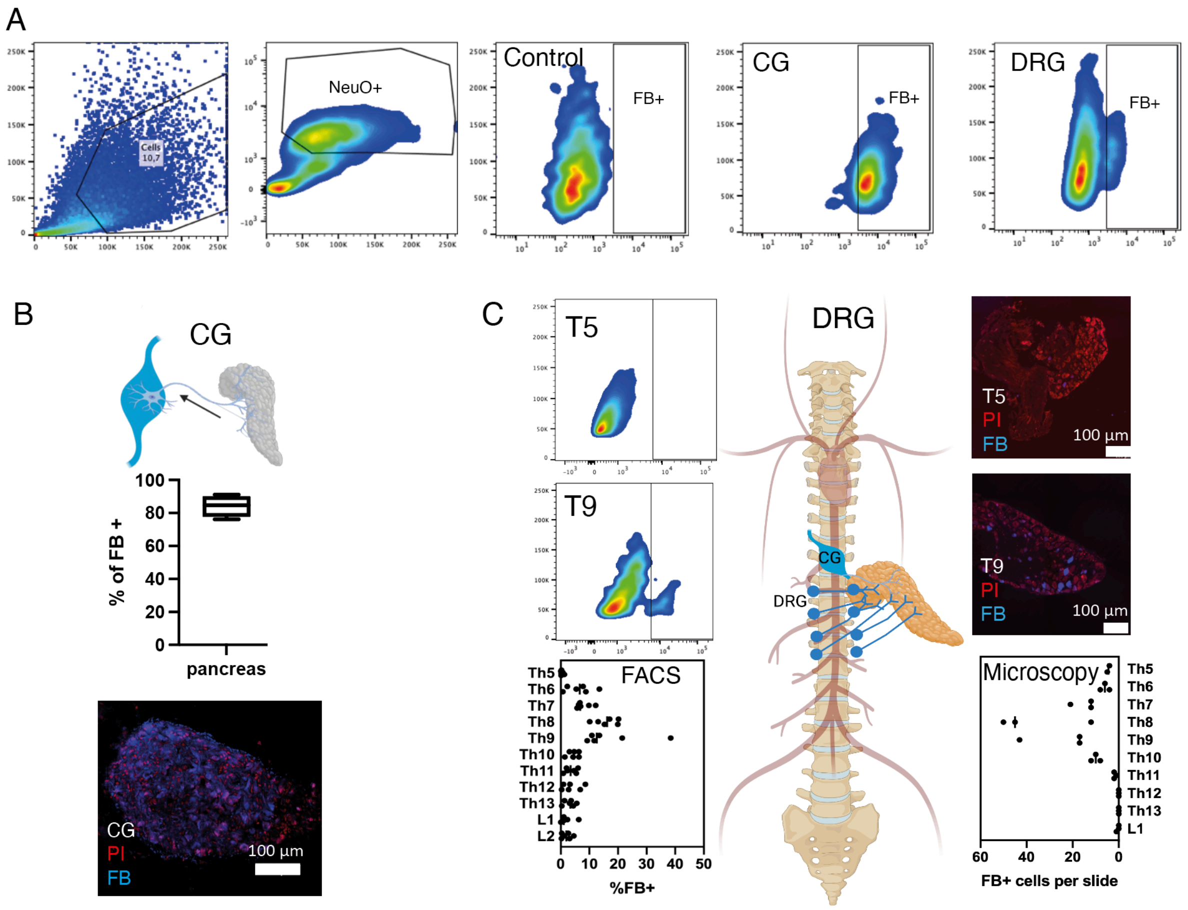

**Figure 12: Innervation pattern via Trace-n-seq.** (A) Flow cytometry scheme of retrogradely labelled neurons. Neurons are enriched with the probe NeuO before gating on FB$^+$ cells. (B) Flow cytometry and microscopy based quantification of FB$^+$ CG neurons (n = 3 mice) (C) Flow cytometry (n=3 mice) and microscopy-based (n=2 mice) quantification of FB$^+$ DRG neurons. T5,T9=Thoracic ganglion 5,9,

## 3.3 Trace-n-Seq: Developing a method to trace neurons *in vivo* step by step

### 3.3.1 Identification of ganglia of the peripheral nervous system

Sensory neuron cell bodies are located in pairs along each level of the spinal column. As they are pseudounipolar afferent neurons, they convert external stimuli into electrical signals that are transmitted back to the spinal cord's dorsal horn [49]. The DRG can be dissected from mice for studying the sensory neuronal cell bodies. I adapted a previously published step-by-step dissection method for DRGs [93]. In short, the pelt is removed from the head to the base of the tail and the arms and head are removed.  Remaining muscles are removed from the tissue as well as fat, spinal nerves, and soft tissue from the exterior and the spinal column was divided along the midline. The spinal column was then rinsed with PBS, and using fine forceps, I carefully removed the isolated ganglia while preserving the meninges (**Figure 13** A). The isolated DRG was validated through H&E staining (**Figure 13** B) and IF staining (**Figure 13** C). The ganglia cells stained positive for pan-neuronal marker peripherin (PRPH) (as well as other neuronal markers like ß3tubulin, S100b or CGRP (**Figure 10**)). I further utilized light sheet microscopy imaging of fully cleared mouse spine to validate localization of DRG and visualize DRG fiber exiting the backbone (**Figure 13** D,E).

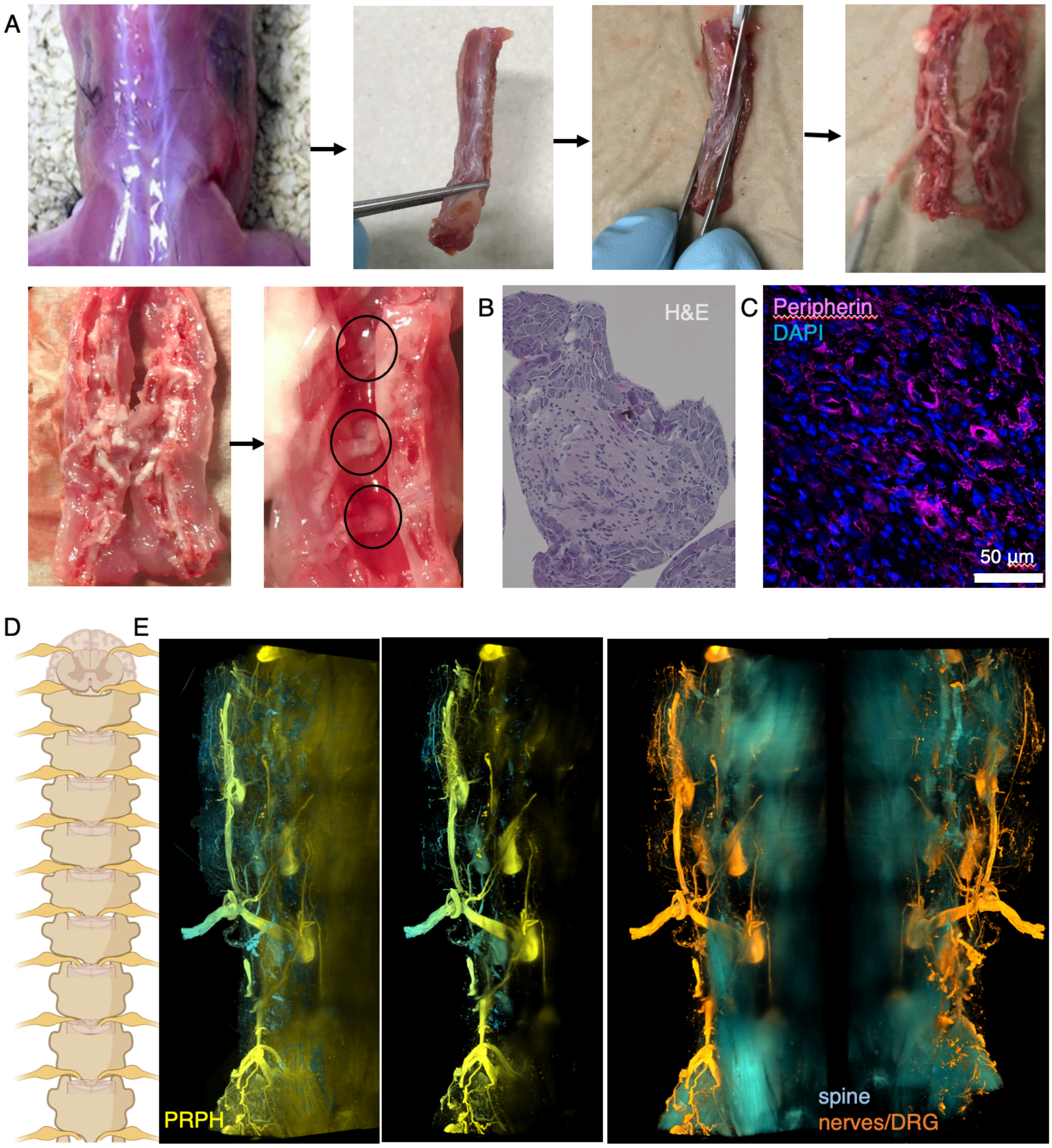

**Figure 13:Dissection protocol of DRG.** (A)representative images of the step-by-step dissection of Dorsal Root Ganglia. (B) H&E of DRG (C)IF of DRG stained for pan-neuronal marker PRPH, scale bar 50 µm (D) Schematic of DRG in the spine. (G) Representative light sheet microscopy image of the spine stained with PRPH.

There was no existing protocol for extracting the CG. I utilized human anatomy literature to determine its location and created a harvesting protocol for mouse CGs (**Figure 14** A). The CG is situated near the vertebra, from where its extrinsic fibers enter the pancreas along major pancreatic blood vessels. To harvest the CG, I opened the mouse torso, carefully removing any overlying organs as shown in **Figure 14** (B). Following the aorta, I cleared away any tissue with fine forceps. Above the renal artery, I removed remaining fat and muscle tissue around the arteria mesenterica superior, where the ganglia tissue surrounds the aorta. By gently lifting the arteria mesenterica superior, the CG can be extracted using fine forceps. The accuracy of the tissue harvest was verified through H&E staining, IHC for peripherin, and IF using ß3tubulin. (**Figure 14** C,D,E). I applied light sheet microscopy imaging to demonstrate CG derived innervation of the pancreas and the spleen (**Figure 14** F,G). As seen in **Figure 14** G the innervation of the pancreas is denser compared to the spleen.

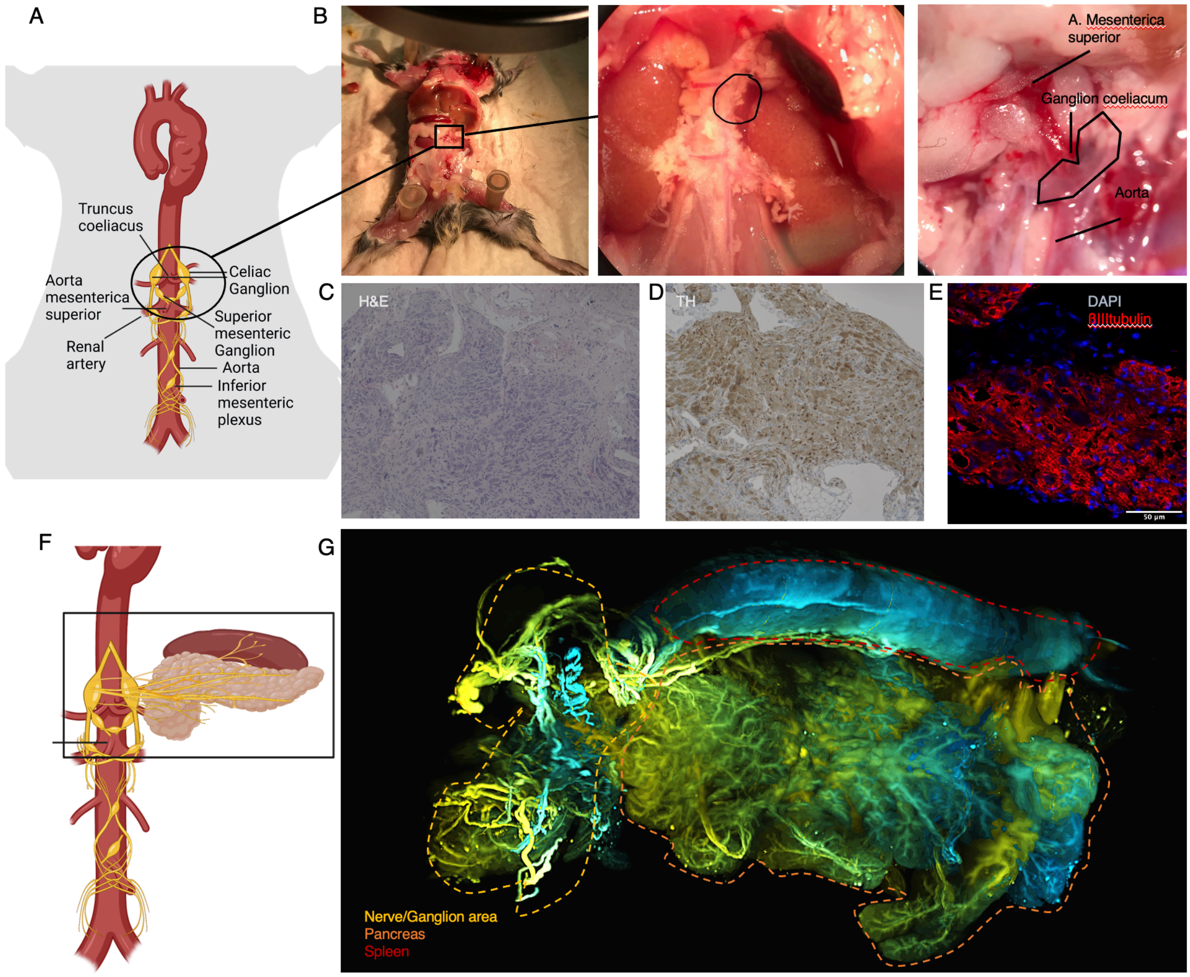

**Figure 14: Dissection protocol for CG. (A)**Schematic of the CG localization (B) representative images of the step-by-step dissection of the Celiac Ganglion. (C) H&E of CG (D) IHC of CG stained for sympathetic marker TH. (E) IF of cryosection specimen of CG stained for pan-neuronal marker ß3tubulin, scale bar 50 µm. (F) Schematic of CG derived innervation of the pancreas. (G) Representative light sheet microscopy image of the peritoneum including the CG or sympathetic nerve tissue (marked yellow), the pancreas (marked orange) and the spleen (marked red) stained for PRPH.

### 3.3.2 Retrograde tracing of tissue innervating neurons

Retrograde tracing is an important tool for identifying neuronal cell bodies innervating tissues of interest, which is crucial for studying their expression profile. I tested different dyes for their ability to retrogradely label pancreas-innervating neurons. The tracers were diluted in various solvents (PBS, H2O, ethanol, etc.) and concentrations and were microinjected into various regions of the pancreas. I evaluated the tracing efficacy several days later by harvesting full ganglia and analyzing the level of fluorescent labeling in cryosections (**Figure 15**). Fast Blue successfully labeled retrogradely traced neurons in a 0.5% dilution in water after five days (**Figure 15** A). The other tested dyes, such as Nuclear Yellow (NY), FluoroRuby (FR), or Dil, showed significant unspecific labeling or could not be detected in the CG after various tracing timepoints (**Figure 15** A). Direct co-tracing of FR (the second-best dye) with FB revealed unspecific labeling and spillover to other cells. Through repeating the experiments at various tracing timepoints, tracer concentrations, and injection strategies, I found that 4-5 microinjections of 1% FB in H2O using a Hamilton 29G (10 µl) syringe obtained a maximal tracing signal in both CG and DRG ten days after the injection (**Figure 15**, **Supplementary Figure 3**).

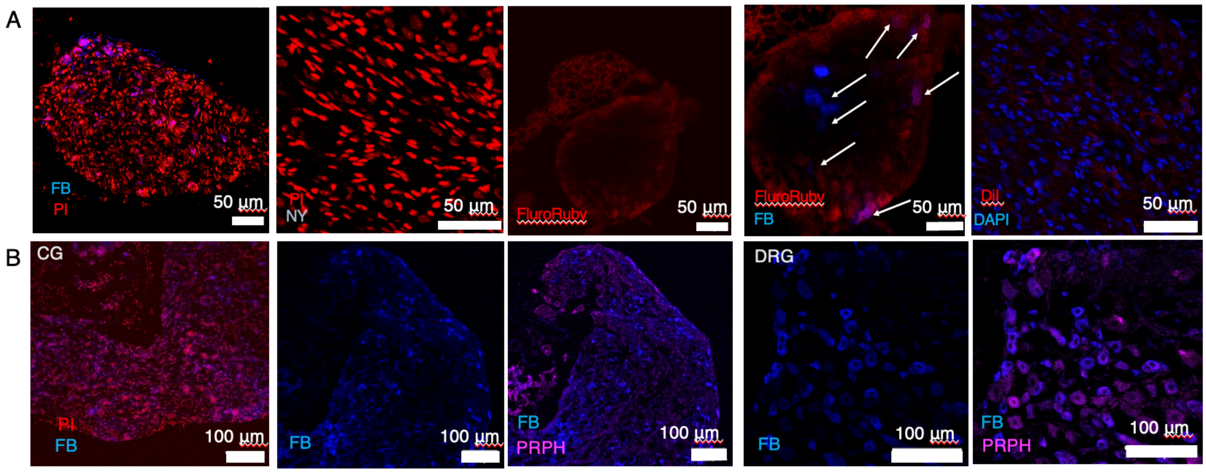

**Figure 15: Tracing capacity of different retrograde dyes.** (A) Representative IF images of the CG after 7 days of tracing with the dyes Fast Blue (FB), Nuclear Yellow (NY), FluroRuby, co-staining of FluroRuby and FB, DiI. (B)Labelling capacity FB tracing after optimization (10 days 4µl 1% BF-H2O via 1 µl microinjections) in the CG with co-staining of PI, alone or PRPH and in the DRG alone or co-stained with PRPH. Scale bars as indicated.

Additionally, using confocal microscopy, no labeling was found in other organs. FB spread throughout the pancreas but was not observed in neighboring organs such as the spleen (**Figure 16**). Thus, I found an effective retrograde tracer to trace tissue-specific infiltrating neurons without any cross-organ labeling after 7-10 days.

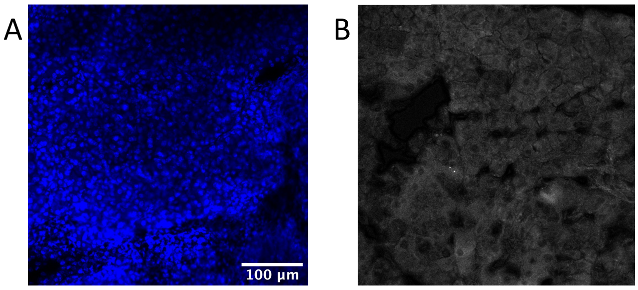

**Figure 16: FB distribution in the pancreas.** (A) IF of full pancreas 7 days after FB microinjection. FB is visible in the DAPI filter(B) Autofluorescence of the DAPI filter of full spleen 7 days after FB microinjection in the pancreas. No FB spillover is visible.

### 3.3.3 Identification of the right digestion and FACS protocol of PNS ganglia with and without retrograde tracing

Digesting peripheral nerve ganglia poses a significant challenge. Additionally, analyzing and sorting neurons is difficult due to their delicate nature and lack of surface proteins that can be used to identify them by flow cytometry.

I evaluated various digestion methods and evaluated the cell quality by manual counting with trypan blue and by flow cytometric analysis. I also considered the time required for the digestion process, as a long digestion process resulted in lower cell quality. I found that Collagenase Type 1 with BSA and trypsin produced good quality cells, but later discovered that neurons did not survive the digestion process and mostly glia cells were recovered.

I assessed the success of the digestion by flow cytometric analysis, using various live/dead dyes such as Annexin V, Dapi, Hoechst, PI, 7AAD, Zombie Yellow, and different Vybrant dyes. The combination of 7AAD and Vybrant dye showed that the digestion mix 3,6,7, and 8 (**Figure 17** A) resulted in the highest number of live cells. An example of the flow cytometry gating scheme is shown in **Figure 17** B.

After various tests and cell identity cross-analysis, I discovered a method in which I quickly removed ganglia without nerves attached and immediately digested with a pre-heated (37°C) digestion mixture, similar as described by Zeisel *et al.* [58]. In brief, 2.7 ml of digestion solution contain 400 ul TrypLE Express, 2000 ul Papain, 100u l DNase I and 200 ul Collagenase/Dispase. Vybrant dye was added to the digestion mix. Vybrant Dye incorporates into nucleated cells to stain for live cells.

Ganglia were digested on a heating block at 37°C and shaking for 1.5 h. Every 30 min the cell suspension was further mechanically disrupted by pipetting up and down starting with a 1 ml pipette going down to a 200 ul pipette. As soon as all ganglia were dissociated the cell suspensions was diluted with RPMI medium containing 5% BSA and 1% FCS (see methods).

A

| Strategy | ~ Live cells % |
|---|---|
| 1. Accutase Max | 2.5 |
| 2. Trypsin | 1.2 |
| 3. CollagenaseTyp1/BSA/Trypsin | 35-63 |
| 4. Accutase | 1.7 |
| 5. Papain | 57.3 |
| 6. Papain/TrypLE/DNase1/ Collagenas-Dispase | 72.6 - 95 |
| 7. Papain/TrypLE/DNase1/ Collagenas-Dispase + percoll | 57.1 |
| 8. Papain/TrypLE/DNase1/ Collagenas-Dispase + OptiPrep | 76 |
| 9. Homgenizer | 30 |

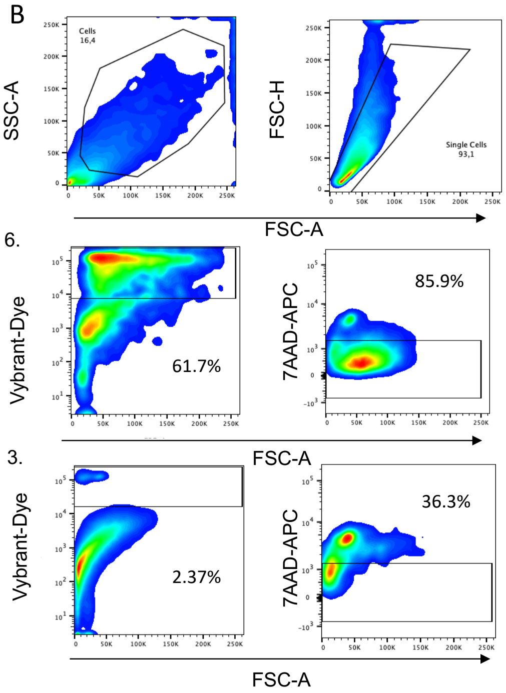

**Figure 17: Adjusting digestion protocol for dissociation of CG and DRG cells.** (A) Different digestion strategies. (B) Representative of a gating scheme after digestion with protocol 6 or 3.

I tested the expression profile of cells obtained through different digestion protocols for pan-neuronal markers *peripherin* (*Prph*) and *neurofilament* (*Nefm*) and a glial marker *Plp1* in comparison to mouse heart using qPCR. I found that digestion conditions 6 and 8 resulted in the highest expression of neuronal markers and the lowest expression of the glial marker *Plp1* (**Figure 18**). This demonstrates that while digestion condition 3 resulted in a high proportion of live cells, it favored the survival of glial cells over neuronal cells.

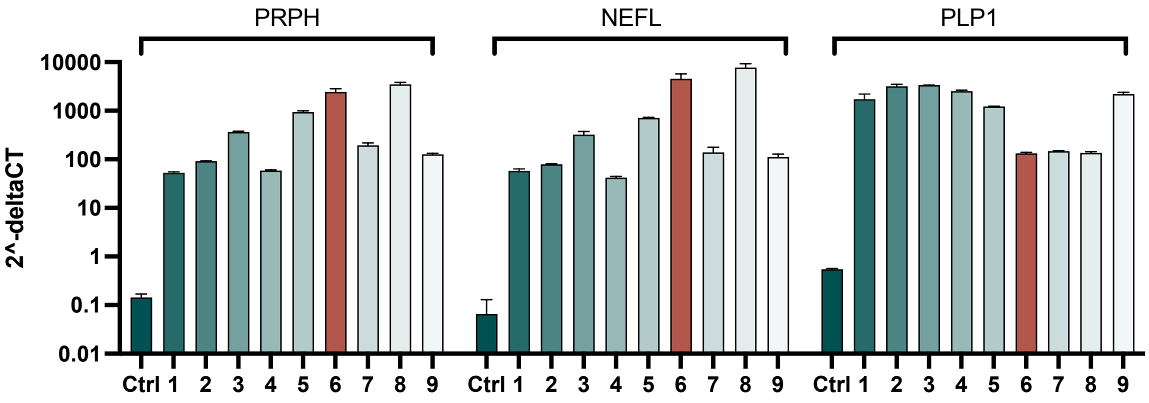

**Figure 18: Neuronal content validation of different digestion protocols** qPCR analysis of the $2^{\text{deltaCT}}$ value of bulk sorted live cell populations for *peripherin (Prph)* and *neurofilament (Nefm)* and the glia marker *proteolipid protein1 (Plp1)* after applying different digestion protocols on dissected DRGs. Ctrl: mouse heart, (n=3DRG, technical replicates. Mean + SD is shown.).

I attempted to determine the proportion of neurons in the live cell population. Due to the lack of reliable surface markers for live neurons, I tested a range of exclusion markers (e.g. CD45, CD31, CD140a/b, CD146, CD44, CD34) and neuronal enrichment markers (e.g. CD171, CD24, PSA-Ncam, CD90, CD271). The combination of using CD45 as an exclusion marker and staining the digested cells with the neuro markers CD24 and PSA-NCAM appeared promising (**Figure 19**). However, upon further analysis, not all CD24/PSA-NCAM positive cells were found to express the intracellular pan-neuro marker ß3tubulin when sorted, fixed and stained with antibodies (**Figure 20**).

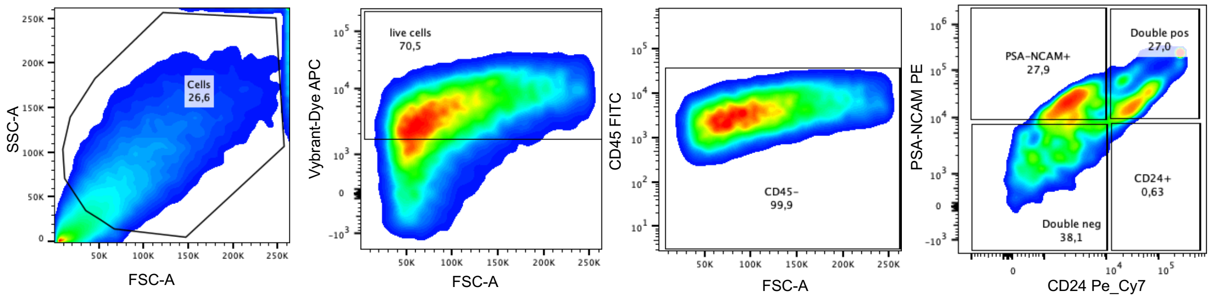

**Figure 19: FACS scheme of neuronal cell enrichment.** Digested DRG and CG cells were stained with Vybrant dye for live/dead cells and after exclusion by CD45 staining, cells were assessed for neuronal content by PSA-NCAM and CD24 staining.

Staining live neurons with antibodies resulted in unspecific staining, as the use of digestion enzymes can also impact the integrity of the epitopes.

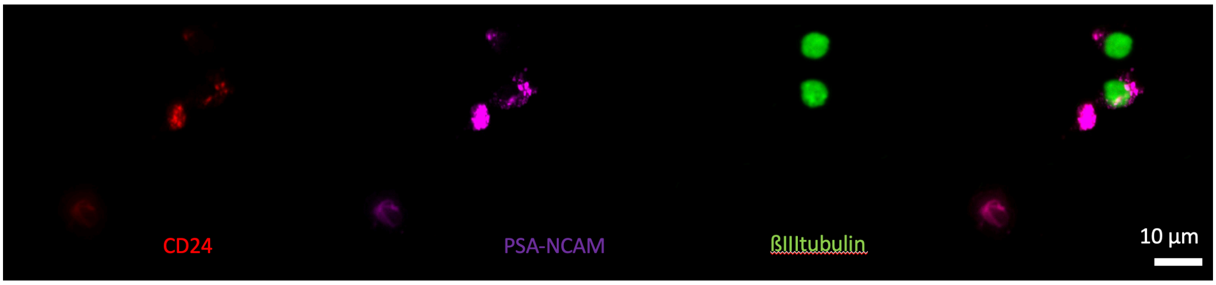

**Figure 20: IF based FACS validation.** Digested and stained cells (Figure 19) were FACS-sorted on a glass slide and fixated. The cells were stained using the FACS marker CD24 and PSA-NCAM and co-stained with the intracellular neuronal marker ßIIITubulin. Scale bar 10 µm

I investigated the neuronal composition of FACS-sorted cells following various digestion protocols and enrichment using CD24 and PSA-NCAM. I conducted qPCR on the bulk-sorted cells and found that while the expression of the pan-neuronal marker slightly increased after enrichment with CD24 and PSA-NCAM, the expression of the glia marker *Plp1* was still present albeit at a reduced level compared to the control (**Figure 21**).

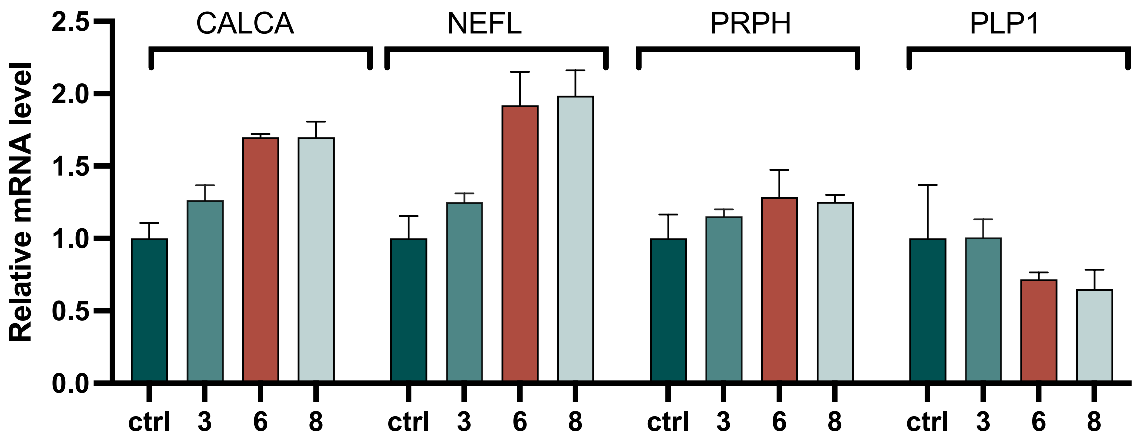

**Figure 21: Validation of neuronal cell content after FACS enrichment.** qPCR analysis of the relative mRNA level of bulk sorted live cell populations after applying three different digestion protocols on dissected DRGs and enrichment of CD24/PSA-NCAM+ cells. Cells were digested according to their protocol number (see Figure 17 and methods) and sorted for live cells and CD45-/CD24+/PSA-NCAM+ cells. As a control the expression was normalized to cells without FACS based enrichment, (n=3 DRG, technical replicates. Mean + SD is shown.).

To increase neuronal enrichment, I utilized the *in vitro* probe NeuO as a marker, which is added to the digestion mixture and taken up by neurons. NeuO (NeuroFluor) is a fluorescent probe that selectively labels live neurons in culture, allowing for their visualization with fluorescent imaging. The labeling is temporary and can be washed off, leaving behind viable cells. I repurposed the probe as a FACS marker for neuronal enrichment. The flow cytometry analysis showed variation in the fraction of NeuO-positive cells among different digestion methods (**Figure 22** A/B). By comparing the NeuO-enriched cells to the NeuO-negative cell fraction of digestion mix 6 using qPCR, I observed a significant increase in the expression of neuronal markers and a decrease in the expression of the glial marker *Plp1* in the sorted populations (**Figure 22** C). Confocal microscopy of NeuO-positive cells confirmed that NeuO effectively enriches for neuronal cells after digestion, as the sorted NeuO-positive cell fraction was positive for b3tubulin (**Figure 22** D).

Therefore, I selected a digestion mixture consisting of Papain, TrypLE, DNase1, and Collagenase/Dispase as the standard digestion mix, along with Vybrant dye and NeuO as markers for live cell detection and neuronal enrichment.

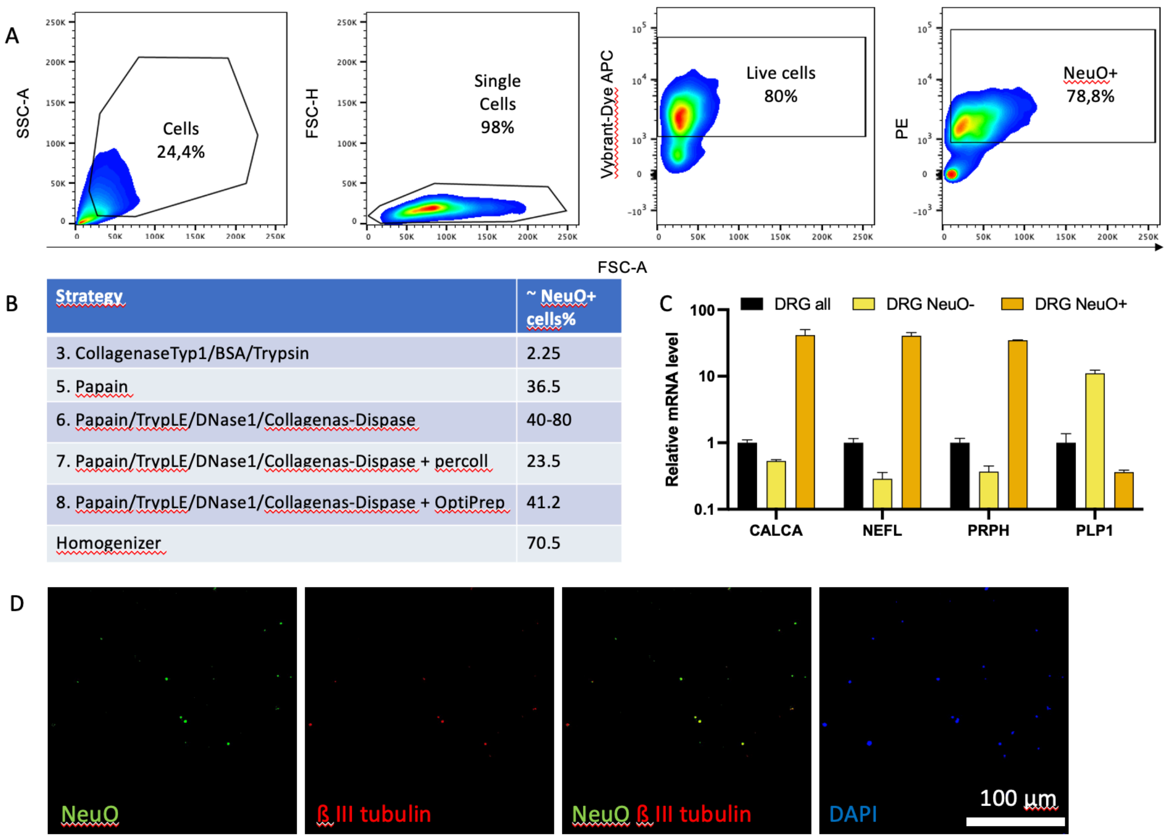

| Strategy | ~ NeuO+ cells% |
|---|---|
| 3. CollagenaseTyp1/BSA/Trypsin | 2.25 |
| 5. Papain | 36.5 |
| 6. Papain/TrypLE/DNase1/Collagenas-Dispase | 40-80 |
| 7. Papain/TrypLE/DNase1/Collagenas-Dispase + percoll | 23.5 |
| 8. Papain/TrypLE/DNase1/Collagenas-Dispase + OptiPrep | 41.2 |
| Homogenizer | 70.5 |

**Figure 22: FACS based isolation of neurons after digestion of mouse PNS ganglia. ((A)** Representative flow cytometric gating scheme of NeuO enriched populations. (B) Results of FACS based analysis of NeuO positive content after different digestion protocols (Figure17, methods), n=3. (C) qPCR analysis of the relative mRNA level of bulk sorted live cell populations with and without NeuO enrichment. As a control the expression was normalized to cells without FACS based enrichment, n=3 technical replicates. Mean + SD is shown. (D) Digested and stained cells were FACS-sorted on a glass slide and fixated. The cells were stained using the probe NeuO and co-stained with the intracellular neuronal marker ßIIItubulin and DAPI.

### 3.3.4 Retrograde tracing of tissue innervating neurons via FACS

After establishing the dye injection, digestion, and neuro-enrichment protocols, I performed flow cytometry analysis of traced neurons. I injected FB and harvested mice at various timepoints to determine the duration needed for the tracer to retrogradely travel into the ganglia. Results showed signals after 4 days which increased with prolonged tracing time (**Supplementary Figure 3**). Flow cytometric analysis of both CG and DRG revealed positive FB signals after 10 days of tracing, which were confirmed through IF microscopy (**Figure 23** A/B). Sorted FB positive cells on a slide were also positive for neuronal markers such as CD24 (**Figure 23** C). I compared the gene expression of several neuro-markers between Fast Blue positive sorted cells and negative sorted cells, as well as FluoroRuby traced cells and their corresponding controls. Results showed a higher expression of *Tubb3, Hand1*, and *Tyrosin Hydroxylase (Th)* in FB$^+$ cells compared to FluoroRuby traced cells (**Figure 23** D). Single cell qPCR analysis of 45 FB$^+$ sorted cells vs 45 FB$^-$ and 30 CD45$^+$ cells revealed significantly lower raw CT values (hence higher expression) for the neuro-markers *Th, Hand1*, and *Tubb3* (**Figure 23** E). Direct gene expression analysis of various neuron-markers and glia markers showed that FB$^+$ cells had significantly higher neuro-marker gene expression compared to all cells in a ganglion and even higher than NeuO enriched cell fraction. Conversely, glia marker expression of *Plp1* was significantly lower in the FB$^+$ fraction (**Figure 23** F), indicating that FB is specific for neuronal tracing.

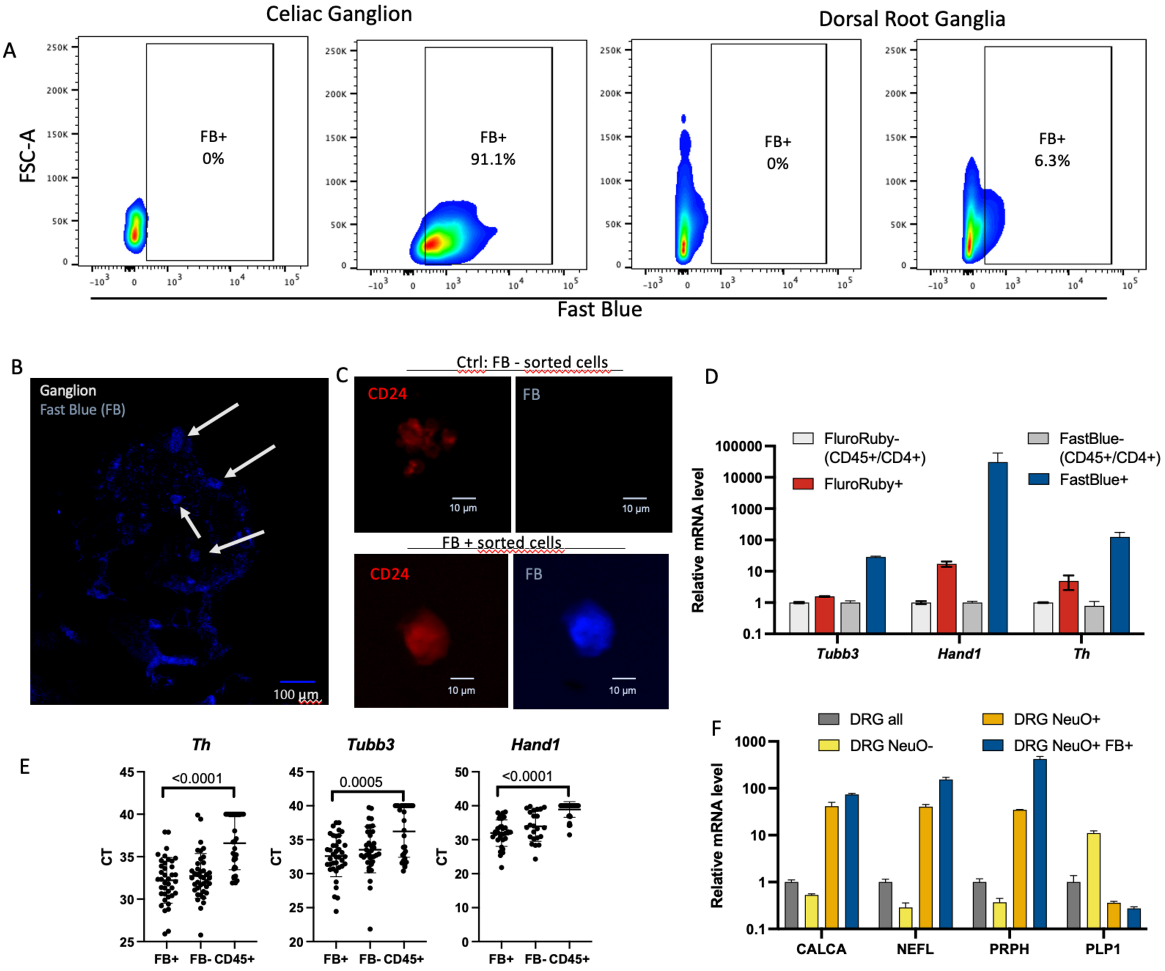

**Figure 23: Retrograde tracing validation.** (A) Representative FACS of digested CG and DRG after 7 days of tracing with FB. Cells were pre-gated as described above (Figure 22). Gates show the proportion of FB+ cells in comparison to the control (no tracer injected). (B) IF staining of a CG ganglion section. 10 µl of 0.1% of FB (in H2O) was injected and traced for 7 days. FB$^+$ cells are marked with white arrows. (C) Digested and traced cells were FACS-sorted on a glass slide, fixated and co-stained with CD24. Scale bar 10 µm. (D) Comparison of neuronal marker expression between FluroRuby (FR) and FB traced cells isolated via FACS. qPCR analysis of the relative mRNA level of bulk sorted live cell populations. Expression was normalized to FB$^-$ or FR$^-$ cells, n=5 mice and technical replicates n=3. Mean + SD is shown. (E) Single-cell qPCR validation of neuronal marker genes tubb3, Hand1 and Th in FB$^+$ vs FB$^-$ and CD45$^+$ control cells (n=96 individual cells in total. Mean +/- SD is shown). (F) qPCR analysis of the relative mRNA level of Prph, Nefm, Calca and Plp1 in bulk sorted live cell populations with and without NeuO enrichment and isolation of the NeuO/FB$^+$ population. As a control the expression was normalized to cells without FACS based enrichment, n=5 mice and technical replicates n=3. Mean + SD is shown.

## 3.4 Pancreas innervating neurons

I aimed to identify and describe the functional properties of healthy pancreas innervating neurons through quantification and sequencing to identify specific PNS axons with distinct sprouting patterns in the healthy pancreas. Further I aimed to differentiate various sensory and sympathetic neuronal subgroups that innervate the pancreas based on their expression profiles.

Bioinformatic analysis of scRNA-sequencing has been performed with Jasper Panten.

### 3.4.1 Pancreas-innervating sympathetic and sensory neurons are heterogeneous and dominated by noradrenergic and neurofilament proprioceptor neurons

As the above-described Trace-n-Seq method results in the isolation of high-quality traced neurons I next aimed to assess the composition of pancreas-innervating sensory and sympathetic neurons using scRNA-seq. I harvested T5-T13 DRGs and CG of NSG and BL6 animals after intrapancreatic FB injection. I isolated individual $FB^+$ neurons and performed plate-based scRNA-seq using a modified SMART-Seq2 approach and the cost-effective BarcodeSeq approach (based on the RNA-seq protocol established for TARGET-seq [94], methods).

In the initial experiments, Jasper Panten (Bioinformatic) and I conducted various quality control evaluations to select high-quality cells for sequencing. We compared two sequencing protocols (SmartSeq and BarcodeSeq) to determine the best method and ensure robust results (**Supplementary Figure 6**, **Supplementary Figure 7**, **Supplementary Figure 8**). I further tested several options for processing full ganglia suspensions, including normal barcoded lipid droplet based scRNA provided by 10x Genomics or barcoded lipid droplet based nuclear scRNA (NucSeq) provided by 10x Genomics of full ganglia suspension or pre-sorted cells, but found that sorting neuronal populations directly into lysis buffer produced the highest quality cells. This approach resulted in lower ambient RNA levels and reduced debris content compared to 10x approaches, while maintaining the quality of RNA in fragile neurons (**Supplementary Figure 4**). Additionally, sorting cells directly in lysis buffer prevented spillover from glial, muscle, or vascular cells, compared to processing full ganglia samples (**Supplementary Figure 4** E/F). The optimal digestion and sorting strategy were essential in obtaining high-quality neuronal cell populations for sequencing, as different strategies resulted in varying cell quality (**Supplementary Figure 4**, **Supplementary Figure 6**, **Supplementary Figure 7**).

To assess the quality of the sequencing results obtained from the plate-based sequencing models, I evaluated various parameters, including the number of detected genes, the number of sequenced reads, the proportion of mitochondrial reads, and the proportion of exonic reads in relation to the total number of mapped genes. Based on these results, I determined the number of sorted cells per lane or experiment that could be processed further. Together with Jasper Panten, I used a 10x-based dataset of the mouse nervous system published by Zeisel *et al.* [58] to annotate cell types. We evaluated the annotation confidence of both SmartSeq and BarcodeSeq sequencing strategies, and only cells that passed all quality controls were used for further analysis (**Supplementary Figure 6**, **Supplementary Figure 7**).

Among the large dataset of neurons sequenced (~n = 5000), about 30% of cells sequenced with SmartSeq passed all quality controls. With BarcodeSeq, I was able to successfully sequence and process over 60% of the sorted cells. However, the sequencing depth was lower with BarcodeSeq compared to SmartSeq. While SmartSeq had a median of 10124 genes per cell, BarcodeSeq only had a median of 3308 genes per cell.

The initial experiments resulted in a low fraction of neuronal cell types as the collagenase digestion favored glial, smooth muscle, and vascular cells, which I identified based on marker gene expression (**Supplementary Figure 5**). After optimizing the Trace-n-Seq approach, I was able to successfully sequence almost exclusively high-quality neurons, which I verified by analyzing the relative expression of several neuro markers and finding robust expression in all cells that passed quality controls (**Figure 24** A, **Supplementary Figure 8**).

With the goal of characterizing the sensory and sympathetic neurons innervating the pancreas, I conducted Trace-n-seq on the DRGs (TH5-TH13) and CGs of NSG and BL6 mice after intrapancreatic FB injection. After quality control, I obtained 216 sensory neurons (74 BL6, 142 NSG) and 273 sympathetic neurons (155 BL6, 118 NSG) using modified SMART-Seq2 and 219 sensory and 249 sympathetic neurons using BarcodeSeq. All neurons expressed robust levels of *PRPH* (**Figure 24** A).

I annotated the neurons based on a scRNA-seq atlas of the mouse nervous system [58] and found significant heterogeneity in the CG and DRG populations infiltrating the healthy pancreas (**Figure 24** B). While I could also annotate the PNS neurons to brain neurons based on Tabula Muris, the annotation confidence was significantly lower compared to annotation to a dataset including PNS neurons (**Supplementary Figure 9**).

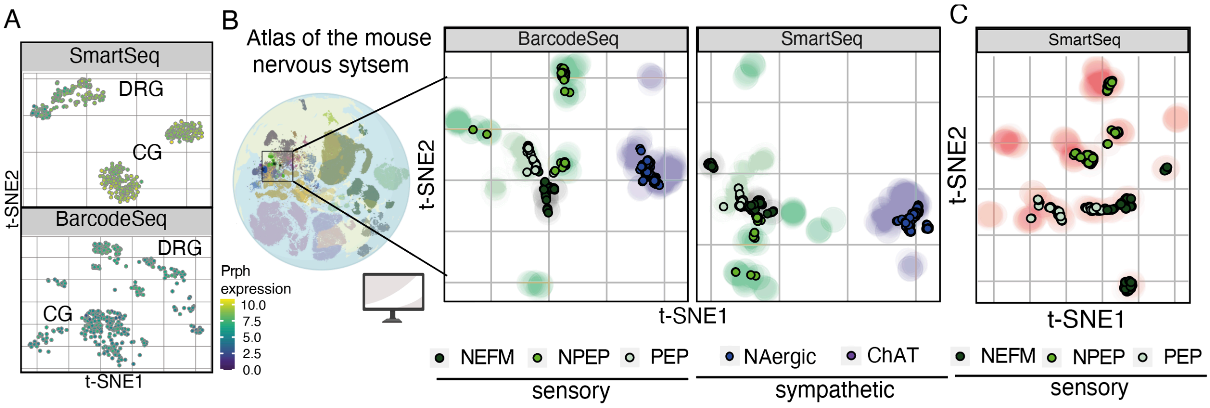

**Figure 24: Pancreas innervating neurons display great heterogeneity.** (A) t-distributed stochastic neighbor embedding (t-SNE) plots of SmartSeq and the BarcodeSeq indicating relative expression of Prph. (B) Pancreas innervating neurons projected to t-SNE of the *Zeisel et al.* [58] (C) t-SNE of the *Sharma et al.* [61] DRG atlas with pancreas innervating neurons projected. NEFM= neurofilament sensory neurons, NPEP= non-peptidergic sensory neurons, PEP= peptidergic sensory neurons, NEergic= sympathetic noradrenergic neurons, ChAT= sympathetic catecholaminergic neurons.

I detected two major subtypes of sympathetic, noradrenergic CG and subpopulations of all three major subtypes of sensory DRG neurons (neurofilament (NEFM)-, peptidergic (PEP)- and non-peptidergic(NPEP) to innervate the pancreas (**Figure 24** B, **Figure 25** A/B) [58].

The three major subtypes can be subdivided into 17 minor subtypes of DRG neurons described by Zeisel *et al.*, of which we only found 12 to project into the pancreas in our dataset (**Figure 25** C). Particularly classic nociceptive neurons were scarce in our pancreas dataset. This indicated a high heterogeneity of pancreas innervating neurons.

To increase robustness, DRG neurons were additionally annotated based on an additional DRG atlas (**Figure 24** C) [61]. Based on the *Sharma et al.* annotation most neurons were classified as proprioceptors or low-threshold mechanoreceptor (LTMR) (also termed neurofilament) and only a minority was classified as CGRP+ nociceptors or nonpeptidergic nociceptors. Not all known subtypes were detected. I observed a good overlap between functionally equivalent populations in the two reference datasets (**Figure 25** D/E).

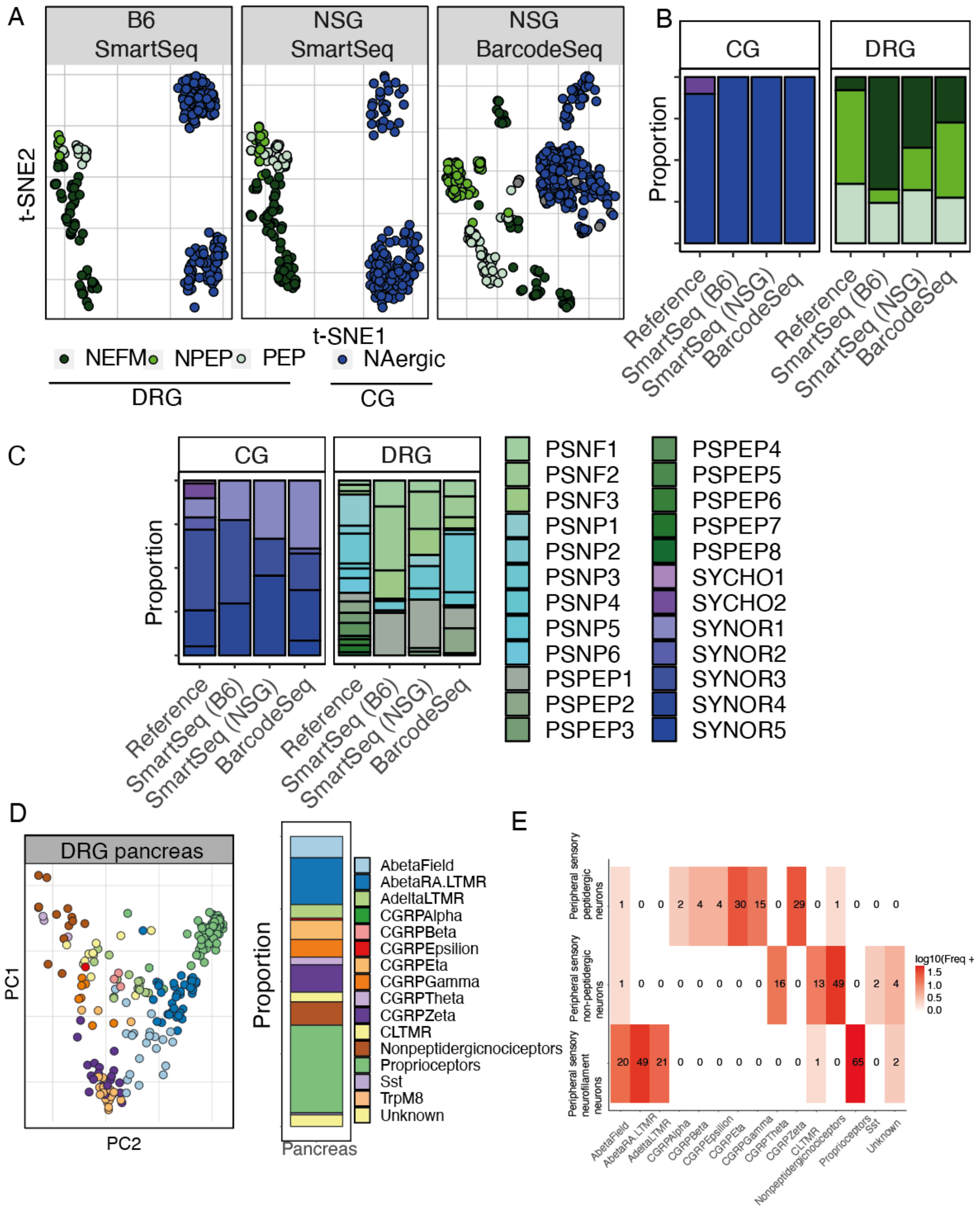

**Figure 25: Characterization of pancreas innervating neurons via the Trace-n-Seq.** (A) t-SNE plot from Trace-n-Seq of 957 pancreas CG and DRG neurons showing 4 annotated main clusters using BL6 and NSG mice with SmartSeq and NSG mice with BarcodeSeq (B) Neuronal subtype proportion of pancreatic sympathetic and sensory neurons compared to reference by Zeisel et al. (C) In depth neuronal subtype proportion of pancreatic sympathetic and sensory neurons compared to reference by Zeisel et al. (D) Neuronal subtype proportion of pancreatic sensory DRG neurons compared to reference by Sharma et al. (E) Overlay of subtype stratification of neuronal subtype proportion of pancreatic sensory neurons by *Zeisel et al*. and *Sharma et al.*

Sympathetic, neurofilament (NF) sensory neurons, peptidergic sensory neurons, and non-peptidergic sensory neurons are different subtypes of neurons with unique molecular, structural, and functional characteristics, including the neurotransmitters they use. Analysis of the composition and neurotransmitter (NT) status of pancreas innervating CG neurons revealed only noradrenergic neurons. Noradrenergic neurons release norepinephrine (NE) (**Figure 26**) which is responsible for regulating the body's response to stress and controlling various physiological functions such as heart rate, blood pressure, and glucose metabolism. Norepinephrine acts on various target cells by binding to different types of receptors, such as alpha and beta receptors, and triggering different physiological responses [50]. CG neurons were annotated based on sympathetic trunk neurons, as no reference map of CG neurons exists. A previously detected subpopulation of cholinergic neurons known to innervate sweat glands and present in the trunk did not project into the pancreas. Zooming in on noradrenergic subpopulations, we identified 3 of the 5 different subtypes described within the references (**Figure 25** C) [56, 58].

The sensory innervation derived mostly from neurofilament neurons and compared to the reference to a lesser extent by peptidergic and non-peptidergic neurons (**Figure 25**). These neurons use mainly glutamate (VGLUT1/2; some VGLUT3) but some are proposed to secrete nitric oxide and/or acetylcholine. (**Figure 26**).

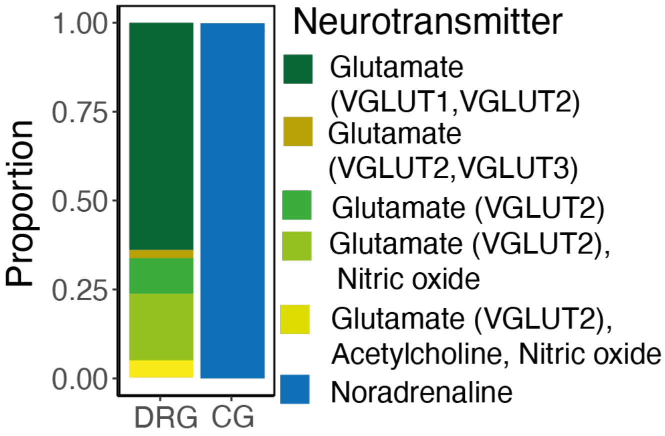

**Figure 26: Pancreas innervating neurons are heterogenous in their neurotransmitter status.** Barplot of the neurotransmitter status of pancreas CG and DRG neurons (489 neurons by SmartSeq).

In the above analysis, the basic clusters were reproduced independent of the sequencing protocol or the mouse strain studied (**Figure 25** A-C). The BarcodeSeq approach enabled me to sequence a large number of neurons in a cost-effective manner as individual cells are barcoded in the initial annealing step and can be pooled afterwards. However, with SmartSeq I identified more genes/cell and therefore used this data for most of the differential expression analysis and used BarcodeSeq as an excellent tool for cell type identification and further validation for analysis obtained with the SmartSeq protocol.

### 3.4.2 Pancreas-innervating sensory neurons are distinct from their skin-innervating neurons

Different neuronal subtypes innervate different tissues and have specialized functions in those tissues. To study whether Trace-n-Seq gives a representative overview of neuronal populations, I next traced neurons from the peritoneum (180 DRG neurons), transverse colon (17 CG neurons) and spleen (76 CG neurons) (**Figure 27** A). The number of neurons that were sequenced was dependent on the tracing capacity and number of neurons innervating the tissue (**Figure 27** B). Composition of splenic and colonic neurons were similar to pancreatic neurons, however, I identified differentially expressed genes indicating for a target organ specific anatomic fingerprint of innervation (**Figure 27** C).

Analyzing the differences in more detail I found different abundances of neuronal subtypes to innervate pancreas or peritoneum (**Figure 27** D-F). By annotating DRG subtypes by the two reference datasets, we detected CGRPAlpha/ Beta/ epsilon sensory, peptidergic nociceptive neurons specifically in the peritoneum compared to an increased frequency of proprioceptive, neurofilament neurons in the pancreas (**Figure 27** D-H).

Peritoneum innervating neurons are responsible for detecting and transmitting information about mechanical and thermal stimuli to the central nervous system. These neurons express a specific set of markers such as substance P and isolectin B4 as well as calcitonin gene-related peptide (CGRP) and transient receptor potential vanilloid 1 (TRPV1) and can be further classified mostly as peptidergic and non-peptidergic (**Figure 27** G,H).

Based on these biological features the composition of pancreas and peritoneum innervating neurons is in line with biological expectations.

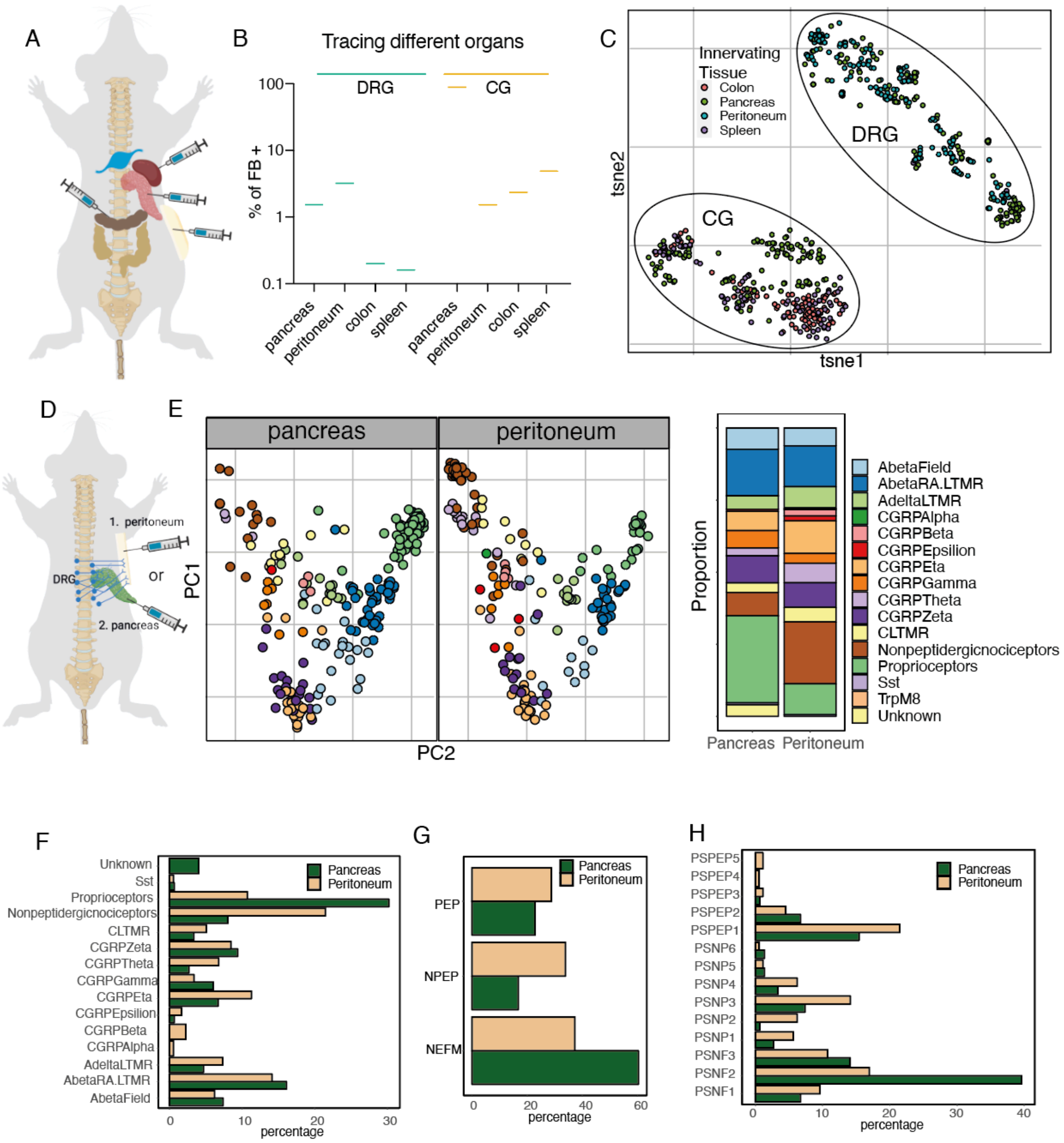

**Figure 27: Pancreas innervating neurons differ from peritoneum, spleen and colon innervating neurons.** (A) Schematic of Trace-n-Seq of periteoneum, spleen and colon injection. (B) FACS based tracing assessment of pancreas in comparison to periteoneum, spleen and colon injected mice (n=3) (C) t-SNE plot of pancreas CG and DRG neurons and peritoneum DRG neurons, spleen CG and colon CG neurons. (D) Schematic of Trace-n-Seq of periteoneum and pancreas. (E) PCA plot of 331 pancreas DRG neurons and 180 peritoneum DRG neurons annotated by Sharma et al. (F) Subtype stratification of pancreas and PDAC innervating neurons annotated by Sharma et al. (G) Basic subtype stratification of pancreas and PDAC innervating neurons annotated by Zeisel et al. (H) In depths subtype stratification of pancreas and PDAC innervating neurons annotated by Zeisel et al.

In summary Trace-n-Seq allowes high throughput plate based scRNA-sequencing of hundreds of neurons with information of the target organ, and thereby provides a map of the neuronal control of pancreas, spleen, peritoneum and colon. By employing this method, I validated textbook features of neuroanatomy such as increased nociceptive innervation of the peritoneum compared to epithelial organs. Trace-n-Seq makes target tissue specific transcriptional profiling feasible and translatable to various physiologic or pathologic conditions.

### 3.4.3 Distinct neuronal subtypes can be identified and validated based on Trace-n-Seq data

I next aimed to classify neuronal subpopulations not only based on reference datasets but on established marker genes. While pan-neuronal markers *Prph* or *Nefm* were expressed in all five major DRG and CG neuronal populations, *Th* was detected in all CG but only few DRG neurons, similar to *Neuropeptide Y* (NPY) (**Figure 28** A). Vice versa, DRG neurons exclusively expressed mechano-sensor *Piezo2* and *Ntrk3* as a marker of glutamatergic neurons. The two CG subtypes displayed distinct expression of *Shox2* and *Bmpr1b* (Cluster 1) or *Socs2, Slit2* and *NRP1* (Cluster 2) on RNA and protein level(**Figure 28** A-C,E,F).

As the CG has not previously been characterized by scRNA-seq, we compared the two main clusters with sympathetic trunk datasets. Cluster 1 showed similarity with neurons regulating piloerection and vasotension [56]. Cluster 2 however did not map to previously described subtypes and expressed markers similar to cholinergic sympathetic neurons. (**Figure 28** D). To get further insights into the CG clusters functions, we performed Gene Set Enrichment Analysis (GSEA). In line with a the proposed role in vasoregulation, Cluster 1 upregulated gensets associated with hypoxia and HMOX1 signaling and transcription was driven by *Per1*, a key regulator of the circadian rhythm, *Hoxa10* and *Atf5* also known to modulate circadian rhythm in adrenal glands [95]. Neurons play a critical role in the regulation of blood vessels and blood flow. Neurons can respond to hypoxia by releasing neurotransmitters and neuropeptides that help to increase blood flow and oxygen to the affected area. Heme oxygenase-1 (HMOX1) is an enzyme that is activated in response to stress and inflammation. It has been shown to be involved in the regulation of blood flow and the response to injury. Recent studies have shown that HMOX1 is also expressed in neurons, and it has been proposed to play a role in the regulation of neuronal function and survival [96].

Hoxa10 is usually expressed in sensory neurons and plays a role in the regulation of the sensitivity of sensory neurons to noxious stimuli but is also involved in the development and maintenance of the nervous system [97]. Activating transcription factor 5 (ATF5) is a transcription factor that is known to be involved in the regulation of cell survival and stress response. Recent studies have shown that ATF5 is usually expressed in sensory neurons and plays a role in the regulation of the sensitivity of sensory neurons to noxious stimuli.

Meanwhile Cluster 2 expressed levels of glutamatergic receptors and enriched for “Regulation of Insulin Secretion” arguing for a role in metabolic and endocrine regulation with transcription driven by *Ap1* and *Mier1*. (**Figure 28** D, **Supplementary Figure 10**). Within the DRG, neuronal subpopulation expressed markers like *Ntrk3, Slit2* (NEFM), *Calca, Bmpr1b* (PEP), *Soc2* (NPEP) uniquely between the 3 major clusters (**Figure 28** A,E,F) and SLIT2 and CGRP (Calca) were validated as uniquely expressed markers of in pancreas-traced FB$^{+}$ DRG subpopulations by confocal microscopy (**Figure 28** E/F/G).

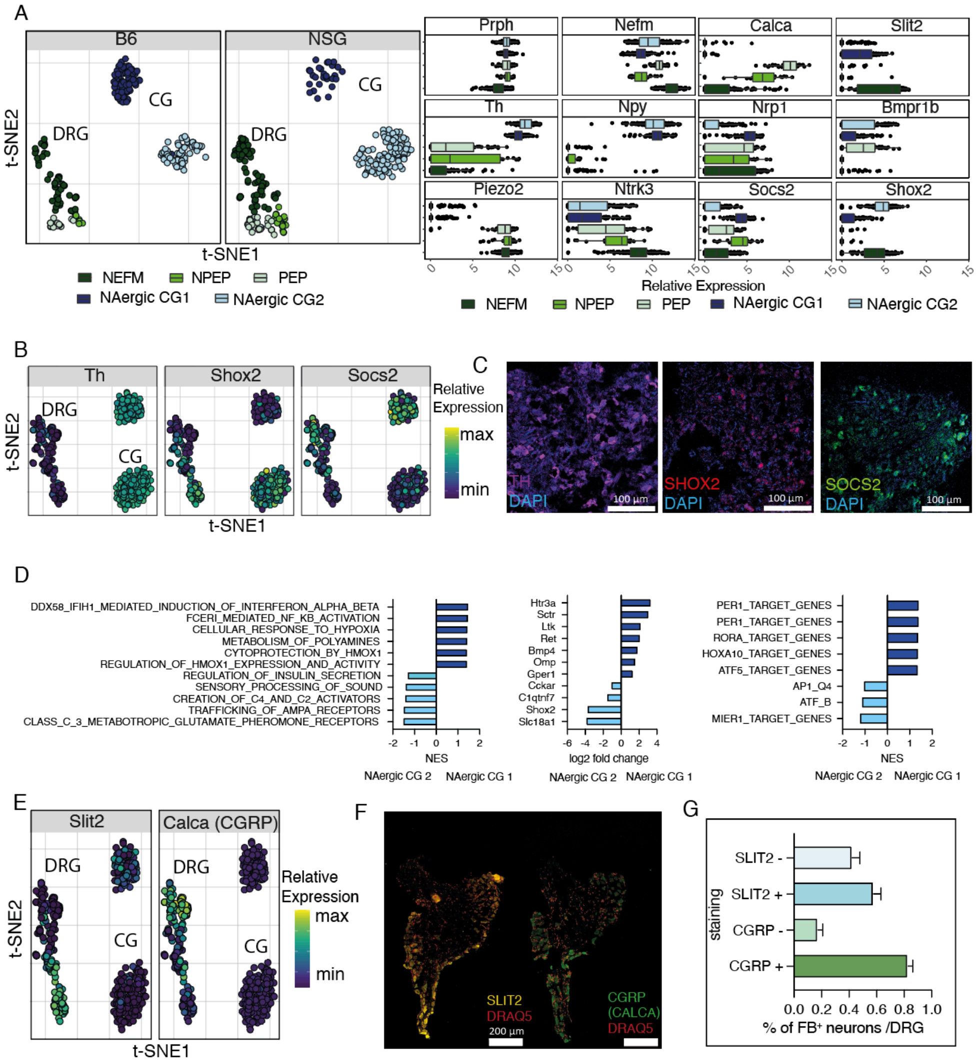

**Figure 28:Pancreas-innervating neurons express unique markers and functional pathways.** (A) t-SNE plot from Trace-n-Seq of 331 pancreas CG and DRG neurons (B6/ NSG) and subcluster specific relative expression of marker genes. (B) Relative expression of tyrosin hydroxylase (TH), Shox2 and Socs2 defining CG clusters. (C) IF staining of CG section with TH, SHOX2, SOCS2; scale bar 100 µm. (D) GSEA, differential expression and transcription factor analysis between clusters NAergic CG1 and NAergic CG2. (E) Relative expression of Slit2 and Calca defining DRG clusters. (F) IF staining of DRG ganglia for SLIT2 (yellow) and CGRP (green) scale bar 200 µm. (G) Quantification of FB+, SLIT2 or CGRP labeled neurons in DRG n=3mice.

Therefore, Trace-n-seq of the pancreas validates established and identifies novel neuronal subtypes and their markers by isolating high quality neurons. This allows for signaling analysis to infer functional differences between rare subpopulations and thereby enables hypothesis generation for experimental validation.

## 3.5 Investigation of PDAC innervating neurons

After quantification and successful sequencing of healthy pancreas innervating neurons and their functional description based on their expression profile, I aimed to analyze nerves innervating PDAC and compare it to the healthy control pancreas. I hypothesized that neurons not only change in sprouting pattern but specifically in their expression profile. I intended to access any transcriptomic changes in the cell body of CG and DRG neurons after axonal contact to cancer cells.

### 3.5.1 Xenograft and genetic mouse models of PDAC display increased axonal sprouting

I employed three different PDAC models, two human Xenograft (PDX) (**Figure 29**) [98] and one genetic mouse model generated by *in vivo* pancreatic electroporation (EPO) of a sleeping beauty transposon carrying mutant KRAS combined with a plasmid allowing Crispr/Cas9 based Tp53 deletion (**Figure 30**, details see methods). The plasmids for the EPO model were kindly provided by Julian Mochayedi (AG Offringa). Induction of tumors by electroporation in mice is a technique that uses electrical pulses to temporarily disrupt the cell membrane and enhance the delivery of DNA/plasmids into the cells. This technique has several benefits compared to alternative cancer mouse models as it allows for a high concentration of plasmid to be delivered into the tumor cells, leading to better efficacy. It allows for better representation of human disease as it mimics real tumors with its invasive and aggressive nature, it does not rely on complex genetically modified mice, and it is possible to induce tumors in any mouse with different genetic backgrounds (**Figure 30** B).

The EPO-based system leads to development of adenocarcinomas within 2-3 months in >90% of mice and neuronal infiltration was detected in all models (**Figure 30** C, **Figure 31**).

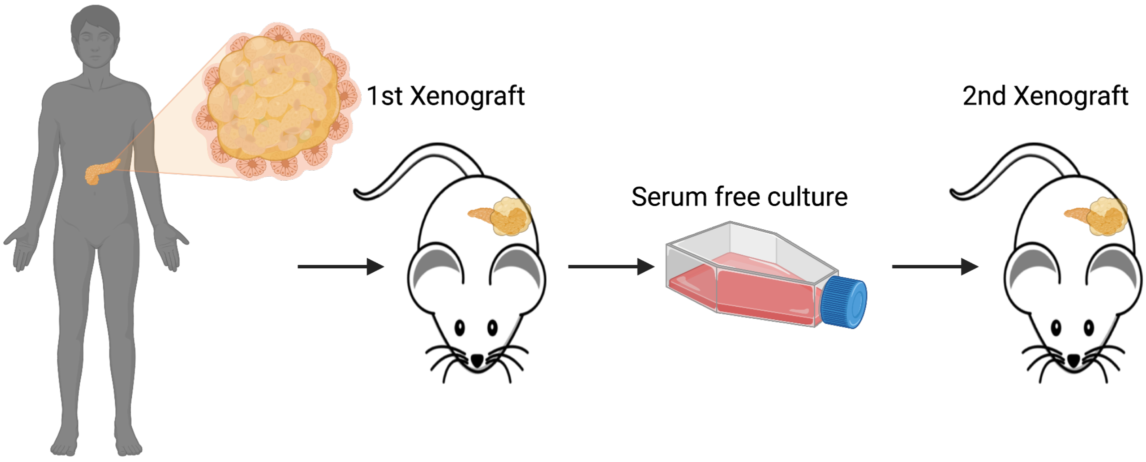

**Figure 29: Establishment of human PDX model.** Primary PDAC patient material is dissociated and injected into recipient mice. After tumor formation cells are digested and brought into 2D serum free cell culture that can be re-transplanted into NSG recipient mice to form a PDX resembling human tumors.

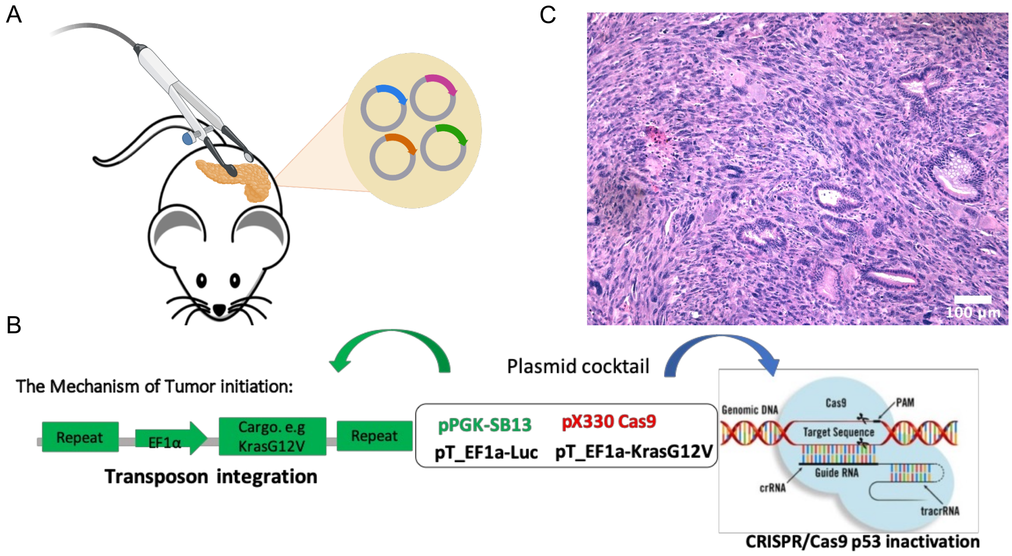

**Figure 30: The Electroporation System.** (A) Schematic of the electroporation process. (B) Tumors are induced by injecting a plasmid cocktail into the pancreas containing a transposon encoding mutated Kras which integrates using a transposase, in combination with CRISPR mediated p53 inactivation. (C) The resulting tumors show the classical characteristic of PDAC.

As quantification of 3-dimensional, neuronal structures by standard histology is limited (**Figure 31** A,B), neuronal infiltration was assessed based on light sheet microscopy of iDISCO cleared tumors (**Figure 31** C,D). Similar to the healthy pancreas, sensory as well as sympathetic neurons infiltrate the entire tumor except for central, necrotic regions, but sprouting patterns were less organized. Of note, in PDX-models mouse-derived neurons innervate human tumors. To detect and quantify small fibers throughout the tumor, we again employed machine learning based algorithm which allowed background reduction and structural reconstruction of signal beyond classic rendering techniques (**Figure 31** E, **Figure 32**, **Supplementary Figure 11**).

Thereby, I compared structural plasticity of PDAC infiltrating neurons to healthy pancreas by comparing nerve/tissue area which increase significantly in 3D quantification and showed a similar hyperinnervation trend applying the VOI quantification (**Figure 31** F,G). In the 3D to 2D approach the innervation quantification remained stable. However, tumor grew about three-fold in size, increasing the total area covered by axons and indicating intense axonal sprouting within the tumor tissue (**Supplementary Figure 11** B).

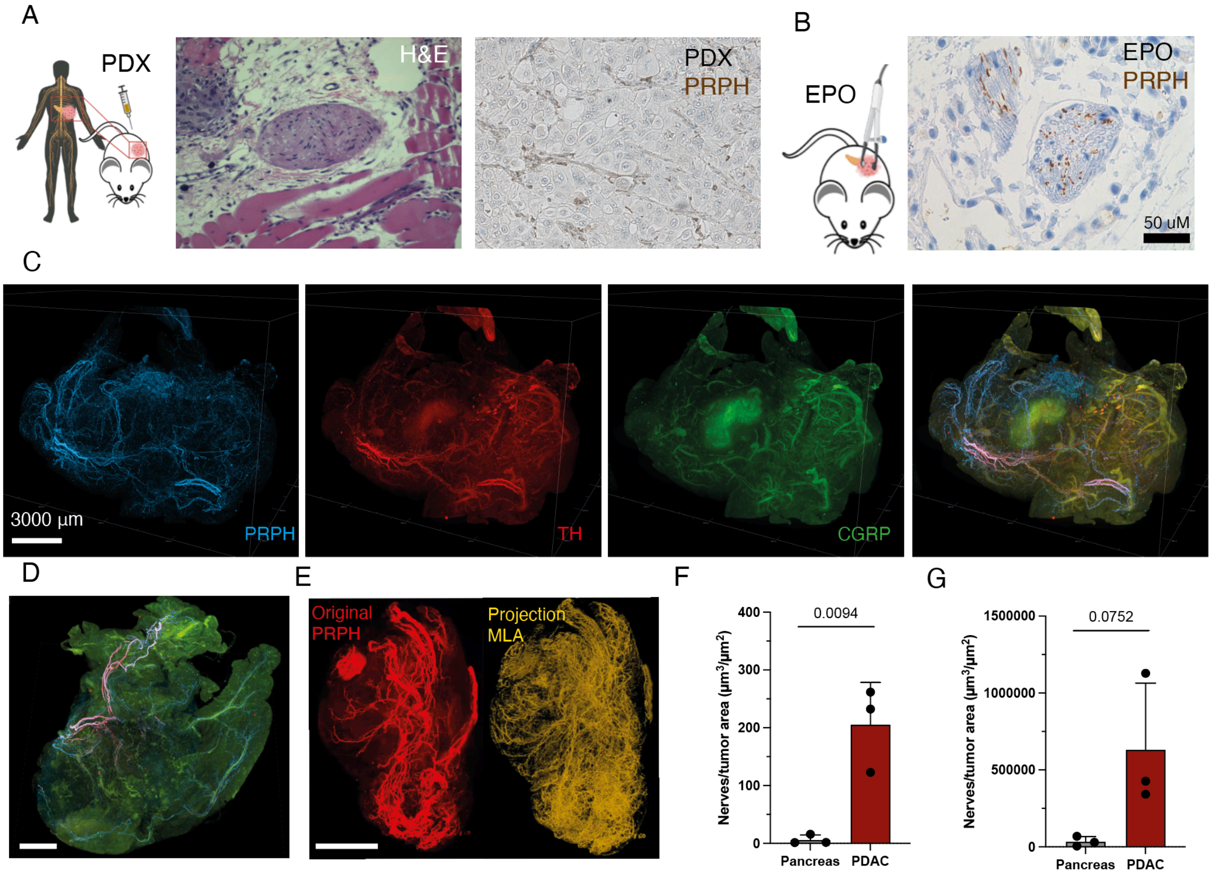

**Figure 31: PDAC innervation is denser compared to pancreatic tissue. (A)** 2D validation of nerval innervation in the PDX model system. (B) 2D validation of nerval innervation in the EPO model system. (C) representative images of PDX tumor innervation obtained using light-sheet microscopy. Marker PRPH (blue), TH (red), CGRP (green). (D) representative merged image of EPO tumor innervation obtained using light-sheet microscopy. Scale bar: 3000 µm, marker PRPH (blue), TH (red), CGRP (green). (E) example of neuron detection using machine-learning algorithm in full 3D analysis. Original Image red, MLA prediction yellow. Scale bar: 3000 µm (F) 3D quantification of neuronal sprouting by nerve/tissue and total nerve area in pancreas (n=3) and PDAC (n=3) innervating neurons using MLA of light sheet microscopy images. (G) VOI quantification of nerve/tissue area. Unpaired t-test. Mean +/- SD is shown.

I found innervation of the pancreas increased in pancreatic cancer and nerve fibers in pancreatic cancer tissue are denser than in normal tissue. Also, subtype composition changes in comparison to healthy pancreas (**Figure 32**). While TH neurons increased, sensory innervation appears weaker.

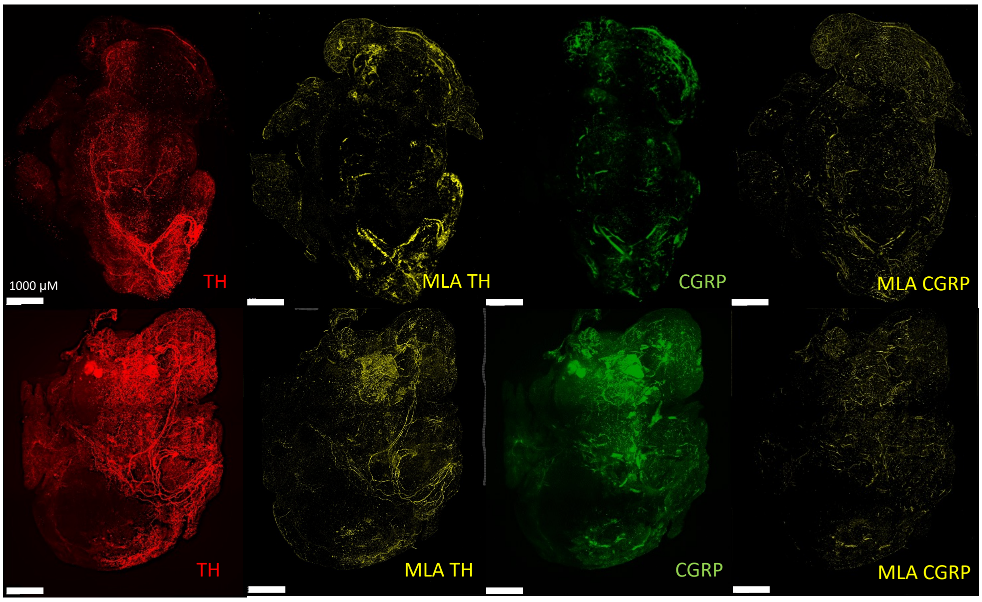

**Figure 32: Neuronal subtype innervation can be visualized with light sheet microscopy and MLA in a 3D to 2D quantification.** Representative images of tumor innervation obtained using light-sheet microscopy (n=4). Sympathetic marker TH (red), sensory marker CGRP (green) and MLA prediction (yellow). Scale bar: 1000 µm

Of note, different quantification methods resulted in slightly different outcome as seen for sprouting pattern, specifically for big samples (**Figure 33**). However, through these methods, I consistently observed increased sprouting in the tumor compared to healthy pancreas.

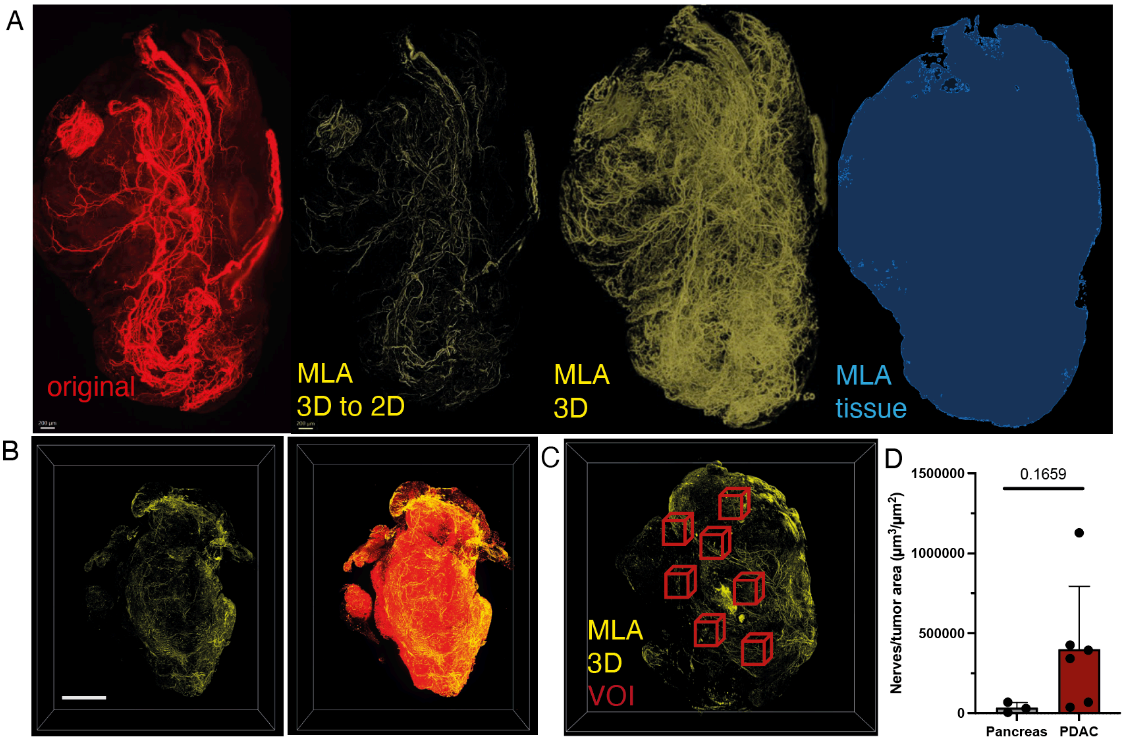

**Figure 33: Quantification of nerval innervation by section-wise MLA-based analysis.** (A), PDAC staining and MLA based nerve quantification of 3D to 3D convolution vs full 3D quantification and tissue prediction. (B) Full 3D MLA prediction without and with tissue prediction. (C) 3D prediction of Volumes Of Interest (VOI). (D) MLA based VOI analysis of pancreas (n=3) vs PDAC tissue (n=6). Nerve/tissue area is depicted. Unpaired t-test. Mean +/- SD is shown.

Our collaboration partners at the Heidelberg Pathology Institute completed these data by further comparing innervation pattern in human specimen. Here however, only staining of 2D specimen of pancreas and PDAC tissue was possible. IHC pictures and assessment of the area of neuronal structure and tissue area ratio reveals a strong increase in neuronal structures in tumor specimen compared to healthy pancreas control staining (**Figure 34** A-C).

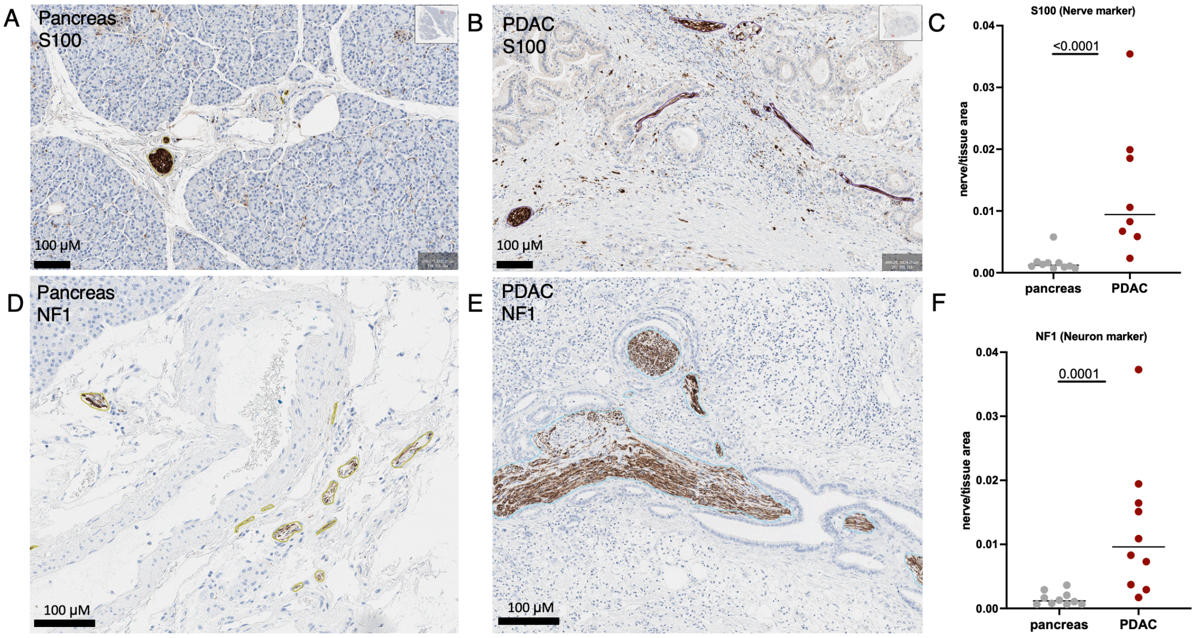

**Figure 34: Nerval innervation is increased in human PDAC samples.** (A) representative images of IHC 2D human pancreas innervation obtained by Brightfield microscopy stained with S100 (B) representative images of IHC 2D human PDAC innervation obtained by Brightfield microscopy stained with S100 (C) quantification of neuronal structures per area between human pancreas and human PDAC samples (n=10), P value was determined by unpaired t-test. Mean +/- SD is shown. (D) representative images of IHC 2D human pancreas innervation obtained by brightfield microscopy stained with NF1 (E) representative images of IHC 2D human PDAC innervation obtained by brightfield microscopy stained with NF1 (F) quantification of neuronal structures per area between human pancreas and human PDAC samples (n=10) P value was determined by unpaired t-test. Mean +/- SD is shown.

Next, I assessed whether this total increase in neuronal structures within PDAC is based on recruitment of additional neurons to the tumor by injecting FB into PDX-tumors. After assessment by flow cytometry or confocal imaging, I again found most DRG neurons to originate from around TH9. The total amount of neurons from DRG or CG ganglia innervating the tumor was not higher than in the healthy pancreas (**Figure 35** A-C), arguing that hyperinnervation is exclusively based on increased sprouting of existing neurons. Within the DRG, I found a slight increase in PDAC-infiltrating neurons originating from DRG-L1, possibly due to the attraction of neurons from nearby epithelial organs like the spleen or peritoneum (**Figure 35** A).

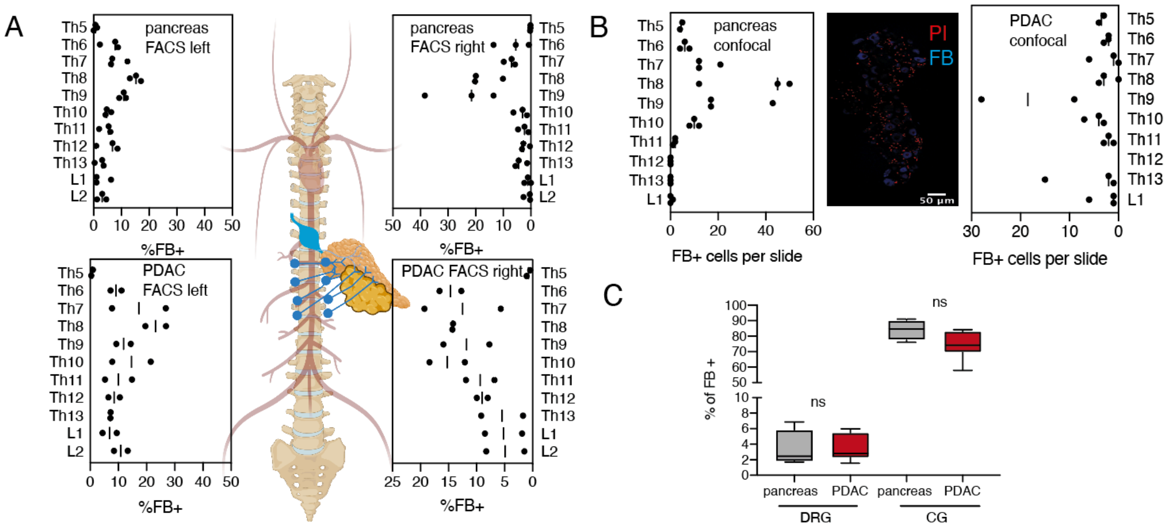

**Figure 35: Increased nerve density in PDAC is due to intense sprouting.** A) Comparison of nerval innervation by neurons from the DRG by flow cytometric analysis after tracing from pancreas (n=3) and PDAC in mice (n=2). (B) Comparison of nerval innervation by neurons from the DRG by microscopy analysis after tracing from pancreas and PDAC in mice (n=2). (C) Comparison of nerval innervation (% of $FB^+$ cells per all neurons) by neurons from the CG and DRG (TH5-TH13) in total by flow cytometric analysis after tracing from pancreas and PDAC in mice (n=3 mice).

In summary, I could show that both tumor models display hyperinnervation based on increased sprouting.

### 3.5.2 PDAC reprograms the transcriptome of sympathetic and sensory neurons

Next, I employed Trace-n-Seq and successfully sequenced 408 PDAC innervating CG (302) and DRG (106) neurons traced from the two PDX- (PACO10, PACO43) and 187 neurons from EPO-tumors (139 CG, 48 DRG) by SmartSeq2 and 302 PDX-neurons (161 CG, 141 DRG) using BarcodeSeq for a total of 897 PDAC-infiltrating neurons and integrated them with control neurons (799 healthy pancreas; total 1696). Thereby, I identified similar clusters as in the healthy setting with both sequencing techniques and in all mouse models (**Figure 36** A). To focus on robust PDAC driven changes and exclude mouse strain, tumor model and/or batch dependent effects, I performed differential expression analysis comparing the SmartSeq2 datasets of healthy B6 and NSG as well as EPO and both xenograft models. By comparing all healthy and PDAC-CG neurons, I identified 431 DEG - 139 up- and 292 down-regulated - in PDAC-neurons. By analyzing the CG sub-clusters individually, we found 312 DEG (130 up, 182 down) in Cluster 1 and 214 (38 up, 176 down) in Cluster 2 (**Figure 36** B). The top downregulated genes contained neuropeptides e.g. *Galanin (Gal),* receptors such as *Erbb2/*3 or *Ntrk3*, matrix proteins including *Matn2* or immune regulators like *Mif*. Genes induced by PDAC were non-coding RNAs such as *Mir6236*, *Neat1* or *Lars2*, receptors like *Robo*1, transcriptions factors including *Hoxc5*, signaling molecules *Fgf14* or *Edn3* and structural proteins like *Ttn*.

Between all DRG neurons I found only 92 DEG between healthy pancreas and PDAC- neurons, but 155 (29 up, 126 down) in NEFM and only 6 in PEP- (5 up, 1 down) or 5 (2 up, 3 down) in NPEP subtypes (**Figure 36** B), arguing that PDAC does not influence expression equally between subtypes. The top DEG upregulated in healthy neurons were related to metabolism (*Gapdh, Got*), but also neuropeptides such as *Calca*, and receptors like *Ntrk1* or *Htr3a* or the immunoregulator *Mif*. Vice versa the master transcription factors *Atf3* and *Dclk2*, secreted factors like *Angptl2* and receptors like *PDGFR* - and again *Lars2* and *Mir6236* were higher expressed in PDAC-neurons.

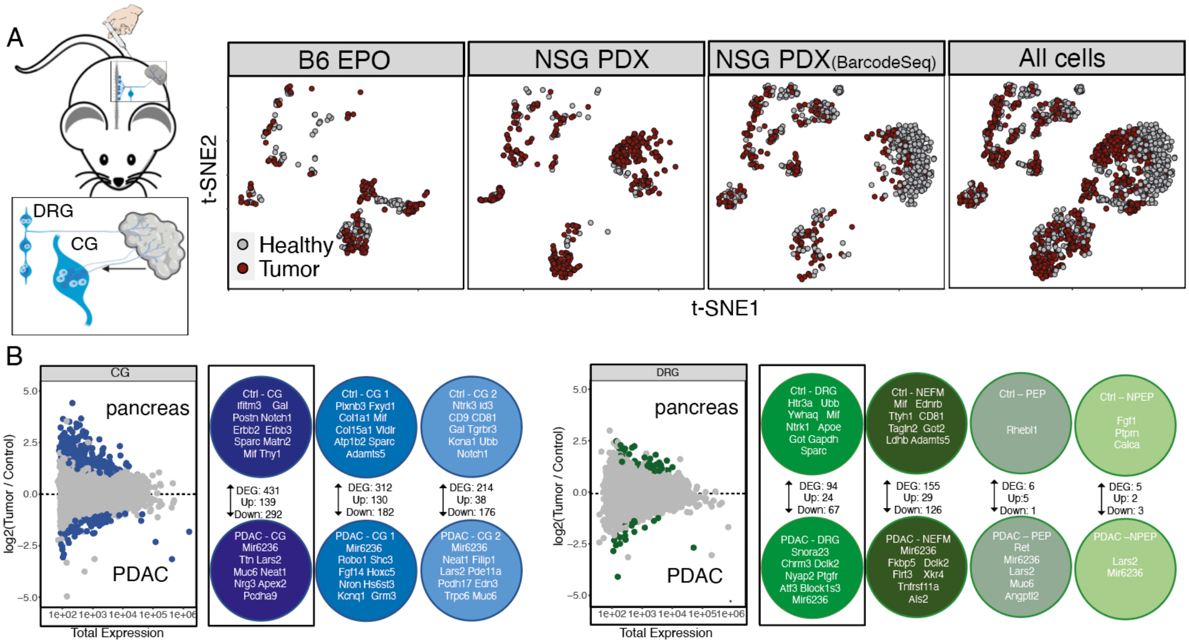

**Figure 36: Neurons are reprogrammed by PDAC.** (A) Schematic: Trace-n-seq in PDAC, t-SNE plot of pancreas vs PDAC neurons by SmartSeq and BarcodeSeq (799 pancreas/ 897 PDAC neurons). (B) Volcano plots, number of and exemplary DEGs between pancreas/PDAC in all CG and DRG neurons and subclusters.

Highlighting the importance of single-cell data, expression changes of *Robo1*, *Tubb5* (**Supplementary Figure 13**) and *Sema5a* in CG and DRG neurons was subtype specific. *Sema5a* expression increased in CG Cluster 2 and for DRG in PEP-neurons only (**Figure 37** A, **Supplementary Figure 13**). Meanwhile master regulator of regeneration transcription factor *Lin28b* was upregulated in all CG or DRG PDX-neurons and in IF images with an increase of nuclear LIN28B (**Figure 37** A,B) [99].

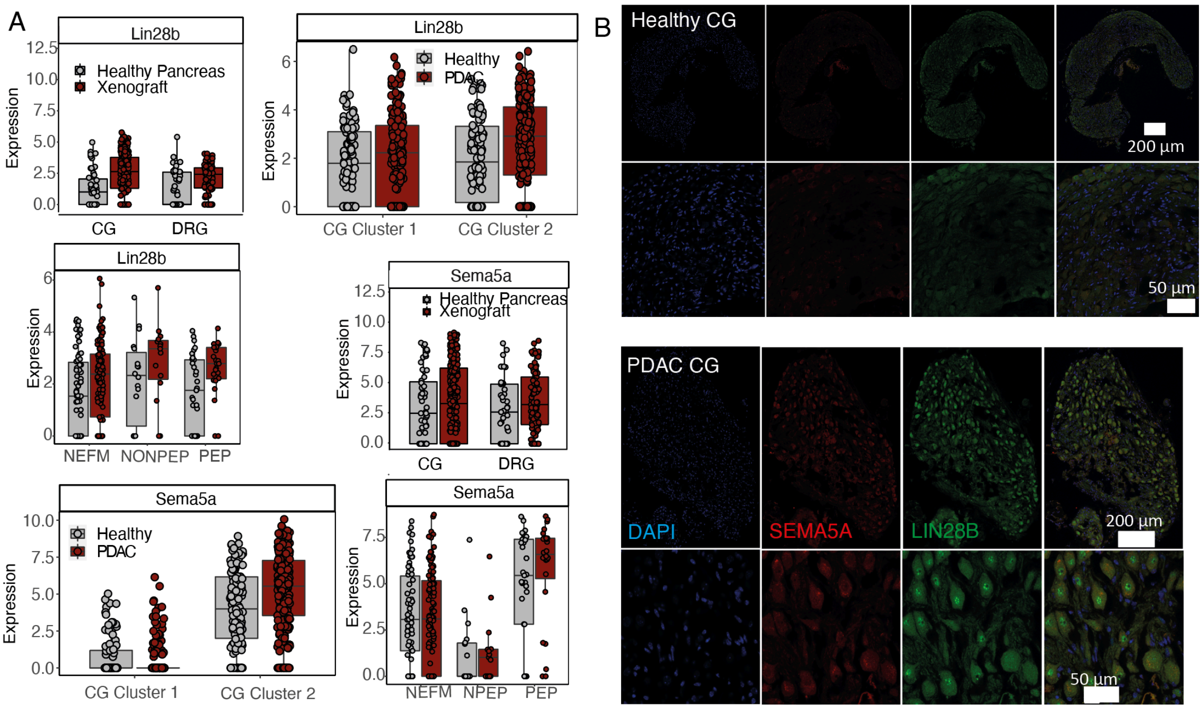

**Figure 37: Genes are differentially expressed between pancreas and PDAC neurons.** (A) Expression analysis of Lin28b and Sema5a in broad and in-depth subtype analysis between pancreas and PDAC innervating neurons (SmartSeq). (B) representative IF staining of SEMA5A, and LIN28B of full CG ganglia section of healthy and PDAC mice.

To get deeper insights into cancer-induced transcriptional changes, I performed GSEA on all subpopulations and found them to more commonly share downregulated than upregulated pathways. All subsets displayed a metabolic switch with pathways like “electron transport chain”, or “metabolism of amino acids and derivates” enriched in healthy neurons. PDAC-neurons upregulated epigenetic processes, “resolution of D-loop structures” and “DNA repair” associated with neuronal damage and regeneration, highlighting reprogramming of the cell state (**Figure 38** A, **Supplementary Figure 14** A) [100, 101]. Again, upregulated gensets were similar between NEFM, CG1 and CG2 neurons, while PEP and NPEP neurons showed less changes (**Figure 38**).

In GSEA on all CG neurons calcium signaling, synapse formation and microtubule formation- indicative of axonal sprouting- were upregulated in cancer infiltrating neurons. Meanwhile DRG neurons enriched for neuronal guidance factors such as *Ntn-1* or *Epha* and glutamate receptor signaling (**Figure 38** B, **Supplementary Figure 14** B). By performing transcription factor analysis next, I identified signatures of master regulators of metabolism *Ppargc1a* upregulated in healthy neurons, while factors associated with neuronal development such as *Hox/Meis1* target genes were upregulated upon PDAC contact [102, 103]. Additionally, some transcription factors were only enriched in subclusters (**Figure 38** C).

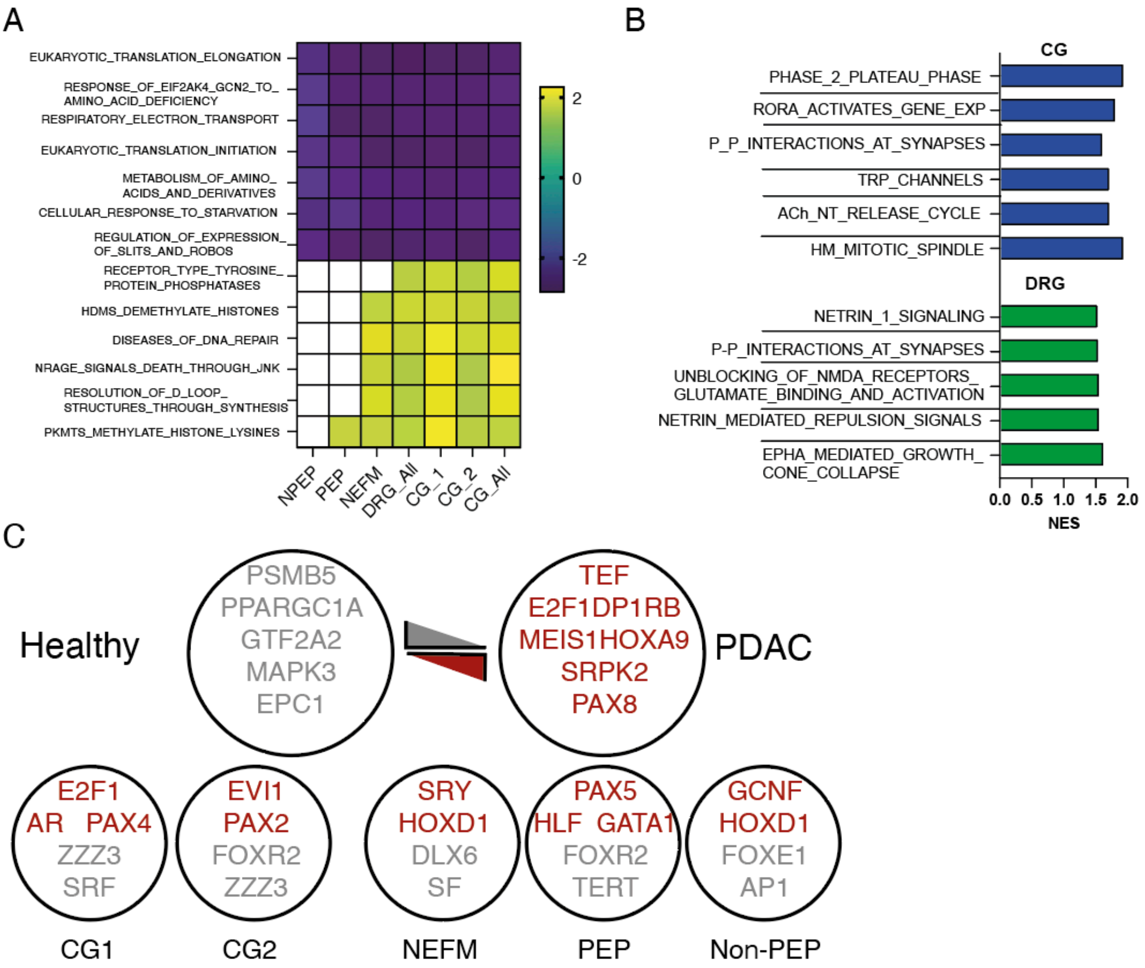

**Figure 38: PDAC induces a tumor specific neuronal expression profile.** (A)GSEA analysis of top shared up and downregulated gene sets between subclusters. (B)GSEA analysis of top upregulated gene sets in PDAC in detected CG or DRG (C)GSEA analysis of transcription factor signatures deregulated in pancreas/PDAC neuron subclusters

In summary, Trace-n-Seq allows the analysis of hundreds of individual tumor-infiltrating neurons and I have thereby uncovered multiple transcriptional changes linked to neuronal outgrowth and development, metabolism as well as microenvironmental processes like stromal and immune regulation.

### 3.5.3 PDAC induces a Cancer-Nerve signature shared between subpopulations

Neural injury and neuronal inflammation are two major pathological conditions that can result in damage or dysfunction of the nervous system. A gene signature is a set of genes that are found to be differentially expressed (either up- or down-regulated) in response to a specific condition or treatment. Gene signatures can be used to identify the underlying mechanisms of a disease, to predict the response to treatment, and to track the progression of a disease. Gene signatures can identify molecular changes in neural injury and neuronal inflammation caused by various stimuli like infection, toxic agents, autoimmune diseases, and injury to the brain, spinal cord, or stroke. These signatures usually include genes involved in immune response, inflammation, and cell death. Research has also shown that pancreatic cancer can potentially damage nerves through the release of proinflammatory cytokines and proteases [104]. These molecules cause damage to the neurons and disrupt their normal function, which in turn can lead to the development of pain and other symptoms associated with pancreatic cancer. However, these findings have not been validated by transcriptomic analysis. To classify cancer-induced transcriptional changes I compared my data with signatures of neuronal stress by dissection or sterile inflammation [54, 55, 62, 105]. While metabolic rewiring in genes downregulated upon sterile inflammation mirrored those genes downregulated in PDAC-neurons, upregulated genes did not correlate in any subpopulation (**Figure 39** A). Moreover, none of the three applied signatures of neuronal injury (surgical denervation) correlated with PDAC induced changes. This argues for a change in the role of *Atf3*, upregulated in PDAC-neurons, and key in response to denervation but apparently inducing different transcriptional programs in cancer [60]. To identify cancer specific neuronal changes, I next combined the top 500 up- and downregulated genes with the highest fold changes from all 5 subpopulations, selected only robustly expressed genes with Normalized Read Counts above 500 to create a PDAC-Nerve (PCN) signature of up- and downregulated genes (**Figure 39** B, **Table 3**). For the PCN-down signature (enriched in healthy pancreas) genes present in at least 2 and for the PCN-up genes present in at least 3 subpopulations were included. When tested these on all subpopulations individually, PCN-up (red)/ PCN-down (grey) signatures enriched in every one with PEP-neurons scoring lowest (**Figure 39** C). I further tested the signatures on the BarcodeSeq dataset as independent validation and although less genes/cell were detected, PCN-signatures enriched correctly in healthy vs. tumor neurons of CG and DRG (**Figure 39** D).

Together, I identified robust general and subtype specific transcriptomic changes induced upon PDAC and generated a common signature of PDAC innervating neurons. Transcriptomic differences where highest in proprioceptive/neurofilament and sympathetic neurons.

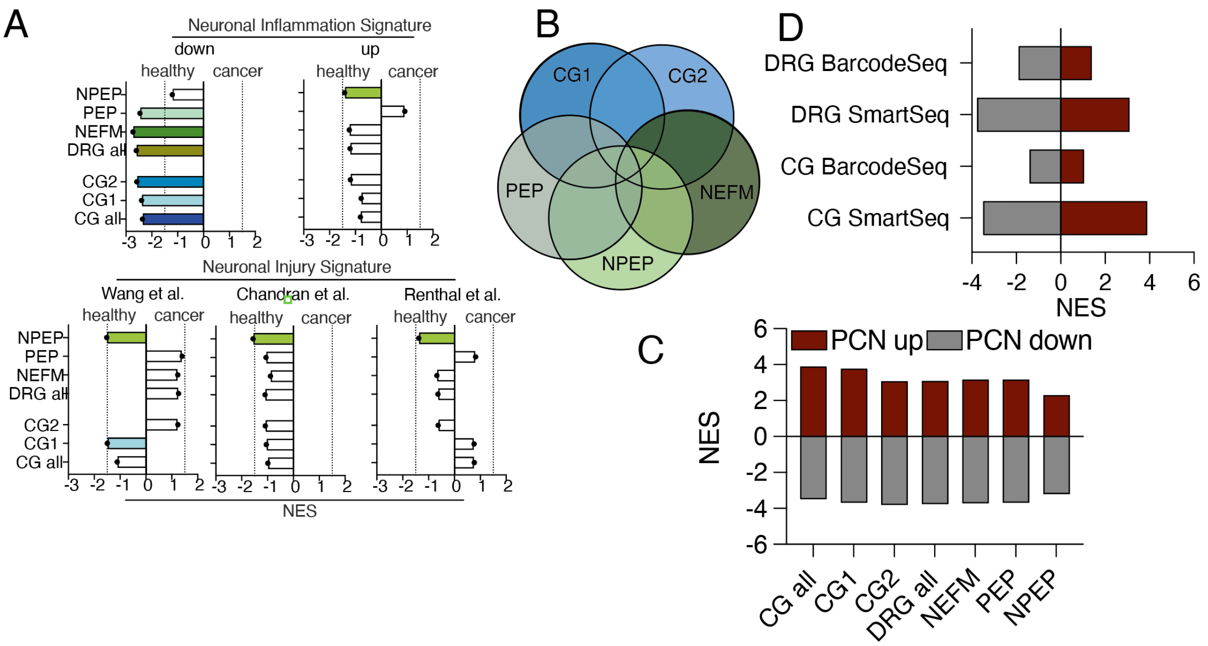

**Figure 39: Definition of a specific Cancer-Nerve-Signature.** (A) GSEA analysis of gensets of signatures neuronal inflammation and injury signatures on our PDAC/pancreas neuron dataset (white=ns). (B) Schematic of shared DEG between subclusters used for Cancer-Nerve signature (CN). (C) Enrichment analysis of PCN up/down signatures on sublcusters of SMART-seq neuron based DEG between pancreas and PDAC (D) Enrichment analysis of PCN up/down signatures of all DRG/ CG neurons based on SMART-seq and Barcode-seq.

### 3.5.4 Transcriptomic changes are induced by proximity to cancer cells

Pancreatic cancer can have a wide range of systemic effects on the body, which can occur as a result of the cancer itself including nutritional deficiencies. Pancreatic cancer can cause malabsorption of nutrients, which can lead to weight loss, malnutrition, and anemia; diabetes- affecting the insulin-producing cells of the pancreas; jaundice- where it blocks the bile duct and cause jaundice (yellowing of the skin and eyes) or fatigue which is often caused by anemia, malnutrition, and cancer-related inflammation [13]. To exclude systemic effects inducing transcriptomic changes in PDAC-neurons, I compared FB-traced neurons from spleens of healthy (76 CG-neurons) and PDX-mice (23 CG-neurons), peritoneum of healthy (180 DRG neurons), PDX-mice tumor adjacent (87 DRG neurons) or at a tumor-distant, pelvic site (25 DRG neurons) (**Figure 40** A). Here, genes high in healthy pancreas CG neurons also enriched in healthy, spleen-traced CG neurons (PCN-down: NES pancreas -3.499, spleen -2.072), whereas the PCN-up signature was induced in PDX-spleen neurons (NES PDAC 3.907, PDAC-PDX-spleen 1.910) (**Figure 40** B). As spleen and pancreas are adjacent, axons may innervate both tissues and tumors may thereby indirectly influence immunobiology via the spleen. Similarly, the PCN-up signature enriched in peritoneum innervating DRG neurons of PDX-mice close, but not distant to the tumor (NES PDAC -3.774, peritoneum: PDX-close 1.9, PDX-distant 1.42).

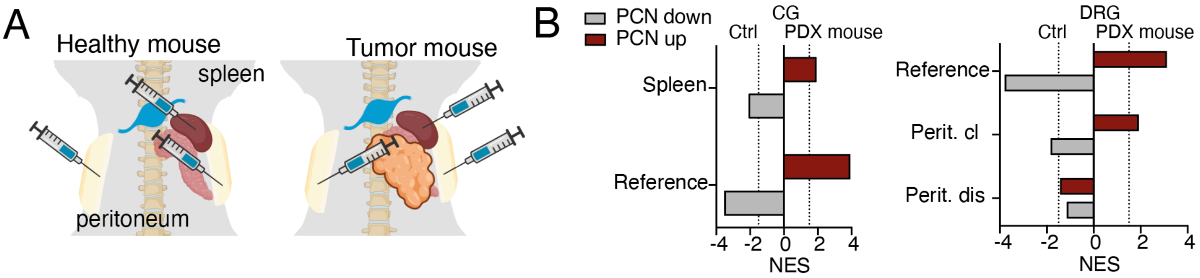

**Figure 40: Proximity and direct contact induces the CN signature.** (A) Schematic: Trace-n-seq of spleen or peritoneum in healthy or PDX-spleen, peritoneum tumor adjacent/ distant of PDAC-mice. (B) GSEA of PCN-signature on PDX-spleen CG neurons and CG PDX-neurons and of DRG traced from tumor adjacent/ distant peritoneum versus PDX-neurons (n=3 mice per condition).

This shows that PDAC orchestrates local, not directly tumor infiltrating neurons reacting to new environments with potential implications for cancer pain, whereas I detected no global transcriptional deregulation in tumors distant DRG neurons excluding a systemic effect (**Figure 40**).

### 3.5.5 PDAC-innervating neurons maintain “cancer-nerve-state” (CNS) after tumor resection

Resection of the primary tumor is the standard treatment for PDAC and is considered the only curative option. Despite the surgical resection of the primary tumor, pancreatic cancer often recurs locally at the surgical site or at distant sites in the body through metastasis [106-109]. However, the exact mechanism that drive recurrence in PDAC remain elusive.

To analyze if persistence of transcriptomic alterations in PDAC-innervating neurons depends on continuous interaction with cancer cells, we used PDX- or sham-operated control mice. After 40 days, we injected FB either into small tumors or healthy pancreas and resected the primary tumor or again sham-operated control mice 7 days later. After 28 days of recovery and absence of cancer cell contact I harvested ganglia and analyzed traced cells of healthy sham operated- and tumor resected mice by scRNA-seq (**Figure 41** A, **Supplementary Figure 15**). I found overexpression of PDAC neurons markers *Lars2* or *Mir6236* (PCN signature genes) specifically within the CG neurons after resection (**Figure 41** C). Vice versa genes downregulated in cancer-infiltrating neurons were downregulated in CG neurons even after resection. This difference was not consistently observed within the DRG neurons. When I tested the complete signatures on all subpopulation, I found positive enrichment of the PCN-up signature in the NEFM, NAergic CG1 and CG2 populations and negative enrichment of the PCN-down signature in NAergic CG1 and CG2 (**Figure 41** B), arguing that sympathetic neurons partially maintain their “cancer-nerve-state” beyond tumor resection.

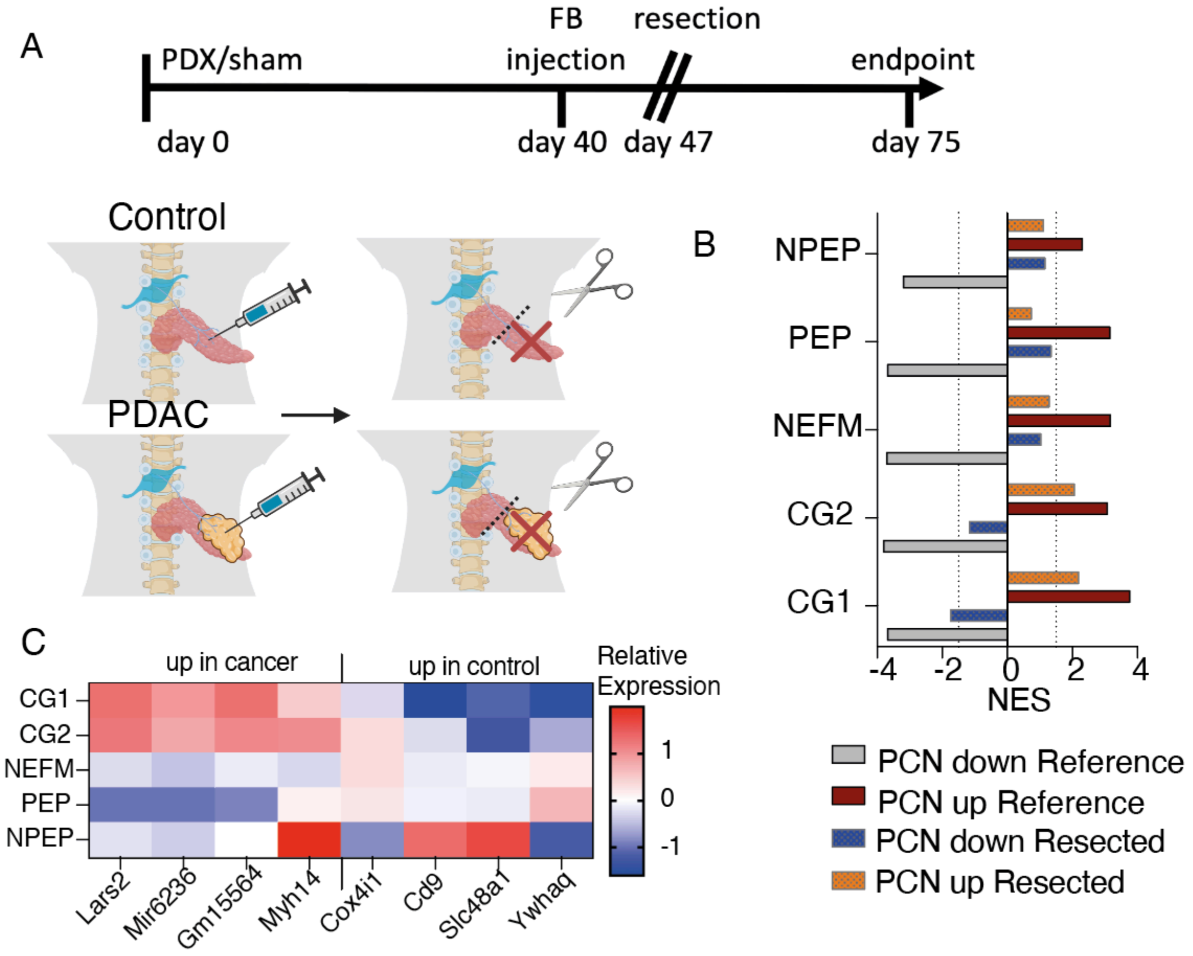

**Figure 41: PCN signature remains after resection of the primary tumor.** (A) Schematic: of PDAC resection after tracer injection. (B) PCN-signature enrichment in neuronal subtypes compared to the PDX-mice (C) Heatmap of differentially expressed genes from the PCN-signature in the resection model.

Taken together, neurons seem to develop into cancer-associated nerve cells that can promote cancer progression and even continue signaling cancer-associated pathways after resection of the primary tumor. Specifically, neurons of the sympathetic nervous system (CG1, CG2) can be activated in the tumor microenvironment, leading to the release of neurotransmitters and promoting cancer growth, invasion and dissemination and remember their “cancer-nerve-state”. In summary, my research suggests that nerves in the tumor microenvironment may play a role in driving the recurrence of pancreatic cancer. Further studies are needed to better understand the mechanisms underlying this association and to identify potential targets for therapeutic intervention.

### 3.5.6 PDAC preferentially attracts proprio- but not nociceptive neurons

As PEP and NPEP neurons displayed less transcriptional changes than other neuronal subtypes, I compared subtype frequencies between PDX and healthy pancreas. In CGs the subtype compositions stayed similar (**Figure 42** A), but for DRG, (enhanced in NSG mice) I detected an increased innervation by the NEFM at the cost of the PEP subtype, independent of sequencing technique (**Figure 42** A,C). When neurons were annotated based on Sharma et al., I identified a decrease in nociceptive neurons as well. In general, the pancreas is mostly innervated by proprioceptive sensory neurons and only the minority of neurons are nociceptors, which further decreased in PDAC (**Figure 42** B,D). This explains, why early stage PDAC is usually pain free. Only in later stages, when the tumor metastasizes, infiltrates ganglia, neurons or the nociceptively innervated peritoneum, patients can experience severe pain [110]. I next analyzed expression of subpopulation markers *Slit2* (NEFM) and *Calca* (PEP/NPEP) in healthy and PDAC-innervating neurons and *Slit2* levels increased in PDAC-neurons, while *Calca* was downregulated (**Figure 43** A/B).

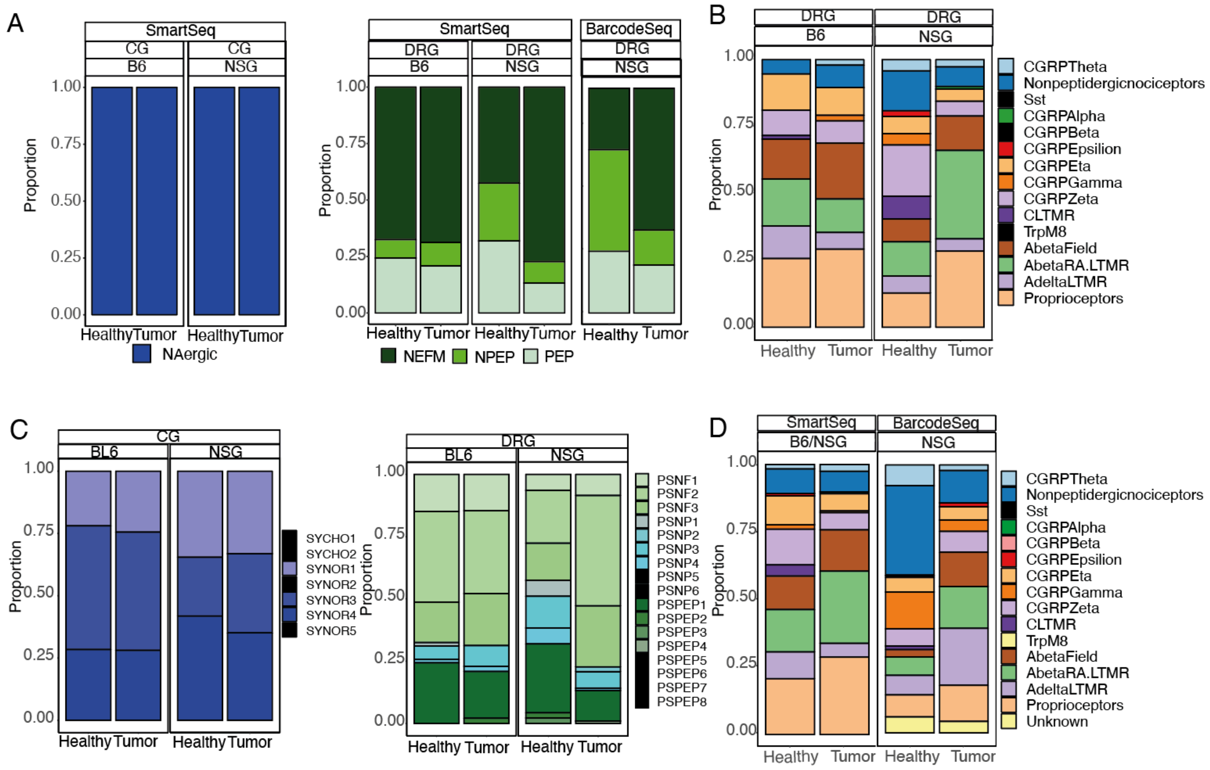

**Figure 42: PDAC attracts specific neuronal subtypes.** (A) Sympathetic CG and sensory DRG subtype composition of pancreas and PDX and EPO-neurons by Zeisel et al. (SmartSeq and BarcodeSeq) (B) Sensory DRG subtype composition of pancreas and PDX and EPO-neurons by Sharma et al. (SmartSeq). (C) Sympathetic CG and sensory DRG in depth subtype composition of pancreas and PDX and EPO-neurons by Zeisel et al. (SmartSeq) (D) Sensory DRG subtype composition of pancreas and PDAC-neurons by Sharma et al. (SmartSeq and BarcodeSeq)

To validate preferential PDAC infiltrating subtypes, I isolated DRG of PDX-mice after intratumoral FB-injection and compared frequencies of SLIT2$^+$ and CGRP$^+$ traced neurons to traced DRGs after intrapancreatic injection (healthy). Compared to the ratios observed in the healthy pancreas, I found an increase in SLIT2$^+$ as well as a decrease in CGRP$^+$ neurons, supporting the scRNAseq data (**Figure 43** C,D, **Supplementary Figure 16**). To investigate, whether this change was reflected by lower intratumoral sprouting of CGRP$^+$ neurons I again assessed iDISCO-cleared 3D-images of pancreatic cancer and found a trend towards a reduction of CGRP$^+$ nerve/tumor area highlighting selective underrepresentation of CGRP$^+$ (nociceptive) neurons in PDAC (**Figure 43** E-G).

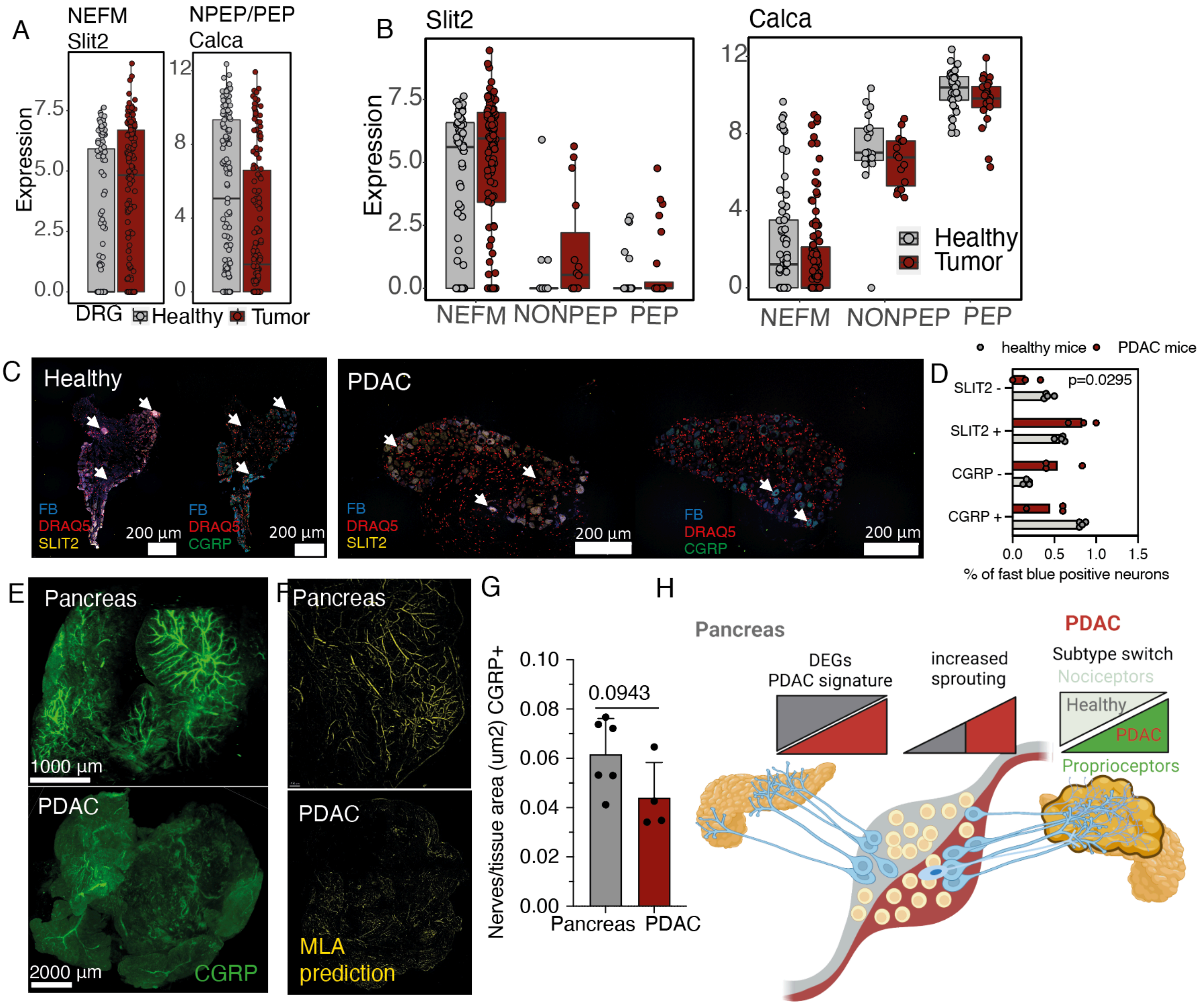

**Figure 43: PDAC attracts proprioceptor but not nociceptor neurons.** (A) Relative gene expression of Slit2 and Calca in pancreas and PDAC neurons (B) Relative gene expression of Slit2 and Calca in pancreas and PDAC neurons in the DRG subtypes (C) Representative IF staining of FB traced healthy pancreas or PDX-DRG ganglia for SLIT2 (yellow) and CGRP (green). (D) Quantification of FB$^+$, SLIT2 or CGRP labeled neurons in DRG n=3mice. Two-way ANOVA-test. Mean +/- SD is shown. (E) Representative LSFM images of whole pancreas and PDAC specimen stained with CGRP. (F) Representative LSFM images after machine learning based axon detection used for quantification of neuronal area (MLA yellow). (G) Quantification of CGRP$^+$ nerve fibers/tissue area between pancreas (n=7) and PDAC (PDX n=4) specimen. P value was

determined by unpaired t-test. (H) Schematic summary of PCN signature, increased sprouting pattern and subtype switch found in PDAC neurons.

Thereby, I provide evidence that hijacking of neurons by cancer is not random but proprioceptive neurons are preferentially attracted.

Previous studies have shown that there is an increased density of nociceptive neurons in the tumor microenvironment of PDAC compared to normal pancreas claiming that PDAC is associated with an increase in the density of sensory nerves in the tumor microenvironment, specifically in the form of nociceptive neurons. Further these studies link this increase in nociceptive neuron density to the development of pain, which is a common symptom of PDAC. They suggest that the activation of these nociceptive neurons and the release of neurotransmitters in the tumor microenvironment may promote cancer growth, invasion and dissemination [79]. However, none of these studies ever analyzed the transcriptome of these neurons to prove the nociceptive character. Also, in staining of full DRGs without tracing it is impossible to quantify the differential innervation pattern. Further, often markers for glia cells like GFAB or ATF3 as injury markers were used in IF to explain their hypothesis [79]. Based on my single cell results however, these are not suitable as markers. In my data, quantification of sensory fibers in the TME does not correlate with innervation of nociceptive neurons. Using Trace-n-Seq in combination with IF staining of ganglia and analyzing innervation fibers with light sheet microscopy I can, for the first time, give an in-depth overview on differential innervation patter of pancreas vs PDAC neurons.

## 3.6 Neurons as an important mediator in the TME of PDAC

I aimed to identify the underlying mechanism how and with which cells neurons- or their axons communicate in the TME of PDAC. Therefore, I applied analysis like scRNAseq experiments of healthy pancreas and PDAC specimen to nominate interaction partners and *in vitro* co-culture experiments.

Bioinformatic analysis of signaling interaction analysis has been performed together with Jasper Panten, I plotted the data.

### 3.6.1 scRNA-seq of PDX tumor cells nominates interacting partners of PDAC-innervating neurons

The tumor microenvironment of PDAC is a complex and dynamic environment that is characterized by interactions between cancer cells, stromal cells, and the extracellular matrix. These interactions play an important role in the development and progression of PDAC.

Compared to the healthy pancreas, the tumor microenvironment of PDAC is characterized by a higher potential for interactions between cells [111, 112]. Studies have shown that cancer cells in PDAC can interact with stromal cells such as fibroblasts, immune cells, and endothelial cells in the tumor microenvironment, leading to the formation of a supportive microenvironment that promotes cancer growth, invasion, and metastasis [112]. For example, cancer cells can secrete molecules that can stimulate the proliferation and activation of stromal cells, leading to the formation of a dense fibrous stroma that can provide physical support for the cancer cells [113]. Cancer cells can also interact with immune cells, leading to the suppression of the immune response and the formation of a "cold" tumor microenvironment that is resistant to immune-mediated attack [26]. Additionally, cancer cells can also interact with endothelial cells and the extracellular matrix, leading to the formation of new blood vessels (angiogenesis) that provide a source of nutrients and oxygen to the cancer cells [112]. However, neurons are missing in current analyses of interacting cells of the PDAC TME.

As a next step, I aimed to identify cell type interactions by integrating pancreas and PDX-innervating neuron transcriptomes with scRNA-seq atlases of PDX-tumors and healthy pancreas (**Figure 44** A) that I generated using the 10x Genomics after FACS-enrichment of EPCAM+, CD31+, CD45+ and unlabeled (fibroblasts etc) cells (**Figure 44** A,B, **Supplementary Figure 17**). Marker based cell type annotation identified endothelial, immune, and epithelial or tumor cells as well as fibroblasts (**Figure 44** B). To determine the relative likelihood of each cell type interacting with neurons, Jasper Panten scored co-expressed ligand-receptor pairs across the two single-cell datasets (**Figure 44** C). Here, fibroblast displayed the highest interaction scores in control and PDAC but cancer associated fibroblasts (CAFs) had scores almost double to controls. I observed this general increase in scores in the PDAC dataset in the endothelial and healthy epithelial cells as well. Cancer cells themselves scored significantly higher than epithelial cells arguing for increased direct interaction. I observed no relevant differences between neuronal subtypes (**Figure 44** D).

Additionally, I analyzed specific correlations of ligand/receptor expression of differentially expressed genes in pancreas vs PDAC neurons with the ligand/receptor expression of an individual human dataset of bulk RNA sequenced healthy pancreas and PDAC cells (pre-sorted) generated by Elisa Espinet in our laboratory. I found that for differentially expressed ligands in PDAC neurons the corresponding receptor is also correlated differentially expressed (**Supplementary Figure 18**).

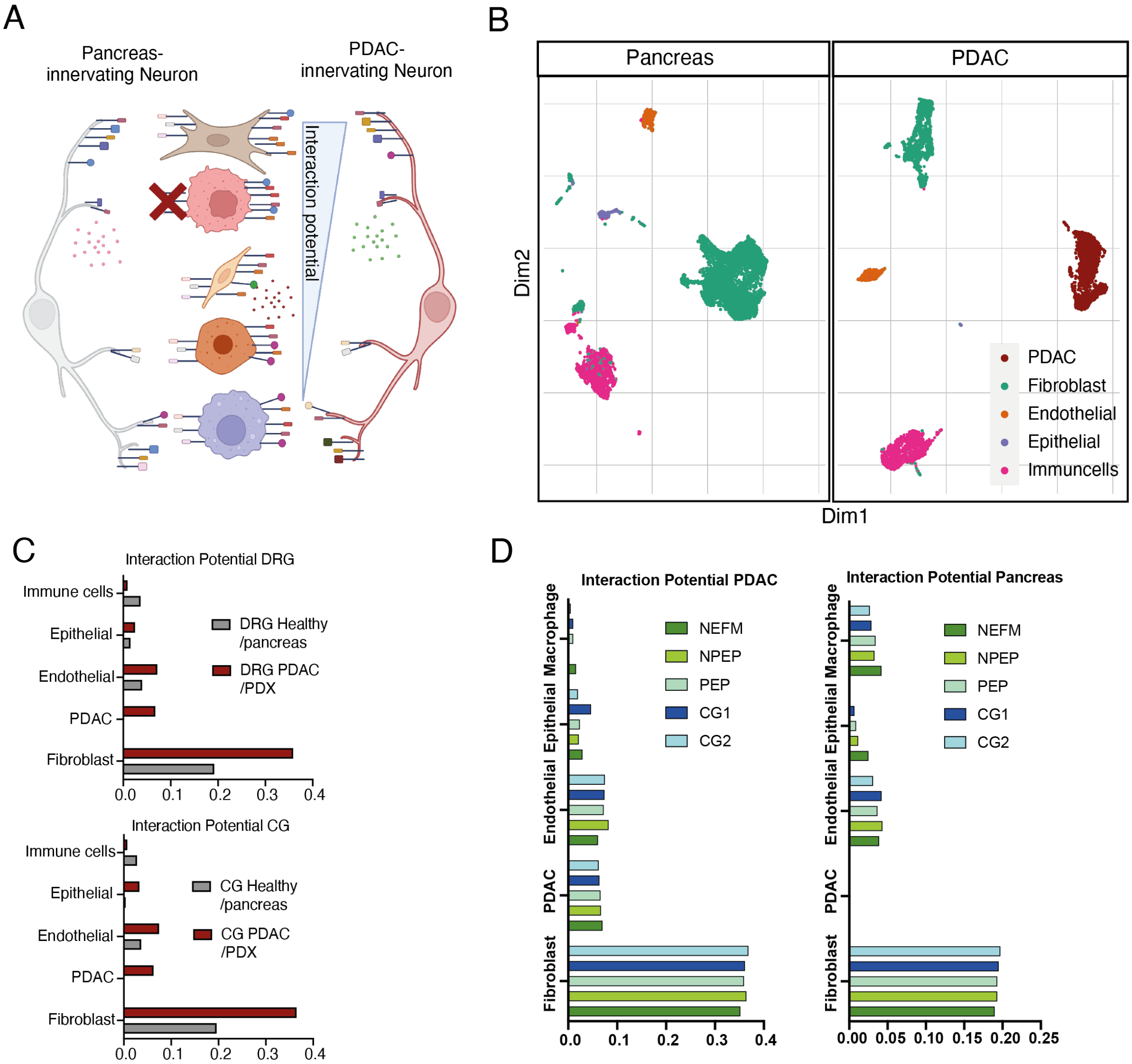

**Figure 44: Cancer milieu interacts with neurons to regulate tumor progression.** (A) Schematic of receptor-ligand analysis. (B) t-SNE of digested pancreas or PDAC cells colored by cell type (n=3 mice). (C) Interaction potential by cell type and ganglion. (D) Interaction potential by cell type and neuronal subtype for pancreas and PDAC TME cells.

After identifying high interaction scores between neurons and fibroblasts in PDAC, I investigated the direct effects of neurons on both by co-culturing the PDAC cells used for the PDX models or human fibroblasts with CG and DRG neurons or with their media supernatants (**Figure 45** A). To do this, I developed a strategy to culture DRG and CG cells in an *in vitro* culture system using PDAC (PACO) or fibroblast serum-free medium and a thin Matrigel layer. Brightfield microscopy showed that the axons grew out from the harvested ganglion and I was able to create a stable culture where neuronal cells could be cultured for several passages while maintaining their morphology (**Figure 45** B). To verify neuronal content, I stained cultured cells with the neuro marker PRPH and the glia marker SOX10 (**Figure 45** C). DRG and CG cultured *in vitro*, maintained their neuronal character and were used to study the function and behavior of neurons and their co-cultured cells. The co-culture system showed a robust increase in cell proliferation and confluence, with stronger effects seen in CG co-cultures regardless of mouse strain (**Figure 45** D,E).

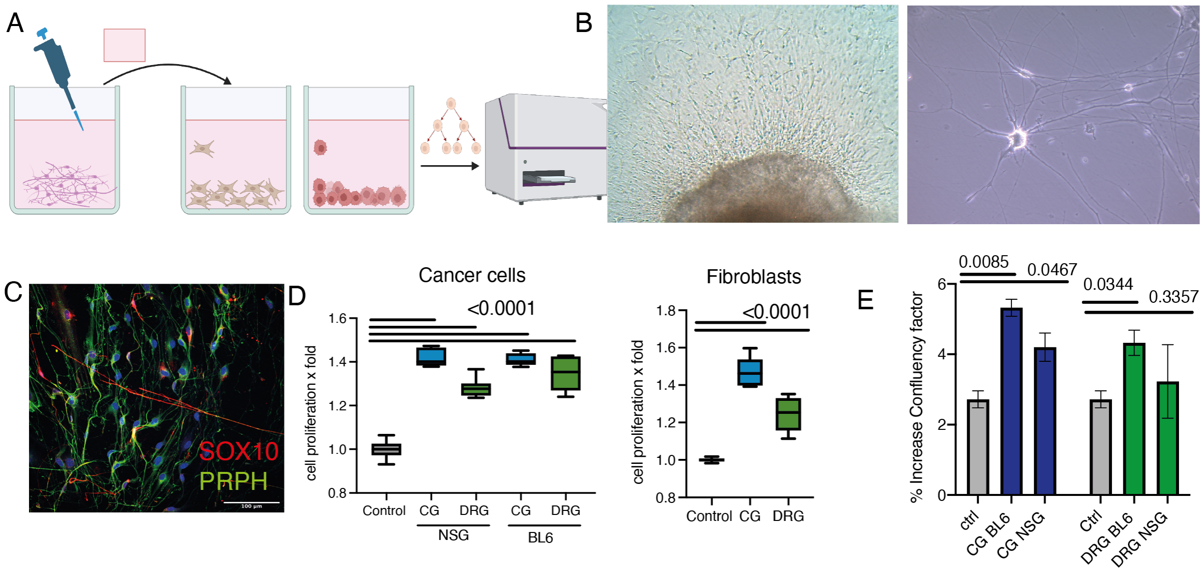

**Figure 45: in vitro neuron-PDAC co-culture drives cancer cell proliferation.** (A) Schematic of co-cultures, (B) Brightfield microscopy image of outgrown neurons in vitro (C) Validation of neuronal cells via IF labelling with PRPH (green) and SOX10 (red, glia marker) after transferring mouse ganglia in vitro. (D) Cell proliferation quantification of PDAC (PACO10) cells (n=12) or human fibroblasts (n=6) alone (ctrl) or co-cultured in CG/DRG conditioned medium for 3 days from three independent experiments. (E) Increased confluency of PDAC (PACO43) cells after co-culture with neurons compared to the ctrl (alone) (n=6) from two independent experiments. P value was determined by unpaired t-test. Mean +/- SD is shown.

This indicates that neuronal secreted factors induce proliferation of both PDAC and fibroblastic cells, fitting to the interaction partner analysis. To investigate this on a molecular basis, I generated bulk RNA-sequencing data of sorted PDAC cells after 3 days of direct co-culture with CG, DRG or control conditions (**Figure 46** A). In line with the functional results, I found proliferation and WNT-signaling or EMT-associated gensets upregulated in the co-cultured PDAC cells (**Figure 46** C). Multiple genes important for PDAC biology, like immediate-early transcription factor FOS, as well as the organization of desmoplastic stroma like *Tgfb1* were induced in co-cultured cells (**Figure 46** B), highlighting direct neuronal control of gene expression in PDAC.

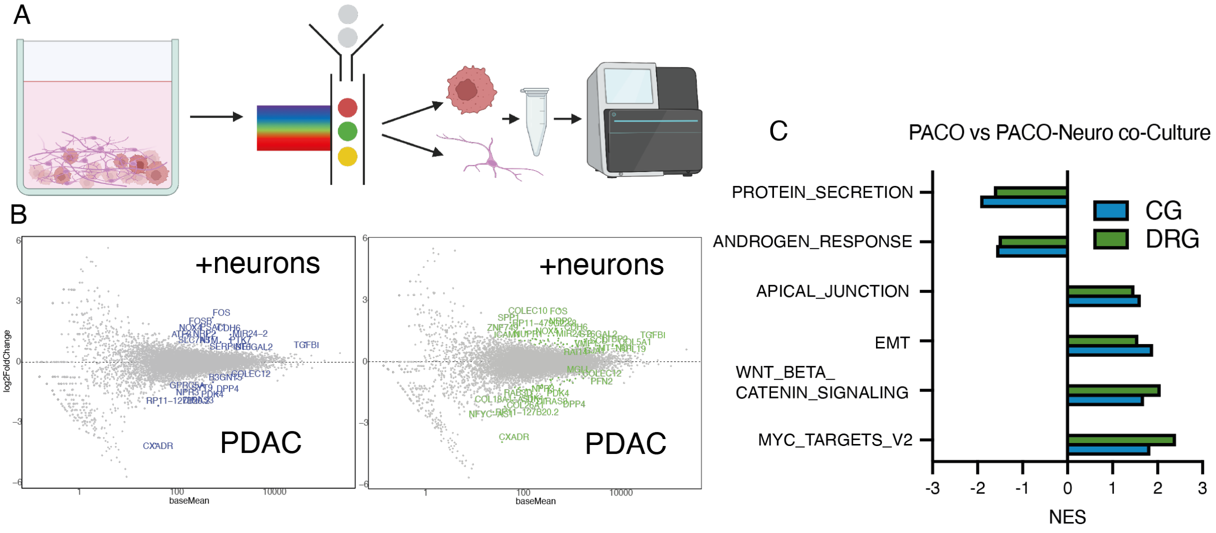

**Figure 46: Neurons change the transcriptomic profile of PDAC cells.** (A) Schematic of co-culture, FACS separation and bulk RNA sequencing approach. (B) Volcano plot of PDAC cells (control vs CG (blue) or DRG (green)) (n=3). (C) GSEA of PDAC cells co-cultured with CG and DRG cells.

However, it is important to note that culturing cells in a dish does not replicate the complexity of the *in vivo* scenario, and it's not a true representation of the interactions that happen within the body. Additionally, the behavior of neurons in culture may differ from that of neurons *in vivo*, therefore *in vivo* experiments are needed to further analyze the effects of neurons for cancer progression.

## 3.7 Modulation of PDAC progression by gain and loss of function models of neuronal control

Activation of nerves in PDAC can lead to the release of catecholamines, growth factors and other molecules that can stimulate the proliferation and migration of PDAC cells. This can ultimately lead to the progression of the disease, making it more aggressive and difficult to treat. Vice versa, the absence of sympathetic nerves in PDAC does not only lead to a decrease in tumor blood flow and an decreased oxygen supply to the tumor, but also to the inhibition of the release of catecholamines, growth factors etc, which can inhibit the proliferation, migration and invasion of PDAC cells, and also inhibit angiogenesis and metastasis [76].

I hypothesized that denervating the sympathetic nervous system would lead to a decrease in tumor progression.

### 3.7.1 Neurons drive tumor progression and denervation can interrupt tumor growth

To test whether neurons drive tumor progression in our PDX-model, I performed different forms of *in vivo* denervation of the sympathetic nervous system.

I denervated the xenograft models by pharmacological and surgical ablation of the sympathetic nerves to analyze the effects on tumor growth and tumor stroma composition with this functional loss-of-function approach. I surgically resected the CG (ganglionectomy) before tumor induction, inject mice with Oxidopamine (6OHDA) – a toxin destroying catecholaminergic neurons- either before tumor induction or after tumors engraftment and assessed tumor growth (**Figure 47** A). The use of 6OHDA is already established in the field and easily performed via i.p. injection. The surgical ganglioectomy however is barely used- to my knowledge only once by Renz *et al* [76] as the celiac ganglion is directly located next to the mesenteric artery.

I quantified denervation efficiency by 3D light sheet microscopy imaging (**Figure 47** C,D). Both ganglionectomy and 6OHDA treatment decreased orthotopic PDX tumor weight significantly. Even when the sympathetic neurons were ablated after PDX-engraftment (late), tumor size was still significantly reduced, highlighting a role of neurons beyond early tumor development (**Figure 47** B-D). To prove this effect depended on the sympathetic neurons, I generated subcutaneous PDAC xenografts, barely innervated by the sympathetic nervous system (**Figure 47** F). In these mice, 6OHDA-treatment had no significant effect on tumor growth (**Figure 47** E), indicating that the effects of 6OHDA in the orthotopic tumors depend on direct cancer -nerve interactions and not systemic effects of the toxin.

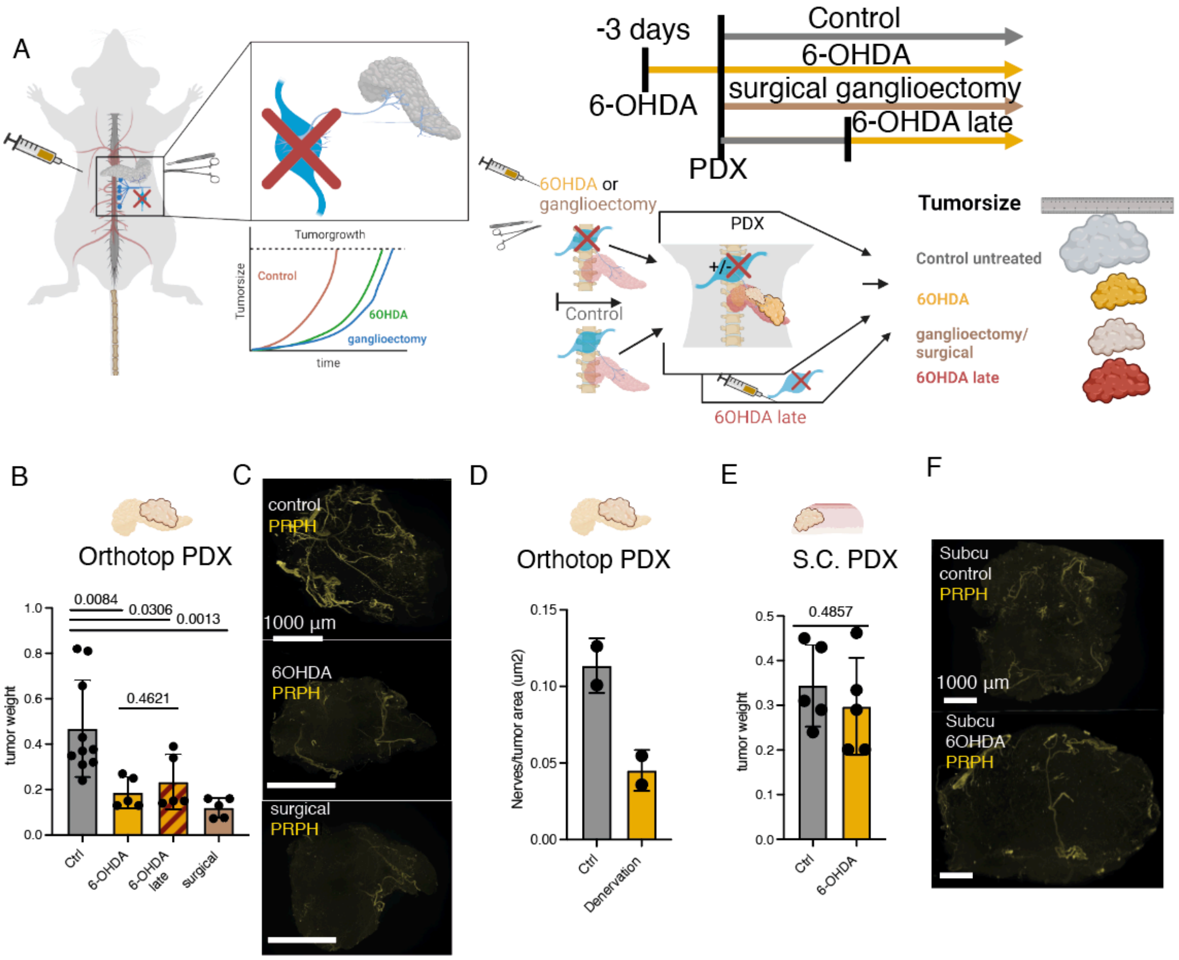

**Figure 47: Sympathetic denervation reduces PDAC progression.** (A) Schematic of denervation approach. (B) Tumor weight of orthotopic PDX-mice, control (n=10) vs. different denervation condition mice (n=5). P value was determined by one-way ANOVA-test. Mean +/- SD is shown. (C) Representative images of whole orthotopic PDX-control versus sympathetic nervous system denervated tumor stained with PRPH and obtained by LSFM. (D) MLA based quantification of PRPH$^+$ nerve fibers/tissue area between PDAC control and denervated specimen. Mean +/- SD is shown. (E) Tumor weight of subcutaneous PDX-mice, control (n=5) vs. denervation (n=5). P value was determined by one-way ANOVA-test. Mean +/- SD is shown. (F) Representative images of whole subcutaneous PDX-control versus sympathetic nervous system denervated tumor stained with PRPH and obtained by LSFM.

In mouse models it was already shown that one approach to inhibit tumor progression is through the inhibition of specific neurotransmitters, such as norepinephrine, that are released by sympathetic nerves [76]. It is important to note that more research is needed to fully understand the mechanisms of inhibition of neurons in the context of PDAC and how these mechanisms contribute to the inhibition of tumor progression.

### 3.7.2 Nab-Paclitaxel treatment induces intratumoral neuropathy in PDAC

Nab-Paclitaxel (Abraxane), formulation of paclitaxel bound to albumin is a chemotherapeutic drug commonly used to treat pancreatic cancer. Nab-Paclitaxel is often used in combination with other chemotherapy drugs such as gemcitabine. The mechanism of action of Nab-

Paclitaxel in PDAC is thought to disrupt the microtubules that make up the cell's cytoskeleton, thereby preventing cell division and leading to cell death of the cancer cells [114, 115].

However, many patients discontinue therapy due to severe neuropathy as Nab-Paclitaxel also interferes with microtubules essential for neuronal transport. As severe neuropathy is linked to good response to Gemcitabin/ nab-Paclitaxel [116], I investigated the effect of Taxanes on tumor infiltrating neurons by treating mice with Nab-Paclitaxel and traced PDX-neurons. I harvested the tumors at early (2 treatment cycles) and late (4 treatment cycles) timepoints and analyzed neuronal infiltration (**Figure 48** A). As expected, tumor size was reduced after treatment at both timepoints compared to control (**Figure 48** B, **Supplementary Figure 20** A) and I assed neuronal sprouting by 3D light sheet microscopy. Neurons/tumor volume was decreased even though Nab-Paclitaxel treated tumors were smaller in size as further quantified using MLA (**Figure 48** C,D, **Supplementary Figure 20** B).

Next, I assessed the abundance of $FB^+$ PDX-neurons during Nab-Paclitaxel treatment. $FB^+$ CG-neurons decreased from ~ 75% in control to ~ 55% after 2 and to ~ 20% after 4 cycles and $FB^+$ DRG-neurons from ~ 3% to ~ 1,3% after 2 and almost 0 % after 4 cycles (**Figure 48** E). These results show a striking reduction of intratumoral neuronal sprouting as well as full number of PDAC-infiltrating neurons.

To investigate transcriptional changes accompanying this effect, I sequenced neurons traced from healthy pancreas-, untreated PDX-, and Nab-Paclitaxel-treated PDX by BarcodeSeq (**Figure 48** F). Between healthy and PDAC infiltrating neurons I detected hundreds of DEG as observed before. However, Nab-Paclitaxel treated PDX-neurons clustered directly with control (untreated) PDX-neurons and almost no DEG were detected after 2 or 4 cycles of therapy (**Figure 48** G). This indicates that while Taxanes cause severe intratumoral neuropathy, the neurons still infiltrating PDAC have not lost their tumor-supportive capabilities and further targeting of neurons could be a therapeutic target.

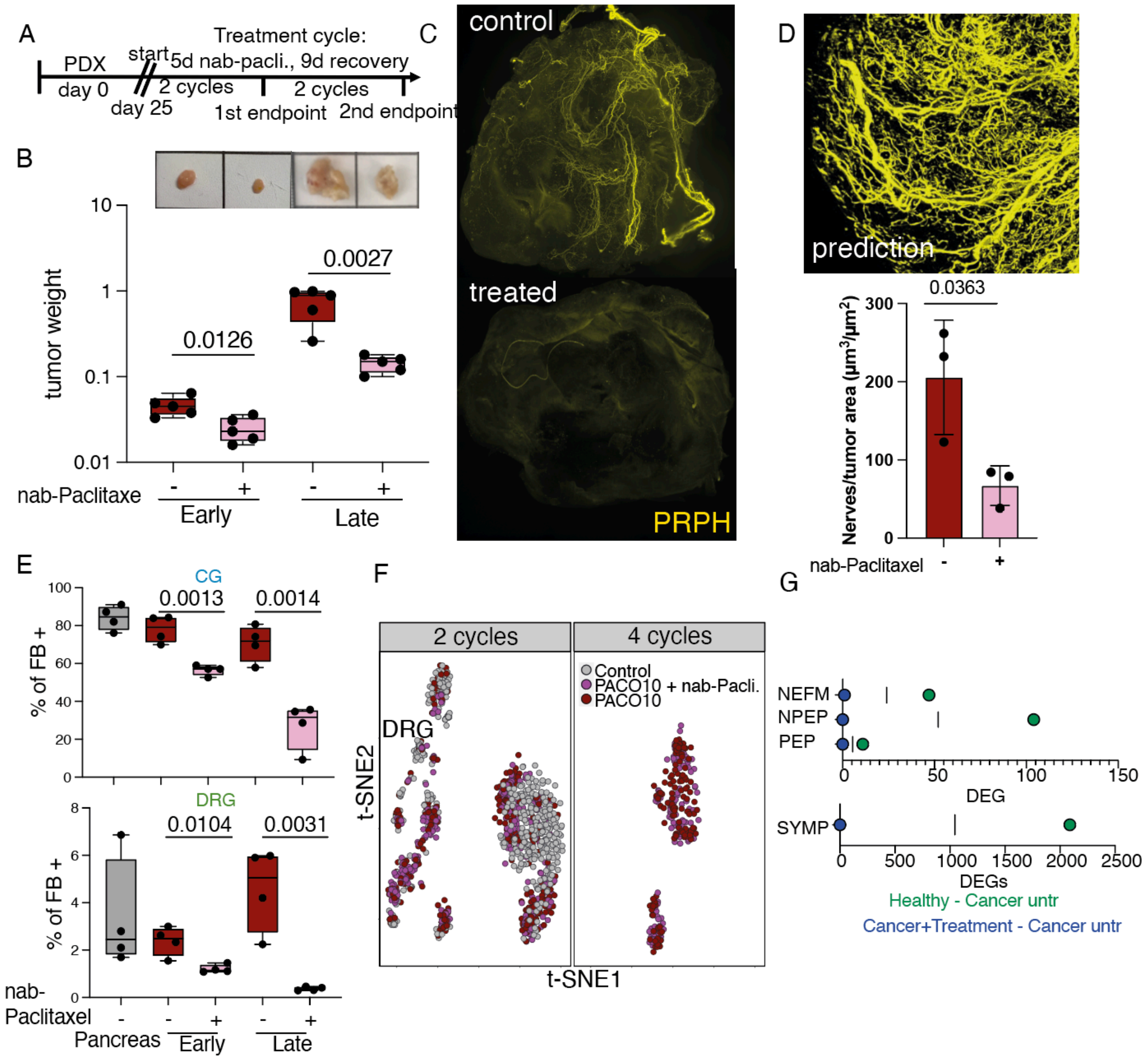

**Figure 48: Nab-Paclitaxel depletes intratumoral neurons and reduces tumor growth.** (A) Schematic of treatment regime. (B) Representative images and tumor weight of Nab-Paclitaxel-treated (100 mg/kg) mice and untreated controls after 2 cycles (early) and 4 cycles (late) n=5 mice per condition. P value was determined by unpaired t-test. Mean +/- SD is shown. (C) Representative images of whole PDAC specimen of control versus Nab-Paclitaxel-treated mice after 2 cycles stained with PRPH+ neuronal cells/axon obtained using light-sheet microscopy. (D) Representative (control mice) visualization of innervation quantification using machine-learning algorithm (prediction yellow) and quantification of nerve volume/tumor area ($\mu m^3/\mu m^2$) between PDAC control and denervated specimen. Unpaired-test, n=3 mice per condition. Mean +/- SD is shown. (E) $FB^+$ neurons in the CG and DRG after retrograde tracing of PDX, control/after Nab-Paclitaxel treatment of 2 and 4 cycles. Unpaired t-test, n=4 mice per condition. (F) t-SNE plot of retrogradely labelled CG and DRG neuronal cells of healthy, PDX and Nab-Paclitaxel-treated PDX-mice after 2 cycles (n=4 mice per condition). Mean +/- SD is shown. (G) Number of identified DEGs between healthy pancreas and PDAC neurons, PDAC control and PDAC neurons of Nab-Paclitaxel-treated mice.

There are several mechanisms that have been proposed to explain the neurotoxicity of Taxanes, including the disruption of microtubules, which are important for the normal function of nerve cells [115].

I further analyzed the sprouting pattern and revealed that specifically small axon fibers were affected by Nab-Paclitaxel treatment whereas big nerve structures were less affected and the structures remained intact after treatment (**Figure 49** A). Big nerves have high levels of microtubules, which are composed of tubulin and are important for cell structure, organization, and molecule transport. In neurons, microtubules are critical for axon functioning, providing support and facilitating molecule transport. Microtubule dysfunction can lead to neurological disorders, such as peripheral neuropathy caused by Taxanes, which disrupt microtubules and cause nerve damage [117]. I hypothesized that big nerves (large diameter nerves) are less affected by neurotoxic agents like Taxanes,- because they have a greater number of neurons, which allows for more redundancy in the nervous system. This redundancy means that if some neurons are damaged or destroyed by a neurotoxic agent, the remaining neurons can still carry out the necessary functions. Additionally, large diameter nerves also have a higher number of axons, allowing for more efficient communication within the nervous system. Moreover, these big bundles of nerve fibers have a greater supply of oxygen and nutrients, which allows them to better withstand the adverse effects of neurotoxic agents. They contain a higher number of glial cells, which provide support and protection to the neurons, and help to remove waste products and debris and can also help to repair the nerve damage that may occur [47]. **Figure 49** A shows a direct comparison of 3D rendered innervation of treated PDAC samples in mice compared to the vehicle control. The number of small fibers is significantly reduced, only the big nerve structures remained after Nab-Paclitaxel treatment. To mirror these findings, I analyzed nerve structures in human specimens in 2D-images with our collaboration partners at the Heidelberg Pathology Institute. The patient treated with Nab-Paclitaxel showed a decrease in the number of axon fibers (**Figure 49** B). Furthermore, when the size of nerve structures was considered, a reduction was observed after the treatment. Large nerve structures remained in the human tumors after Nab-Paclitaxel treatment. Notably, cancer cells were mostly present around or within these large nerve structures, suggesting that those provide a safe haven for cancer cells by supplying them with growth factors and shielding them from the effects of the treatment (data not shown).

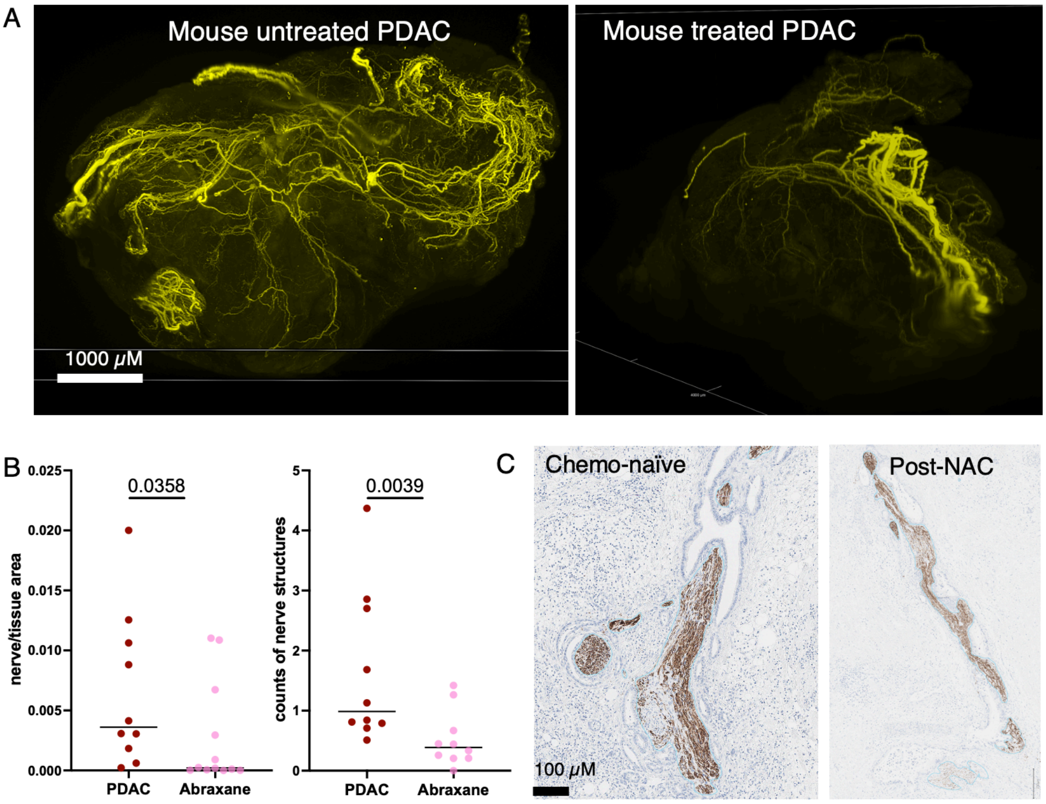

**Figure 49: Neuropathy inducing chemotherapy reduced neuronal innervation in mice and human.** (A) Representative images of whole orthotopic PDX-control versus Nab-Paclitaxel treated tumor stained with PERIPHERIN and obtained by LSFM. (B) Quantification of IHC of human samples stained with NF1 of PDAC chemo-naïve and post-NAC (Nab-Paclitaxel treatment) as nerve per tissue area and count of nerve structures per tissue area. (n=10) P value was determined by unpaired t-test. Mean +/- SD is shown. (C) Representative IHC images obtained by brightfield microscopy stained with NF1 of human PDAC chemo- naïve and treated (Nab-Paclitaxel) PDAC samples.

It is worth noting that the number of microtubules in an axon is not the only factor that determines its size and function. Other factors, such as the number and distribution of other cytoskeletal elements, the number and types of receptors, and the strength of the connections between neurons, also play a role. Therefore, more research is needed to fully understand the impact of neuropathic agents like Nab-Paclitaxel or Oxaliplatin on nerves and hence, tumor progression.

### 3.7.3 Combinatorial denervation increases the effect of Taxanes in PDAC

After observing that Taxanes only damaged small axon fibers and not the larger ones, I theorized that by eliminating the remaining big nerve structures that serve as a “sanctuary” for cancer cells, I could enhance the effectiveness of chemotherapeutic drugs like Nab-Paclitaxel.

To validate this hypothesis, I paired Nab-Paclitaxel treatment with the destruction of any remaining sympathetic neurons using 6OHDA (**Figure 50** A) and discovered a synergistic impact on tumor growth. This effect was only observed in heavily innervated orthotopic but not subcutaneous tumor (**Figure 50** B-D). While sympathetic ablation (6OHDA) and Nab-Paclitaxel treatment by themselves reduced tumor growth the combination reduced neuronal sprouting in the tumor to a minimum (**Figure 50** C,D). It resulted in a 16.5-fold reduction in tumor size compared to a 2.5-fold reduction for 6OHDA and a 5.5 -old reduction for Nab-Paclitaxel only (**Figure 50** E).

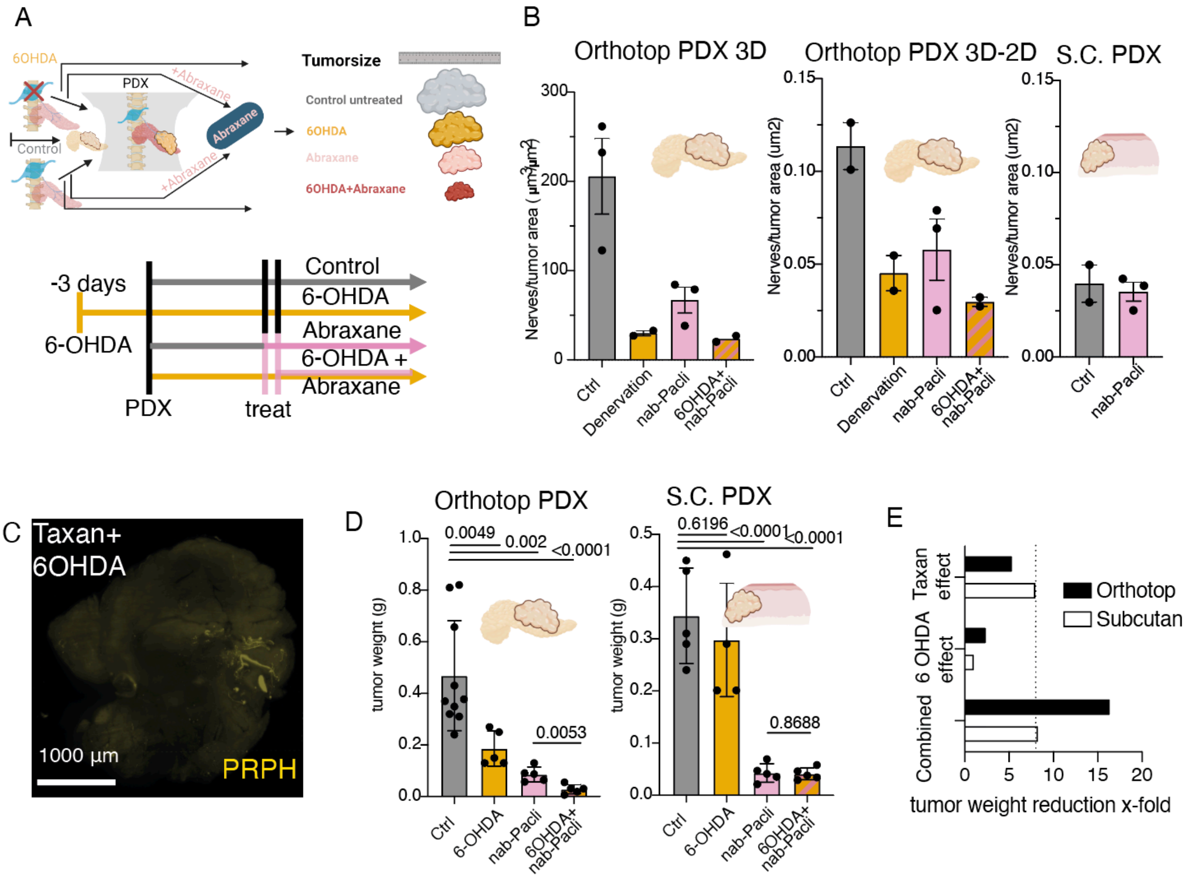

**Figure 50: Denervation of the sympathetic nervous system and Nab-Paclitaxel treatment have a synergistic effect on tumor growth.** (A) Treatment scheme. (B) MLA based quantification of control PDAC (orthotopically left full 3D quantification, middle 3D to 2D quantification, subcutaneously right), 6OHDA denervated, nab-Paclitaxel (100 mg/kg) and combination treated PDX-tumors based on LSFM. Mean +/- SD is shown. (C) Representative images of whole PDAC specimen after combined 6-OH and nab-Paclitaxel treatment, stained by PRPH$^+$ neuronal cells/axon obtained using light-sheet microscopy. (D) Tumor weight of control (orthotopically left, subcutaneously right), 6OHDA denervated, nab-Paclitaxel (100 mg/kg) and the combination of treated PDX-mice n=5. P value was determined by one-way ANOVA-test. Mean +/- SD is shown. (E) relative tumor weight reduction upon different treatments in the orthotopic and subcutaneous model in comparison to control mice.

These results provide a strong rational for targeting neurons or the “neuro-cancer connectome” in PDAC and suggest that one of the major mechanisms of action of Taxanes as anti-cancer drugs *in vivo* is intratumoral neurotoxicity, making Taxanes a microenvironment targeting drug. Moreover, inhibition of neuronal innervation by systemic or local techniques in combination with Nab-Paclitaxel could increase efficiency and optimize the side effect profile for patient.

## 3.8 Outlook: Understanding PNS neurons – “The Nerve Atlas”

### 3.8.1 Further deciphering the role and interaction of PDAC innervating neurons

Our investigation of healthy pancreas and PDAC infiltrating neurons has revealed specific transcriptional programs related to injury, neural regeneration, and development. This signature persists even after tumor removal or exposure to neurotoxic drugs, suggesting that it may prepare the microenvironment or remaining tumor cells for local relapse. Additionally, pancreatic or PDAC neurons can spread to surrounding tissues such as the spleen, potentially affecting neuro-immune or neuro-endocrine interactions, indicating that the cancer-neuron footprint may extend beyond the tumor itself.

To gain insight into the role of neurons in the TME, two ongoing approaches are being taken. In the first approach I compare the single-cell landscape of normal patient-derived xenograft (PDX) tumors to those in which I ablated the nervous system via 6OHDA treatment, with the aim of identifying direct interaction partners and the effect that neurons have on TME-associated cells. The second approach involves identifying the effect of hyperactivation of neurons on surrounding TME cells using optogenetics-based activation. While my previous attempts using optogenetic AAVs were insufficient (**Figure 51** A), I use Wnt1-Cre;R26-CAG-LSL-2XChETA-tdtomato mice, which carry two copies of channelrhodopsin and the reporter tomato to activate peripheral neurons with light.

The surgical setup for optogenetic activation is illustrated in **Figure 51** B, where nerve bundles are activated using a laser. Currently, the 10x-based scRNAseq data of EPO- tumors that were activated versus those that were not activated are being analyzed.

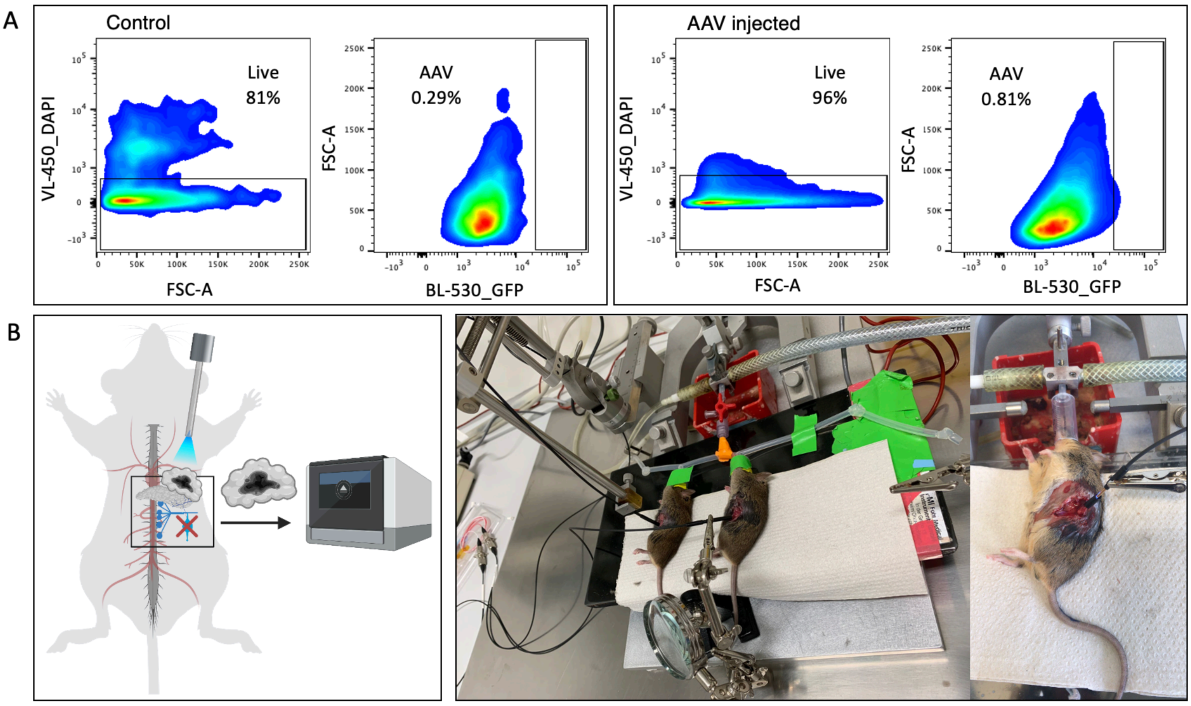

**Figure 51: Optogenetic based hyperactivation of neurons of the PNS.** (A) Exemplary FACS gating scheme of live AAV (GFP) positive traced neurons in a DRG after intrapancreatic injection and 4 weeks of tracing. (B) Schematic and experimental setup of optogenetic activation of nerves entering the EPO based PDAC in mice.

Targeting the cancer-nerve state may be a promising strategy for developing novel drugs. In fact, we may have already targeted this interaction without realizing it, as Taxanes have been shown to reduce neuronal infiltration. However, many questions remain unanswered, such as the role of neurons beyond the primary tumor. Therefore, visualizing, characterizing at the molecular level, and dissecting the function of how cancers exploit the peripheral nervous system for their benefit is a crucial area to consider when developing novel and effective cancer treatment strategies.

To investigate whether neuropathic agents induce denervation of nerves, I am currently testing Oxaliplatin as a potential neuron-denervating substance. I will treat mice with Oxaliplatin for three cycles and trace number of neurons after treatment, comparing them to numbers traced in chemo-naïve control tumors.

Additionally, in collaboration with the Heidelberg Pathology Institute, I evaluated the effect of FOFIRINOX (which includes Oxaliplatin) on innervation in human specimens. Neither staining with S100 (**Figure 52** A,B), nor staining with NF1 (a direct neuron marker) showed a decrease in innervation (**Figure 52** C). However, in the neoadjuvant therapy setting, vital cancer cells often display a predominant location around and within hypertrophied neural structures, and the size of neural structures in this subgroup is highly variable. An example of extreme neurotropism can be seen with vital cells found almost exclusively in the immediate vicinity of hypertrophied neural bundles (**Figure 52** D).

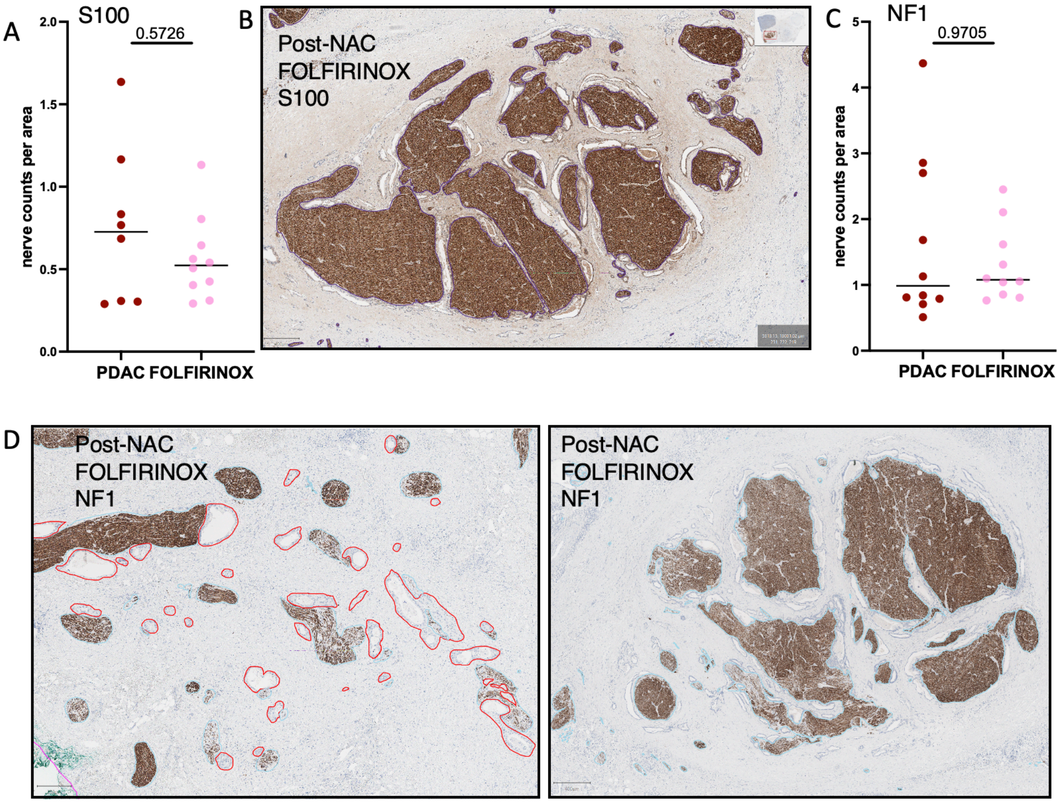

**Figure 52: FOLFIRINOX changes innervation pattern in human post-NAC specimen.** (A) Analysis of nerve counts per area of S100 stained IHC human specimen. P value was determined by unpaired t-test (n=10). Mean +/- SD is shown. (B) Exemplary IHC S100 staining post-NAC (FOLFIRINOX). (C) Analysis of nerve counts per area of NF1 stained IHC human specimen. P value was determined by unpaired t-test (n=10) Mean +/- SD is shown. (D) Exemplary IHC NF1 staining post-NAC (FOLFIRINOX). Alcian blue neural bundles; red vital tumor cells. (Images stained and manually annotated by the Heidelberg Pathology Institute)

After demonstrating that the cancer-nerve signature persists following resection of the primary tumor, my next objective will be to explore the level of innervation and expression of neurons infiltrating metastatic sites. To achieve this, I plan to trace neurons from liver and lung PDAC derived metastases and compare their expression profile with the dataset of neurons infiltrating the primary PDAC tumor, as well as with a dataset that I intend to generate of primary HCC tumor-infiltrating neurons.

### 3.8.2 Heterogenous innervation pattern and transcriptome of organ infiltrating neurons

In general, the peripheral nervous system (PNS) innervates all organs and structures, but the pattern of innervation can vary depending on the organ.

Organs such as the pancreas, the prostate, and the salivary glands have a mixed innervation by both sensory and autonomic (sympathetic and parasympathetic) – and in case of the GI tract-enteric nerves [118].

Different organs are innervated by different types of neurons with unique expression patterns, making it necessary to use advanced imaging techniques to accurately quantify nerve structures. Tissue clearing and light sheet microscopy are techniques used to create a 3D map of the entire organ, allowing for more detailed analysis of nerve structures. I applied full tissue clearing and light sheet microscopy on a variety of different organs to show different innervation pattern, branching and sprouting of PNS neurons throughout these tissues (**Figure 53**).

These results show that organs are innervated in different density and sprouting patterns.

However, due to the heterogeneity of nerve infiltration, a machine learning algorithm (MLA) approach is necessary to accurately quantify the different innervation patterns in different regions of the organs. This combination of techniques allows for a better understanding of the innervation of various organs and can provide insights into the role of nerves in organ function and disease and is currently ongoing together with the assistance of Daniel Azorin.

Previous studies have only focused on a limited number of tissue-innervating neurons [56, 64-66]. However, with the Trace-n-Seq method, I can now trace and functionally describe a variety of tissue-innervating neurons based on their expression profile. In addition to spleen, colon, and peritoneum, I also sequenced pancreas and bone marrow (BM) innervating neurons using sc-BarcodeSeq. The results showed differences in the quantity and expression profile of neuronal subtypes, even within the same subtype, depending on the tissue they innervate. This highlights the unique anatomical characteristics or “anatomic fingerprint” of tissue-innervating neurons. (**Figure 54**).

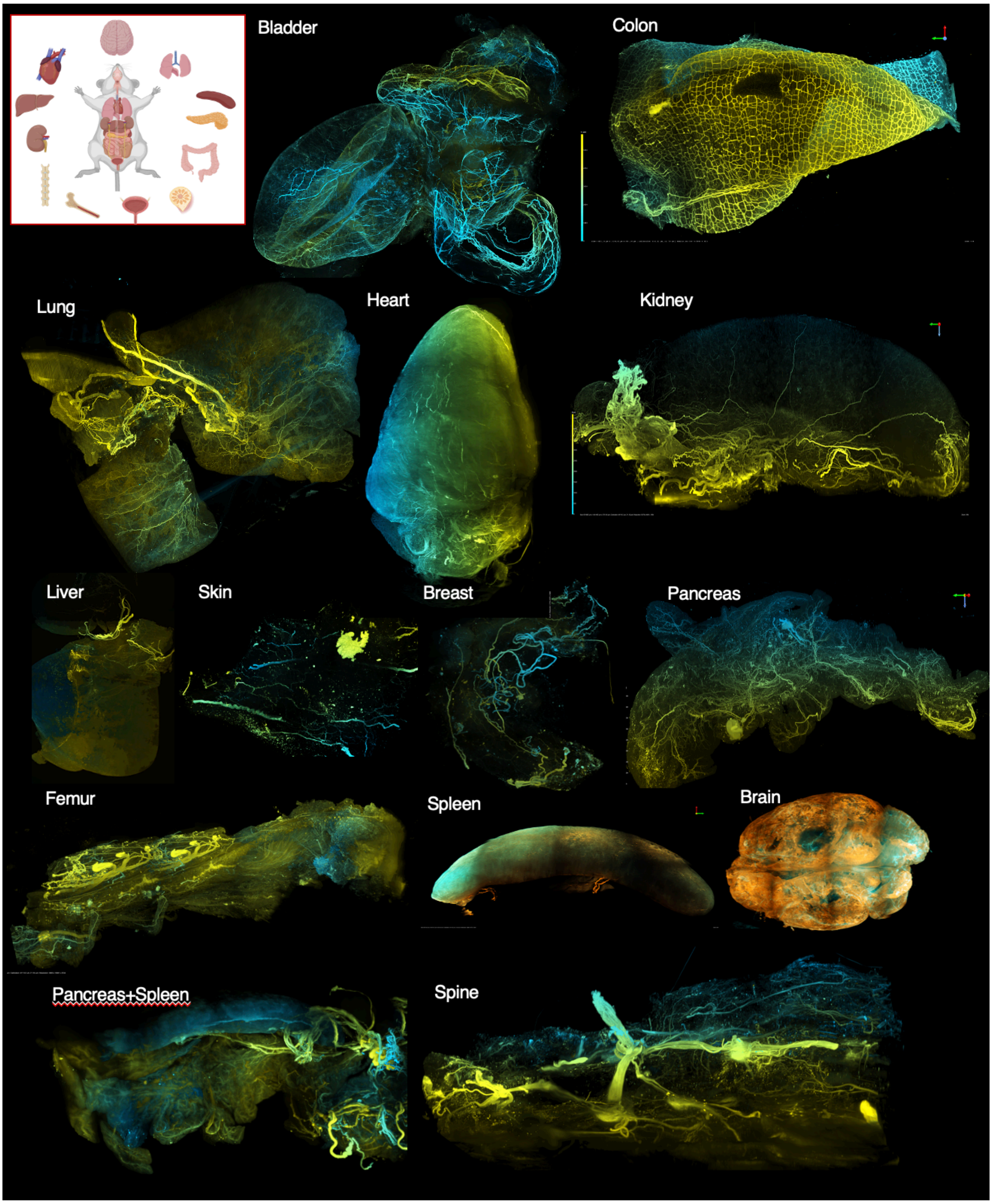

**Figure 53: Innervation pattern of different organs.** Representative images of different full tissue cleared organs (iDISCO) stained with peripherin (PRPH) and imaged by light sheet microscopy.

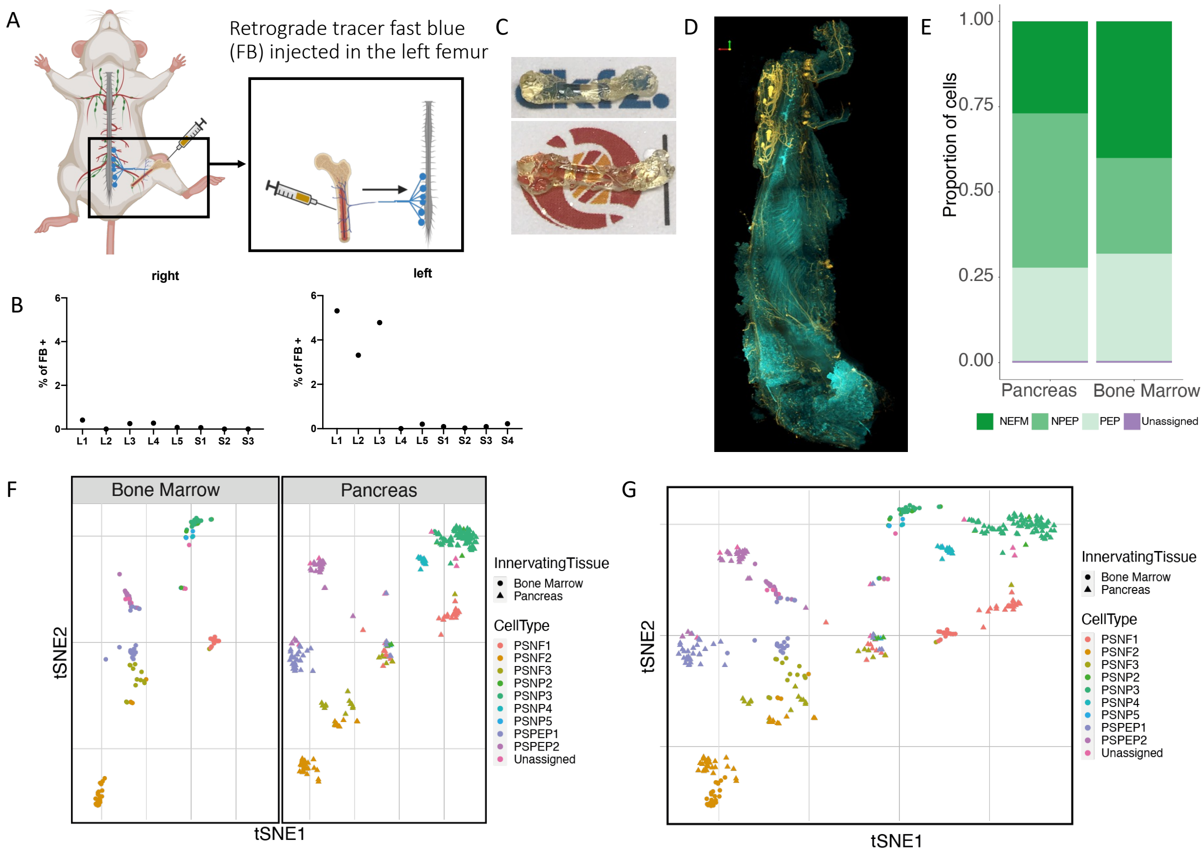

**Figure 54: The bone marrow is innervated by a specific subset of DRG neurons that differ from pancreas neurons.** (A) Schematic of retrograde tracing from the mouse bone marrow. (B) Flow cytometric analysis of DRG L1-S3 on both side after FB injection in the bone marrow. (C) Image of a fully cleared mouse femur. (D) Representative image of a fully cleared femur imaged with light sheet microscopy. (E) Sensory DRG subtype composition of pancreas and bone marrow neurons annotated by *Zeisel et al.* (BarcodeSeq), n=6 mice. (F) t-SNE plot from Trace-n-Seq of either Bone marrow or pancreas DRG neurons showing in depth annotated clusters with BarcodeSeq by *Zeisel et al*. (G) Combined t-SNE plot from Trace-n-Seq of either bone marrow or pancreas DRG neurons showing in depth annotated clusters with BarcodeSeq by *Zeisel et al*.

### 3.8.3 The Cancer-Nerve Atlas

Pancreatic cancer is not the only entity that is characterized by strong neuronal innervation. Innervation by PNS neurons in tumors, now referred to as tumor-associated nerve fibers (TANFs), has been found to play a role in the progression and metastasis of various types of cancers. Studies have shown that tumors with a high density of TANFs tend to have a poorer prognosis and are more resistant to treatment. The relationship between TANFs and cancer progression is complex and not fully understood, but several different studies indicate that TANFs promote cancer growth by releasing growth-promoting molecules, recruiting immune cells to the tumor, and promoting angiogenesis. Additionally, TANFs may also protect cancer cells from chemotherapy as I also show in chapter **3.7 and 3.8.1** presumably by providing them with a source of nutrients and oxygen. Studies have shown that also cancer types such as hepatocellular carcinoma (HCC), colorectal cancer, acute myeloid leukemia (AML), melanoma, and lung cancer have a high density of TANFs. I identified nerval innervation in a variety of different tumor types like breast cancer (PDX), colorectal cancer (KPN, KPC) and PDAC- derived liver and peritoneal carcinosis as well as human hepatocellular carcinoma (HCC) material via tissue clearing and light sheet microscopy (**Figure 55**).

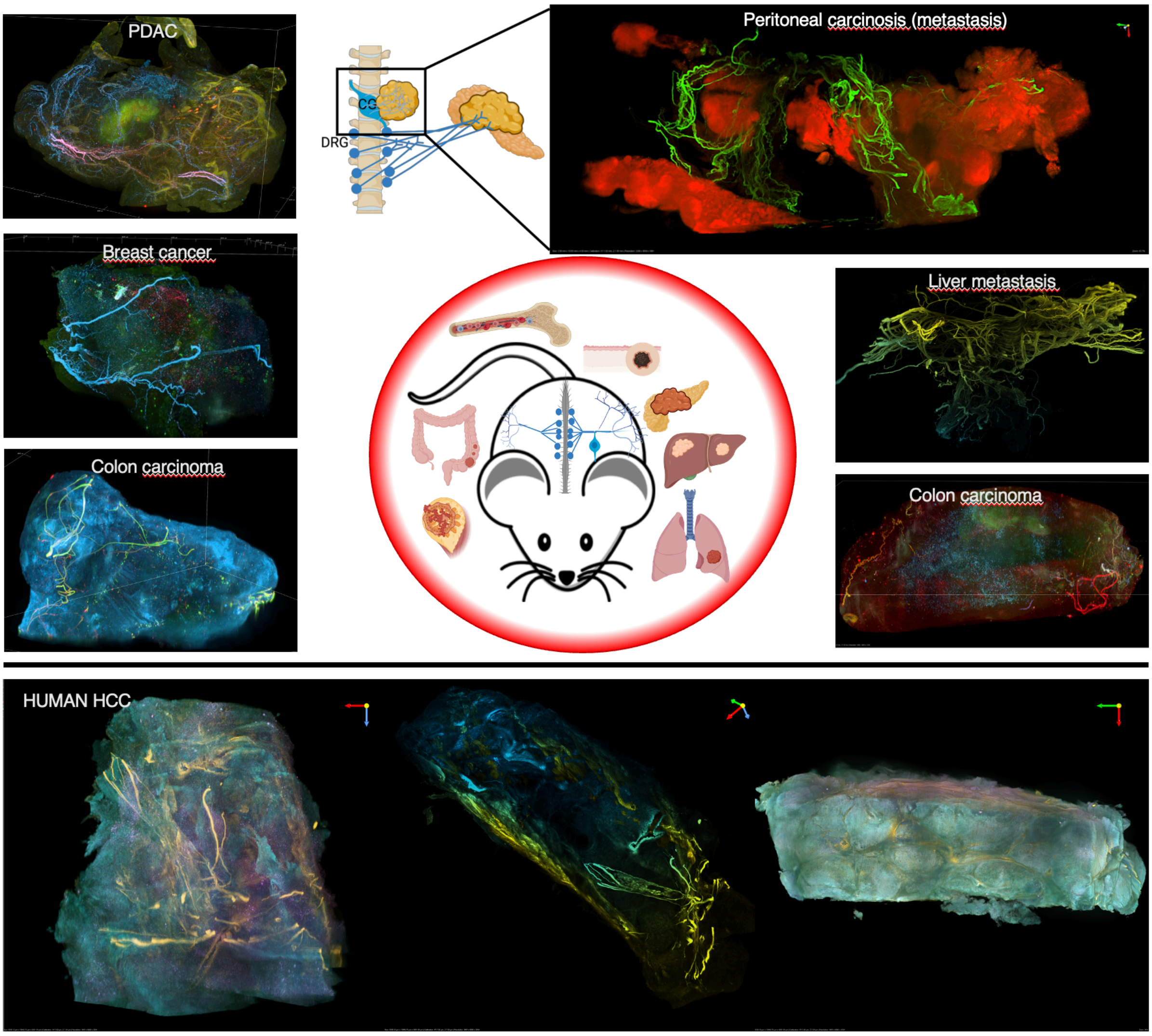

**Figure 55: Different solid cancers are innervated by the peripheral nervous system.** Representative light sheet microscopy images of different cancer entities (PDAC, Brest cancer, colorectal cancer and metastases) stained for innervation from mice (top) and human (bottom).

In my research, I have delved into the branching patterns of both healthy and cancerous colon tissue in the early stages of cancer. The enteric nervous system (ENS) is a network of neurons and glial cells that is embedded in the gut wall, extending from the esophagus to the anus. It is composed of two main plexuses: the myenteric (Auerbach's) plexus controls gastrointestinal motility and the submucosal (Meissner's) plexus controls local secretion and blood flow [47]. The colon is further innervated by sympathetic and sensory neurons. Sympathetic, sensory, and enteric neurons play important roles in regulating the functions of the gut. Sympathetic axons project into the gut, where they mainly innervate the blood vessels, smooth muscle, and mucosa. Sensory axons project into the gut, where they sense different stimuli such as pressure, stretch, and chemical signals.

Although the tumor is not yet heavily innervated, I have observed a significant shift in the nerve structure surrounding it (**Figure 56**). In healthy tissue, I mainly find axons of the enteric nervous system, which is well-structured as expected. However, in the colon tissue containing a small tumor, the branching becomes more chaotic and I observe different nerve structures that do not seem to belong to the enteric nervous system but rather sympathetic and sensory axons based on morphology. Interestingly, distant tissue still retains its normal pattern, while chaotic nerve sprouting is directed towards the tumor. This provides valuable insight into early-stage tumor innervation. It seems that the tumor cells attract nerves, presumably axon structure of sympathetic and/or sensory neurons.

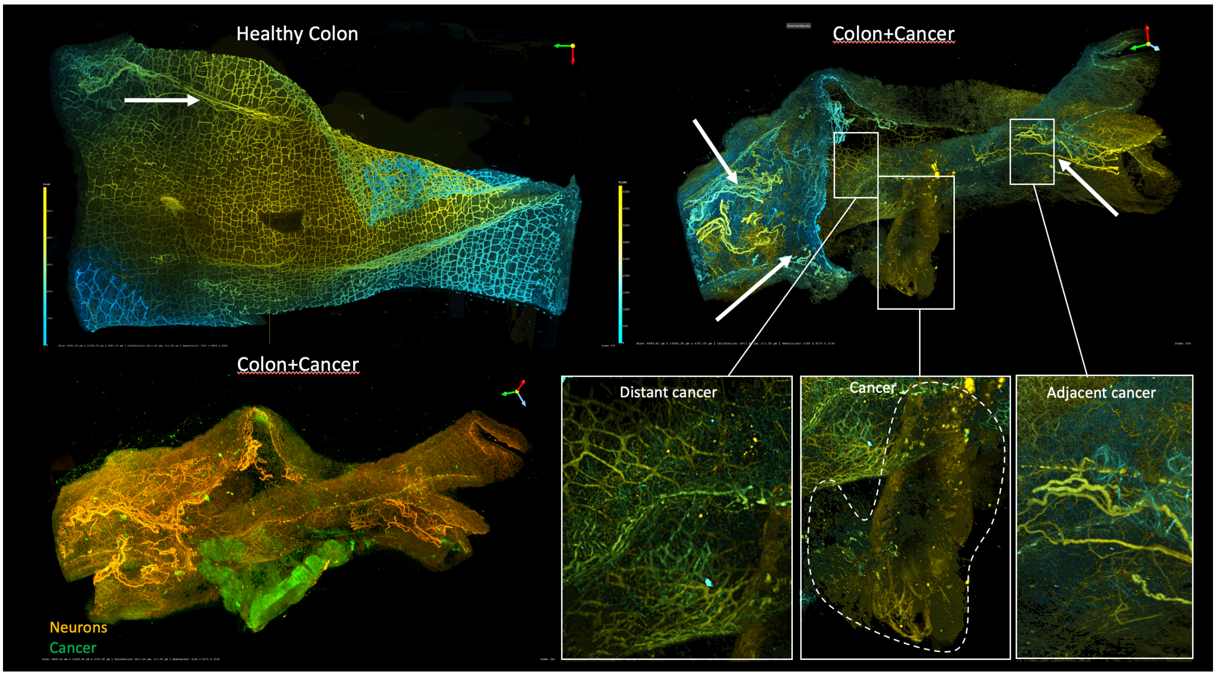

**Figure 56: Innervation pattern of healthy and cancerous colon tissue.** Representative light sheet microscopy images of healthy colon and cancerous colon tissue.

All single-cell datasets of the tumor microenvironment (TME) of certain cancer types outside the brain, such as PDAC, lack information about neurons due to their cell bodies being located in distant ganglia. Therefore, further research is needed to fully understand the relationship between the peripheral nervous system and different types of cancer. The Trace-n-Seq approach allows to study these neurons on a transcriptomic level, and it is intended to complete these datasets and analyze whether the Cancer-Nerve signature is present across various cancer types or is tumor(PDAC)-specific.

# 4 Discussion

## 4.1 Heterogenous innervation of the pancreas

Studying nerve tissue interactions in the peripheral nervous system, particularly in the context of cancer, is important as it provides insights into the mechanisms underlying cancer progression and opens up new avenues for therapeutic intervention. Cancer neuroscience is a rapidly growing field that is driving advances in our understanding of cancer biology and the development of new treatments. I utilized full tissue clearing and 3D light sheet microscopy to study the distinct patterns of sympathetic and sensory innervation in the pancreas as few other studies showed before [80-82]. Daniel Azorin (AG Winkler) applied machine learning algorithms to analyze these patterns, which is challenging due to the large data size and complex 3D structures. Machine learning algorithms have been widely used in neuroscience to analyze and extract information from images [83, 119]. I found that sympathetic neurons showed more concentrated branching pattern while sensory neurons displayed a more ubiquitous distribution, and the staining patterns indicated significant heterogeneity. We employed various methods, including splitting the data into fractions and analyzing it as a 2D projection, to reduce the data size. Nonetheless, we found that analyzing complete datasets in 3D was essential to capture all the small branching patterns as neuronal structures were not equally distributed within the tissue leading to biases.

To study pancreas innervating neurons on a transcriptomic level, I developed the Trace-n-Seq approach. However, several challenges had to be addressed before obtaining a reliable dataset, and to my knowledge, very few studies have analyzed organ-specific neurons on a transcriptomic level, particularly none were conducted in the cancer setting [56, 57, 64, 65].

A major challenge of cancer-neuro science is a lack of information on which neurons directly interact with tumor cells to select neurons for molecular analysis. Our study bridges these gaps and opens organ specific neuronal characterization for a multitude of different physiological and pathophysiological situations and organs. Recently, various elegant approaches to connect neuronal origin with target organ have been developed, based either on dyes or injection of adeno-associated viruses [56, 57, 64-66, 120].

AAV-based approaches are highly effective in the brain and can be modified with barcodes or load like channelrhodopsins, but remain dependent on AAV-tropism. In the PNS only small numbers of neurons could be labelled with AAV approaches [65, 66]. So far, dye or AAV-based approaches rely on microscopy-based picking of labeled cells, a tedious, subjective method which results in low number of neurons for analysis [56, 64, 65]. In addition, AAV-based tracing is not suitable for tracing fast-growing tumors due to its slow tracing capacity (2 months vs 7-10 days for a dye). FACS-based isolation of traced cells with Trace-n-Seq allows high-throughput profiling of hundreds or thousands of neurons and enables downstream processing with single cell pipelines. As the neuronal heterogeneity within peripheral ganglia is extensive, numbers are key to extract biology expression analysis from the comparison of subpopulations [58, 61].

For the establishment of Trace-n-Seq several more obstacles needed to be resolved. PNS neurons are difficult to isolate and purify from other cell types, such as glial cells, which can lead to contamination of the sequencing data. Traced neurons are often found in small numbers, which makes it difficult to obtain enough cells for sequencing, specifically with previous microscopy-based picking approaches. Moreover, several different techniques for scRNAseq with different output exist and there is considerable variation in the quality and reliability of different sequencing platforms. Additionally, there are only few datasets available for comparison of healthy tissue innervating neurons and none for cancer innervating neurons [51, 58, 61, 65].

Using Trace-n-Seq I identified 2 distinct clusters of sympathetic neurons that I annotated as noradrenergic neurons. Of note, the celiac ganglion has never been sequenced and the annotation is based on sympathetic trunk ganglia.

Based on my analysis cells from Cluster 1 release norepinephrine, which binds to alpha and beta receptors on blood vessels and causes vasoconstriction or vasodilation. In contrast, for Cluster 2 I suggest a role in metabolic and endocrine regulation based on my analysis. [47, 62, 96, 102, 121]. The transcriptomic profile is in line with biological expectation of pathways needed in the pancreas.

I conducted a study to sequence and further characterize the sensory innervation of the pancreas from the dorsal root ganglia. This area had been previously studied in various publications, but without tracing information. Using the annotation from Zeisel *et al.* and Sharma *et al.*,[58, 61, 63] I identified the three major subtypes of sensory neurons: neurofilament, peptidergic, and non-peptidergic. I also generated a second dataset of peritoneum innervating neurons for comparison, which showed a high level of tissue-specific subtype innervation heterogeneity. In the pancreas, the majority of sensory fibers were a myelinated neurofilament subtype, critical for transmitting signals related to the regulation of digestive and metabolic processes. Peritoneum innervating neurons were mainly derived from peptidergic and non-peptidergic sensory neurons, also known as nociceptors, which are important for transmitting pain signals to the central nervous system and regulating inflammatory responses.[47, 59-62]. I found that the identified clusters and expression profiles were present independent of mouse strain or sequencing technology, indicating the robustness of the data. The different innervation patterns of pancreas and peritoneum are in line with biological expectation. Detection and transmitting of information of stimuli such as pain, temperature, pressure, and texture to the central nervous system in a key regulator in the peritoneum. The sensory innervation of the peritoneum is important for maintaining the body's ability to respond to internal and external stimuli and for regulating the functions of the abdominal organs. It enables the body to respond to changes in the environment and to respond to injury or disease by transmitting information about pain and other sensations to the central nervous system [47, 57, 62, 63, 79].

It's worth noting that these classifications are not mutually exclusive and that some sensory neurons may express both peptide and non-peptide neurotransmitters, and some sensory neurons may have intermediate diameter, and therefore, the classification of sensory neurons is still an active area of research and new discoveries could modify or expand the current understanding.

## 4.2 Neurons are reprogrammed by PDAC cells

Next, I aimed to analyze differences between healthy pancreas and PDAC neurons. First of all, I could analyze distinct innervation patterns of PDX and GEMM PDAC models and identify intense neuronal sprouting in cancerous tissue via light sheet microscopy and MLA based validation as well as by tracing (**Figure 31**, **Figure 32**, **Figure 33**). Compared to the fast growing mouse models, the slower growing human PDAC patient samples also showed a significant increase in neuronal innervation (**Figure 34**).

In my map of pancreas and PDAC neurons I found activation of a unique transcriptional program with elements of injury, neural regeneration and development. The Trace-n-Seq technique enables to examine hundreds of single tumors infiltrating neurons. This method has revealed numerous transcriptional alterations related to the expansion and maturation of neurons, metabolism, and microenvironmental factors such as stromal and immune regulation. My analysis revealed significant and distinct transcriptomic changes in individual tumor-infiltrating neurons within PDAC. In all neuronal subpopulations I discovered that the majority of pathways were down-regulated in the tumor microenvironment. A metabolic switch was observed in all neuronal subgroups, and the downregulation of pathways such as "electron transport chain" and "metabolism of amino acids and derivatives" in neurons in the presence of cancer may be due to the cancer cells' high demand for nutrients and energy, leading to a depletion of resources for neighboring neurons. The upregulation of processes involved in histone modifications, "resolution of D-loop structures," and "DNA repair" suggests that the neurons are undergoing damage and repair in response to the malignancy. These processes may enable the neurons to adapt to the stress and damage caused by the cancer cells [100]. GSEA analysis of sympathetic neurons showed enrichment in pathways contributing to the observed increased axonal sprouting.

In PDAC, infiltrating neurons, neuropeptides (e.g. Galanin, Gal, Calca), genes related to metabolism (*Gapdh, Got*), receptors (*Ntrk1*, *Htr3a, Erbb2/3* and *Ntrk3),* genes for extracellular matrix proteins controlling cell adhesion (*Matn2*, *Postn*, *Sparc*), and immune regulators (*Mif*) were among the top downregulated genes, while genes induced by PDAC included axon guidance receptor Robo1, non-coding RNAs (*Mir6236*, *Neat1* or *Lars2*), transcription factors (Hoxc5), signaling molecules (Fgf14, Edn3), the master transcription factors *Atf3* and *Dclk2*, secreted factors (*Angptl2)*, receptors (*PDGFR),* and structural proteins (*Ttn*).

There are several possible reasons why neurons might down regulate certain genes in the presence of cancer cells. One possibility is that cancer cells may secrete factors that alter the local microenvironment, leading to changes in gene expression in neighboring cells. Another possibility is that the down regulation of certain genes may be a response to stress or damage caused by the cancer cells which is further reflected in the GSEA. Additionally, some of the down regulated genes, such as neuropeptides and immune regulators, may play a role in modulating pain and inflammation, which could be dysregulated in the presence of cancer cells. Cancer cells have been shown to secrete factors that can alter the surrounding environment and impair neuronal function, leading to reduced gene expression of neuropeptides, metabolism, receptors, extracellular matrix proteins controlling cell adhesion, and immune regulators [47, 54, 59, 65, 72, 122, 123]. The specific mechanisms underlying these changes in gene expression are still being studied and are not fully understood and have to be assessed in future functional studies (**Figure 36**, **Figure 37**, **Figure 38**).

The upregulation of the genes induced in neurons by PDAC suggests that the cancer cells induce changes in the neurons' transcriptional program, potentially altering their phenotype and function. The axon guidance receptor ROBO1 has been implicated in cancer progression and metastasis, particularly in breast cancer, and its upregulation in PDAC infiltrating neurons could indicate a similar role in promoting tumor invasion and migration [123, 124]. Non-coding RNAs, such as *Mir6236*, *Neat1*, and *Lars2*, have been shown to play various roles in cancer progression and are often dysregulated in cancer cells. In neurons, their upregulation in the presence of PDAC could reflect changes in RNA processing and regulation that contribute to the neuronal response to cancer cells. Transcription factors, such as HOXC5, ATF3, and DCLK2, can regulate gene expression and control cell fate and differentiation. Their upregulation in PDAC infiltrating neurons suggests a potential reprogramming of neuronal cells in response to the presence of cancer cells. Signaling molecules, such as FGF14 and EDN3, can regulate cell growth and survival and may play a role in cancer progression. Their upregulation in neurons could suggest a possible crosstalk between cancer cells and neurons via signaling pathways. Secreted factors, such as ANGPTL2, can have pro-tumorigenic effects and may promote cancer cell invasion and metastasis. Their upregulation in neurons suggests a possible role in creating a favorable microenvironment for cancer cells. Receptors, such as PDGFR, can respond to growth factors and may promote cancer cell proliferation and survival. The upregulation of PDGFR in neurons could reflect a potential interaction with cancer cells and their growth factors. Structural proteins, such as TTN, may be involved in cell adhesion and migration and their upregulation could suggest changes in neuronal cytoskeletal organization in response to PDAC infiltration. The upregulation of these genes in PDAC infiltrating neurons suggests a complex interplay between cancer cells and neurons, potentially influencing the behavior of both cell types (**Figure 38**).

I was able to identify a common signature and found the greatest transcriptomic differences in neurofilament and sympathetic neurons. The defined PCN signature is specific for cancer innervating neurons and differs from known gene signatures of nerve injury and inflammation (**Figure 39**) proven that it is a direct PDAC-neuron crosstalk effect.

Importantly, this PDAC- induced signature persists beyond tumor resection or axonal damage by neurotoxic drugs (**Figure 48**) and may therefore prime the microenvironment (**Figure 41**). This cancer-neuron footprint may act beyond the tumor itself, as pancreas or PDAC neurons sprout to spleen and other surrounding tissues (**Figure 40**) as well potentially modulating neuro-immune and other interactions biology [59]. Similar integration of the tumor into neuronal networks have recently been described to control progression in gliomas and CNS-metastasis [121, 122, 125-128].

Of note, not only expression profile of PDAC neurons changed compared to healthy pancreas, also the innervation pattern was affected. In PDAC tissue I detected an increased amount of neurofilament neurons (Figure **42**, **Figure 43**). As described above, neurofilament neurons are large diameter neurons, being important for adapting to stretch, stabilization and fast signal transduction. I hypothesize that fast growing tumors specifically attract this subtype as this subtype is predominantly required in the tumor microenvironment. Also, the absence of nociceptors delays recognition as patient do not experience pain in early stage PDAC.

## 4.3 Targetability of PDAC innervating neurons

Targeting this cancer-nerve state may be an attractive target for drug development, we may have unknowingly used for decades, as we identify Taxanes as an unselective drug disrupting intratumoral neurons (**Figure 48**). I was able to show that denervation (surgical and pharmacological) reduced tumor growth even at late stage (**Figure 47**) and tumors weight was reduced similarly as after chemotherapeutic treatment (**Figure 50**). Of note, I found that Taxanes specifically denervated thin axons, while big nerve structures remained. The same results I could further show in 2D staining of human specimen. Compared to untreated PDAC samples, treated tumors showed only remaining big nerve structures (**Figure 49**).

Taxanes disrupt microtubules, which are important for the normal function of nerve cells, leading to axonal degeneration and nerve damage, which can cause the nerves to shrink and become smaller. Large diameter nerves have a greater number of microtubules than thin axons. This is because the microtubules are necessary for the structural integrity and maintenance of the axon and its ability to support the transport of molecules. Also, they have a greater number of blood vessels and therefore have a greater supply of oxygen and nutrients, which allows them to better withstand the adverse effects of neurotoxic agents. They also have a higher number of glial cells, which provide support and protection to the neurons, and help to remove waste products and debris, they also can help to repair the damage that may occur.

My hypothesis is that fast-growing tumors specifically attract a certain type of nerve structure because it is highly needed in the TME and only big nerve structures remain after Taxane treatment. By targeting these large nerve structures through the use of 6OHDA denervation and co-treating mice with Nab-Paclitaxel, I observed a 16-fold decrease in tumor size. This suggests that in the absence of (big) nerve structures, cancer cells can be effectively eliminated. Further findings showed that under treatment, remaining cancer cells resided within or near large nerve structures. I hypothesize that these structures might provide a "sanctuary" for the cancer cells, protecting them from treatment and supplying them with growth factors.

The results of this study indicate the potential interaction between neurons and cancerous tissue, particularly in PDAC. However, these results need to be further validated on a functional level. One approach could involve applying denervation and activation experiments to compare expression and direct crosstalk of neurons with the cells in the tumor microenvironment (TME).

I found that interaction potential was high between neurons and fibroblasts in PDAC, and in general, the interaction potential was higher with all cells in cancerous tissue (**Figure 44**, **Figure 46**). Further validation using optogenetics could provide additional evidence to support these findings. Optogenetics is a technique that uses light to activate neurons. Optogenetics has been used to study the function of neurons in innervating tissues, including the regulation of pain and inflammation [129]. By selectively activating or inhibiting specific neurons, I will be able to better understand their role in these processes, analyze direct interaction and potentially develop new therapies.

As pancreatic cancer is not the only cancer entity characterized by nerval innervation (**Figure 53**, **Figure 55**) the Trace-n-Seq technique can be applied for further questions like: is there a common cancer-nerve signature shared among different cancer types or is it unique for PDAC? Does metastasis also share the signature and does it drive metastasis? Many questions like the role of neurons beyond primary tumor remain elusive, therefore visualization, molecular characterization and functional dissection of how cancers hijack our nervous system for their advantage is a key keystone of how we should “think cancer”.

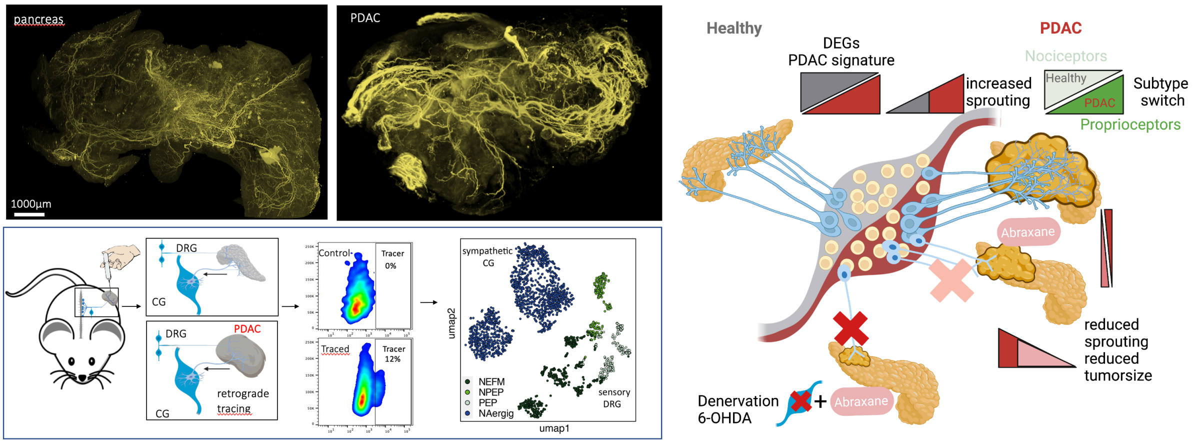

**Figure 57: Summary of the Trace-n-Seq approach.** The presence of PDAC cells increases axonal sprouting in both mice and humans and causes the reprogramming of neurons in mice. The tumor attracts specific neuronal subtypes, particularly proprioceptors. The use of Taxanes can reduce tumor burden by denervating innervating neurons, which can be strengthened through additional pharmacological denervation.

# 5 Material and Methods

Human tissue samples were obtained and approved by the ethical committee of the University of Heidelberg (case number S-206/2011, S-206/2011, 206/2005) and experiments were conducted in accordance with the Helsinki Declaration; written informed consent was obtained from all patients.

## 5.1 Animal experiments

Animal experiments were approved by the national authorities (Regierungspräsidium Karlsruhe). Studies were conducted according to authorization number (Tierversuchsantrag) G230/19, G49/19, G105/17, G and G148/21. Mice were housed and bred at the DKFZ Animal Facility under specific pathogen free (SPF) conditions and maintained in individually ventilated cages (IVCs).

## 5.2 Xenograft

For xenograft experiments, female NOD.Cg-*Prkdc*$^{scid}$ *Il2rg*$^{tm1Wjl/SzJ}$ (NSG) immunocompromised mice were used. To generate orthotopic tumor of human PDAC cells, 200,000 cells were mixed with Matrigel (2 mg/mL; BD) and injected into the mice's pancreas. Engraftment of tumors and subsequent growth were monitored by regular palpation of the implantation site. In brief, PACO cells were injected into the pancreas - mice were anaesthetized with 3% isoflurane and 1.5% $O_2$. Isoflurane was decreased to 1.7% once mice were asleep. Before surgery, mice were weighted. Approx. 100-150 µl carprofen (5 mg/kg) was injected subcutaneously. The abdomina of mice were shaved and disinfected using iodine solution. A straight cut was performed at the abdominal wall with scarp scissors and widened. 100 µl cells in matrigel/PBS were injected into the pancreas. The incision was clamped using 3-4 wound clamps which were removed ten days after surgery. Carprofen was given according to the corresponding TVA. For detailed analgesia pleas view the TVA.

## 5.3 Electroporation of the pancreas

Wild-type mice had a C57BL/6 (BL6) background (Janvier Labs). Tumors were induced by injecting a plasmid cocktail into the pancreas containing a transposon encoding mutated kras which integrates using a transposase, in combination with CRISPR mediated p53 inactivation. Mice were anesthetized using isoflurane 1.8% in air (v/v) and Carprofen was injected. Bepanthen was applied to the eyes. 10 ul of the plasmid cocktail in TE Endofree buffer (Qiagen Maxi/Gigaprep kit) were injected into the pancreas using a 29G 20 ul Hamilton syringe. The bubble was grabbed and electroporated with a 5 $mm^2$ electrode. The orientation was switched and the pancreas was electroporated a second time (Settings: Voltage: 40V, Pulse Interval: 500ms, pulse length 35 ms, number of pulses: 4)

## 5.4 Sympathetic denervation via 6OHDA

For sympathetic nerve disruption in mice, 2 doses of 6OHDA or vehicle, 100 mg/kg on day 0 and 250 mg/kg on day 2 were injected i.p. either 3 days before tumor induction (orthotopic and subcutaneous) or at the first timepoint at which a tumor was palpable.

## 5.5 Sympathetic denervation via surgical ganglioectomy

NSG mice were anesthetized using isoflurane. A Carprofen depot (10 mg/g) was injected subcutaneously 30 min prior to the surgery. Ganglioectomy was performed as described before [76]. In brief, a midline laparotomy was performed and the pancreatic tail was exteriorized. After dissecting the pancreas until the level of the portal vein, the celiac artery and the superior mesenteric artery (AMS) were identified. The celiac ganglion was subtly resected using micro-surgical instruments under an operating microscope. The incision was checked for cessation of bleeding. Directly after, PDAC cells were injected into the pancreas as described above and the abdominal muscles were closed using 6 mm vicryl sutures (Ethicon).

## 5.6 In vivo drug treatment

NSG mice were palpated for any mass in the pancreas. Once tumors were palpable they were randomly assigned to control and treatment group. Abraxane (100 mg/kg) was intraperitoneally injected daily for 5 days followed by a nine-day drug holiday. This treatment scheme was performed twice for an early timepoint and four times for a late timepoint. Mice were FB injected on the last treatment day and sacrificed 9 days later. Ganglia were processed as described below. Tumors were resected and measured by weight and size.

## 5.7 In vivo drug co-treatment

For sympathetic nerve disruption in mice, 3 doses of 6OHDA or vehicle, 100 mg/kg per day were injected i.p. 3 days before tumor induction. NSG mice were palpated for any mass in the pancreas or a subcutaneous tumor respectively. Once tumors were palpable, Abraxane (100 mg/kg) was intraperitoneally injected as described above for 3 rounds. Mice were sacrificed 9 days after the last treatment. Tumors were resected and measured by weight and size. As controls, mice received either only Abraxane or vehicle control.

## 5.8 Whole-mount immunostaining and clearing procedure

Intact tissues (tumors, pancreata or other organs) were immunostained and cleared following the iDISCO+ protocol [130]. Briefly, mice were euthanized and pancreas or tumor was resected, briefly washed in 10 mL of phosphate-buffered saline (PBS) followed by fixation in 10 mL of 4% paraformaldehyde (PFA) in PBS. Dissected tissues were fixed overnight at 4 °C in 4% PFA and washed in PBS. Then, organs/tumors are dehydrated using graded series of methanol solution (20%, 40%, 60%, 80%, 100% methanol, diluted in PBS) 1 h each at room temperature (RT). Dehydration is followed by a bleaching step in methanol/5% hydrogen peroxide overnight at 4 °C. Samples were rehydrated using graded series of methanol solution, before permeabilization in 20% dimethylsufoxyde (DMSO), 0.16% triton X and 23 g/L of glycine in PBS for 2 days at 37 °C. Samples were incubated in blocking buffer: PTwH (0.2% Tween-20, 10 mg/L heparin in PBS), 5% DMSO and 3% BSA for 3 days at 37 °C before incubation with primary antibodies (PRPH, TH, CGRP, ß3TUB) at 37 °C for 1 week (antibodies **Table 1**). After washing in PTwH buffer, samples were incubated with secondary antibodies for 2–3 days at 37 °C. Samples were washed in PTwH, dehydrated in graded methanol series, and equilibrated in 66% dichloromethane/33% methanol overnight at RT. Methanol was washed off in 100% dichloromethane twice for 15 min. Samples were put in dibenzyl ether to complete the clearing.

**Table 1: List of antibodies**

| **Antibodies** | **Source** | **Cat** |
|---|---|---|
| Donkey Anti-Goat IgG H&L | abcam | ab150129 |
| Anti-Peripherin Antibody | Merck | AB1530 |
| Anti-Peripherin antibody | abcam | ab39374 |
| SLC2A1 / GLUT-1 Antibody | aa92-492 | LSBio/Biozol |
| Anti-S100 antibody | abcam | ab14849 |
| TH (F-11) | Santa Cruz | sc-25269 |
| Recombinant Anti-Tyrosine Hydroxylase antibody [EP1533Y] | abcam | ab75875 |
| Anti-SHOX2 antibody | St John's Laboratory Ltd | STJ194828 |
| CD326 (EpCAM)-FITC, human | Miltenyi | 130-113-263 |
| Polyclonal Rabbit anti-Human LIN28B Antibody | LSBio | LS-C748024 |
| SLIT2 Polyclonal Antibody | ThermoFisher | PA5-31133 |
| Goat Anti-Chicken IgY H&L (Alexa Fluor 647) | abcam | ab150171 |
| beta III Tubulin antibody - 100MICROG | abcam | ab18207- |

| | | |
|---|---|---|
| Alexa Fluor® 647 AffiniPure Donkey Anti-Chicken IgY (IgG) (H+L) | Jackson Immuno Research/Biozol | 703-605-155 |
| Anti-CGRP antibody | abcam | ab36001 |
| Socs 2 Polyclonal Antibody | ThermoFisher | BS-1896R |
| SEMA5A Polyclonal Antibody | ThermoFisher | PA5-47791 |
| CD326 (EpCAM)-FITC | Miltenyi | 130-113-26 |
| APC anti-human CD45 | BioLegend | 304012 |

## 5.9 LSFM and image analysis

Cleared samples were imaged on a light-sheet fluorescent microscope (LaVision Biotech Ultramicroscope II) equipped with an Andor Neo sCMOS camera (Andor) and a LaVision LVMI 4x NA 0.3 objective with a working distance of 6 mm and a correction ring allowing the refractive index to be adjusted in the range from 1.30 to 1.60 (here: DBE, NA: 1.55) (LaVision Biotech GmbH, Bielefeld). Single mosaic images were first stitched using TeraStitcher within ImSpector (Lavision GmbH), then converted to Nis-Elements files (.nd2) within the software. 3D reconstruction of samples was then performed in NIS-Elements (version 5.21, 5.41 and 5.42 Nikon GmbH, Germany) as well as the belonging 3D-view and movies, using various render-modes (Maximum Intensity Projection, Alpha Blending, Depth Coded Alpha Blending, Alpha Blending shading and Depth Coded Alpha Blending with shading).

## 5.10 Quantification MLA

Machine-learning software: Commercial software (Aivia 10.5.1, Leica microsystems, Bellevue, WA) was used to apply the random forest machine-learning algorithm (MLA). By painting regions of interest of the different neural markers and background in a single image, the pixel classifier was trained. The set used for training includes the most common image transforms at medium and large kernel sizes (Gaussian, Hessian, Laplacian and structural tensor). Using an interactive process and fast preview of results allowed to create a model that is then applied to the rest of the images. Thresholding was adapted for each resulting confidence map.

For quantifying the tumor areas (or tumor masses areas or tissue) the light-sheet microscopy volumes were projected in the plane using the maximum intensity projection method in Fiji. Following the same steps as for the neural markers, another model was created by training the classifier with annotations for tumor mass and background.

The values obtained for the different neural markers were then normalized to the tumor mass of each sample.

Videos and animations were created using commercial software Aivia.

## 5.11 Retrograde labelling of neurons

To retrogradely label pancreas- or PDAC-innervating neurons, adult animals (8-15 weeks) were anesthetized by isoflurane and application of a subcutaneous Carprofen-depot 30 min (5 mg kg-1) prior to the surgery. The skin overlying the organs was shaved and a 5 mm incision was made directly on top of the pancreas or the tumor, respectively. The tissue was microdissected and fast blue (FB) (Polisciences, #17740-1), reconstituted as a 1% solution in distilled water was injected slowly at several spots into the pancreas or PDAC of NSG and BL6 animals using a Hamilton (20 ul, 29G) syringe. The injection site was rinsed with 0.5 mL of saline (Patterson Vet) to wash away any leaking dye before the incision was closed. Animals were sacrificed between 5 days and 30 days after injection for histology or scRNA-seq. For retrograde labeling of the colon and spleen, operation the method was used as described above but the tracer was slowly injected into the spleen and the colon. For the retrograde labelling of peritoneum-innervating neurons the tracer was further diluted to obtain 50 uL solution and injected i.p..

Animals were sacrificed between 5 days and 30 days after injection for immunohistochemistry or scRNA-seq.

Further dyes and AAVs were tested as tracers. DiL, Nuclear yellow, FluroRuby and AAV S2 were all injected into the pancreas. All dyes were diluted as described by the manufacturer' protocol. Different tracing periods, dilutions and injection schemes were used as described in chapter 3.2.

## 5.12 Dissection of the Celiac Ganglion (CG)

Dissection was carried out using a stereotactic microscope equipped with a light source. NSG and BL6 mice were used for single cell experiments and for retrograde tracing from the pancreas, PDAC, peritoneum, colon, spleen and. Stainings of the whole ganglia (with and without retrograde tracing) were used for quantification of the proportion of sympathetic cell types and their soma area. Mice were euthanized and overlying organs were removed. The CG was prepped out and put in ASCF on ice for further usage.

## 5.13 Dissection of the Dorsal Root Ganglion (DRG)

Mice were sacrificed and DRGs of interest collected in freshly oxygenated, ice cold ACSF. Dissection was carried out using a stereotactic microscope equipped with a light source. NSG and BL6 mice were used for single cell experiments and for retrograde tracing from the pancreas, PDAC, peritoneum, colon, spleen and. Stainings of the whole ganglia (with and without retrograde tracing) were used for quantification of the proportion of sensory cell types and their soma area. Mice were euthanized and the spine was removed and cut in the middle. The DRGs in every segment were prepped out and put in ASCF on ice for further usage.

## 5.14 Tissue digestion

Mouse pancreas, xenograft and electroporated tumors were digested using the Tumor Dissociation Kit (Miltenyi, 130-095-929) according to the manufacturer’s protocol.

In brief, tissue was harvested and washed in ice cold PBS. Pancreas was further blocked in RPMI+FCS and FCS was injected using a syringe to block digestion enzymes within the pancreas. Tissue was cut in pieces and the digestion mixture was added to RPMI medium containing tumor or pancreas tissue. PDAC samples were digested according to the tough tissue and pancreas according to the soft tissue protocol. The samples were diluted with 40 ml of RPMI medium, centrifuged and washed before further staining.

## 5.15 Cell lines and cell culture

I used a well established protocol for cell cultivation developed in our laboratory. To culture Patient-derived xenograft (PACO) cell lines, Corning Primaria T75 or T25 cell culture flasks (#353810, Corning) were used with a specific cancer stem cell (CSC) medium previously established in the lab and available at Miltenyi. To passage the PDX cell lines, adherent cells on the flask were treated with 1.5-3 mL of Accutase for approximately 15 minutes at 37°C and 5% CO2 until they detached (#A11105, Life Technologies). The cells were then collected in 5-7 mL of CO2-independent medium (#18045070, Life Technologies) supplemented with 1% BSA (#11020-039, Thermo Fisher) and 2 mM glutamine (#25030024, Life Technologies), centrifuged at 300 x g for 5 min at RT, and resuspended in 1 ml of CSC medium [44].

Human fibroblast cell lines were already present in our lab. Cells were cultured in T75 cell culture flasks in fibroblast medium. In order to passage cell lines, cell culture medium of adherent cells was aspirated, cells were washed once with PBS and 3 mL Trypsin (#T3924, Sigma Aldrich) was added to cells on flask and incubated at 37°C and 5% $CO_2$ for roughly 5-10 min until they were completely dissociated and detached. Subsequently, 7 mL appropriate

FCS-containing medium was added to collect cells in a total volume of 10 mL in order to stop trypsinization. Next, cells were centrifuged at 300 x g for 5 min at RT. Supernatant was removed and cell pellet was resuspended in 1 mL appropriate cell culture medium

For cell counting, the Beckman automated cell counter ViCell was used. 50 µl of cell suspension was diluted in (1:10 ratio) in 450 µl PBS supplemented with 0.1% Pluronic™ F-68 Non-ionic Surfactant (#24040032, Thermo Fisher) in ViCell tubes.

Cell counting was done using a Beckman automated cell counter ViCell. Cryopreservation was done using CryoStor CS10 (Sigma-Aldrich (#C2874)) cell freezing medium and Mr. Frosty freezing container, while thawing was performed using CO2-independent medium supplemented with BSA and glutamine, followed by centrifugation and resuspension in appropriate cell culture medium.

## 5.16 *In vitro* culture of mouse ganglia cells

Mouse CG and DRG were dissected as described above. The ganglia cells were washed in ice-cold aSCF and the outer layer of the ganglion was removed under a stereomicroscope. For culturing of ganglia cells primaria 24 well plates were used. A thin Matrigel layer (1:30 diluted in CSC medium) was plated on the well. One ganglion was further plated on the thin layer covered in 10 µl of 1:30 Matrigel dilution and incubated at 37°C and 5% $CO_2$. CSC (or Neurobasalmedium respectively) was added to the well and the cells were cultured in serum-free conditions at 37°C and 5% $CO_2$. Medium was changed every 4 days by slightly aspirating ¾ of the medium and adding fresh CSC medium. Axons usually started growing out about 3-4 days after seeding. After 2 weeks cells could be “splitted”. Either the remaining ganglion was picked out of the well and replaced in a new well under the same conditions as described before, or the entire well was accutased and splitted as described for human PACO cell lines and seeded on a thin 1:30 Matrigel layer.

## 5.17 *In vitro* co-cultures

Co-Culture experiments of mouse CG and DRG with human PACO cells or fibroblast respectively were performed similar as described before [131] in three different ways. 1: Ganglia cells were seeded as described above and after axons started to grow out, cells were incubated for 1 hour with cell-trace violet for labelling. Cells were washed several times, fresh medium was added and PACO10-GFP cells were added to the well. The cells were cultured together for 3-5 days before flow cytometric analysis of PACO and ganglia cells respectively. 2: Ganglia cells were seeded as described above and PACO/fibroblast were cultured in a transwell chamber. In detail- PACO10, PACO43, fibroblasts were seeded in 0.4 µm pore transwells (Becton Dickinson). Cell numbers were adapted experimentally to ensure equal values during the experiment. The same number of cells was seeded in a transparent 96-well plate to monitor cell confluence during the experiment. 24 h later, fibroblasts were preincubated in CSC medium for 1 h prior to setting the co-culture. After 3 days of co-culture, transwells were placed on a new plate and cell amount was estimated using CellTiter-Blue stock solution (Promega) following manufacturer's instructions. Axonal sprouting could be measured using the Cytosmart imaging system. The plate was measured at timepoint before and after co-culture to analyze axonal sprouting. 3: CG and DRG were seeded as described above. After 3 days medium was changed and cells were incubated in this medium for 5 days. PACO and fibroblast cells were seeded in a 24 well plate. 24 hours later, cell density was assessed using the Cytosmart reasout and the medium was removed and new medium (1:1 fresh + supernatant of ganglia cells) was added. After 3 days of culture, cell amount was estimated using CellTiter-Blue stock solution (Promega) following manufacturer's instructions and via Cytosmart quantification

## 5.18 Immunofluorescent Imaging

Tumor or pancreas tissue was collected and washed in 10 mL of PBS before fixation in 10 mL of 4% PFA at 4 °C ON. DRGs and CGs were subsequently dissected, washed in ACSF fixed in 4% PFA for 20 min at RT, incubated in sucrose ON and processed for cryosectioning.

10 mm serial cryosections were collected and processed for immunohistochemistry. In brief, sections were washes with PBS and incubated with blocking buffer (PBS with 5% normal goat serum and 0.3% Triton-100) for 1 h at RT. The sections were then incubated with the primary antibody in the same blocking buffer overnight at 4 °C. The following day, sections were washed three times with wash buffer (PBS with 0.3% Triton-100) before incubation secondary conjugated antibody for 1 h at RT. Sections were then washed for three times with wash buffer before mounting in Fluoromount Aqueous Mounting Medium (Sigma). Antibodies see **Table 1**. Samples were analyzed using a Leica Zeiss confocal microscope.

## 5.19 Immunohistochemistry

Hematoxylin and eosin (H&E) and immunohistochemistry (IHC) staining was performed by Vanessa Vogel (HI-STEM gGmbH) according to her protocol. Tumor specimens were fixed in 10% formalin (Sigma) for at least 48 h. Subsequently, samples were dehydrated with increasing concentrations of ethanol, followed by xylene and finally embedded in paraffin.

H&E staining was conducted using an automatic tissue stainer. Briefly, slides were incubated in hematoxylin according to Mayer (Sigma), rinsed in water and stained with Eosine Y (Sigma). Staining was fixed with acetic acid, followed by increasing concentrations of ethanol. Afterwards, slides were covered with a xylene-based mounting medium and a cover slip.

For IHC staining, paraffin-embedded tumor blocks were cut into serial sections, and slices were deparaffinized with xylol and ethanol. This was followed by heat-induced epitope retrieval using damp heat in a steam pot with citrate buffer (pH 6.0) (#S2368, Dako 1:10). Primary antibodies (**Table 1**) were incubated 30 min at RT or overnight at 4°C. Slides were washed three times with PBS/Tween buffer and peroxidase blocking solution (#S2023, Dako) was added for 5 min at RT. Afterwards, EnVision+ Dual Link System-HRP (#K4061, Dako) was applied and incubated for 20-30 min at RT. Slides were washed again three times with PBS/Tween buffer and liquid DAB+ Substrate Chromogen System #(K3468, Dako) was applied to visualize staining. Slides were covered with aqueous based mounting medium (Sigma) and a cover slip.

## 5.20 Quantitative real-time PCR analysis of bulk samples

Cells were FACS-sorted according to cell type (antibody/live cell) or tracer (dependent on the experiment) and RNA extraction and purification of FACS-sorted cells was done using PicoPure RNA Isolation Kit according to manufacturer’s instructions (Thermo Fisher, cat # KIT0214). RNA concentration and quality were determined using Nanodrop or Qubit 3.0 fluorometer (Thermo Scientific) according to manufacturer’s instructions. and RNA was reverse transcribed using the high-capacity cDNA reverse transcription kit (Applied Biosystems) combined with RNase-Free DNase (Qiagen) treatment according to the manufacturer's protocol. RT-qPCR was performed and analyzed on ViiA7 (Applied Biosystems) using TaqMan gene-expression assay (Applied Biosystems;). The following TaqMan probes (Applied Biosystems) were used to acquire expression data with the Viia 7 Real-Time PCR System (Applied Biosystems): TaqMan Probes:

**Table 2:** TaqMan probes for qPCR

| **Probes** | **Source** | **Cat** |
|---|---|---|
| Gapdh | ThermoFischer | Mm99999915_g1 |
| Th tyrosin hydroxylase | ThermoFischer | Mm00447557_m1 |
| NEFL | ThermoFischer | Mm01315667_gH |
| PRPH | ThermoFischer | Mm00449704_m1 |
| CALCA | ThermoFischer | Mm00801462_m1 |
| OAZ1 | ThermoFischer | Mm01611061_g1 |
| PLP1 | ThermoFischer | Mm01297209_m1 |

The single cell qPCR protocol was adapted from Simon Haas: Single cells were FACS sorted into 96 well plates (Thermo Scientific) containing 5 µL master mix of 2.5 µL Cells Direct Reaction Mix (Invitrogen), 0.5 µL primer pool (1 µM), 0.1 µL RT/Taq (Invitrogen) and 1.9 µL H2O. Plates were briefly spin down and run for following programs:

| | | | |
|---|---|---|---|
| Cell lysis and RT | 50 °C | 60 min | Cycles |
| Inactivation of RT and Taq pol activation | 95 °C | 3 min | |
| Preamplification | 95 °C | 15 sec | 23x |
| | 60 °C | 60 sec | |
| Final elongation | 60 °C | 15 min | |

Afterwards 95 µL H2O were added and 2 µL were used for further qPCR

## 5.21 Sorting of retrogradely labelled neurons

Adult mice with retrogradely-labeled neurons were sacrificed by cervical dislocation. T5-T13 DRGs and CG were quickly removed without nerves attached Ganglia were immediately digested with a pre-heated (37°C) digestion mixture as described by Zeisel et al. [58].

In brief, 2.7 ml of digestion solution contain 400 ul TrypLE Express (Life Technologies), 2000 ul Papain (Worthington; 25 U/ml in aCSF), 100 ul DNase I (Worthington; 1 mM in aCSF) and 200 ul Collagenase/Dispase (Roche; 20 mg/ml in CS). Vybrant dye (Vybrant Ruby XY) and NeuO dye (Stem Cell Technology) was added to the digestion mix. Vybrant Dye incorporates into nucleated cells to stain for live neurons while NeuO is a dye used for *in vitro* enrichment of neurons. We implemented the dye to further enrich for the neuronal cell population.

Ganglia were digested on a heating block at 37°C and shaking for 1.5 h. Every 30 min the cell suspension was further mechanically disrupted by pipetting up and down starting with a 1 ml pipette going down to a 200 µl pipette. As soon as all ganglia were dissociated the cell suspensions were filtered using a 40 mm cell strainer (FALCON) and collected in a 15 ml plastic tube. The digestion solution was diluted with 10 ml RPMI medium containing 5% BSA and 1% FCS and centrifuged at 100 g for 4 min at 4°C. The supernatant was removed and the pellet resuspended in 200 µl (CG) and 500 µl (DRG) RPMI medium containing 5% BSA and 1% FCS. The tissue of interest-innervating neurons were FACS-isolated and pre-gated on nucleated (Vybrant Ruby+) and NeuO+ cells and finally selected for fast blue signal. The cells were sorted using a BD sorter. in 384 well plates containing 1.2 µl of lysis buffer (0.2% Triton, RNse inhibitor, 10 µM polyTPrimer, 10 mM dNTPs). Plate was briefly centrifuged and snap frozen and stored on -80°C until further processing.

## 5.22 scRNA seq of retrogradely labelled neurons using SmartSeq2.5

Single-cell libraries were generated according to the SMART-seq2.5 protocol [65, 132]. Briefly, RNA from single-cell lysates in oligo-dT primer (SMART-seq2 30 Oligo-dT Primer), dNTPs (NEB), and RNase inhibitor (Fisher Scientific) were annealed at 72°C for 3 min on a thermal cycler. Reverse transcription was carried out in a master mix of Maxima RNaseH-minus RT enzyme and buffer (Fisher Scientific), PEG 50%, H2O, RNase inhibitor, and a 50-template switch oligonucleotide (SMART-seq2 50 TSO) using the following protocol: 42°C for 90 min, followed by inactivation at 70°C for 15 min. Whole transcriptome amplification was achieved by addition of KAPA HiFi HotStart ReadyMix (Kapa Biosystems) and IS PCR primer (ISPCR) to the reverse transcription product and amplification on a thermal cycler using the following protocol: 98°C for 3 min, followed by 16 cycles of 98°C for 20 s, 67°C for 15 s, 72°C for 6 min, followed by a final 5-min extension at 72°C. cDNA was exemplarily assessed using a High-Sensitivity DNA chip (Agilent Bioanalyzer), confirming the expected size distribution of 1000-2000 bp and to dilute to 0.3 ng/µl. Tagmentation reactions were carried out with the Nextera XT DNA Sample Preparation Kit (Illumina) using 300 pg of cDNA per single cell as input, with modified manufacturer’s instructions as described. Libraries were indexed, pooled and purified twice with AMPure XP SPRI beads at a volume ratio of 0.9x, size distribution assessed using a High Sensitivity DNA chip (Agilent Bioanalyzer) and Qubit High-Sensitivity DNA kit (Invitrogen). Libraries were sequenced using NextSeq500/550 High Output v2 kits (75 cycles, Illumina) using single end sequencing.

## 5.23 scRNA seq of retrogradely labelled neurons using adapted version of BarcodeSeq

Single-cell libraries were generated similar to the SMART-seq2.5 protocol with small adjustments. Briefly, RNA from single-cell lysates in barcoded oligo-dT primer [94] (for Primer sequences, see publication [94]), dNTPs (NEB), and RNase inhibitor (Fisher Scientific) were annealed at 72°C for 3 minutes on a thermal cycler. Reverse transcription was carried out in a master mix of Maxima RNaseH-minus RT enzyme and buffer (Fisher Scientific), PEG 50%, H2O, RNase inhibitor, and a 50-template switch oligonucleotide (SMART-seq2 50 TSO) using the following protocol: 42°C for 90 min, followed by inactivation at 70°C for 15 min. Whole transcriptome amplification was achieved by addition of KAPA HiFi HotStart ReadyMix (Kapa Biosystems) and IS PCR primer (ISPCR) to the reverse transcription product and amplification on a thermal cycler using the following protocol: 98°C for 3 min, followed by 16 cycles of 98°C for 20 s, 67°C for 15 s, 72°C for 6 min, followed by a final 5-min extension at 72°C. Samples from one 384 well plate were pooled and cDNA was purified with AMPure XP SPRI beads at a volume ratio of 0.7x and quality was assessed using a High-Sensitivity DNA chip (Agilent Bioanalyzer), confirming the expected size distribution of 1000-2000 bp and to dilute to 1 ng/µl. Tagmentation reactions were carried out with the Nextera XT DNA Sample Preparation Kit (Illu-mina) using 1 ng of cDNA per 384 well pooled single cells as input, with modified manufacturer's instructions as described. Libraries were purified with AMPure XP SPRI beads at a volume ratio of 0.7x, size distribution assessed using a High Sensitivity DNA chip (Agilent Bioanalyzer) and Qubit High-Sensitivity DNA kit (Invitrogen). Libraries were sequenced using NextSeq500/550 High Output v2 kits (75 cycles, Illumina) using single end sequencing.

## 5.24 GSEA

The 'limma pipeline' was utilized to perform differential gene expression (DGE) analysis between contrast groups. Differentially expressed genes were identified based on a log2 fold-change (L2FC) of expression ≥q a cut-off and with adjusted p-value < a cut-off. Statistical significance was determined using an unpaired, two-tailed t-test followed by Benjamini-Hochberg correction. Gene Set Enrichment Analysis (GSEA) was performed using the 'GSEABase' and 'fGSEA' packages with a pre-ranked gene list based on previously identified DEGs. All annotated gene sets were provided by the Molecular Signature Database (MSigDB, release v. 7.0, UC San Diego and Broad Institute). The 'fGSEA' package implemented an algorithm for fast GSEA, allowing for more permutations and accurate standard approaches to multiple hypothesis correction.

## 5.25 Flow cytometry

For FACS and flow cytometry analysis, cells were harvested dependent of the tissue as described above and cell pellets were resuspended in sterile PBS supplemented with 1% BSA. Cells were filtered to achieve a single-cell suspension and transferred to appropriate FACS tubes. FACS sorting was performed using BD Bioscience Aria I, II or Aria Fusion at the DKFZ Flow Cytometry Core Facility. For flow cytometric analysis, Fortessa or LSR II (BD Bioscience) were used. Digested xenograft, electroporated tumor and mouse pancreas cells were stained with a total of 3 fluorescent cell surface antibodies and DAPI. Cells were sorted into four populations according to CD326+ (EPCAM+), EPCAM-/CD31+, EPCAM-/CD45+ and EPCAM-/CD31-/CD45- expression. Cells were incubated in the dark for 15 min on ice and washed once with PBS supplemented with 1% BSA. Cell pellet was resuspended in 150-100 µL PBS supplemented with 1% BSA according to cell number and analyzed by flow cytometry.

Data analysis was performed using the FlowJo software. Cells from each population were sorted in PBS+5%BSA and mixed in a 2:1:1:1 ratio. 30,000 cells of each sample were further processed for single cell analysis. Neurons and PACO10-GFP cells from co-culture experiments were sorted for GFP signal (PACO10) and size and APC signal (Neurons) from cell labelling using Cell Tracer dye. Cells were sorted directly into RNA extraction buffer (Thermo Fisher, cat # KIT0214), snap-frozen and stored at -80 °C until RNA extraction.

## 5.26 RNA Sequencing of co-culture bulk samples

Protocol was conducted as described before [133].RNA extraction and purification of FACS-isolated cells was performed using PicoPure RNA Isolation Kit according to manufacturer's instructions (Thermo Fisher, cat # KIT0214). RNA quality assessment and quantification were performed with Bioanalyzer using Agilent RNA 6000 Pico Kit (Agilent, cat # 5067-1513). Whole transcriptome amplification was performed using a modified SMART-seq2 protocol [132],with 5µl of a modified RT buffer containing 1× SMART First Strand Buffer (Takara Bio Clontech, cat # 639538), 1 mM dithiothreitol (Takara Bio Clontech), 1 µM template switching oligo (IDT), 10 U µl−1 SMARTScribe (Takara Bio Clontech, cat # 639538) and 1 U µl−1 RNasin Plus RNase Inhibitor (Promega, cat # N2615). Tagmentation of cDNA was done using Nextera XT DNA Library Preparation Kit (Illumina, cat # FC-121-1030). All RNA libraries were pooled and sequenced together on an Illumina NextSeq 550 high output sequencer (1.4 pM with 1% PhiX loading concentration, single-end 75bp read configuration).

## 5.27 Single cell RNA-Seq using 10X Genomics

The single cell RNA sequencing analysis of full tumor and pancreas was carried out with 10X Genomics Chromium Single Cell Kit Version 3,. Suspensions were prepared as described above and diluted in PBS, 30.000 cells were used as input and added to 10x Chromium RT mix. For downstream cDNA synthesis (12-14 PCR cycles), library preparation, and sequencing, we followed the manufacturer's instructions.

## 5.28 *In vitro* proliferation treatment assays

CellTiter-Blue® (CTB) cell viability assay (#G8021, Promega) was used to assess cell proliferation upon co-culture experiments as described above. For this purpose, 15,000 cells/well of a Corning® Primaria™ 24-well plate (#353872, Corning) were seeded in 500 µL CSC BC medium in triplicates for PACO10, PACO43 and hFibroblast cell lines. Cells were incubated for ON at 37°C and 5% $CO_2$. Subsequently, co-cultures were set up as described above. After 3-5 days (depending on the condition and experiment), 500 µL fresh CSC medium was added. Cell viability was assessed by adding 1:5 CTB reagent to each well and incubated for 3 h. Conversion of the redox dye resazurin to resorufin by metabolically active cells was measured by fluorescence intensity ($560_{Ex}/590_{Em}$) using the SpectraMax iD3 microplate reader (Molecular Devices). Staurosporine (STS, #S1421, Selleckchem/Hölzel) treatment was used as positive control and fluorescent background. Relative cell viability/proliferation was calculated by normalizing to cell only control.

## 5.29 GFP / Luceferin-Venus vector constructs

Vectors for stable GFP expression in PDX cells were bought from sigmaaldrich (MISSION® pLKO.1-puro-CMV-TurboGFP™ Positive Control Plasmid DNA #SHC003).

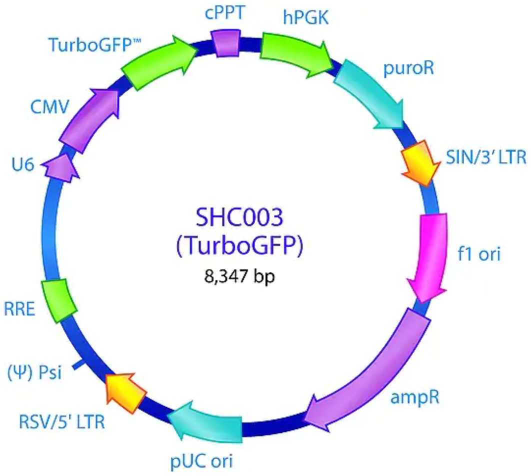

**Figure 58:** Vector for stable GFP expression.

Vectors for stable Luciferase and Venus expression were cloned and kindly provided by Jonas Schwickert.

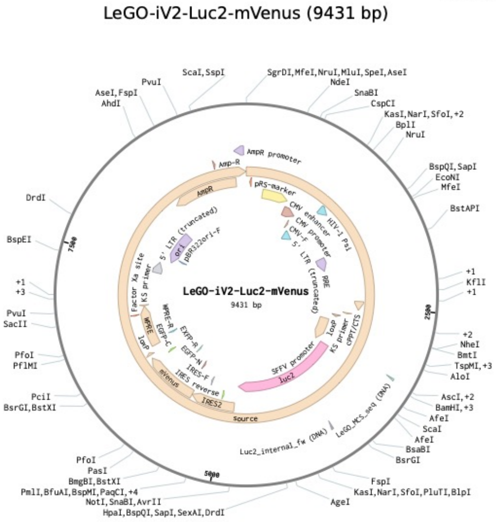

**Figure 59:** Vector for stable Luciferase expression. The construct was cloned by Jonas Schwickert

## 5.30 Virus production

HEK293T cells were seeded in T150 cell culture flasks with IMDM and 10% FCS and incubated overnight at 37°C and 5% CO2. On the day of transfection, the cells were at an optimal confluency of around 70%. The medium was then replaced with IMDM supplemented with 10% heat-inactivated FCS and 25 μM chloroquine. To achieve heat-inactivated FCS, the FCS was incubated at 52°C for 1 hour before adding to the medium. The calcium-phosphate co-precipitation method was utilized for transfecting the HEK293T cells. The respective reagents were thawed on ice, and a transfection mix was prepared in a 50 mL falcon tube.

50 μg lentiviral plasmid of interest ,37.5 μg pSPAX2 (Gag/pol) packaging 1 mg/mL, 5 μg pMD2.G envelope plasmid 1 mg/mL , 72 μL 2.5 mM $CaCl_2$ and filled up to a total volume of 750 μL with sterile $ddH_2O$

he transfection mix was prepared in a falcon tube and mixed with 2X HBS. After 15 minutes of incubation, the transfection mix was added to the cells and incubated at 37°C, 5% CO2. The next day, the medium was replaced with collection medium containing IMDM supplemented with 10% heat-inactivated FCS, 4 mM caffeine, and 1 mM sodium butyrate. After 48 hours, the collection medium was harvested, filtered (Vacuum Filtration System 0.45 μm (#S2HVU02RE)), and centrifuged. The pellet was resuspended in PBS or Advanced DMEM F12 and stored at -80°C in aliquots of 10-15 μL.

## 5.31 Transduction of cell lines

One million cells were seeded in a 100 mm Corning Primaria dish (#353803) in CSC medium supplemented with 10 μg/mL polybrene. After three to four hours, PDX cell lines were transduced with the appropriate amount of virus to achieve a transduction efficiency of approximately 30%. Medium was changed after 14 hours, and cells were cultured and sorted by fluorescent activated cell sorting (FACS) for the fluorescent marker as described.

## 5.32 Microscope image acquisition

Brightfield microscope images were acquired using the Zeiss Axio Scan.Z1 slidescanner at the DKFZ Light Microscopy Facility. The following settings were used:

Coarse: 1-4
Focus: ‘run auto focus’ after navigating on tumor region
Navigator range: 400 μm, 3800 – 4200

Fine: 70 µm

Lossy compression: 85%

## 5.33 Human specimen staining

The Nab-Paclitaxel treated cohort (11 cases) was matched using cases from the Pathology Institute Heidelberg. Cases were matched for gender, age group (accepted were cases within a 10-year range, plus or minus 5 years, according to availability) and anatomical location of the tumor (considering the following sublocations: pancreatic head, body or tail).

For the non-tumoral pancreatic tissue cases were selected using tissue from patients with non-malignant diagnosis (e.g., serous cystic neoplasia) that was not located in tumor vicinity and without any obvious parenchymatous atrophy, inflammation, in situ neoplasia or any other morphologically identifiable tissue alteration.

The chemotherapy-naïve PDAC tissue selection was based on the most representative predominantly intrapancreatic part of the tumor. A clear anatomical separation between intra-pancreatic and extra-pancreatic tumor components was frequently unviable due to the strong desmoplastic reaction that characterizes PDAC, and the subsequent effacement of the background tissue morphology.

Neoadjuvantly-treated PDAC tissue was selected based on the most representative predominantly intrapancreatic FFPE block of the case, independently of the tumor regression signs observed.

Selected FFPE blocks were 3 mm sectioned and stained using the standardized assay for neurofilament (Clone 2F11 mouse monoclonal, Cell Marque with a concentration 0,09 µg/mL) using a on the Ventana Benchmark Ultra platform (Ventana Medical Systems, Tucson, AZ). Langerhans-Islets normally present were used as internal control.

One whole section of each case was annotated for one as large as possible region of interest (ROI) which was subclassified as “pancreas tissue”; “PDAC” and “NAC-PDAC_1(NAB-PACLITAXEL)”. All morphologically identifiable nerve fascicles, independent of size and Neurofilament intensity of staining, as well as all, NF-positive nerve fibers were annotated using Q-Path (version 0.3.2, downloaded at 15.09.2022).

## 5.34 GSEA based signature of the PDAC-Nerve Signature

The signature was created based on the DEG list of the top, significantly deregulated genes between pancreas and PDAC innervating neurons among the five different neuronal subtypes.

**Table 3: PCN signature genes**

| PCN DOWN | PCN UP |
|---|---|
| **COX4I1** | GM15564 |
| **GAPDH** | MIR6236 |
| **UBB** | LARS2 |
| **COX5B** | MYH14 |
| **TUBA1B** | D7ERTD715E |
| **NDUFA11** | ZFP407 |
| **CD9** | RP23-459L15,8 |
| **SLC48A1** | RAB11FIP3 |
| **YWHAQ** | CLIP2 |
| **APOE** | TNRC18 |
| **SLC25A5** | DDX23 |
| **C330006A16RIK** | LINCPINT |
| **ATP5J** | PPP1R9B |
| **UQCR11** | MTCL1 |
| **PSMA3** | D10WSU102E |
| **NDUFB8** | KIF3C |
| **VDAC3** | MIAT |
| **LAMTOR1** | FAM131B |
| **PSMB6** | SPTBN4 |
| **TECR** | SNRPN |
| **NDUFB3** | MICAL3 |
| **NDUFS8** | RP23-459L15,7 |
| **COX6C** | SMG1 |
| **PEBP1** | ROBO2 |
| **SYNGR3** | CNOT1 |
| **FTL1** | PIP4K2B |
| **RPL18A** | USP24 |
| **TCEB2** | DOCK4 |
| **NDUFS7** | FKBP5 |
| **SPCS1** | FLNB |
| **NDUFA13** | PTPRD |
| **GMPR** | GM23935 |
| **GM1821** | DMXL1 |
| **PSMB3** | NAP1L2 |
| **COX8A** | PTMS |
| **SHISA4** | ZFHX3 |
| **GSTP1** | MYH10 |
| **PSMB2** | RANBP2 |
| **MORF4L1** | RAPGEF4 |
| **LYRM4** | CGNL1 |
| **SDHB** | KLC2 |
| **CISD1** | MT-ND5 |
| **ATP5F1** | NTRK3 |
| **AI413582** | SLC24A2 |
| **ENO1** | |
| **SOD1** | |

## 5.35 Alignment of scRNA-Seq data and gene expression quantifications

For Smart-Seq2 data, raw sequencing reads were aligned to the reference genome (mm10, GRCm38) using STAR (v2.5.3a, [134]) and gene expression was quantified using htseq-counts (v2.0.1, [135]). For the Barcode-Seq data, data was aligned to the mm10 genome, quantified and split into cell barcodes using STAR and the BRB-Seq pipeline (v3.1, https://github.com/DeplanckeLab/BRB-seqTools, [136]). For bulk RNA-Seq data, reads were aligned to a combined mouse and human genome using STAR (mm10 and hg38, GRCh38) and quantified using htseq-count, equivalently to the Smart-Seq2 data. For 10x scRNA-Seq data, cellranger (v3.1.0) was used against a combined mm10 and hg38 index with default options.

## 5.36 Low-level analysis of scRNA-Seq data

Low-level analysis of scRNA-Seq data was performed using largely functions from the scran (v1.20.1) and scater (v1.20.1) R packages [137]). First, cells with less than 50.000 mapped reads and 4000 detected genes and cells with more than 20% of reads mapping to mitochondria were removed. Next, counts were normalised using the computeSumFactors function and log-transformed. The resulting gene expression matrix was used for dimensionality reduction by principal component analysis (prcomp, stats), tSNE (Rtsne, Rtsne, v0.15) and UMAP (umap, umap, v0.2.7.0). To identify clusters, we used graph-based community detection using the Louvain algorithm implemented by the functions buildSNNGraph and cluster_louvain of the package igraph (v1.2.10).

## 5.37 Cell type annotation of single neurons

Cell types were annotated using a label-transfer approach from a previously annotated reference dataset [58].To this end, we identified highly variable genes using the findTopHVGs function from the scran package in the query dataset, and only used these genes for further annotation. We then computed pairwise pearson-correlation coefficients between each query and each reference cell type and annotated each query cell as the cell type with the highest correlation coefficient. We also annotated the dataset using the SingleR function in the SingleR package (v1.6.1 [138]) and found high concordance between the two approaches. We lifted both main and subcelltypes as well as neurotransmitter status from the [58] dataset, and furthermore annotated the DRG neurons with a separate reference dataset [61] with higher resolution. To visualize the integration, we used an MNN-based correction algorithm [139] to integrate the reference and query datasets, subset to the intersection of the 1000 most highly variable genes each and computed a joint UMAP.

## 5.38 Differential expression analysis

To identify differentially expressed genes between pancreas- and tumor-innervating neurons, we used DESeq2 (v.1.32.0) on pseudobulk libraries. Pseudobulks were generated across experimental replicates ($n = 2$ for healthy and $n = 3$ for cancer). Genes were considered significantly differentially expressed when they showed $padj < 0.1$. DEG analysis was performed separately for whole ganglion aggregates and individual cell types. For Figure 6, DEGs are considered as genes with $padj < 0.1$ in a Wilcoxon rank sum test when comparing individual cells due to the lack of biological replicates.

DEG analysis was performed in an analogous manner for the bulk RNA-Seq experiment of co-cultured PDAC cells, fibroblasts and ganglia.

## 5.39 Analysis of 10x scRNA-Seq of sorted pancreatic and PDAC stromal cells

10x scRNA-Seq data was processed by first removing cells with <1000 UMIs and <500 detected genes as well as >10% mitochondrial RNA content. For the tumor-bearing sample, we identified cancer cells as cells with primarily reads aligning to the human genome. We used computeSumFactors for size-factor normalization and louvain clustering for community detection, similarly to the Smart-Seq2 data analysis. We then assigned cell types based on marker genes. Finally, we visualized the datasets using dimensionality reduction by UMAP on the first 50 PCs. We processed the healthy pancreas and the tumor bearing sample separately.

## 5.40 Interaction potential analysis

The interaction potential analysis quantifies the total expression of receptors and ligands in potential target cells, for which the cognate receptor or ligand is expressed in innervating neurons. We closely followed the approach outlined in [65]. We first identified expressed receptors or ligands in neuronal sub-populations by obtaining gene lists encoding receptors and ligands from the SingleCellSignalR (v1.4.0 [140]) and considered them expressed in neurons if their log aggregate read counts exceeded 2. We then calculated the z-scored mean expression of all cognate genes in interaction partners and subtracted the minimum interaction score to yield a final interaction potential. We performed the analysis by comparing pancreas-innervating neurons with stroma from healthy mice and tumor-innervating neurons with PDAC cells and associated stroma.

## 5.41 Additional reagents

**Table 4: Reagents**

| **Reagents** | **Source** | **Cat** |
|---|---|---|
| RNasin Plus RNase Inhibitor | Promega | N2615 |
| ACSF | R&D | 3525/25ML |
| Maxima H Minus Reverse Transcriptase (200 U/µL)-1 x 10,000 units | ThermoFisher | EP0752 |
| Nextera XT DNA Library Preparation Kit (96 samples) | Illumina | FC-131-1096 |
| KAPA HiFi HS RM | Roche | 07958935001 |
| Chromium Next GEM Chip G Single Cell Kit | 10X | 1000127 |
| Fast Blue | Polyscience, Inc | 17740-1 |

| | | |
|---|---|---|
| Papain, Suspension | Worthington Biochemical/Cellsystems | LS003126 |
| TrypLE Express Enzym (1X) | ThermoFisher | 12605010 |
| Dichloromethane | Sigma | 270997-100ML |
| Benzylether | Sigma | 108014-1KG |
| Glycine | Sigma | G7126-500G |
| Heparin | Sigma | H3393-50KU |
| DNase Vial (D2) | Worthington Biochemical/Cellsystems | LK003170 |
| NeuroFluo NeuO | stem cell technologies | #01801 |
| 6-ohda | Merck | H4381 |
| Collagenase/Dispase | Sigma-Aldrich | 10269638001 |
| Hydrogen peroxide solution | Fisher | 216763-100ML |
| Poly-L-Ornithin solution | MerckMillipore | A-004-C |
| Fibroblast Growth Medium | PromoCell | C-23010 |
| SuperScript II Reverse Transcriptase | Thermo Fisher Scientific | 18064-014 |
| Vybran DyeCycl Ruby | ThermoFischer | V10309 |
| Eppendorf twin.tec-PCR-Platte 384 LoBind, skirted, | Eppendorf | 0030129547 |

# 6 Supplement

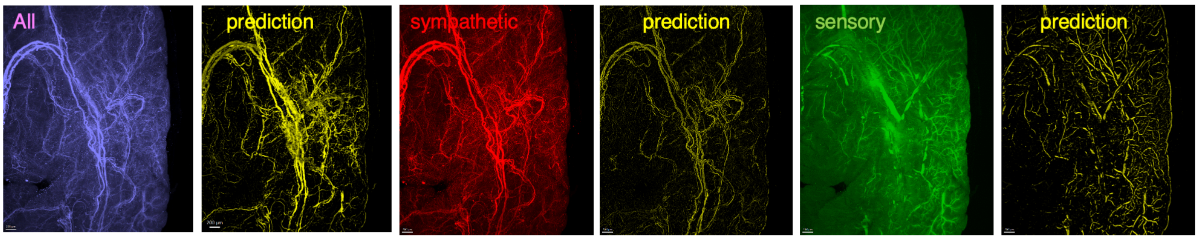

**Supplementary Figure 1: MLA based quantification of pancreas innervating nerve axons.** Channels of pan-nerves (purple), sympathetic nerves (red, TH) and sensory nerves (green, CGPR) were predicted (yellow).

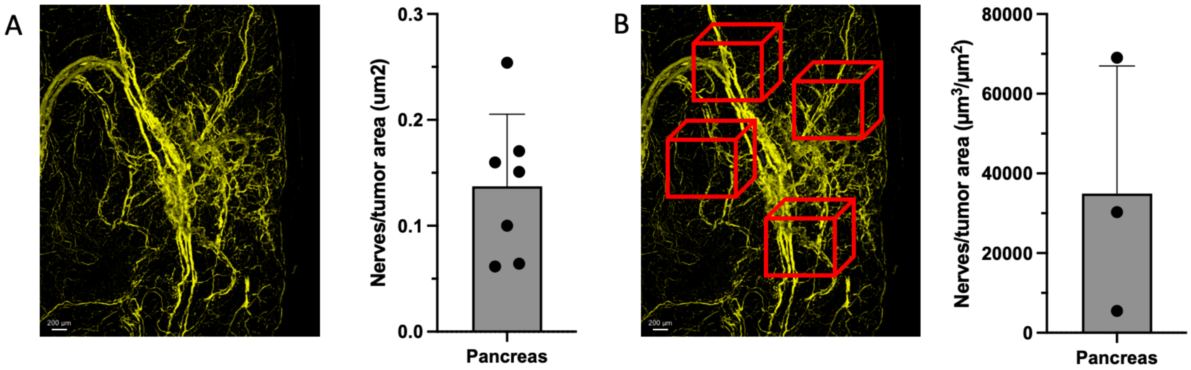

**Supplementary Figure 2: Comparison of (A) 3D to 2D and (B) 3D cube quantification.** Mean +/- SD is shown.

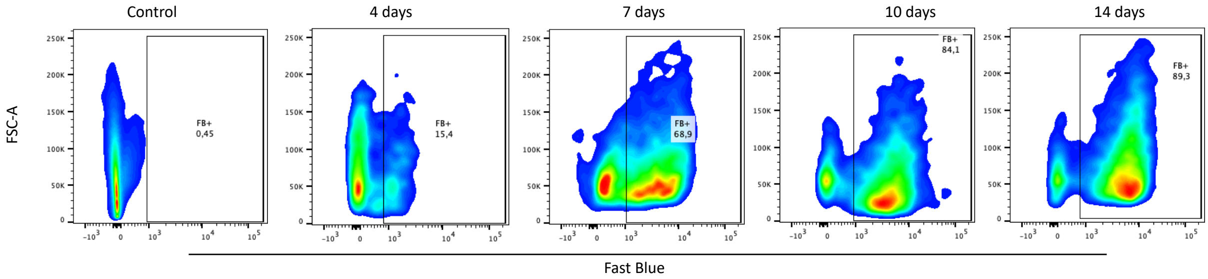

**Supplementary Figure 3: Timeline of retrograde tracing capacity in the CG after intrapancreatic Fast Blue Injection.** 4 µl 1% FB in H2O were intrapancreatic injected via microinjections of 1 µl. FB positive signal was assessed via FACS after 4d, 7d, 10d and 14d and compared to a negative control (without tracing). Cells were pre-gated on size and live cells (n=3).

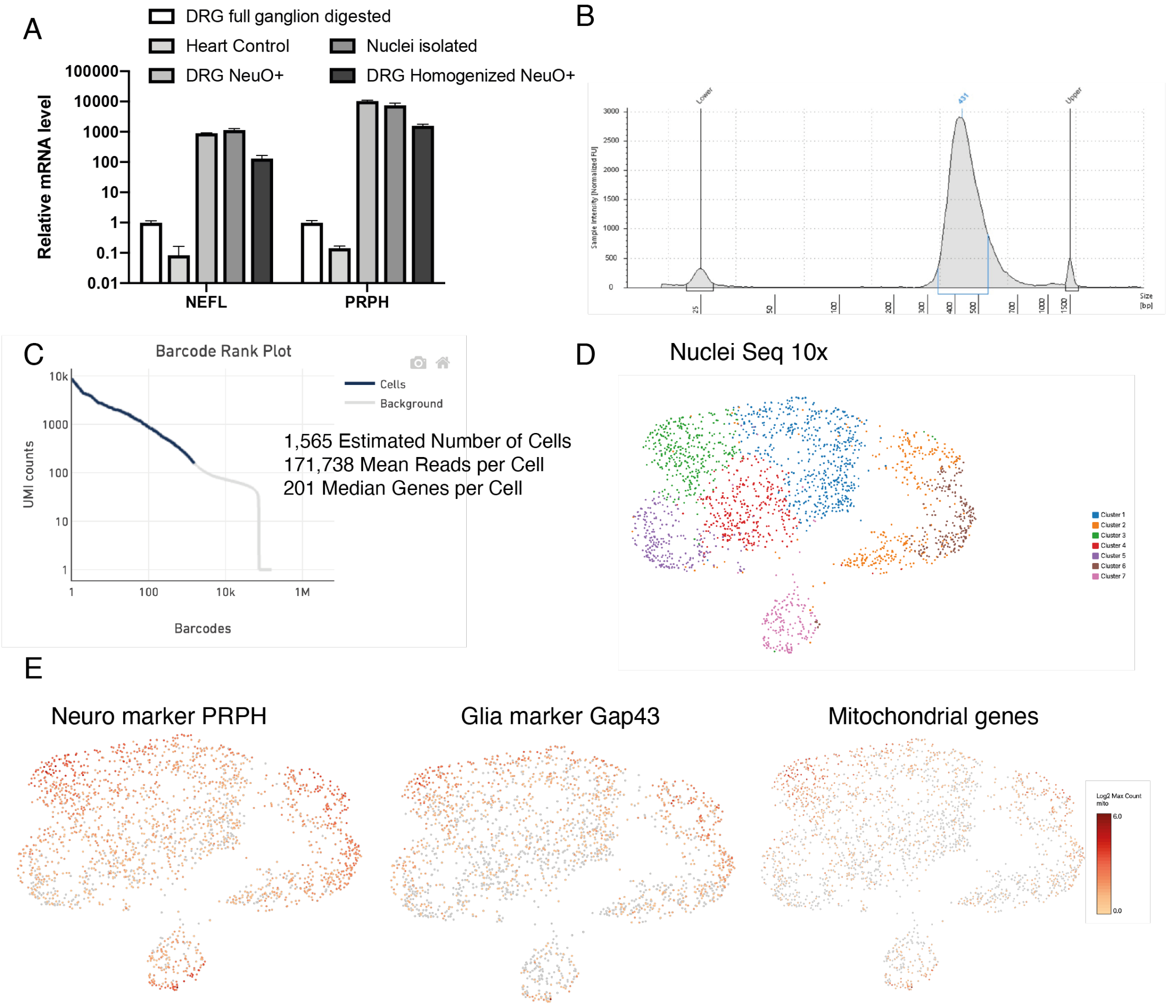

**Supplementary Figure 4: 10x based sequencing results of full ganglia. (A)** qPCR analysis of different protocols tested for 10x single cell suspension. Cells were dissociated as stated and relative mRNA level was assessed of neuronal marker neurofilament (Nefm) and peripherin (PRPH). Expression was normalized to cells of a full DRG ganglion, n=3. (B) Representative library plot of 10x library. (C) Barcode Rank blot extracted from Cell Ranger after sequencing full ganglia following nuclear extraction. Nuclei were extracted using nuclear separation lysis and FACS isolated. Cells were counted and 13,000 nuclei were loaded onto a 10x chip. (D) Uniform Manifold Approximation and Projection (UMAP) of 10x NucSeq sequencing run. (E) Quality control of the NucSeq 10x sequencing run. Cells were analyzed for their expression of peripherin, glia marker gap43 and for their mitochondrial reads to estimate quality of cells.

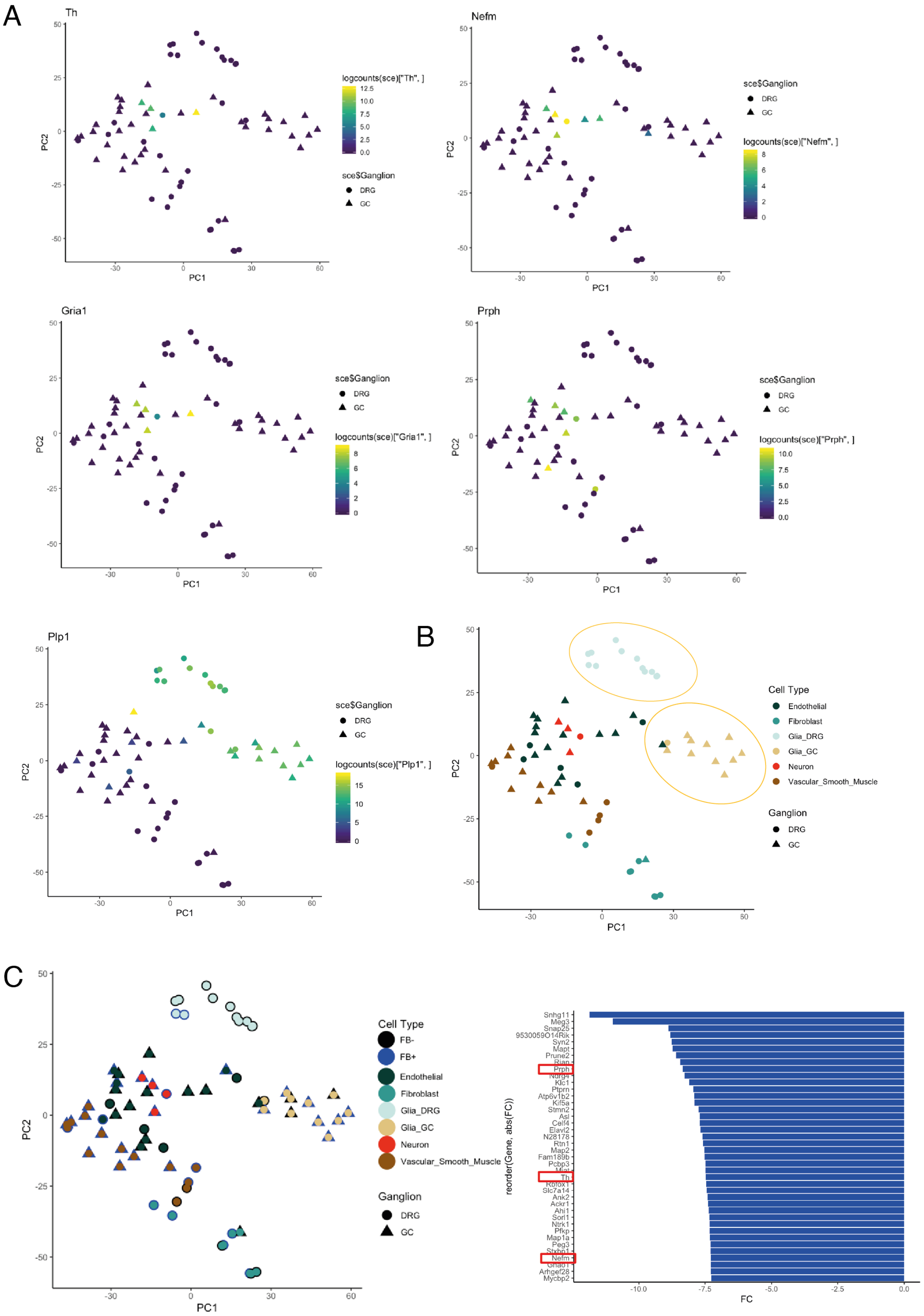

**Supplementary Figure 5: SmartSeq analysis and first annotation results of FB+ and FB- FACS isolated cells.** (A)Marker gene expression of the initial sequenced approach. (B)Annotation of cells based on marker gene expression. (C)Cell type annotation of FB+ and FB- cells and assessment of highest genes expressed, neuronal marker genes highlighted in red.

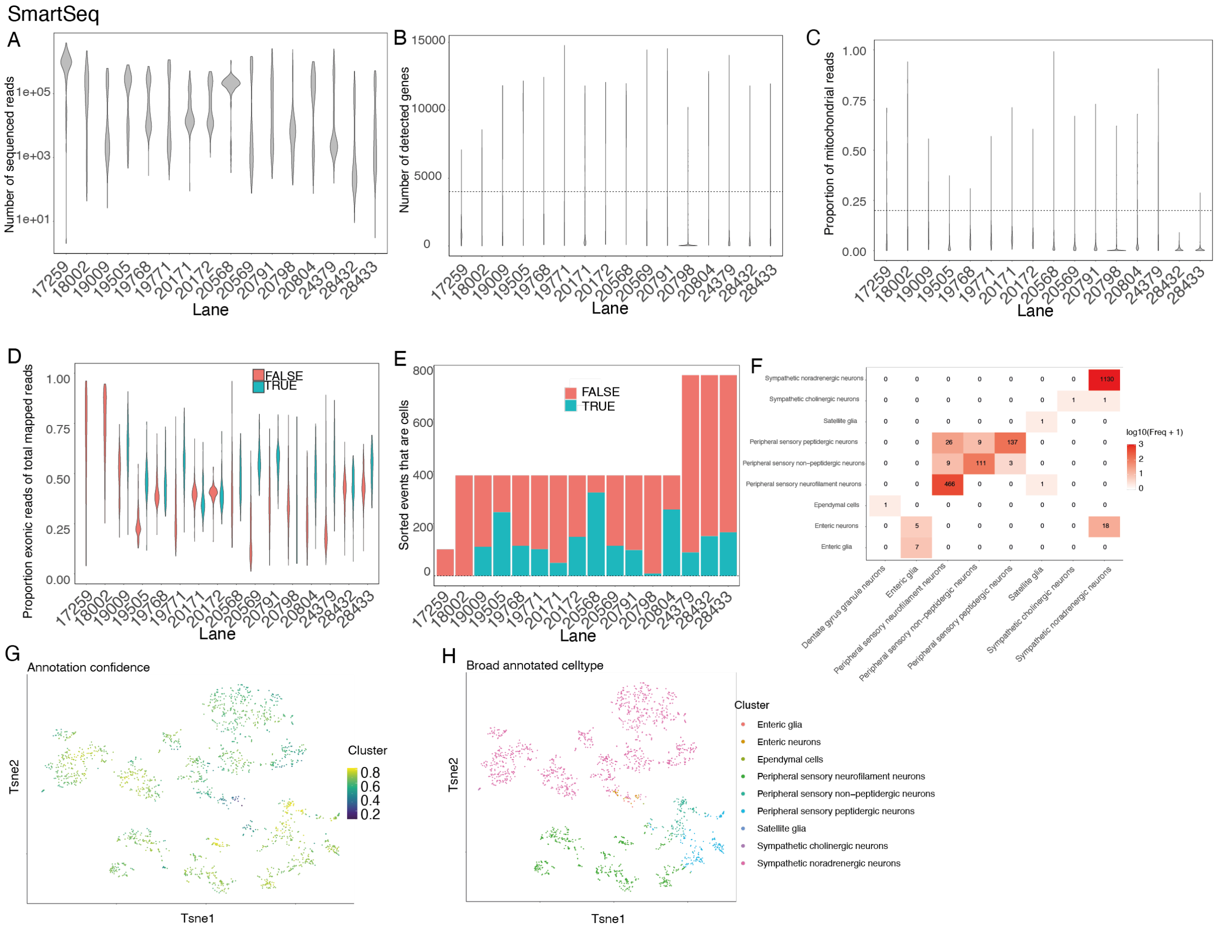

**Supplementary Figure 6: Quality assessment of sequencing results using the SmarSeq2.5 approach.** (A) Number of sequenced reads per lane. (B) Number of detected genes per lane. (C) Proportion of mitochondrial reads. (D) Proportion of exonic reads of total mapped reads. (E) Sorted events that were assigned as cells. (F) Overlay of annotation confidence. (G) t-SNE of all cells plotted for annotation confidence to the Zeisel et al. dataset. (H) Cell type annotation by Zeisel et al.

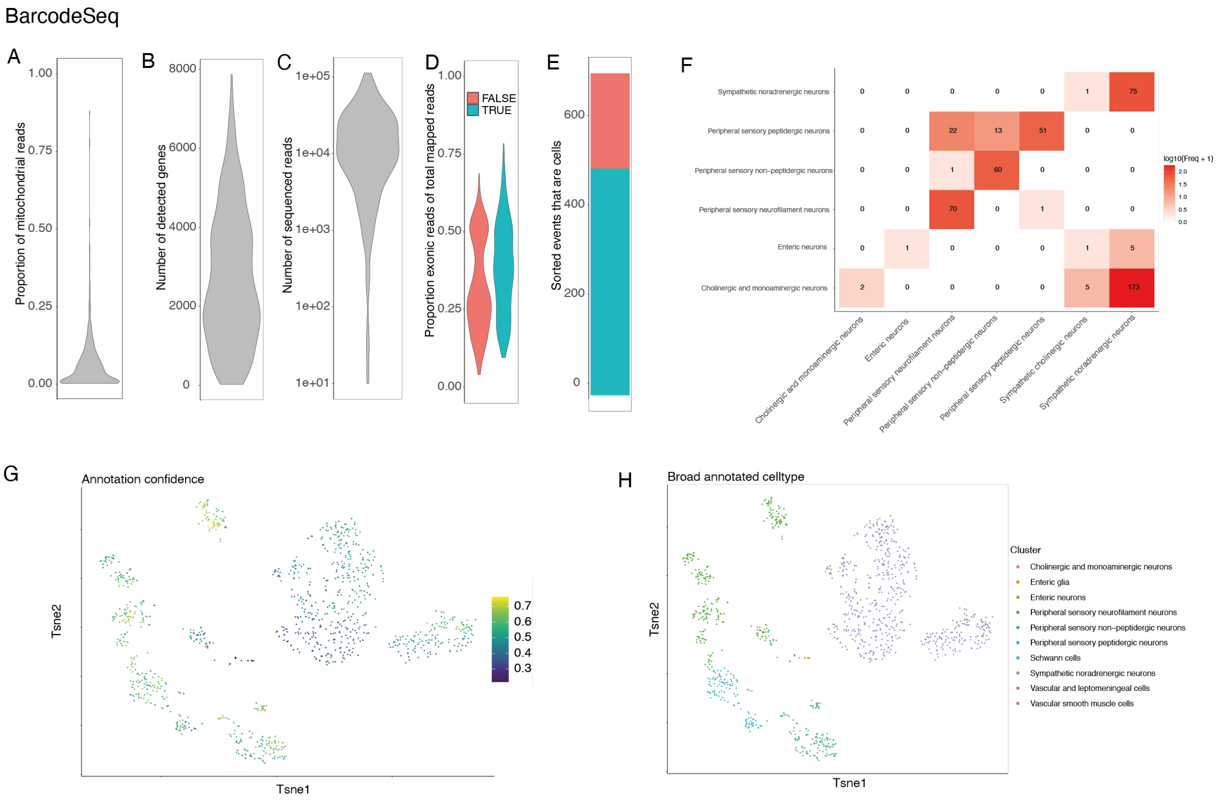

**Supplementary Figure 7: Quality assessment of sequencing results using the BarcodeSeq approach.** (A) Number of sequenced reads per lane. (B) Number of detected genes per lane. (C) Proportion of mitochondrial reads. (D) Proportion of exonic reads of total mapped reads. (E) Sorted events that were assigned as cells. (F) Overlay of annotation confidence. (G) t-SNE of all cells plotted for annotation confidence to the Zeisel et al. dataset. (H) Cell type annotation by Zeisel et al.

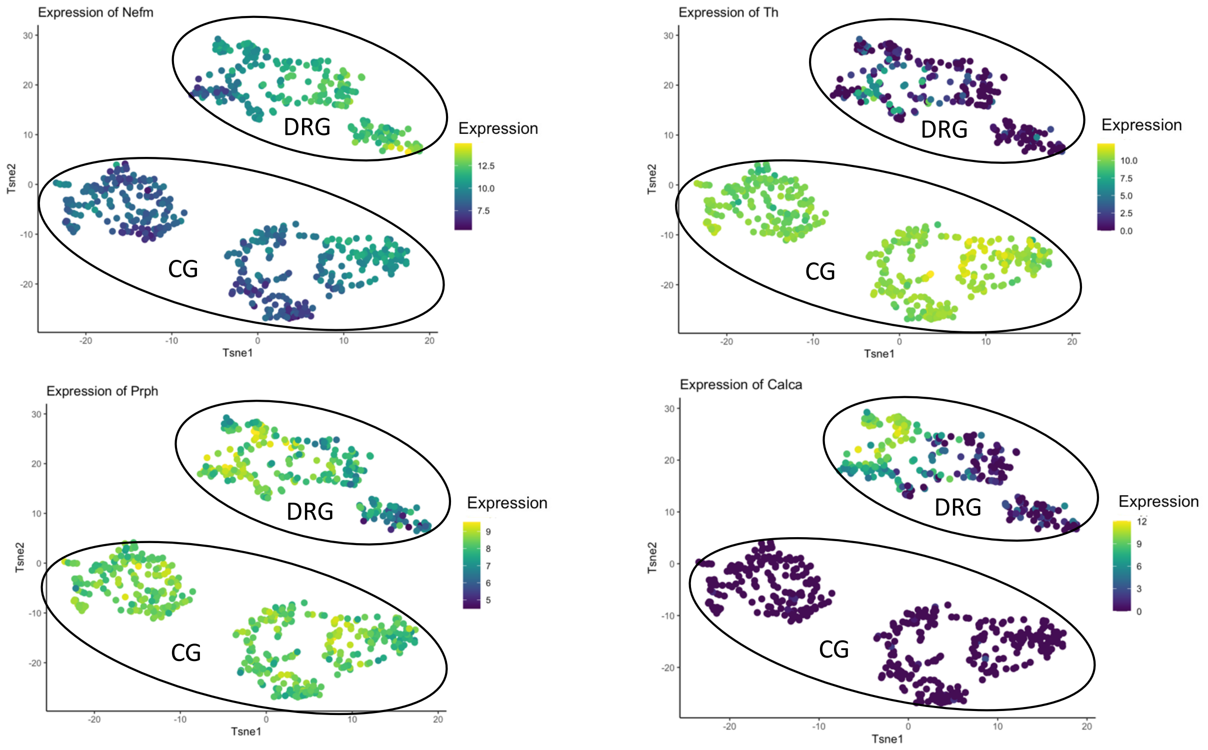

**Supplementary Figure 8: Quality control of sequenced neurons using SmartSeq2.5**. tSNE of NSG and Bl6 CG and DRG neurons plotted for neuronal markers neurofilament (Nefm), peripherin (Prph) as pan-neuronal marker and Th as sympathetic CG marker and Calca as sensory DRG marker.

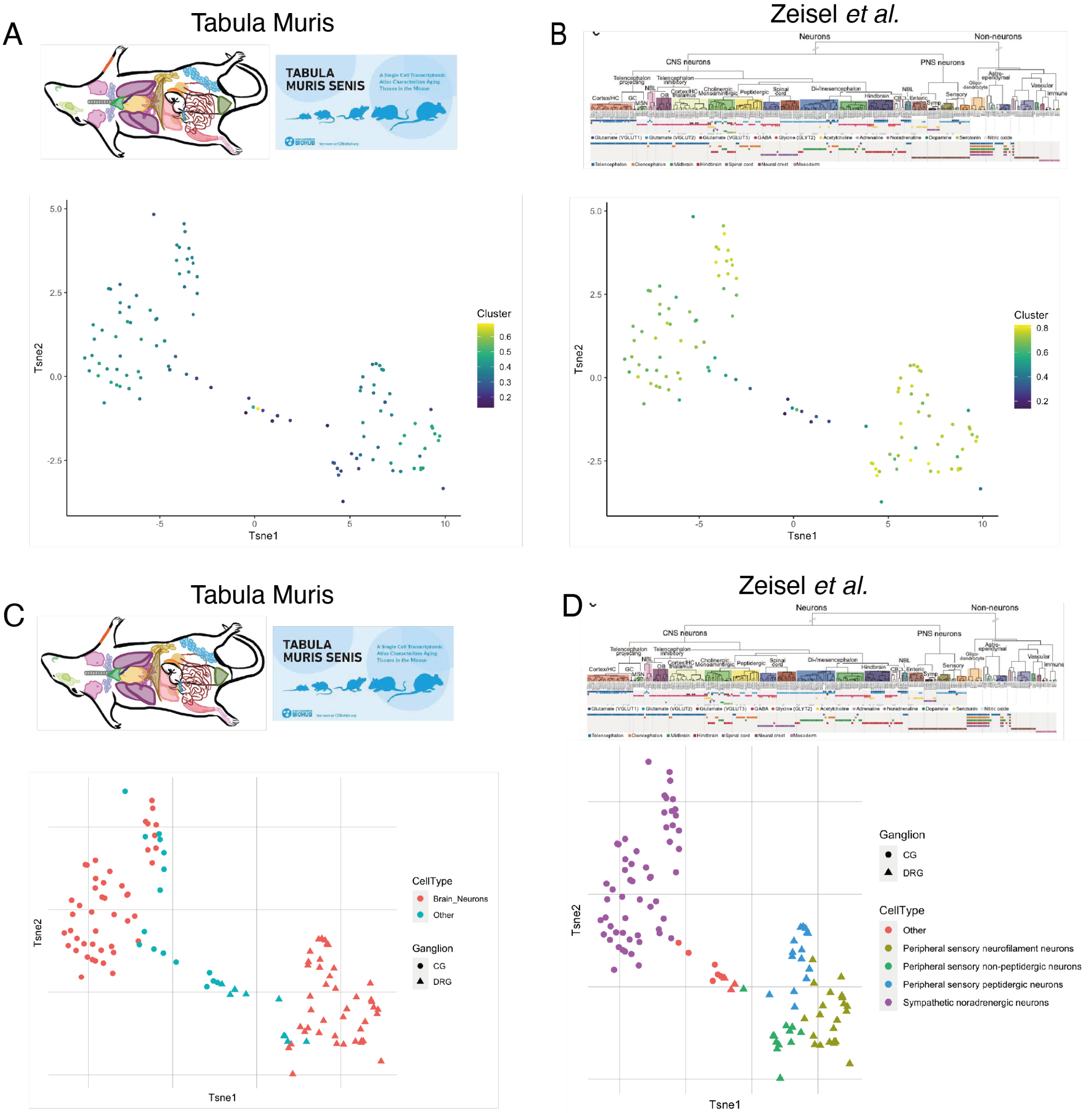

**Supplementary Figure 9: Cell Type annotation comparison of Tabula muris and Zeisel et al. (A)** tSNE of annotation confidence of neurons annotated by Tabula muris. (B)tSNE of annotation confidence of neurons annotated by Zeisel et al. (C) tSNE of cell annotation of neurons annotated by Tabula muris. (D) tSNE of annotation cell annotation of neurons annotated by Zeisel et al.

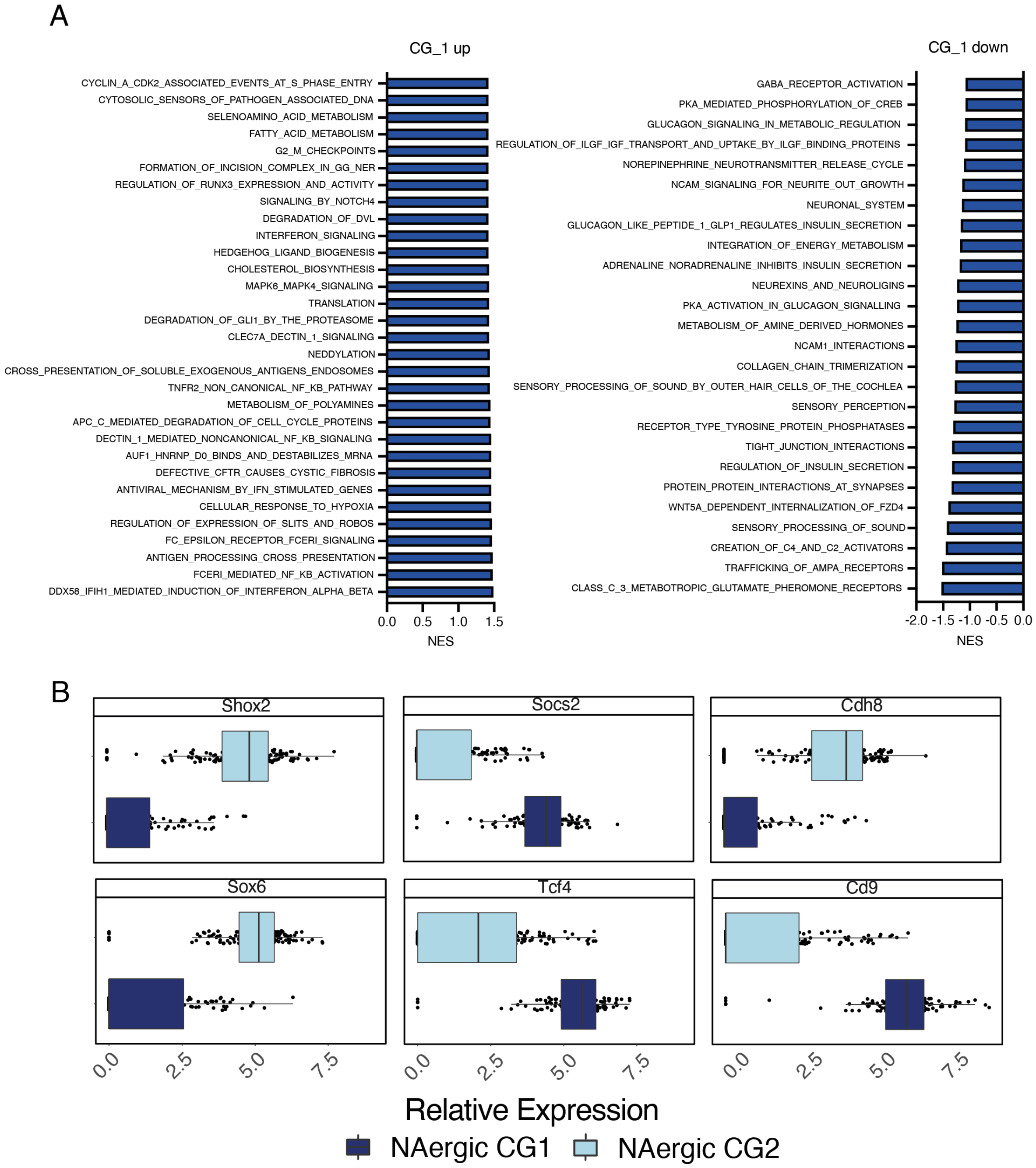

**Supplementary Figure 10: Gene expression based stratification of sympathetic CG Cluster types.** (A) GSEA, differential expression and transcription factor analysis between clusters NAergic CG1 and NAergic CG2. (B) Relative expression of marker genes defining CG clusters.

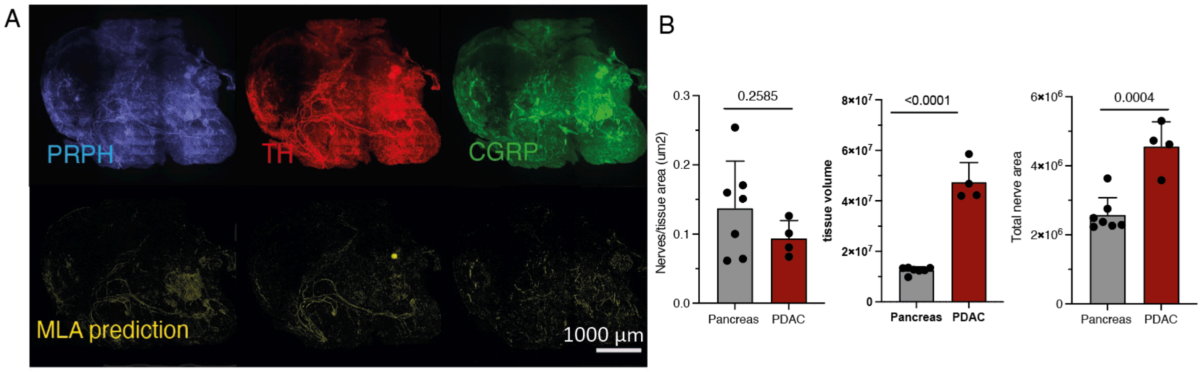

**Supplementary Figure 11: Increased sprouting of PDAC innervating Neurons.** (A) Different channels of the pan-neuronal marker PRPH (blue), sympathetic marker TH (red) and sensory marker CGRP (green) imaged by light sheet microscopy were predicted using MLA (yellow). (B) (F) 3D to 2D quantification of neuronal sprouting by Nerve/tissue and total nerve area in pancreas (n=7) and PDAC (n=4) innervating neurons using MLA of light sheet microscopy images. 1. Nerve/tissue area. 2. Increase in tissue size. 3. Total nerve area prediction. Upaired t-test. Mean +/- SD is shown.

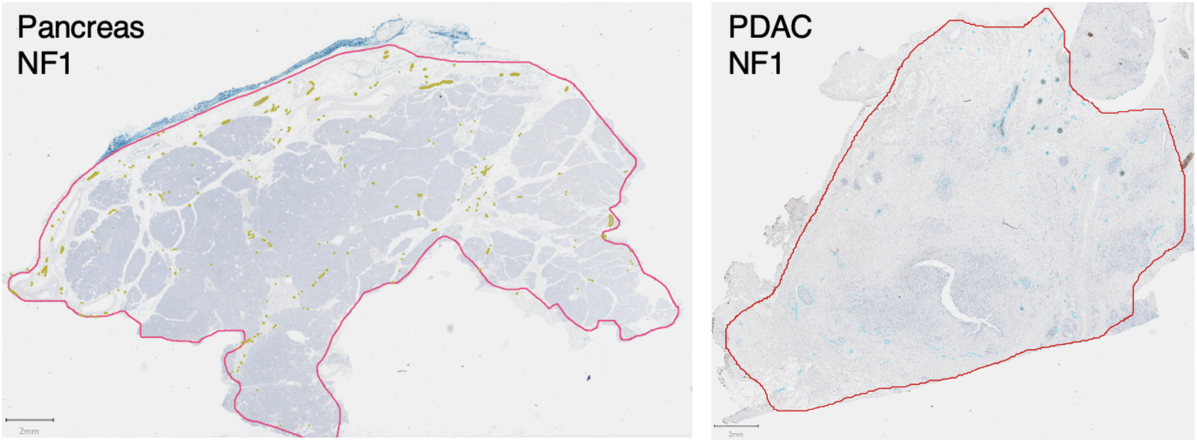

**Supplementary Figure 12: Increased Innervation in human PDAC compared to healthy pancreatic tissue.** Representative images of human IHC (NF1 stained) of healthy pancreas and PDAC specimen.

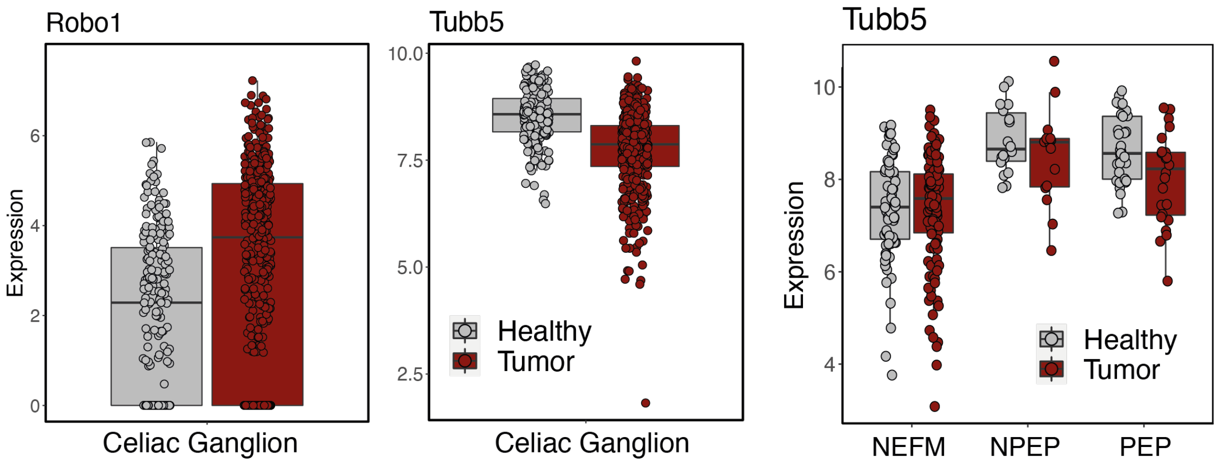

**Supplementary Figure 13: Relative gene expression of Robo and Tubb in pancreas and PDAC neurons.** Relative expression in the CG and DRG (between subtypes) plotted per cell.

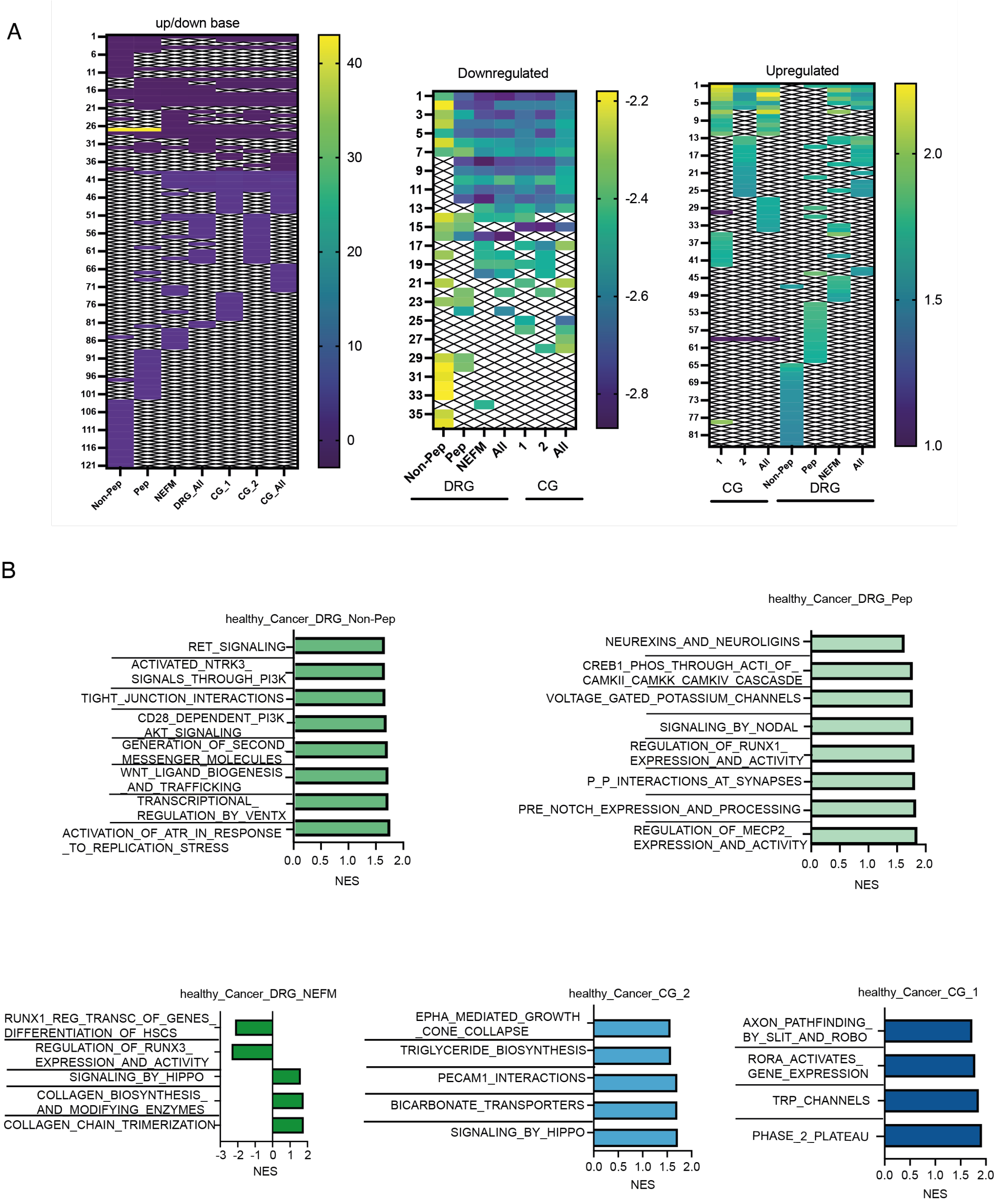

**Supplementary Figure 14: Gene Enrichment Analysis pancreas and PDAC neurons.** (A)GSEA analysis of shared up and downregulated genesets between subclusters. (B)GSEA analysis of top upregulated genesets in PDAC detected in CG or DRG subclusters. All differentially expressed genes were pre-ranked based on t-value. NES, normalized enrichment score;

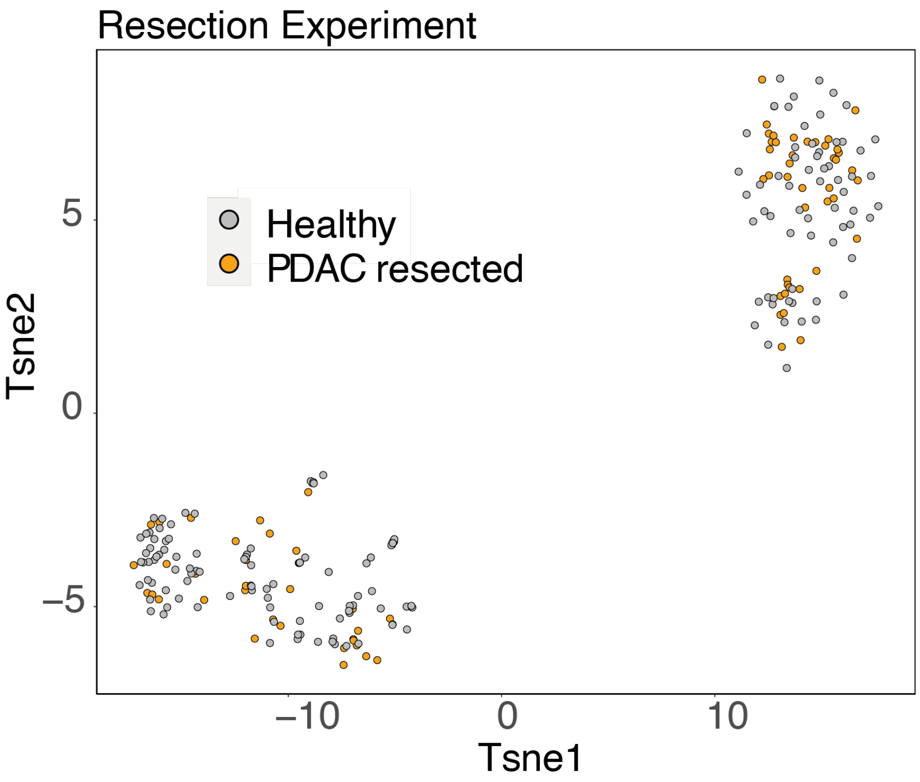

**Supplementary Figure 15: Resected and sham-operated control neuros.** tSNE of CG and DRG neurons after tracing from resected primary tumor material in comparison to healthy sham operated traced neurons from the pancreas (n=6 mice per group).

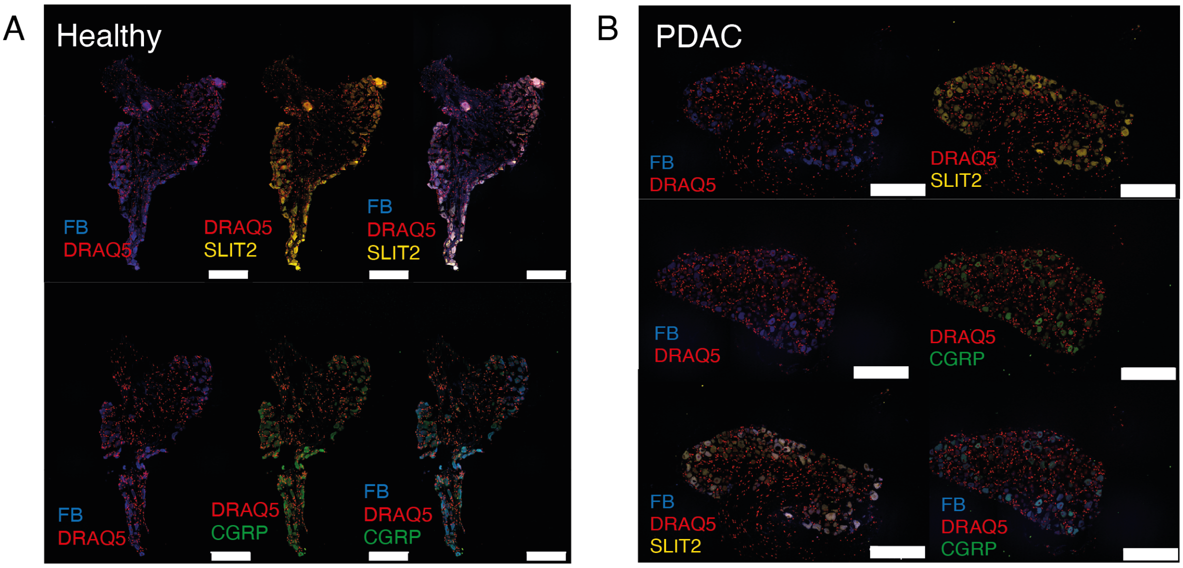

**Supplementary Figure 16: Subtype-specific marker protein expression between healthy pancreas and PDAC ganglia.** IF staining of FB traced healthy pancreas or PDX-DRG ganglia for SLIT2 (yellow) and CGRP (green) scale bar 200 (healthy)/100 (PDX) µm Nuclear stain Draq5 (red) (A) IF of FB (blue) traced DRG for NEFM marker SLIT2 and NPEP marker CGRP from healthy mice (n=4) Scale bar 200 µm. (B)IF of FB (blue) traced DRG for NEFM marker SLIT2 and NPEP marker CGRP from PDAC mice (n=4) Scale bar 100 µm

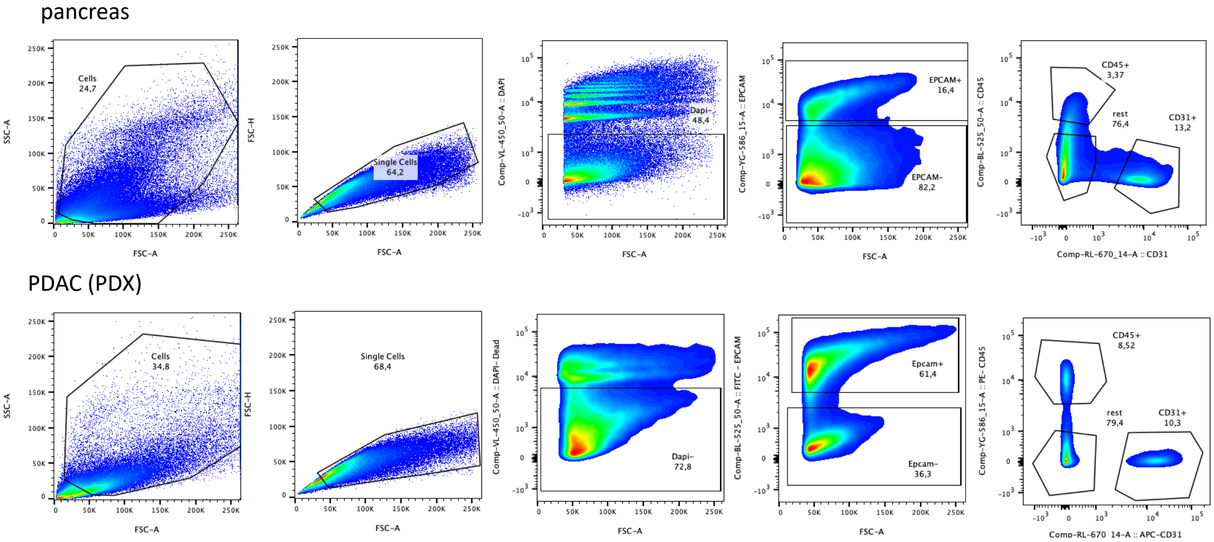

**Supplementary Figure 17: Representative FACS scheme of pancreas and PDAC tissue.** Pancreas and PDAC tissue were dissociated as described in the methods and stained for EPCAM, CD45, CD31 and DAPI. According to the gating scheme Cells were for the different proportions of cells (n=3 mice combined).

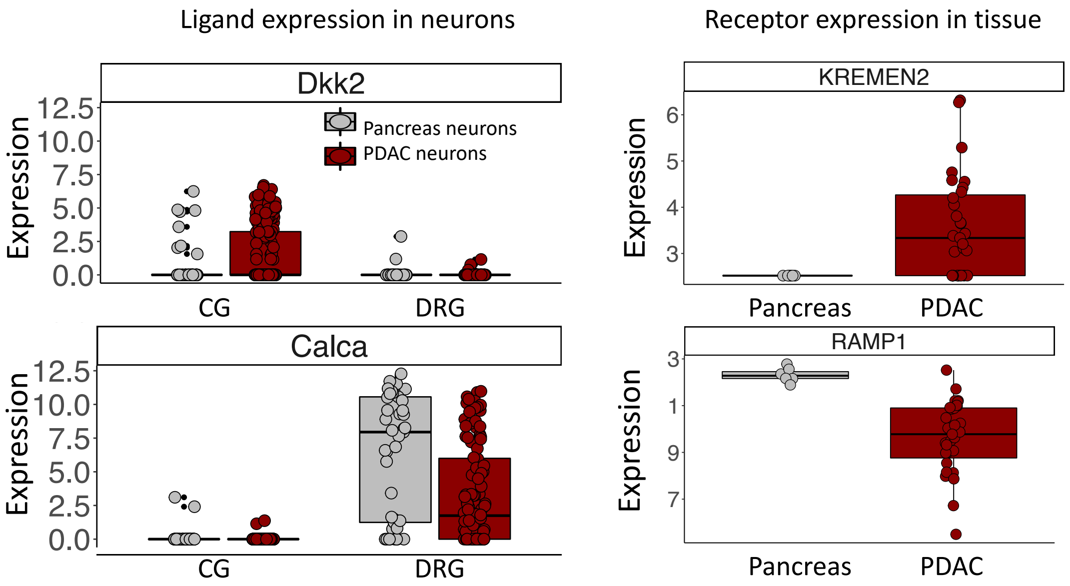

**Supplementary Figure 18: Ligand-receptor expression in pancreas/PDAC neurons and corresponding ligand/receptor in human healthy pancreas and PDAC tissue.** Left the expression of ligands (Dkk2, Calca) in pancreas and PDAC neurons is shown and left the corresponding receptor expression (Kremen2, Ramp1) in human samples of the healthy pancreas an PDAC pre-sorted for EPCAM+ cells (by Elisa Espinet). Mean +/- SD is shown

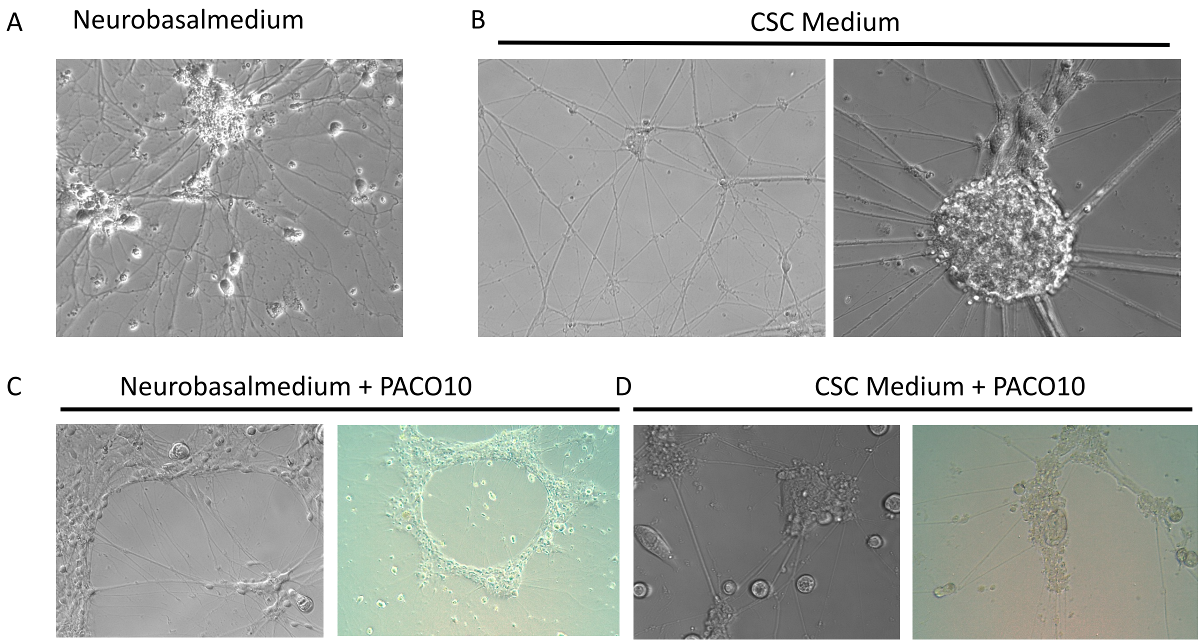

**Supplementary Figure 19: in vitro cultivation of mouse ganglia.** Ganglia were dissected, washed and put in a fine matrigel layer in 24 well plates. They were either cultured with (A)neurobasal medium or (B)CSC medium and outgrowth was assessed and in vitro neurons were co-cultured with PACO cells in (C)Neurobasal medium or (D)CSC medium.

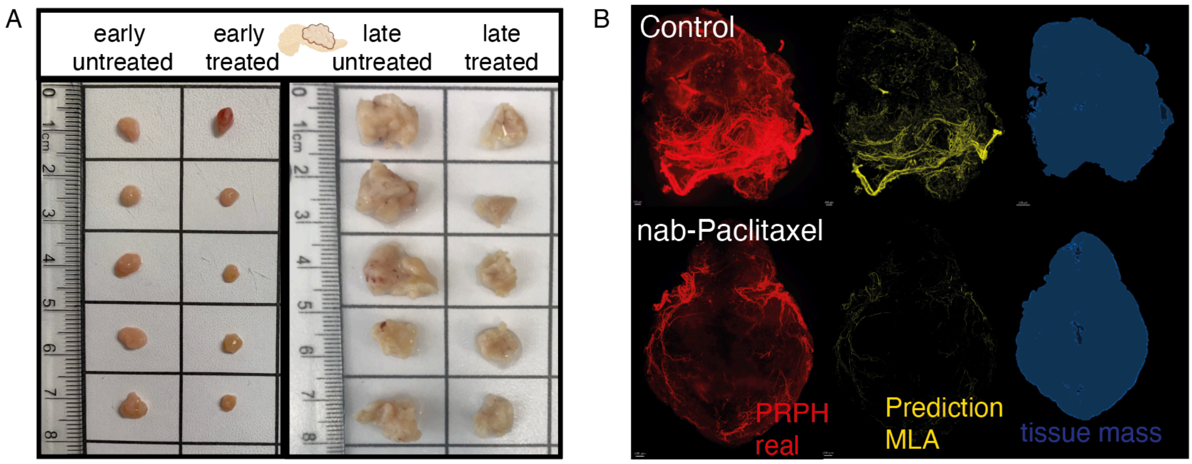

**Supplementary Figure 20: Nab-Paclitaxel reduces tumor growth and neuronal innervation**. Mice were intrapancreatic injected with PACO PDAC cells and either treated with 100mg/kg Nab-Paclitaxel or the vehicle control. Tumor size was assessed after 2 cycles (early) and after 4 cycles (late, methods)(n=5 per group). (A) Tumor size is displayed at early and late stage to corresponding controls. (B) Light sheet microscopy imaging and MLA based prediction of neuronal innervation.

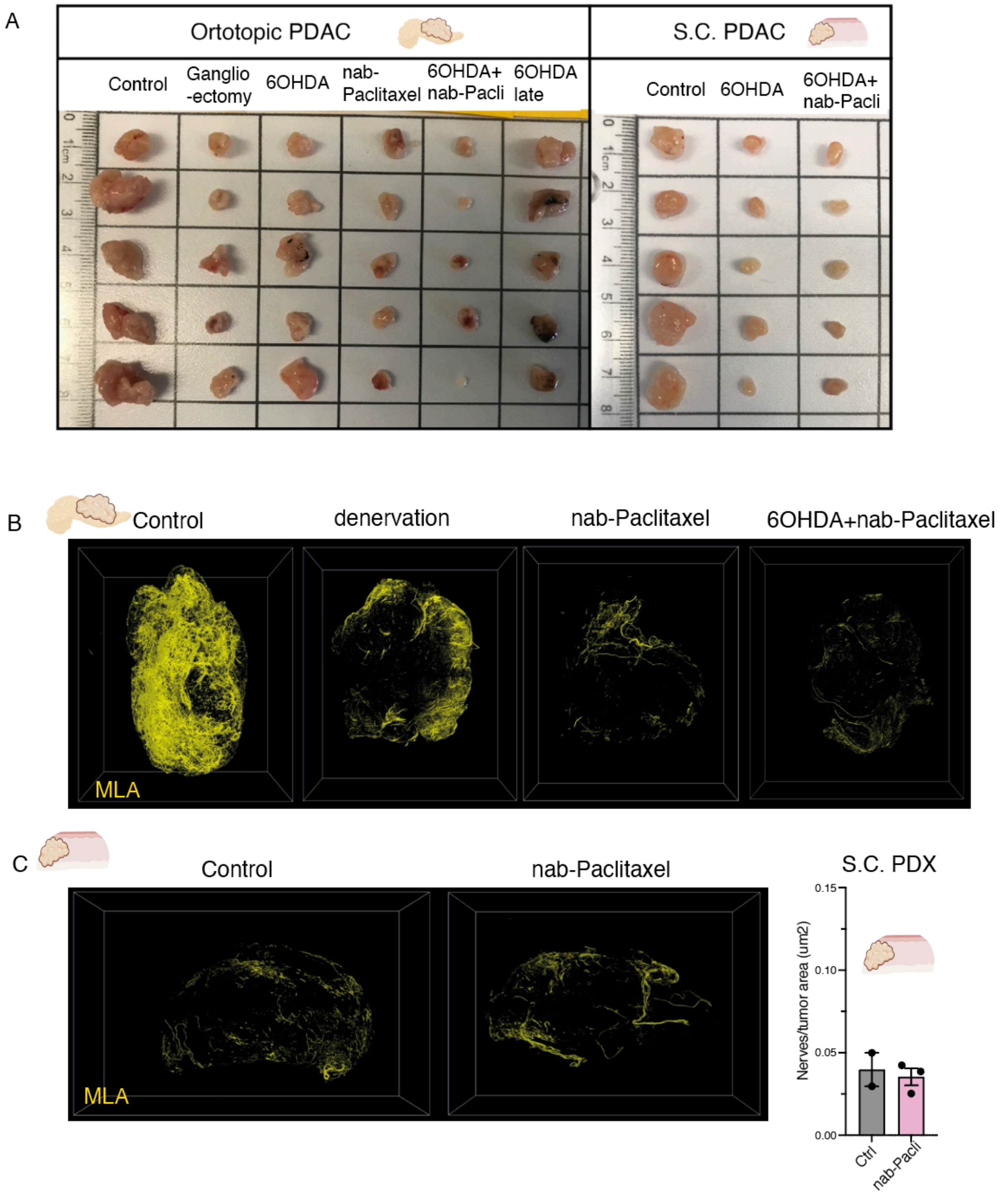

**Supplementary Figure 21: Treatment effect on tumor size and innervation.** (A) Tumor size of orthotopically and subcutaneous PDX after Nab-Paclitaxel, denervation and co-treatment. Mice (n=5 per group) were injected either intrapancreatic or subcutaneous with PACO10 cells . Mice were either denervated prior to cell injection or vehicle treated and further treated with vehicle controls or Nab-Paclitaxel treatment (100mg/kg) for 4 cycles. Tumor size was assessed. (B) Representative MLA based prediction of orthotopical PDAC samples upon different treatment (denervation, nab-paclitaxel and combi)based on light sheet microscopy imaging (C) Representative MLA based prediction of subcutaneous PDAC samples in control and nab-Paclitaxel treated mice based on light sheet microscopy imaging and MLA based (3D to 2D) quantification of nerves per tissue area. Mean +/- SD is shown

# 7 References

1. Siegel, R.L., K.D. Miller, and A. Jemal, *Cancer statistics, 2019.* CA: a cancer journal for clinicians, 2019. **69**(1): p. 7-34.
2. Rahib, L., et al., *Projecting cancer incidence and deaths to 2030: the unexpected burden of thyroid, liver, and pancreas cancers in the United States.* Cancer research, 2014. **74**(11): p. 2913-2921.
3. Haeberle, L. and I. Esposito, *Pathology of pancreatic cancer.* Translational gastroenterology and hepatology, 2019. **4**.
4. Hidalgo, M., *Pancreatic cancer.* New England Journal of Medicine, 2010. **362**(17): p. 1605-1617.
5. Zhou, Q. and D.A. Melton, *Pancreas regeneration.* Nature, 2018. **557**(7705): p. 351-358.
6. Longnecker, D.S., *Anatomy and Histology of the Pancreas (version 1.0).* Pancreapedia: The Exocrine Pancreas Knowledge Base, 2014.
7. Orditura, M., et al., *Pancreatic neuroendocrine tumors: nosography, management and treatment.* International Journal of Surgery, 2016. **28**: p. S156-S162.
8. Landi, S., *Genetic predisposition and environmental risk factors to pancreatic cancer: A review of the literature.* Mutation Research/Reviews in Mutation Research, 2009. **681**(2-3): p. 299-307.
9. Midha, S., S. Chawla, and P.K. Garg, *Modifiable and non-modifiable risk factors for pancreatic cancer: A review.* Cancer letters, 2016. **381**(1): p. 269-277.
10. Board, P.A.T.E., *Pancreatic Cancer Treatment (Adult)(PDQ®): Patient Version.* PDQ Cancer Information Summaries [Internet], 2002.
11. Connor, A.A. and S. Gallinger, *Pancreatic cancer evolution and heterogeneity: integrating omics and clinical data.* Nature Reviews Cancer, 2022. **22**(3): p. 131-142.
12. Hussain, S.P., *Pancreatic cancer: current progress and future challenges.* International journal of biological sciences, 2016. **12**(3): p. 270.
13. McGuigan, A., et al., *Pancreatic cancer: A review of clinical diagnosis, epidemiology, treatment and outcomes.* World journal of gastroenterology, 2018. **24**(43): p. 4846.
14. Siregar, L., et al., *Signet-Ring Cell Carcinoma of the Ampulla of Vater.* The Indonesian Journal of Gastroenterology, Hepatology, and Digestive Endoscopy, 2020. **19**(2): p. 126-129.
15. Klöppel, G., *Neuroendocrine neoplasms: dichotomy, origin and classifications.* Visceral medicine, 2017. **33**(5): p. 324-330.
16. Esposito, I., et al., *Pathology of pancreatic ductal adenocarcinoma: facts, challenges and future developments.* World journal of gastroenterology: WJG, 2014. **20**(38): p. 13833.
17. Saluja, A. and A. Maitra, *Pancreatitis and pancreatic cancer.* Gastroenterology, 2019. **156**(7): p. 1937-1940.
18. Paik, K.Y., et al., *Analysis of liver metastasis after resection for pancreatic ductal adenocarcinoma.* World journal of gastrointestinal oncology, 2012. **4**(5): p. 109.

19. Kanji, Z.S. and S. Gallinger, *Diagnosis and management of pancreatic cancer.* Cmaj, 2013. **185**(14): p. 1219-1226.

20. Amin, M.B., et al., *The eighth edition AJCC cancer staging manual: continuing to build a bridge from a population-based to a more "personalized" approach to cancer staging.* CA: a cancer journal for clinicians, 2017. **67**(2): p. 93-99.

21. Edge, S.B. and C.C. Compton, *The American Joint Committee on Cancer: the 7th edition of the AJCC cancer staging manual and the future of TNM.* Annals of surgical oncology, 2010. **17**(6): p. 1471-1474.

22. Mohammed, S., I. George Van Buren, and W.E. Fisher, *Pancreatic cancer: advances in treatment.* World journal of gastroenterology: WJG, 2014. **20**(28): p. 9354.

23. Basturk, O., et al., *A revised classification system and recommendations from the Baltimore consensus meeting for neoplastic precursor lesions in the pancreas.* The American journal of surgical pathology, 2015. **39**(12): p. 1730.

24. Maitra, A., S.E. Kern, and R.H. Hruban, *Molecular pathogenesis of pancreatic cancer.* Best practice & research Clinical gastroenterology, 2006. **20**(2): p. 211-226.

25. Wolfgang, C.L., et al., *Recent progress in pancreatic cancer.* CA: a cancer journal for clinicians, 2013. **63**(5): p. 318-348.

26. Li, K.-Y., et al., *Pancreatic ductal adenocarcinoma immune microenvironment and immunotherapy prospects.* Chronic diseases and translational medicine, 2020. **6**(01): p. 6-17.

27. Yonezawa, S., et al., *Precursor lesions of pancreatic cancer.* Gut and liver, 2008. **2**(3): p. 137.

28. Conroy, T., et al., *FOLFIRINOX versus gemcitabine for metastatic pancreatic cancer.* New England journal of medicine, 2011. **364**(19): p. 1817-1825.

29. Lee, S. and C. Lee, *Toward advanced neural interfaces for the peripheral nervous system (PNS) and their future applications.* Current Opinion in Biomedical Engineering, 2018. **6**: p. 130-137.

30. Maitra, A. and S.D. Leach, *Disputed paternity: the uncertain ancestry of pancreatic ductal neoplasia.* Cancer cell, 2012. **22**(6): p. 701-703.

31. Kopp, J.L., et al., *Identification of Sox9-dependent acinar-to-ductal reprogramming as the principal mechanism for initiation of pancreatic ductal adenocarcinoma.* Cancer cell, 2012. **22**(6): p. 737-750.

32. Chuvin, N., et al., *Acinar-to-ductal metaplasia induced by transforming growth factor beta facilitates KRASG12D-driven pancreatic tumorigenesis.* Cellular and molecular gastroenterology and hepatology, 2017. **4**(2): p. 263-282.

33. Hruban, R.H., et al., *Progression model for pancreatic cancer.* Clinical cancer research, 2000. **6**(8): p. 2969-2972.

34. Hruban, R.H., A. Maitra, and M. Goggins, *Update on pancreatic intraepithelial neoplasia.* International journal of clinical and experimental pathology, 2008. **1**(4): p. 306.

35. Cohn, I., *Recent progress in pancreatic cancer. Semin.* Ultrasound, 1980. **1**: p. 228-230.

36. Hosoda, W., et al., *Genetic analyses of isolated high-grade pancreatic intraepithelial neoplasia (HG-PanIN) reveal paucity of alterations in TP53 and SMAD4.* The Journal of pathology, 2017. **242**(1): p. 16-23.

37. Waddell, N., et al., *Whole genomes redefine the mutational landscape of pancreatic cancer.* Nature, 2015. **518**(7540): p. 495-501.

38. Silverman, B.R. and J. Shi, *Alterations of epigenetic regulators in pancreatic cancer and their clinical implications.* International journal of molecular sciences, 2016. **17**(12): p. 2138.

39. Provenzano, P.P., et al., *Enzymatic targeting of the stroma ablates physical barriers to treatment of pancreatic ductal adenocarcinoma.* Cancer cell, 2012. **21**(3): p. 418-429.

40. Pothula, S.P., et al., *Key role of pancreatic stellate cells in pancreatic cancer.* Cancer letters, 2016. **381**(1): p. 194-200.

41. Neesse, A., et al., *Stromal biology and therapy in pancreatic cancer: a changing paradigm.* Gut, 2015. **64**(9): p. 1476-1484.

42. Blumenfeld, H., *Neuroanatomy through clinical cases*. 2010: Sinauer Associates Sunderland.

43. Kumar, A. and J.P. Brockes, *Nerve dependence in tissue, organ, and appendage regeneration.* Trends in neurosciences, 2012. **35**(11): p. 691-699.

44. Faulkner, S., et al., *Tumor neurobiology and the war of nerves in cancer.* Cancer discovery, 2019. **9**(6): p. 702-710.

45. Zahalka, A.H. and P.S. Frenette, *Nerves in cancer.* Nature Reviews Cancer, 2020. **20**(3): p. 143-157.

46. Lanigan, L.G., et al., *Comparative pathology of the peripheral nervous system.* Veterinary pathology, 2021. **58**(1): p. 10-33.

47. Jakob, M.O., et al., *An Integrated View on Neuronal Subsets in the Peripheral Nervous System and Their Role in Immunoregulation.* Frontiers in immunology, 2021. **12**: p. 679055.

48. Babic, T. and R.A. Travagli, *Neural control of the pancreas.* Pancreapedia: The Exocrine Pancreas Knowledge Base, 2016.

49. Haberberger, R.V., et al., *Human dorsal root ganglia.* Frontiers in cellular neuroscience, 2019. **13**: p. 271.

50. McCorry, L.K., *Physiology of the autonomic nervous system.* American journal of pharmaceutical education, 2007. **71**(4).

51. Usoskin, D., et al., *Unbiased classification of sensory neuron types by large-scale single-cell RNA sequencing.* Nature neuroscience, 2015. **18**(1): p. 145-153.

52. Bai, Q., et al., *Protein kinase C-α upregulates sodium channel Nav1. 9 in nociceptive dorsal root ganglion neurons in an inflammatory arthritis pain model of rat.* Journal of Cellular Biochemistry, 2020. **121**(1): p. 768-778.

53. Kupari, J., et al., *Single cell transcriptomics of primate sensory neurons identifies cell types associated with chronic pain.* Nature communications, 2021. **12**(1): p. 1510.

54. Renthal, W., et al., *Transcriptional reprogramming of distinct peripheral sensory neuron subtypes after axonal injury.* Neuron, 2020. **108**(1): p. 128-144. e9.

55. Chandran, V., et al., *A systems-level analysis of the peripheral nerve intrinsic axonal growth program.* Neuron, 2016. **89**(5): p. 956-970.

56. Furlan, A., et al., *Visceral motor neuron diversity delineates a cellular basis for nipple- and pilo-erection muscle control.* Nature neuroscience, 2016. **19**(10): p. 1331-1340.

57. Hockley, J.R., et al., *Single-cell RNAseq reveals seven classes of colonic sensory neuron.* Gut, 2019. **68**(4): p. 633-644.

58. Zeisel, A., et al., *Molecular architecture of the mouse nervous system.* Cell, 2018. **174**(4): p. 999-1014. e22.

59. Balood, M., et al., *Nociceptor neurons affect cancer immunosurveillance.* Nature, 2022: p. 1-8.

60. Seijffers, R., C.D. Mills, and C.J. Woolf, *ATF3 increases the intrinsic growth state of DRG neurons to enhance peripheral nerve regeneration.* Journal of Neuroscience, 2007. **27**(30): p. 7911-7920.

61. Sharma, N., et al., *The emergence of transcriptional identity in somatosensory neurons.* Nature, 2020. **577**(7790): p. 392-398.

62. Wang, K., et al., *Single-cell transcriptomic analysis of somatosensory neurons uncovers temporal development of neuropathic pain.* Cell research, 2021. **31**(8): p. 904-918.

63. Meltzer, S., et al., *The cellular and molecular basis of somatosensory neuron development.* Neuron, 2021. **109**(23): p. 3736-3757.

64. Fontaine, A.K., et al., *Optical vagus nerve modulation of heart and respiration via heart-injected retrograde AAV.* Scientific reports, 2021. **11**(1): p. 1-12.

65. Huang, S., et al., *Lymph nodes are innervated by a unique population of sensory neurons with immunomodulatory potential.* Cell, 2021. **184**(2): p. 441-459. e25.

66. Zhao, Q., et al., *A multidimensional coding architecture of the vagal interoceptive system.* Nature, 2022. **603**(7903): p. 878-884.

67. Bejarano, L., M.J. Jordão, and J.A. Joyce, *Therapeutic targeting of the tumor microenvironment.* Cancer discovery, 2021. **11**(4): p. 933-959.

68. Kim, K.J., et al., *Inhibition of vascular endothelial growth factor-induced angiogenesis suppresses tumour growth in vivo.* Nature, 1993. **362**(6423): p. 841-844.

69. Iwai, Y., et al., *Involvement of PD-L1 on tumor cells in the escape from host immune system and tumor immunotherapy by PD-L1 blockade.* Proceedings of the National Academy of Sciences, 2002. **99**(19): p. 12293-12297.

70. Leach, D.R., M.F. Krummel, and J.P. Allison, *Enhancement of antitumor immunity by CTLA-4 blockade.* Science, 1996. **271**(5256): p. 1734-1736.

71. Suvà, M.L. and I. Tirosh, *Single-cell RNA sequencing in cancer: lessons learned and emerging challenges.* Molecular cell, 2019. **75**(1): p. 7-12.

72. Dominguez, C.X., et al., *Single-Cell RNA Sequencing Reveals Stromal Evolution into LRRC15+ Myofibroblasts as a Determinant of Patient Response to Cancer ImmunotherapyCharacterization of TGFβ-activated LRRC15+ CAFs in PDAC.* Cancer discovery, 2020. **10**(2): p. 232-253.

73. Demir, I.E., et al., *Future directions in preclinical and translational cancer neuroscience research.* Nature cancer, 2020. **1**(11): p. 1027-1031.

74. Demir, I.E., et al., *Clinically actionable strategies for studying neural influences in cancer.* Cancer Cell, 2020. **38**(1): p. 11-14.

75. Takahashi, R., H. Ijichi, and M. Fujishiro, *The Role of Neural Signaling in the Pancreatic Cancer Microenvironment.* Cancers, 2022. **14**(17): p. 4269.

76. Renz, B.W., et al., *β2 adrenergic-neurotrophin feedforward loop promotes pancreatic cancer.* Cancer cell, 2018. **33**(1): p. 75-90. e7.

77. Roger, E., et al., *Schwann cells support oncogenic potential of pancreatic cancer cells through TGFβ signaling.* Cell death & disease, 2019. **10**(12): p. 1-19.

78. Wakiya, T., et al., *Roles of the nervous system in pancreatic cancer.* Annals of Gastroenterological Surgery, 2021. **5**(5): p. 623-633.

79. Saloman, J.L., et al., *Ablation of sensory neurons in a genetic model of pancreatic ductal adenocarcinoma slows initiation and progression of cancer.* Proceedings of the National Academy of Sciences, 2016. **113**(11): p. 3078-3083.

80. Molbay, M., et al., *A guidebook for DISCO tissue clearing.* Molecular Systems Biology, 2021. **17**(3): p. e9807.

81. Ueda, H.R., et al., *Tissue clearing and its applications in neuroscience.* Nature Reviews Neuroscience, 2020. **21**(2): p. 61-79.

82. Mai, H., et al., *Whole mouse body histology using standard IgG antibodies.* bioRxiv, 2023: p. 2023.02. 17.528921.

83. LeCun, Y., Y. Bengio, and G. Hinton, *Deep learning.* nature, 2015. **521**(7553): p. 436-444.

84. Yu, Y.-l., et al., *Comparison of commonly used retrograde tracers in rat spinal motor neurons.* Neural Regeneration Research, 2015. **10**(10): p. 1700.

85. Wang, Q., et al., *Systematic comparison of adeno-associated virus and biotinylated dextran amine reveals equivalent sensitivity between tracers and novel projection targets in the mouse brain.* Journal of Comparative Neurology, 2014. **522**(9): p. 1989-2012.

86. Kristensson, K. and Y. Olsson, *Retrograde axonal transport of protein.* Brain research, 1971. **29**(2): p. 363-365.

87. Van Der Kooy, D., H.G. Kuypers, and C.E. Catsman-Berrevoets, *Single mammillary body cells with divergent axon collaterals. Demonstration by a simple, fluorescent retrograde double labeling technique in the rat.* Brain Research, 1978. **158**(1): p. 189-196.

88. Saleeba, C., et al., *A student's guide to neural circuit tracing.* Frontiers in neuroscience, 2019: p. 897.

89. Brockett, A.T., et al., *What Does Medial Frontal Cortex Signal During Behavior? Insights from Behavioral Neurophysiology*. 2021: Academic Press.

90. Yang, J.-H. and A.C. Kwan, *Secondary motor cortex: Broadcasting and biasing animal's decisions through long-range circuits.* International review of neurobiology, 2021. **158**: p. 443-470.

91. Elmentaite, R., et al., *Single-cell atlases: shared and tissue-specific cell types across human organs.* Nature Reviews Genetics, 2022: p. 1-16.

92. Thiel, V., et al., *Trace'n'Seq: Assessing neuronal infiltration and its impact in pancreatic ductal carcinoma.* Cancer Research, 2022. **82**(12_Supplement): p. 3650-3650.

93. Sleigh, J.N., G.A. Weir, and G. Schiavo, *A simple, step-by-step dissection protocol for the rapid isolation of mouse dorsal root ganglia.* BMC research notes, 2016. **9**(1): p. 1-7.

94. Rodriguez-Meira, A., et al., *TARGET-Seq: a protocol for high-sensitivity single-cell mutational analysis and parallel RNA sequencing.* STAR protocols, 2020. **1**(3): p. 100125.

95. Lemos, D.R., et al., *Evidence for circadian regulation of activating transcription factor 5 but not tyrosine hydroxylase by the chromaffin cell clock.* Endocrinology, 2007. **148**(12): p. 5811-5821.

96. Chen, K., K. Gunter, and M.D. Maines, *Neurons overexpressing heme oxygenase-1 resist oxidative stress-mediated cell death.* Journal of neurochemistry, 2000. **75**(1): p. 304-313.

97. Hedlund, E., et al., *Identification of a Hoxd10-regulated transcriptional network and combinatorial interactions with Hoxa10 during spinal cord development.* Journal of neuroscience research, 2004. **75**(3): p. 307-319.

98. Noll, E.M., et al., *CYP3A5 mediates basal and acquired therapy resistance in different subtypes of pancreatic ductal adenocarcinoma.* Nature medicine, 2016. **22**(3): p. 278-287.

99. Wang, X.-W., et al., *Lin28 signaling supports mammalian PNS and CNS axon regeneration.* Cell reports, 2018. **24**(10): p. 2540-2552. e6.

100. Madabhushi, R., et al., *Activity-induced DNA breaks govern the expression of neuronal early-response genes.* Cell, 2015. **161**(7): p. 1592-1605.

101. Cheng, Y.-C., et al., *Topoisomerase I inhibition and peripheral nerve injury induce DNA breaks and ATF3-associated axon regeneration in sensory neurons.* Cell reports, 2021. **36**(10): p. 109666.

102. Bouilloux, F., et al., *Loss of the transcription factor Meis1 prevents sympathetic neurons target-field innervation and increases susceptibility to sudden cardiac death.* Elife, 2016. **5**: p. e11627.

103. Philippidou, P., et al., *Sustained Hox5 gene activity is required for respiratory motor neuron development.* Nature neuroscience, 2012. **15**(12): p. 1636-1644.

104. Ceyhan, G.O., et al., *Pancreatic pain.* Best Practice & Research Clinical Gastroenterology, 2008. **22**(1): p. 31-44.

105. Liu, Q., et al., *Transcriptional Alterations of Mouse Trigeminal Ganglion Neurons Following Orofacial Inflammation Revealed by Single-Cell Analysis.* Frontiers in Cellular Neuroscience, 2022. **16**.

106. Tanaka, M., et al., *Meta-analysis of recurrence pattern after resection for pancreatic cancer.* Journal of British Surgery, 2019. **106**(12): p. 1590-1601.

107. Loos, M., et al., *Surgical treatment of pancreatic cancer.* Annals of the New York Academy of Sciences, 2008. **1138**(1): p. 169-180.

108. Tummers, W., et al., *Impact of resection margin status on recurrence and survival in pancreatic cancer surgery.* Journal of British Surgery, 2019. **106**(8): p. 1055-1065.

109. Hishinuma, S., et al., *Patterns of recurrence after curative resection of pancreatic cancer, based on autopsy findings.* Journal of gastrointestinal surgery, 2006. **10**(4): p. 511-518.

110. Ceyhan, G.O., et al., *Pancreatic neuropathy and neuropathic pain—a comprehensive pathomorphological study of 546 cases.* Gastroenterology, 2009. **136**(1): p. 177-186. e1.

111. Herting, C.J., I. Karpovsky, and G.B. Lesinski, *The tumor microenvironment in pancreatic ductal adenocarcinoma: Current perspectives and future directions.* Cancer and Metastasis Reviews, 2021. **40**(3): p. 675-689.

112. Ho, W.J., E.M. Jaffee, and L. Zheng, *The tumour microenvironment in pancreatic cancer—clinical challenges and opportunities.* Nature reviews Clinical oncology, 2020. **17**(9): p. 527-540.

113. Zhang, T., et al., *Cancer-associated fibroblasts in pancreatic ductal adenocarcinoma.* Cell Death & Disease, 2022. **13**(10): p. 897.

114. Adamska, A., A. Domenichini, and M. Falasca, *Pancreatic ductal adenocarcinoma: current and evolving therapies.* International journal of molecular sciences, 2017. **18**(7): p. 1338.

115. Desai, N., *Nanoparticle albumin-bound paclitaxel (Abraxane®).* Albumin in medicine: Pathological and clinical applications, 2016: p. 101-119.

116. Goldstein, D., et al., *Development of peripheral neuropathy and its association with survival during treatment with nab-paclitaxel plus gemcitabine for patients with metastatic adenocarcinoma of the pancreas: A subset analysis from a randomised phase III trial (MPACT).* European Journal of Cancer, 2016. **52**: p. 85-91.

117. Kulkarni, R., A. Thakur, and H. Kumar, *Microtubule Dynamics Following Central and Peripheral Nervous System Axotomy.* ACS Chemical Neuroscience, 2022. **13**(9): p. 1358-1369.

118. Hubbard, J., *The peripheral nervous system*. 2012: Springer Science & Business Media.

119. Stanley, K.O., et al., *Designing neural networks through neuroevolution.* Nature Machine Intelligence, 2019. **1**(1): p. 24-35.

120. Veerakumar, A., et al., *Molecularly defined circuits for cardiovascular and cardiopulmonary control.* Nature, 2022: p. 1-8.

121. Pan, Y., et al., *NF1 mutation drives neuronal activity-dependent initiation of optic glioma.* Nature, 2021. **594**(7862): p. 277-282.

122. Zeng, Q., et al., *Synaptic proximity enables NMDAR signalling to promote brain metastasis.* Nature, 2019. **573**(7775): p. 526-531.

123. Göhrig, A., et al., *Axon Guidance Factor SLIT2 Inhibits Neural Invasion and Metastasis in Pancreatic CancerSLIT2 Inhibits Metastasis and Invasion of Pancreatic Cancer.* Cancer research, 2014. **74**(5): p. 1529-1540.

124. Li, J., R. Kang, and D. Tang, *Cellular and molecular mechanisms of perineural invasion of pancreatic ductal adenocarcinoma.* Cancer Communications, 2021. **41**(8): p. 642-660.

125. Venkataramani, V., et al., *Glutamatergic synaptic input to glioma cells drives brain tumour progression.* Nature, 2019. **573**(7775): p. 532-538.

126. Hausmann, D., et al., *Autonomous rhythmic activity in glioma networks drives brain tumour growth.* Nature, 2022: p. 1-8.

127. Venkatesh, H.S., et al., *Electrical and synaptic integration of glioma into neural circuits.* Nature, 2019. **573**(7775): p. 539-545.

128. Venkatesh, H.S., et al., *Targeting neuronal activity-regulated neuroligin-3 dependency in high-grade glioma.* Nature, 2017. **549**(7673): p. 533-537.

129. Duebel, J., K. Marazova, and J.-A. Sahel, *Optogenetics.* Current opinion in ophthalmology, 2015. **26**(3): p. 226.

130. Renier, N., et al., *iDISCO: a simple, rapid method to immunolabel large tissue samples for volume imaging.* Cell, 2014. **159**(4): p. 896-910.

131. Espinet, E., et al., *Aggressive PDACs Show Hypomethylation of Repetitive Elements and the Execution of an Intrinsic IFN Program Linked to a Ductal Cell of OriginAutonomous IFN Program in Aggressive Ductal-Derived PDAC.* Cancer discovery, 2021. **11**(3): p. 638-659.

132. Picelli, S., et al., *Full-length RNA-seq from single cells using Smart-seq2.* Nature protocols, 2014. **9**(1): p. 171-181.

133. Waclawiczek, A., et al., *Combinatorial BCL-2 family expression in Acute Myeloid Leukemia Stem Cells predicts clinical response to Azacitidine/Venetoclax.* Cancer Discovery, 2023: p. CD-22-0939.

134. Dobin, A., et al., *STAR: ultrafast universal RNA-seq aligner.* Bioinformatics, 2013. **29**(1): p. 15-21.

135. Putri, G.H., et al., *Analysing high-throughput sequencing data in Python with HTSeq 2.0.* Bioinformatics, 2022. **38**(10): p. 2943-2945.

136. Alpern, D., et al., *BRB-seq: ultra-affordable high-throughput transcriptomics enabled by bulk RNA barcoding and sequencing.* Genome biology, 2019. **20**(1): p. 1-15.

137. McCarthy, D.J., et al., *Scater: pre-processing, quality control, normalization and visualization of single-cell RNA-seq data in R.* Bioinformatics, 2017. **33**(8): p. 1179-1186.

138. Aran, D., et al., *Reference-based analysis of lung single-cell sequencing reveals a transitional profibrotic macrophage.* Nature immunology, 2019. **20**(2): p. 163-172.

139. Haghverdi, L., et al., *Batch effects in single-cell RNA-sequencing data are corrected by matching mutual nearest neighbors.* Nature biotechnology, 2018. **36**(5): p. 421-427.

140. Cabello-Aguilar, S., et al., *SingleCellSignalR: inference of intercellular networks from single-cell transcriptomics.* Nucleic Acids Research, 2020. **48**(10): p. e55-e55.

# 8 List of Abbreviations

| | |
|---|---|
| % | percent |
| °C | degree Celsius |
| µg | Microgramm |
| µL | Microliter |
| µM | Micromolar |
| µm | Micrometer |
| ANOVA | analysis of variance |
| B6/Bl6 | C57BL/6J MICE |
| CTB | Cell Titer Blue |
| CG | Celiac Ganglion |
| CG1 | Celiac Ganglion Cluster 1 |
| CG2 | Celiac Ganglion Cluster 2 |
| CNS | central nervous system |
| CN | Cancer-nerve signature |
| d | days |
| DAPI | 4′,6-Diamidin-2-phenylindol |
| DMSO | Dimethyl Sulfoxide |
| DN | Double Negative |
| DNA | Deoxyribonucleic Acid |
| DRG | Dorsal Root Ganglion |
| EDTA | Ethylenediaminetetraacetic Acid |
| EPO | Electroporation (mouse model) |
| FACS | Fluorescence-activated cell sorting |
| FB | Fast Blue |
| FCS | Fetal Calf Serum |
| FDA | Federal Drug Administration |
| FSC-A | Forward Scatter Area |
| FSC-H | Forward Scatter Height |

| | |
|---|---|
| fwd | Forward |
| GAPDH | Glycerinaldehyd-3-phosphat Dehydrogenase |
| GFP | green fluorescent protein |
| h | Hours |
| HBS | HEPES Buffered Saline |
| HEK | Human Embryonic Kidney |
| HEPES | 4-(2-Hydroxyethyl)-1-Piperazineethanesulfonic Acid |
| HI-STEM | Heidelberg Institute for Stem Cell Technology and Experimental Medicine |
| HK | Housekeeping |
| IC50 | half-maximal inhibitory concentration |
| IF | Immunofluorescence |
| IU | Infectious Units |
| KD | Knockdown |
| l | Liter |
| L-glut | L-Glutamine |
| M | Molar |
| min | Minutes |
| ml | Milliliter |
| MLA | mashine-learning algorithm |
| MOI | Multiplicity of Infection |
| MOPS | 3-(N-Morpholino) Propanesulfonic Acid |
| mRNA | messenger RNA |
| NaCl | Natrium Chloride |
| NAergic | Noradrenergic |
| NEFM | Neurofliament |
| NGS | Next Generation Sequencing |
| NPEP | non-peptidergic |
| NSG | NOD.Cg-$Prkdc^{scid}$ $Il2rg^{tm1Wjl/SzJ}$ |
| nM | Nanomolar |
| ns | not significant |

| | |
|---|---|
| NT | Non-Trageting |
| O/N | Over Night |
| PACO | Primary Pancreatic Adenocarcinoma |
| PCR | Polymerase chain reaction |
| PEP | Peptidergic |
| PDAC | Pancreatic Ductal Adenocarcinoma |
| PDX | patient derived xenografts |
| PNS | peripheral nervous system |
| P/S | Penicillin-Streptomycin |
| PBS | Phosphate Buffered Saline |
| p-value | Probability Value |
| rcf | Relative Centrifugal Force |
| rev | Reverse |
| RNA | Ribonucleic Acid |
| rpm | Rounds per Minute |
| RT | Room Temperature |
| QRT-PCR | Real Time Quantitative Polymerase Chain Reaction |
| s | Second |
| SD | Standard Deviation |
| WHO | World health organization |
| WT | Wildtype |

# 9 List of Figures

# 10 List of Supplement

# 11 Contributions

## 11.1 Trace-n-seq deciphers identity and reprogramming of pancreatic cancer infiltrating neurons

Co-authors:

Vera Thiel, Simon Renders, Jasper PantenDaniel Azorin, Nicolas Dross, Katharina Bauer,Vanessa Da Silva Mourato Henriques, Julian Mochayedi, Vanessa Vogel , Corinna Klein, Ornella Kossi, Carsten Müller-Tidow, John Neoptolemos, Thilo Hackert, Oliver Stegle, Duncan Odom, Rienk Offringa, Frank Albrecht Stenzinger, Frank Winkler, Martin Sprick, Andreas Trumpp

The work presented in this thesis was conceptualized and guided by Prof. Dr. Andreas Trumpp and Dr. Martin Sprick and predominantly carried out by myself. I developed the experimental setup of the Trace-n-Seq approach and performed all experiments involving *in vitro* and *in vivo* work (mouse preps, surgeries, treatments, staining, tissue clearing, library preps etc) with some exceptions: Our TAs Corinna Klein assisted in the first intrapancreatic injection and Vanessa Vogel/Ornella Kossi assisted in the IHC and H&E staining. The Pathology Institute Heidelberg (Vanessa Vogel, Dr. Vanessa Henriques, Prof. Dr. Albrecht Stenzinger, Iordanis Ourailidis) analyzed human 2D IHC specimen. Simon Renders assisted with both ideas and FACS and microscopy experiments. Light sheet microscopy imaging was set up with the help of Nicolas Dross at the Nicon Imaging Center and the plasmids for the pancreatic electroporation (EPO) were kindly provided by the group of Prof. Dr. Rienk Offringa.

The bioinformatic analysis was performed by Jasper Panten. I discussed and planned analysis with Simon Renders and Jasper Panten.

For their technical help we would like to thank the DKFZ core facilities for Flow Cytometry, Microscopy, animal facility, Aino-Maija Leppa and special thanks to Katharina Bauer from the single cell open Lab (assisted in the setting up of the robot-assisted SmartSeq Library (384 well plate) preparation).

This main project of the thesis is currently being compiled into a manuscript. We aim to submit to *Nature* in April 2023.

## 11.2 Interactive machine learning analysis of cleared tissues images using light sheet fluorescence microscopy

Co-authors:

Vera Thiel, Daniel Azorin, Nicolas Dross, Wolfgang Wick, Martin Sprick, Frank Winkler, Andreas Trumpp

The work presented in this thesis includes the analysis and quantification of full tissue cleared healthy organs (specifically pancreas) in comparison to tumor samples. I performed all organ/tumor preparation and tissue clearing and MLA based quantification was carried out by Daniel Azorin. Data and methodology were discussed between me and Daniel Azorin. Nicolas Dross assisted in setting up the light sheet microscopy imaging and performed image rendering.

This secondary part of the thesis is currently compiled into a manuscript. We aim to submit to *Nature Methods* in August 2023.

## 11.3 Additional projects

### 11.3.1 Identifying novel drug resistance in PDAC

In a secondary PhD project, I assessed BRCAness related resistance mechanism to Parp-inhibitors like Olaparib in PDAC. The work was carried out by myself with some help from Jonas Schwickert. Since January 2023 my master student Jianing Zhang continues to work on the same project. We aim to complete the work by the end of 2023.

### 11.3.2 Proteomic characterization reveals CYP2S1 as a mediator of drug resistance in PDAC

Co-authors:

Wiebke M. Nadler, Vera Thiel, Alexander Kerner, Bernd Klaus, Laura Kuhlmann, Manuel Reitberger, Elisa Noll, Nathalia A. Giese, Hsi-Yu Yen, Katja Steiger, Vanessa Vogel, Corinna Klein, Thilo Hackert, Ronald Koschny, Christiane A. Opitz, Wilko Weichert, Andreas Trumpp, Martin R. Sprick and Christoph Rösli

In the transition from master to PhD I continued working on CYP2S1 mediated resistance to SN-38 in PDAC. Wiebke Nadler analyzed the proteomic profile in PDAC cell lines representing the different subtypes. In the HNF1A+ subtype, the levels of various biotransformation proteins were upregulated, like CYP2S1, which I showed is inducible by SN38 and functionally analyzed CYP2S1 mediated metabolism of the drug. During my PhD, I continued and finished this project.

The manuscript is currently in the re-submission process.

## 11.4 Co-authorships during the PhD

1. Waclawiczek, A. …**Thiel, V**….et al. BCL-2 family expression in Acute Myeloid Leukemia Stem Cells predicts clinical response to Azacitidine/Venetoclax. Cancer Discov. (2023).

2. Espinet, E. …**Thiel, V**….et al. Aggressive PDACs Show Hypomethylation of Repetitive Elements and the Execution of an Intrinsic IFN Program Linked to a Ductal Cell of Origin. Cancer Discov. 11, 638–659 (2021).

3. Demir, I. E. …**Thiel, V**….et al. Future directions in preclinical and translational cancer neuroscience research. Nat. Cancer 1, 1027–1031 (2020).

4. Demir, I. E. …**Thiel, V**….et al. Clinically Actional Strategies for Studying Neural Influences in Cancer. Cancer Cell (2020).

# 12 Acknowledgements

'No one can whistle a symphony. It takes an orchestra to play it.' (H.E. Luccock). Completing a PhD is like conducting an amazing concert - it takes the talent and hard work of many people to make it a success. I am incredibly grateful to everyone who played a part in making my PhD journey the best it could have been. You rock!!!

I would like to express my deepest gratitude to my two amazing bosses, **Prof. Dr. Andreas Trumpp** and **Dr. Martin Sprick**, for your unwavering support and guidance throughout this project. Your knowledge, expertise, and creativity have been invaluable in shaping my research and pushing me to achieve my best. Moreover, both of you made sure to create a friendly and fun atmosphere not just during work but also at conferences and parties, which made our time together even more enjoyable.

Many thanks to **Martin Sprick** for giving me the freedom to develop my own PhD project, that you always had an open door and could discuss science and other topics like the “marble mating machine”. Your constant positive atmosphere is highly appreciated.

I am deeply grateful to **Andreas Trumpp**, not only for providing me with the great opportunity to pursue my PhD at HI-STEM, but also for supporting my rather unconventional research area. Your enthusiasm for science, as well as social events, made my research experience more enjoyable beyond a normal work environment.

I would like to express my gratitude to **Prof. Dr. Ingrid Lohman** and **Prof. Dr. Albrecht Stenzinger** for serving as members of both my TAC and defense committee. Additionally, I would like to thank **PD. Dr. Karin Müller-Decker** for joining my defense committee. Thank you so much for taking the time to participate and for your positive feedback.

I would like to express my heartfelt gratitude to all the core facilities, including FACS, microscopy, animal facility, sc-Open lab and Nikon Imaging Center, for their invaluable support during this work. I would like to extend special thanks to **Katharina Bauer** and **Nicolas Dross**, without whose contributions this project would not have been possible.

I also want to thank my wonderful colleagues in the entire **METICS** group and technicians, specifically **Corinna Klein, Vanessa Vogel** and **Ornella Kossi** who have been instrumental in this research. Their hard work, dedication, and expertise have been crucial in ensuring the success of this project.

I would like to extend my sincere thanks to all the colleagues and friends who supported me throughout my PhD. Their insights, feedback, and enthusiasm have been a great source of inspiration, and I have learned so much from them. I am especially grateful to **Simon Renders** and **Jasper Panten**, my partners in crime for this project. Thank you both for your help and the wonderful times we spent working on the project, as well as the many nonsense talks we shared in between. **Simon**, I appreciate your never-ending positivity and all the idea-sharing over carrot or cheesecake. You are not only a colleague but also a good friend. **Jasper**, thank you not only for analyzing all the project's data but also for being a great friend for the past 12 years.

I would also like to express my heartfelt gratitude to all the friends I have made during my time at HI-STEM and DKFZ. Without their support and camaraderie, my PhD journey would not have been as enjoyable and fulfilling. Whether it was sharing a coffee break or dancing in the cell culture room, they always created a welcoming and positive atmosphere that made me look forward to coming to work every day. I want to acknowledge all the amazing people with whom I spent significant time. Big thanks to **Felix Geist, Andrea Barnert** (now Geist), **Lisa Becker, Kristin Decker, Pia Sommerkamp, Manuel Reitberger and Sarah-Jane Neubert.** All of you were part of the reason that made me decide to stay at HI-STEM. **Sarah**, I remember the first day I met you and deeply appreciate the friendship that began on that day and has lasted since. I will never forget our dance sessions and time that we spent together in the US. You are a great friend on whom I can always rely.

Special thanks to **Shub (Shubhankar Sood)** for your amazing “honeyness” and for being the most positive human I know, for all the cooking, dance nights, drinks, and deep talks we enjoyed over the years.

I also want to thank the entire lunch crew (who joined me to have lunch at 11:30 a.m.), whose positivity and funniness always made my day. I greatly appreciate all the amazing times we had at Happy Hours, Friday drinks, (glüh)wine hikes, party nights, or any other events we joined together. Big thanks to **Maija-Aino Leppa, Jonas Schwickert, Andreas Narr, Manuel Mastel, Paul Schwerd-Kleine, Tim Vorberg, Carolin Andresen, Tasneem Cheytan** and **Nikolai Schleußner**. You made my time here a daily social event!

My deepest thanks go to the "fun office" or "the other side of the lab" for all the fun times. I can't imagine having a better office than with **Dominik Vonficht, Florian Grünschläger, Pablo Hernāndez, Raphael Lutz** and **Patrick Stelmach** (whose neighboring office also counts). Thank you for always having nonsense talks or deep talks, for always celebrating

Happy Hours (or creating the cocktails for it with me), and for making my time definitely more fun!

A big thanks to **Maija** for being not only an amazing colleague but also an incredible friend. Our close friendship extended beyond the lab and I always felt supported by you, whether it was during our numerous jogging sessions, hikes, or while teaching me tennis. Thank you for all the wonderful times we spent together, I cannot imagine my time here without you.

To **Manuel Mastel –** "my male-counterpart"-, thank you for the incredible and fun times we shared, and for being the amazing and funny person that you are. "Normal would be boring!"

To **Jonas**, my "fastest" friend, thank you for always being such a helpful, happy, and funny person. Whether you intended to or not, you always managed to put a smile on my face, whether it was laughing with you or "at you" ☺.

I would like to express my deep appreciation to the Biocontact team and the Social Event and Networking team! I am truly grateful to every member who contributed to making my time at DKFZ even more enjoyable.

As a member of "**the other side of the lab**," I also want to thank the entire 4th floor and all the friends I made during my time here. A special shout-out to **Michael Kilian** - you have been my friend for the past 12 years, and I appreciate our friendship, our countless sporty activities and the eating afterwards, the numerous legendary parties, our vacations, and just hanging with you being "you." You made my time at DKFZ and in Heidelberg so much fun. I also want to mention **Selina Jansky, Manuel Piechutta** and **Kevin Lu**. Thank you for making my PhD the best party of my life. Halle02 90th will never be the same without you. Additionally, I want to thank **Laura Zechner** and **Jana Fehr** for always being there and being amazing friends!

Zuletzt möchte ich meiner Familie meinen Dank für ihre unerschütterliche Unterstützung und Ermutigung ausdrücken. Eure Liebe und euer Glaube an mich waren die treibende Kraft hinter meinem Erfolg, und ich bin für eure Präsenz in meinem Leben unendlich dankbar. Ganz besonders danken möchte ich meinen Eltern **Helga** und **Frank** und meiner Schwester **Maren**. Ihr habt mich zu der Person erzogen, die ich bin und ohne euch hätte ich es nie soweit geschafft. Ihr habt mir immer den Rücken frei gehalten. Danke, dass ihr mich zu Unabhängigkeit, Neugierde und Disziplin erzogen und mir dabei immer eure ganze Liebe geschenkt habt. Danke für eure unermüdliche Unterstützung, Hilfsbereitschaft, Verständnis und Liebe. Ohne euch wäre ich nicht da wo ich jetzt bin. Ich habe euch lieb. DANKE!